UNIVERSITY OF L'AQUILA

DEPARTMENT OF INDUSTRIAL AND INFORMATION ENGINEERING AND ECONOMICS

Doctor of philosophy course on Industrial and Information Engineering and Economics:
Curriculum Ingegneria elettrica, elettronica e dell'informazione
XXXVII cycle

Title of the Thesis

Assessing the Impact of Advanced Technologies in Power Converters and Synchronous Reluctance motor Drives: Study Cases and Perspectives

SSD IIND-08/A

PhD student:
Davide Angrilli

Coordinator of the course
Prof.ssa Katia Gallucci

Tutor
Prof. Marco Tursini

A.A. 2024/2025

Abstract

The growing demand for sustainable and high-performance electric drives is accelerating the transition from internal combustion engine (ICE) vehicles to electric vehicles (EVs). This shift is driven by stringent environmental regulations, advancements in electric mobility, and the need for rare-earth-free motor technologies to mitigate supply chain vulnerabilities and environmental concerns. Synchronous reluctance motors (SynRMs) have emerged as a promising alternative to permanent magnet synchronous motors (PMSMs), offering a rare-earth-free solution with potential for high efficiency and cost-effectiveness. However, their adoption has been limited by lower power density, torque capability, and control complexity compared to PMSMs. This doctoral research aims to enhance the viability of SynRMs by addressing key challenges in motor design, control strategies, and power conversion. The study leverages advanced materials, innovative manufacturing techniques, and state-of-the-art power electronics to improve SynRM performance. Novel motor topologies, including asymmetric rotor configurations and the use of amorphous and nanocrystalline alloys, are explored to enhance magnetic properties and reduce losses. Additive manufacturing (AM) is investigated as an enabling technology to optimize rotor geometries, reduce torque ripple, and support rapid prototyping, aligning with the principles of circular economy and sustainability. Silicon carbide (SiC) power modules are employed to increase power density, efficiency, and switching frequency, enabling higher-speed operation while maintaining system efficiency. The use of innovative power components, such as SiC MOSFETs, significantly accelerates the performance of power electronics, making the system much faster. However, this increase in speed is counterbalanced by the growing complexity of control systems, which must manage parametric variations and system nonlinearities. These two opposing effects, faster power electronics and increasingly complex control algorithms, necessitate the development of advanced control systems that go beyond standard microcontrollers. To reconcile these challenges, this research explores the implementation of multiprocessor control architectures, including FPGA-based solutions, which offer the computational power needed to handle real-time control efficiently. Special attention is given to back-to-back converter systems for bidirectional power flow, which are critical for energy recovery, regenerative braking, and grid integration in modern EV applications. To further optimize drive performance, machine learning-based control methods, including artificial neural networks and reinforcement learning, are explored for real-time adaptation to dynamic operating conditions. These techniques improve torque control, efficiency, and fault tolerance compared to conventional control approaches. To validate the proposed solutions, real-time simulation platforms based on multiprocessor architecture are utilized to model and test the SynRM drive system before physical implementation. This approach reduces development time and enhances design accuracy. Additionally, the research aligns with industrial and sustainability goals

by supporting the development of rare-earth-free, high-performance electric drives for mobility and industrial applications. Through a multidisciplinary approach that integrates motor design, advanced power electronics, artificial intelligence, and real-time control, this thesis contributes to the ongoing innovation in electric drive systems. By overcoming the existing limitations of SynRMs, the study paves the way for their widespread adoption in sustainable transportation, renewable energy, and industrial automation, thereby supporting global efforts toward energy efficiency and reduced environmental impact.

Table of Contents

Chapter 1

Introduction

1.1 Research Context and Motivation

The rapid expansion of the electric vehicle (EV) market has brought about a transformative shift in both mobility and industrial sectors. This evolution is driven by the urgent need for sustainable energy solutions, heightened environmental awareness, and stringent regulatory policies. Governments and industries worldwide are implementing measures to promote electrification, including incentives for EV purchases, bans on internal combustion engine (ICE) vehicles, and investments in infrastructure development such as charging stations, energy storage systems, and vehicle-to-grid (V2G) technologies. These efforts aim to not only support the growing adoption of EVs but also address challenges in energy efficiency, grid stability, and environmental sustainability [1][2].

- **The Transition to Electric Mobility**

The transition from ICE vehicles to EVs has gained significant momentum in recent years. A combination of stricter emissions regulations, technological advancements, and shifting consumer preferences has accelerated this shift. For example, the European Union's Clean Vehicles Directive mandates lower pollutant and CO2 emissions, while the Energy Efficiency Directive anticipates nearly 40 million EVs on European roads by 2030. In parallel, some EU member states have introduced incentives for EV adoption and set deadlines for phasing out ICE vehicles, with 2030 often cited as a target year for these bans. China, a global leader in EV adoption, has seen particularly rapid progress, with EVs now comprising 50% of new car sales. This trend highlights the growing acceptance of electric mobility worldwide, emphasizing the need for high-performance, reliable, and cost-effective technologies to support the transition.

- **The Role of Electric Drives in EVs**

Electric drives are at the core of EV functionality, converting electrical energy into mechanical motion with high efficiency. To meet the demands of modern EVs, electric motors must deliver optimal torque, power density, and efficiency across a wide range of operating conditions. Currently, many EV motors rely on rare-earth (RE) permanent magnets, which provide excellent performance but pose significant challenges. These include high and volatile material costs, limited long-term availability, and environmental concerns related to rare-earth mining and

processing. These factors have spurred interest in alternative motor technologies that avoid the use of RE materials while maintaining high performance [2].

- **The H2020 ReFreeDrive Project**

One notable initiative addressing these challenges is the H2020 ReFreeDrive (Rare Earth Free e-Drives featuring low-cost manufacturing) project, funded by the European Union. The project's primary objective is to develop RE-free electric drivetrains that are both cost-effective and industrially feasible for mass production. By eliminating the dependence on RE materials, the project aims to reduce manufacturing costs, enhance sustainability, and address supply chain vulnerabilities.
The ReFreeDrive Consortium, composed of 13 partners from six European countries, including the University of L'Aquila, has explored three key motor configurations:

- Induction Motor (IM): Featuring fabricated and copper die-cast rotors.
- Permanent Magnet-assisted Synchronous Reluctance Motor (PMaSynRM): Utilizing ferrite magnets.
- Pure Synchronous Reluctance Motor (SynRM): Without magnets.

The University of L'Aquila led the development of pure SynRM motors, focusing on fully electric vehicle applications. This involved a detailed analysis of the mechanical, magnetic, and economic properties of various electrical steels to identify the most suitable materials for the application. Two motor sizes, 75 kW and 200 kW peak power, were designed with shared components such as electrical steel, stator and rotor shapes, and housing to reduce manufacturing costs and ensure scalability.

- **Technological Innovations in Power Electronics and SynRM Drives**

Power electronics systems play a critical role in electric drives, managing the flow of energy between the battery, motor, and other components. In the ReFreeDrive project, silicon carbide (SiC) power modules were chosen for power electronics to improve power density and efficiency. These modules enable higher switching frequencies, which are essential for RE-free motors operating at higher speeds than their RE-based counterparts. While SiC technology is currently expensive, its cost is expected to decline as the technology matures, aligning with trends observed in advanced EVs like the Tesla Model 3, which uses custom SiC MOSFETs.
The motors designed under this project were benchmarked against the Tesla Model S 60 (2012), setting ambitious performance goals:

- A 30% increase in specific power.
- A 50% increase in maximum operating speed.
- A 50% reduction in energy losses.
- Compatibility with cooling systems used in ICE vehicles.

By increasing motor speed to 20,000 rpm, the required torque—and consequently the motor weight—was reduced, enhancing power density. However, higher speeds necessitate gearboxes with higher split ratios, which introduce additional losses and reduce overall drivetrain efficiency. Addressing these trade-offs requires a complex optimization process to balance performance, cost, and scalability.

- **Advancements and Challenges in SynRMs**

Among the alternatives to RE-based motors, SynRMs are emerging as a promising solution due to their simple design, absence of rare-earth materials, and potential for high efficiency. However, traditional SynRMs have faced challenges such as lower specific torque, power density, and power factor compared to permanent magnet motors. These limitations have restricted their use in high-performance applications like EVs. Advancements in motor design, including topology optimization, asymmetric rotor configurations, and the use of new materials like amorphous alloys, are helping to address these challenges. Additionally, innovative techniques such as additive manufacturing (AM) with the use of new insulation and conductive materials have improved rotor performance and manufacturability.

- **Integration of Digital Technologies**

The integration of artificial intelligence (AI) into SynRM drives is further transforming the landscape. These technologies enable real-time optimization of control strategies, advanced fault detection, and predictive maintenance. Combined with high-performance hardware such as field-programmable gate arrays (FPGAs), these innovations are enhancing the precision, adaptability, and efficiency of electric drives.

Moreover, the development of fast-charging stations and V2G technology is revolutionizing energy management in EVs. These innovations allow vehicles to dynamically interact with the grid, improving energy efficiency, grid stability, and overall system reliability. In summary, the research and development of electric drives and power converters are at the forefront of innovation in both the mobility and industrial sectors. As the world shifts towards more sustainable and energy-efficient technologies, there is an urgent need for advanced motor designs, more efficient power converters, and smarter control strategies [2],[3].

1.2 Objectives of the Thesis

The primary objective of this doctoral thesis is to advance the development of synchronous reluctance motor (SynRM) drives by exploring how these motors can become a viable and sustainable alternative to permanent magnet synchronous motors (PMSMs). SynRMs are inherently advantageous due to their simpler design and independence from rare-earth materials, which makes them more cost-effective and environmentally friendly. However, their full potential remains underutilized, largely due to challenges related to performance, control strategies, and manufacturing techniques. This thesis aims to address these challenges through a multidisciplinary approach that combines advanced motor design, innovative manufacturing methods, state-of-the-art control strategies, and the latest

developments in electronic technologies. Replacing PMSMs with SynRMs is particularly significant in applications like electric mobility and industrial automation, where high performance, reliability, and efficiency are crucial. PMSMs have long been favored for their high torque density and efficiency, but their reliance on rare-earth materials has raised concerns about supply chain vulnerabilities and environmental impact. SynRMs, with their simpler rotor structure made from standard electrical steel, offer a compelling alternative. To position SynRMs as a strong competitor, this thesis will focus on improving their performance in areas such as torque, efficiency, and power density by leveraging advanced materials, new technologies like amorphous and nanocrystalline alloys that reduce losses and enhance magnetic properties. The thesis also explores the use of innovative manufacturing techniques, such as additive manufacturing (AM). AM enables the production of complex rotor geometries that were previously unachievable, helping to reduce torque ripple and improve overall motor performance. Additionally, AM supports rapid prototyping, which accelerates the development process and reduces material waste, aligning with the principles of a circular economy. Power electronics play a critical role in SynRM drives, particularly bridge converters that control energy flow between the power source and the motor. In this thesis, particular attention will be given to the analysis and simulation of back-to-back converter systems, which are critical components in modern electric drive applications. These converters allow bidirectional power flow, making them essential for energy recovery and advanced functionalities such as regenerative breaking and grid integration. The study will explore their performance under various operating conditions, aiming to optimize their efficiency and reliability. Additionally, the thesis will investigate the use of neural networks for the control and fault management of these converter systems. Neural networks, with their ability to model complex nonlinear relationships and adapt to dynamic changes, offer a promising alternative to traditional control strategies. They will be applied to improve the precision and robustness of control algorithms while also enabling advanced fault detection and diagnosis. By analyzing these aspects, the research seeks to develop innovative solutions for enhancing the performance and reliability of electric drives and power conversion systems. Control strategies are another focal point of the thesis. SynRMs pose unique challenges due to their nonlinear characteristics and time-varying parameters, which traditional PID controllers struggle to manage. This work explores advanced control techniques, such as Field Oriented Control (FOC), while integrating machine learning-based methods, including neural networks and reinforcement learning. These approaches allow the control system to adapt dynamically to changing operating conditions, ensuring robust and efficient performance.

To support these advanced control strategies, high-performance hardware platforms, such as field-programmable gate arrays (FPGAs) and system-on-chip (SoC) architectures, will be required. These platforms enable real-time implementation of computationally intensive algorithms, offering the speed and flexibility needed for precise control. Additionally, real-time simulation tools will be utilized to test and optimize designs before physical implementation, significantly reducing development time and costs. This thesis not only aims to improve the technical aspects of SynRM drives but also aligns with broader goals of sustainability and innovation. By addressing key challenges in motor design, manufacturing, control, and hardware, this research seeks to pave the way for SynRMs to play a central role in the future of electric mobility, renewable energy,

and industrial applications. Through a combination of cutting-edge technologies and forward-thinking strategies, the work presented here aspires to redefine the standards for sustainable, efficient, and high-performance electric drive systems.

Chapter 2

Literature Review

The literature review in this doctoral thesis provides a comprehensive analysis of existing research related to power converters and synchronous reluctance motor (SynRM) drives. It contextualizes the study within the broader academic field, identifying key advancements, theories, and methodologies. By examining previous work, the review highlights gaps and unresolved challenges, justifying the need for this research and its contribution. Additionally, it explores the latest developments in motor design, control strategies, manufacturing techniques, and emerging technologies like machine learning and additive manufacturing. This foundation establishes the theoretical and methodological frameworks for the thesis, positioning the study within the academic discourse and underscoring its relevance and significance.

2.1 Rapid Control Prototyping: Tools and Methodologies

Rapid Control Prototyping (RCP) has become a critical methodology in the development of control systems for electrical drives. Its significance lies in addressing the growing demands for performance, safety, and flexibility in modern industrial applications. The following literature review delves into the tools and methodologies pivotal to RCP, examining the challenges, advancements, and specific implementations relevant to Synchronous Reluctance Motor (SynRM) drives.

2.1.1 The Role of Rapid Control Prototyping

The prototyping phase is instrumental in achieving stringent requirements for control system performance. Increasing innovation and complexity necessitate rapid testing and experimental validation to ensure efficient designs while reducing time-to-market. RCP fulfills these requirements by providing iterative testing capabilities through both offline and real-time simulations [4], [5].

2.1.2 Offline Simulation: Foundation of RCP

Offline simulation is typically the initial step in RCP. It involves validating preliminary control designs by replacing physical components such as motors, converters, and sensors with analytical models. This approach enables:

- Rapid Validation: Using detailed models to assess the dynamic performance of electrical drives without hardware.
- Flexible Execution: Running simulations on PCs, ranging from seconds to hours, depending on the model complexity [6], [7].

Moreover, tools like MATLAB/Simulink support code generation for microcontrollers, allowing a seamless transition from simulation to hardware implementation. This automation reduces implementation time and minimizes manual coding errors, providing a comprehensive approach to control system design [8], [9].

2.1.3 Real-Time Simulation: Bridging Theory and Practice

Real-time simulation plays a complementary role by enabling the execution of control algorithms on hardware while maintaining real-world timing constraints. This step involves:

- Integration with Target Hardware: Using microcontrollers such as the TI C2000 family to test control strategies under realistic conditions.
- Experimental Validation: Assessing system performance with the identical control code used in offline simulations [10], [11].

2.1.4 Hardware-in-the-Loop (HIL) and Software-in-the-Loop (SIL)

HIL and SIL are crucial methodologies within RCP [4]-[13]:

- HIL: Simulates the power system on hardware test boards, enabling high-fidelity emulation of real-world dynamics.
- SIL: Uses software environments to simulate the plant, offering a cost-effective and scalable testing framework.

These approaches ensure comprehensive validation of control systems before deploying physical prototypes.

2.1.5 Detailed Analysis of Offline and Real-Time Simulations

- **Offline Simulation**

Advantages

1. Flexibility in Model Complexity: Offline simulations allow for the use of highly detailed and complex models without real-time constraints [6].
2. Ease of Debugging: Developers can pause, replay, and modify simulations, enabling in-depth debugging and optimization.
3. Cost-Effective: Does not require specialized real-time hardware, reducing upfront costs [5].
4. High Accuracy: With no time constraints, solvers can use smaller time steps and advanced algorithms to achieve high accuracy [9].

Disadvantages

1. Lack of Real-Time Validation: Offline simulations cannot mimic the dynamic interactions of real-world conditions accurately.
2. Time-Intensive for Complex Models: Simulating intricate systems may take hours or days, especially for large-scale models [6], [12].
3. Limited Interfacing: Does not integrate with actual hardware components, making hardware-specific issues hard to predict [10].

- **Real-Time Simulation**

Advantages

1. Realistic Testing: Enables dynamic validation under real-world conditions, improving reliability and robustness [4], [11].
2. Hardware Integration: Directly interfaces with physical components, allowing hardware-specific optimizations [13].
3. Supports Iterative Development: Real-time feedback facilitates rapid adjustments and validation of control algorithms [15].
4. Time Efficiency in Prototyping: Speeds up the transition from simulation to deployment [9].

Disadvantages

1. Hardware Dependency: Requires specialized hardware like real-time processors or FPGAs, increasing cost and complexity [8], [11].
2. Reduced Model Complexity: Real-time constraints limit the computational complexity of models that can be used [7].
3. Debugging Challenges: Limited ability to pause or rewind during execution makes debugging more complex [10].
4. Accuracy Trade-offs: Real-time simulations may sacrifice accuracy for computational speed, particularly for highly dynamic systems [11], [13].

2.1.6 Tools and methodologies

MATLAB/Simulink, enhanced by Embedded Coder Support Packages, is a primary tool for RCP.

It supports:

- Code Generation: Automating the transition from simulation to hardware implementation.
- Hardware Peripherals Integration: Facilitating I/O management for microcontrollers.
- Interrupt-Driven Scheduling: Ensuring real-time control loop execution [9].

The methodology generally used today to achieve accurate and efficient real-time simulation with MATLAB/Simulink is the following.

The process starts with detailed system modeling and offline simulations to validate and refine control strategies. Once the model is accurate, hardware-compatible code is generated using Embedded Coder and deployed to the target microcontroller (e.g., TI C2000) via Code Composer Studio. Real-time execution is achieved by synchronizing control algorithms and plant simulations with hardware timing constraints, using interrupt-driven scheduling. Performance is monitored, and the system is iteratively refined to ensure fidelity with the physical system and optimal computational efficiency. It ensures a robust and reliable process for validating and deploying control strategies in modern industrial applications [5],[16],[19],[20].

2.2 Real-Time Simulation for Drive Control Systems

Real-time simulation has emerged as an indispensable tool for the development and testing of drive control systems. By enabling the execution of control algorithms on hardware while maintaining real-world timing constraints, real-time simulation facilitates accurate testing of system dynamics and control strategies. The key applications in Synchronous Reluctance Motor Drives are**:**

1. Dynamic Performance Validation: Real-time simulation allows for the validation of drive control systems under dynamic operating conditions, ensuring that control algorithms can respond effectively to changes in load, speed, and other variables [12], [16], [17].
2. Hardware Integration: Direct interfacing with physical components, such as sensors and actuators, helps to fine-tune the control system for real-world applications. This integration is critical for validating hardware-specific issues, such as latency and signal noise [17], [18],[19].
3. Advanced Control Strategies: Real-time simulation supports the implementation and testing of advanced control algorithms, such as Maximum Torque Per Ampere (MTPA), field-oriented control (FOC), and

self-commissioning techniques. These strategies enhance the efficiency and performance of drive systems [14],[16],[17],[19],[21].

4. Parallel Processing for Accuracy: Leveraging parallel processing capabilities, such as those provided by the Control Law Accelerator (CLA) in TI microcontrollers, real-time simulation reduces computation times, enabling the use of more complex and accurate motor models [17]-[19],[21].

2.3 Fundamentals of Power Converters and Drives

Power converters and electric drives are critical technologies enabling the transformation, regulation, and utilization of electrical energy in diverse applications. These systems form the backbone of modern energy and industrial systems, addressing the growing demands for efficiency, sustainability, and advanced functionality. This section explores the fundamental principles of power converters and drives, their classifications, structure and applications, control strategies and the recent advancements that have shaped the field.

2.3.1 Power Converters: Classification and Principles of Operation

Power converters are devices designed to transform electrical energy from one form to another with high precision and efficiency. Based on their input and output types, they are broadly classified into four categories:

1. AC-AC Converters: These modify AC power by adjusting amplitude, frequency, or phase. Examples include cycloconverters and matrix converters for variable-speed drives and industrial applications [22],[37]
2. AC-DC Converters (Rectifiers): These convert alternating current (AC) into direct current (DC). Applications include renewable energy systems, battery charging stations, and industrial motor drives [23]-[32].
3. DC-AC Converters (Inverters): These transform DC into AC. They are widely used in solar inverters, uninterruptible power supplies (UPS), and electric vehicle drive systems [33]-[37].
4. DC-DC Converters: These converters change DC voltage levels for applications like electric vehicles, telecommunications, and power distribution in microgrids [31],[37].

Power converters play even a crucial role in EV charging systems, enabling efficient energy transfer and voltage regulation. AC-DC converters transform grid electricity into DC power for battery charging, while DC-DC converters regulate and optimize voltage levels during the charging process. Integrated converters leverage the vehicle's drive inverter and motor inductance, reducing costs, weight, and complexity. Modular converter designs enable scalable fast and ultra-fast charging solutions. These technologies support various charging configurations, including onboard, offboard, unidirectional, and bidirectional systems, essential for smart charging and grid integration [38].

2.3.2 Electric Drives: Structure and Applications

Electric drives consist of a motor, a power converter, and a control system working in tandem to regulate speed, torque, and position. Based on motor types, electric drives are classified as:

1. DC Drives: Known for their simplicity and precise speed control, DC drives are widely used in applications such as elevators and rolling mills [39].
2. AC Drives: These control AC motors, including induction motors, synchronous motors, and synchronous reluctance motors. AC drives dominate industrial applications due to their robustness and energy efficiency [40].
3. Servo Drives: Designed for high-precision applications, such as robotics and CNC machinery, servo drives integrate advanced feedback mechanisms [41].

Advancements in digital signal processing (DSP) and microcontroller technologies have enabled sophisticated control algorithms and real-time monitoring, making drives smarter and more adaptable to dynamic conditions.

2.3.3 Control Strategies for Power Converters and Drives

Control strategies are critical to ensuring optimal performance under varying operating conditions. Key methods include:

1. Pulse-Width Modulation (PWM): A widely used technique for controlling converter switches, enabling precise voltage and current regulation [42].
2. Vector Control: Primarily used for AC drives, this method decouples torque and flux components, offering dynamic and efficient motor control [43].
3. Direct Torque Control (DTC): An alternative to vector control, DTC provides fast torque and flux control without requiring complex transformations [44].
4. AI-Based Control: Machine learning algorithms are increasingly used to improve fault detection, and for estimation purposes [45]-[53].

2.3.4 Advancements and Challenges

The field has witnessed significant advancements driven by energy efficiency and sustainability demands. Key trends include:

- AI-Based Control: The fundamental characteristics of neural networks [141]-[145] and Machine learning algorithms are increasingly used to power electronics control, optimization, fault diagnosis, and predictive maintenance [54]-[55].
- Additive Manufacturing (AM): Facilitates the production of passive components (i.e., resistors, inductors, and capacitors), circuit boards, and packages of power electronic devices [56],[57].
- GaN and SiC power devices: The evolution of wide-bandgap semiconductors, such as silicon carbide (SiC) and gallium nitride (GaN), has enhanced the performance of converters by offering higher efficiency, faster switching, and reduced thermal losses [58],[59].

  However, challenges such as electromagnetic interference (EMI), thermal management, and reliability under extreme conditions remain areas of ongoing research [60]-[62]

2.4 Testing of Synchronous Reluctance Motors.

The optimal control of synchronous reluctance motors (SynRMs) relies on precise knowledge of their specific control maps, which are highly dependent on motor parameters [63],[64].
Traditional methods for experimentally determining these maps across the full torque-speed range are both time-intensive and energy-demanding, typically involving purely dissipative braking benches.
A more energy-efficient approach involves the use of a back-to-back testing bench [65],[66], where two mechanically coupled and electrically connected machines operate in tandem, sharing the same DC power supply [67]-[69].
In this configuration, one machine functions as a motor, delivering mechanical power to the other, which acts as a brake and regenerates electrical energy back to the motor [70].
This setup minimizes the energy drawn from the supply, as it only compensates for losses in the machines and converters.
Key control maps, such as maximum torque per ampere (MTPA), maximum torque per voltage (MTPV), maximum power factor, and maximum efficiency, are experimentally determined while respecting current and voltage constraints [64],[71].

2.5 Evolution of Technologies in Synchronous Reluctance Motors

Electric motors (EMs) are at the forefront of modern industrial applications and the electrification of transportation. The global electric machinery market is projected to grow to $195 billion by 2030, with an annual growth rate of 6.3% [1]. This growth underscores the pressing need for enhancing the performance and efficiency of these electromechanical devices. Among electric motors, synchronous reluctance motors (SynRMs) are emerging as a promising alternative to permanent magnet synchronous motors (PMSMs) and induction motors (IMs) due to their simple construction, cost-effectiveness, and reduced reliance on rare earth materials [2].

2.5.1 The Role of SynRMs in Modern Applications

PMSMs, widely used in electric vehicles (EVs) and plug-in hybrids (PHEVs), offer superior power-to-weight ratios and high torque across varying speeds, [3]. However, the reliance on rare earth magnets introduces challenges related to high production costs, supply chain fragility, and environmental concerns [72].[73]. SynRMs, which leverage reluctance torque generated by differences in magnetic reluctance along orthogonal axes, are increasingly viewed as viable candidates for the next generation of electric motors, particularly in traction applications.
The appeal of SynRMs lies in their simple rotor design, which uses only electrical steel and eliminates the need for magnets or windings. However, they exhibit lower efficiency and power factors compared to PMSMs, necessitating innovations in design and control to bridge the performance gap [74]-[80].

2.5.2 Advances in SynRM Technologies: Material Innovations

Recent developments in materials have significantly improved SynRM performance:

Magnetic Materials

- High-Performance Magnetic Materials: Improved silicon steel laminations reduce core losses, enhancing efficiency at high operating speeds [78]-[81].
- Soft Magnetic Composites (SMCs): These materials enable three-dimensional magnetic flux paths, minimizing eddy current losses [82]-[85].
- Amorphous and nanocrystalline irons: they exhibit excellent magnetic properties, including low coercivity, high permeability, and low hysteresis losses, making its ideal for achieving IE5 motor efficiency standards due to its significantly reduced iron losses. [85][86].

Conductive Materials

- Copper– chromium–zirconium powder (CuCrZr) and aluminum alloy powder (AlSi10Mg) : Its combine low mass density and suitable conductivity for HF operation and eddy current limitation [87]-[89].
- Carbon Nanotubes (CNT)-Cu composites: The synergy between graphene and copper represents a particularly intriguing avenue of investigation. They have a conductivity 2.6 times greater than that of pure copper. Furthermore, these composites demonstrate a resistivity temperature coefficient one order of magnitude lower than conventional copper.[90][91].

Advanced Insulation Material

- Ceramics: A Shield Against Extreme Thermal Conditions
  Traditional enamel coatings on conductor wires (magnet wires) can be substituted with ceramics, which offer superior temperature resistance. Ceramic insulation, known for its excellent thermal stability, allows these wires to withstand temperatures exceeding 300°C,far surpassing the 180°C maximum limit of the H-class insulation used in electric motors [92].
- PEEK Polymers: Augmented Safeguards Against Hazardous Currents.
  Polyether Ether Ketone (PEEK) polymers are highly reliable materials in the field of insulation. They can be used in electric motors for applications such as slot and bearing insulation, effectively reducing the risks posed by harmful leakage currents [93].

2.5.3 Advances in SynRM Technologies: Additive Manufacturing (AM)

Additive manufacturing (AM) has emerged as a revolutionary tool in the production of SynRM components [80]-[94], [146]-[148]:

- Customized Topologies: AM enables the creation of complex geometries that improve flux distribution, reduce torque ripple and improve performance.
- Sustainability: AM processes minimize material waste and promote the use of recyclable materials, aligning with the principles of a circular economy.
- Integration of Cooling Systems: AM facilitates the production of integrated cooling channels, enhancing thermal management.

2.5.4 Variants of SynRMs: Line-Start Synchronous Reluctance Motors (LSSynRMs)

LSSynRMs are gaining traction in industrial applications with low inertia and fixed speeds [95],[96]:

- **Efficiency:** LSSynRMs offer higher efficiency than induction motors with minimal changes to the manufacturing process.
- **Applications:** They are suitable for replacing IE3 induction motors in IE4 motor categories for low-inertia applications.

2.5.5 Variants of SynRM: Permanent Magnet Assisted Synchronous Reluctance Motors (PMaSynRMs)

By incorporating ferrite magnets, PMaSynRMs improve the performance of SynRMs [97],[98]:

- **Advantages:** PMaSynRMs achieve higher torque and efficiency while maintaining cost-effectiveness compared to PMSMs.
- **Challenges:** The inclusion of magnets increases manufacturing complexity, requiring advancements in rotor construction techniques [83].

2.6 Machine Learning in Control Systems

2.6.1 Machine Learning-Based Control

The increasing complexity of electric motor systems, including synchronous reluctance motors (SynRMs), has driven the adoption of machine learning (ML) techniques in control strategies. Traditional control methods, such as proportional-integral-derivative (PID) controllers or model-based approaches like vector control and direct torque control (DTC), often struggle with nonlinearities, parameter variations, and dynamic operating conditions [42]-[44][15][17][18][20] [24][67][68][70]. ML-based control has emerged as a powerful solution to address these challenges by leveraging data-driven models that adapt and optimize control performance in real-time, effectively replacing traditional PID controllers to handle the nonlinearities of the SynRM and the time-varying nature of its parameters [99]-[105].

Key Advantages and Applications

Machine learning enables advanced capabilities in control systems through:

1. Adaptive Control: ML algorithms, such as reinforcement learning (RL) and neural networks, dynamically adjust control parameters to account for variations in motor characteristics, environmental conditions, and load profiles [105]-[112].
2. Predictive Maintenance: By analyzing historical and real-time data, ML algorithms predict potential failures, facilitating proactive interventions [113],115].

3. Fault Detection and Diagnosis: ML models can analyze patterns in system behavior to detect anomalies and diagnose faults, improving reliability and reducing downtime [116][118].
4. Nonlinear Control: Reinforcement learning and deep learning methods effectively manage nonlinear dynamics, enabling precise torque and speed control in SynRMs under complex conditions [119][122].

2.6.2 MATLAB/Simulink Toolboxes development Suite.

MATLAB and Simulink offer a comprehensive suite of toolboxes to support machine learning applications, enabling seamless model development, training, and deployment. The Reinforcement Learning Toolbox™ provides tools to design and train reinforcement learning agents, which are particularly suited for dynamic control applications like electric motor drives. The Deep Learning Toolbox™ supports the creation and optimization of neural networks with prebuilt algorithms and layers for tasks such as classification, regression, and control. Additionally, the Statistics and Machine Learning Toolbox™ provides tools for traditional ML workflows, including data preprocessing, feature selection, and predictive modeling. These toolboxes integrate seamlessly with Simulink, allowing users to simulate real-time control systems with ML components. Deployment to embedded hardware platforms, such as FPGAs and microcontrollers, is supported through code generation tools like MATLAB Coder™, making it an efficient environment for implementing ML-based control in industrial applications [123],[124].

2.6.3 Hardware Advances

Microcontrollers with a single CPU are inadequate for implementing neural network-based control systems due to their inability to meet the stringent execution times required, typically between 25 to 100 µs. In contrast, FPGAs are highly suitable for ML-based SynRM drives due to their ultra-low latency capabilities, optimized hardware acceleration, and support for hardware-software co-design. FPGAs, particularly those with System-on-Chip (SoC) architecture, integrate memory, processors, and programmable logic, offering flexibility, efficiency, and high performance [125],[128].
Platforms like Xilinx Zynq Ultrascale+ MPSoC have demonstrated exceptional capabilities, achieving neural network inference for reinforcement learning [129],[130]. These advancements highlight the potential of FPGA-based architectures for next-generation electric drive control systems [131].

Chapter 3

Rapid Control Prototyping

Part of the work presented in this chapter has been previously published in [16]

The significance of rapid prototyping lies in its ability to address the increasing demands for performance, safety, and flexibility in modern electrical drive control systems. As drive systems become more complex and innovative, rapid testing and experimental validation have become essential to reduce time-to-market and ensure optimal performance and efficiency [4][5]. Offline simulations play a critical role in the early stages of development, allowing engineers to assess the feasibility of their designs and refine control strategies before real-time implementation [6].
This chapter focuses on the rapid control prototyping (RCP) of electrical drives, specifically addressing both offline and real-time simulations implemented on a Texas Instruments Delfino F28379S microcontroller (Figure 3.1). The study examines a synchronous reluctance motor (SynRM) drive, which introduces additional complexity due to its inherent electromagnetic nonlinearities. The approach integrates both offline and real-time simulation methodologies, each offering unique benefits to the development process while utilizing the same control algorithm across different platforms.

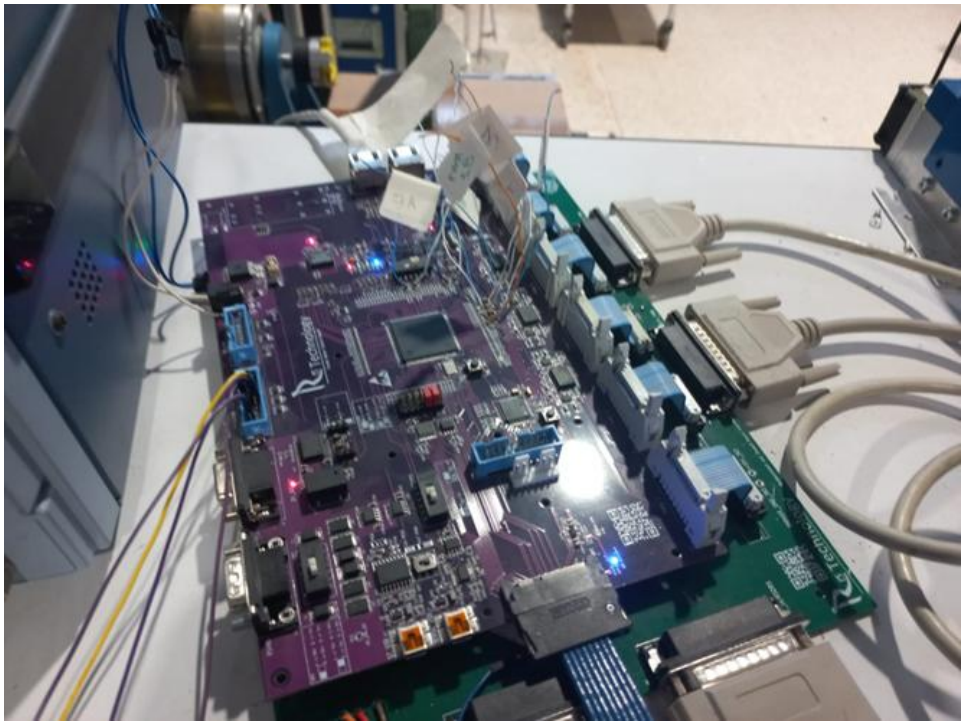

Figure 3.1: Development board based upon Delfino F28379S microcontroller.

In the **offline prototyping phase**, the motor, power converter, and transducers are modeled within the MATLAB/Simulink environment. This phase provides a comprehensive framework for analyzing and validating the dynamic performance of the electrical drive. Offline simulations replace physical hardware components with analytical models, enabling rapid testing and refinement of control algorithms. These simulations are typically executed on PCs, with computational times ranging from seconds to hours depending on the model's complexity and the desired level of accuracy [7]. Furthermore, the capability of MATLAB/Simulink to generate custom-target code allows developers to transition seamlessly from simulation to hardware deployment. This automation reduces implementation time and eliminates potential errors associated with manual coding.

In the **real-time prototyping phase**, the validated models are deployed directly onto the microcontroller, where both the motor dynamics and control algorithms are executed in real-time. By maintaining identical control logic between offline and real-time simulations, the methodology ensures consistency and minimizes discrepancies. The transition from offline to real-time simulation is achieved using MATLAB/Simulink's Embedded Coder, which simplifies code generation and deployment onto the target hardware [8].

Real-time simulations are particularly valuable because they replicate the exact timing constraints of the final application. This approach facilitates direct interaction with hardware peripherals, such as ADCs and PWMs, enabling accurate testing under realistic conditions [9].

3.1 Development and Implementation Methodologies

Traditional approaches to RCP often involve stages where the control Software Under Test (SUT) operates on the final target hardware but is not directly connected to the physical plant [10][11]. These methods are typically categorized into two classes:

1. **Hardware-in-the-Loop (HIL)**: The plant is simulated on an external hardware platform that interfaces with the control system. This method offers high fidelity but comes with increased hardware costs.
2. **Software-in-the-Loop (SIL)**: The plant is simulated entirely within software, often on PCs or other digital platforms such as microcontrollers, FPGAs, or DSPs. SIL provides a cost-effective and scalable solution but may lack the physical accuracy of HIL [12][13]

In this study, the proposed RCP methodology combines elements of both HIL and SIL by simulating the plant and control system directly on the same hardware platform. This unified approach reduces costs while maintaining high levels of accuracy and realism. The methodology also ensures a seamless transition between offline simulations running on a PC and real-time simulations running on the final target hardware (Figure 3.2).

Experimental validation is a key component of this work. The tests conducted focused on critical aspects of drive prototyping, such as:

- **Sensor Initialization and Compensation**: Ensuring accurate sensor readings under varying operating conditions.
- **Parameter Self-Commissioning**: Automating the identification and optimization of system parameters to improve performance.
- **Regulator Tuning**: Fine-tuning control algorithms to achieve the desired dynamic response and stability.

The study's application to SynRM drives is particularly noteworthy, as these motors present unique challenges due to their electromagnetic nonlinearities. Advanced modeling and control strategies are required to accurately represent and manage these dynamics [14][15]. Despite the importance of real-time simulations, experimental validations of such simulations for SynRM drives have not been widely reported in the literature, making this study a significant contribution to the field.

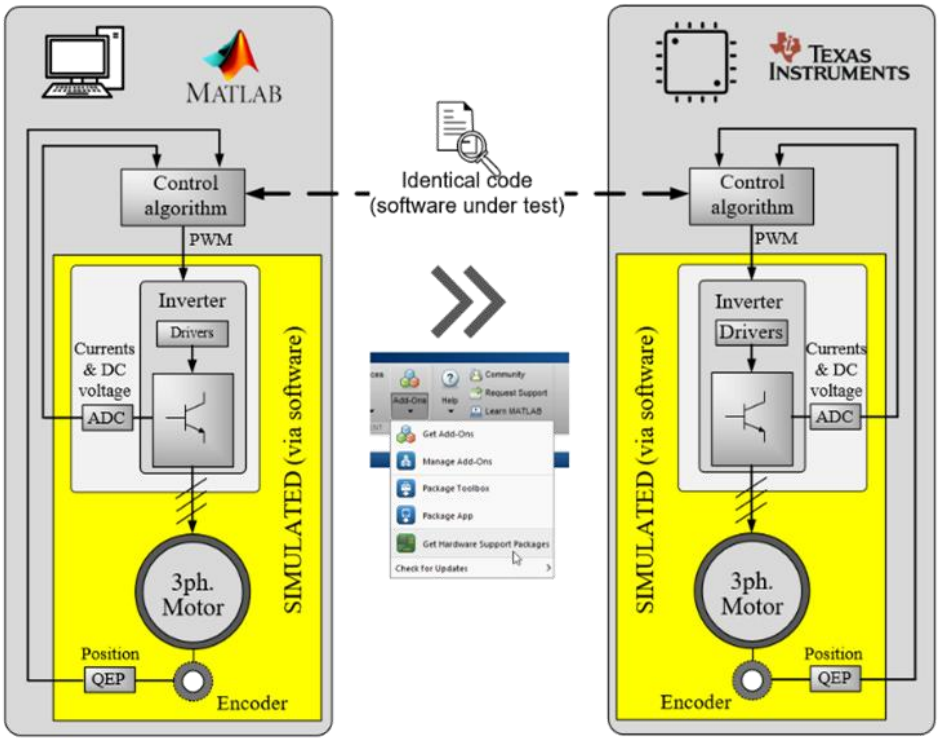

Figure 3.2: Prototyping schemes: from the offline simulation (left) to real-time simulation (right) with Matlab/Simulink Embedded Coder Support Packages

In conclusion, this RCP methodology provides a robust and efficient framework for the development of modern electrical drive systems. By integrating offline and real-time simulations, this approach minimizes development time and costs while ensuring high accuracy and reliability. The experimental results demonstrate the effectiveness of this methodology in addressing the complex requirements of SynRM drives, paving the way for further advancements in rapid prototyping and control system design.

3.2 Using Matlab/Simulink for Rapid Control Prototyping

An essential requirement in control prototyping is the ability to simulate the real-time control code as implemented in the final application. Achieving this involves two critical capabilities: first, a simulation environment capable of generating code for the target microcontroller, and second, the possibility to use that same code for offline simulation. This dual functionality ensures that the control algorithms developed and tested in simulation can seamlessly transition to hardware deployment without discrepancies.
The availability of Embedded Coder Support Packages for widely used controllers, such as the Texas Instruments (TI) C2000 family, positions MATLAB/Simulink as a robust platform for the rapid prototyping of electric drives (e-drives). These support packages enable dialog-based programming of the target microcontroller's hardware peripherals, linking their I/O signals to the control logic developed in Simulink. They also provide the capability to generate executable code directly from the Simulink model. Furthermore, the packages support interrupt-driven scheduling, which is crucial for real-time control applications, as it allows the control code to respond promptly to peripheral-generated events.

3.2.1 Real-Time Control Architecture

Figure 3.3 depicts the standard real-time control architecture of an e-drive, implemented using a Simulink model. The design includes key blocks such as:

- **Hardware Interrupt**: This block manages time scheduling for interrupt-driven tasks, assigning appropriate priorities. Two main Interrupt Service Routines (ISRs) are configured:
    - **Control Algorithm ISR**: Executes the real-time motor-drive control routine.
    - **Serial Receive ISR**: Manages data reception from the host user.
- **Idle Task**: Handles low-priority tasks, such as sending debugging data to the host user via serial communication. The scheduling blocks activate these ISRs in response to events generated by the microcontroller's peripherals.

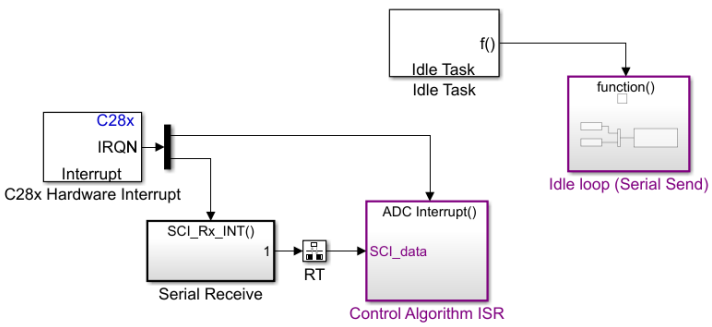

Figure3.3: The typical interrupt-based control architecture in Simulink is designed to efficiently handle real-time tasks by leveraging hardware interrupts for accurate timing

3.2.2 Simulation and Code Generation Capabilities

To bridge simulation and real-time execution, Simulink provides specific functionalities such as the **variant source block**, which dynamically switches outputs between the "sim" input for simulation and the "codegen" port for code generation. Similarly, interrupt blocks have a "sim" input to replicate their behavior during simulation. These features allow developers to prototype the actual real-time control architecture at the simulation stage, facilitating a seamless transition to hardware implementation.

Figure 3.4 showcases a Simulink model arranged for fast prototyping. In this setup:

- The **Hardware Interrupt** block triggers ISRs in response to simulated events from microcontroller peripherals, represented by the "SimIRQ" input.
- **I/O signals** from the control ISR interact with the simulated e-drive components, including the motor, power converter, transducers, and the peripherals of the target microcontroller involved in the control loop.

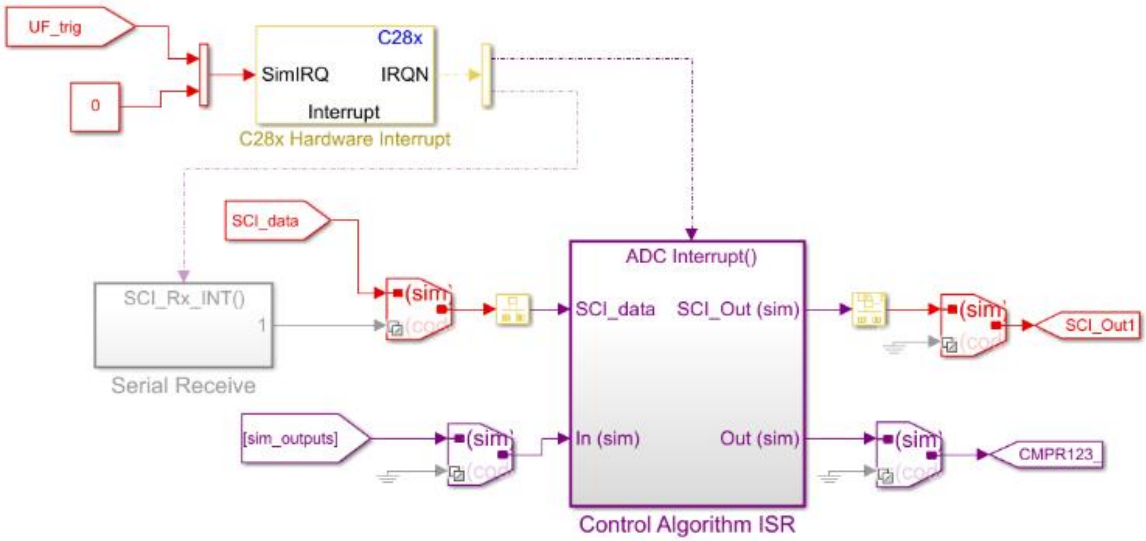

Figure 3.4: The control architecture used for offline simulation in Simulink is structured to replicate the behavior of the real-time control system in a simulated environment.

3.2.3 Timing and Synchronization in Real-Time Control

The timing of the control code is critical and is shown in Figure 3.5, which details a field-oriented control (FOC) architecture for an AC motor using space-vector pulse width modulation (SV-PWM). The control ISR is synchronized with the fixed modulation period of the PWM inverter (T_{PWM}) via the underflow signal of the modulation carrier (UF_trig). This signal also triggers the high-dynamic measurement of control inputs, such as motor currents and DC bus voltage, using the microcontroller's ADC peripheral.

Within each PWM period, the control ISR performs the following actions:

1. **Rotor Position Measurement**: The ISR reads the rotor position from the Quadrature Encoder Peripheral (QEP), computes the rotor speed, and aligns the field orientation.
2. **Execution of Control Logic**: Using the position and current feedbacks, the ISR calculates the required control actions to achieve the desired motor performance.
3. **Data Exchange Tasks**: The remaining time within the PWM period is allocated to low-priority tasks, such as exchanging data with the host user via a serial link.

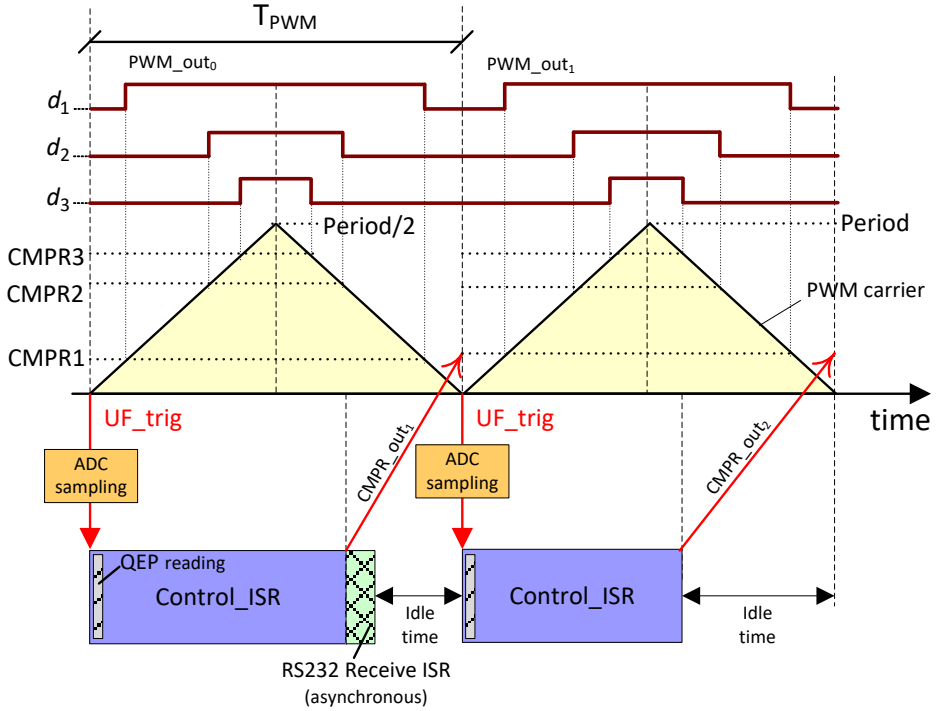

Figure. 3.5. The real-time control timing of a Space Vector Pulse Width Modulation (SV-PWM) e-drive

3.2.4 Code Generation and Peripheral Integration

An exploded view of the control ISR implemented in Simulink is presented in Figure 3.6, highlighting its configuration for both code generation and offline simulation. During code generation, measurement feedbacks (currents and DC bus voltage) and PWM outputs are linked to the software drivers of the target controller peripherals. These peripherals—such as the ADC, QEP, and PWM units—are represented as Simulink blocks within the Embedded Coder library.
In the example shown, the target device is the TI Delfino F28379S microcontroller. The Simulink model ensures that the code integrates seamlessly with the microcontroller's hardware drivers, allowing for a smooth transition from simulation to real-time implementation. The resulting system leverages advanced

features like interrupt scheduling and peripheral integration to deliver a high-performance control solution.
In doing so, by combining advanced simulation tools with real-time execution capabilities, this methodology enables rapid prototyping of control systems for e-drives. The ability to simulate the actual real-time control architecture during the development phase ensures accuracy, reduces debugging time, and accelerates deployment. The integration of Simulink's simulation and code generation features with hardware-specific support packages like Embedded Coder makes it an invaluable tool for modern motor control applications.

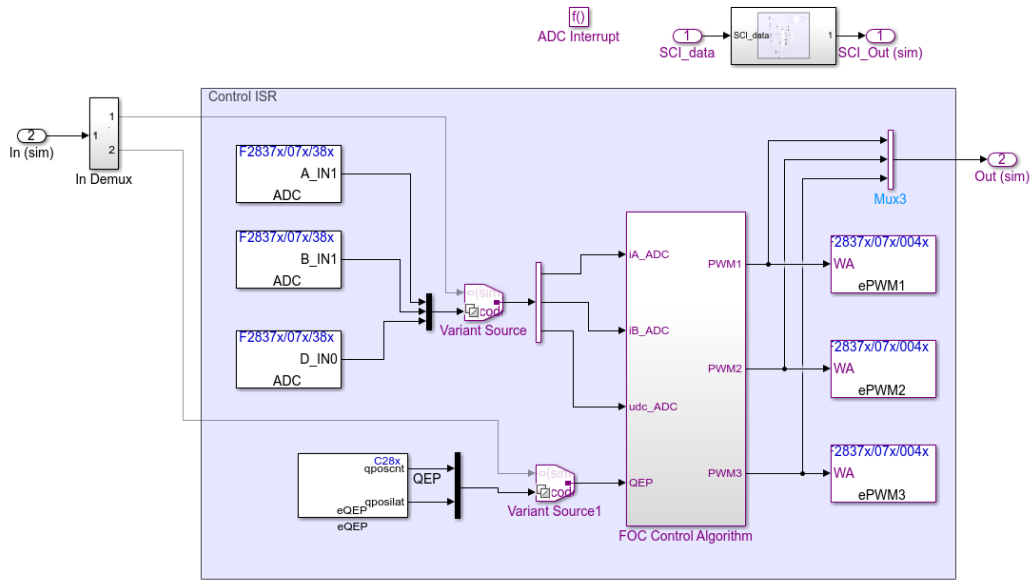

Figure 3.6: Control ISR arranged for offline simulation in Simulink

3.2.5 Comparison Between Offline and Real-Time Simulation Implemented in MATLAB/Simulink

The comparison between offline and real-time simulation highlights the distinct methodologies and considerations required for effective prototyping of e-drives.

- **Offline Prototyping**

In offline prototyping, the e-drive model, which includes the motor, power converter, and transducers, is integrated into the control scheme depicted in Figure 3.4.
The resulting system is then simulated entirely within Simulink. Key aspects of offline prototyping include:

1. **Placement Outside the Control ISR**: The e-drive model is positioned outside the interrupt-driven control ISR block. As a result, the system is computed as a time-continuous model using either a fixed-step or variable-step solver, depending on the simulation settings.

2. **Target-Specific Peripheral Simulation**: To align closely with the microcontroller-dependent implementation, the behavior of I/O peripherals (e.g., ADC, QEP, PWM) must also be simulated. This includes replicating the signal attributes and interactions with the control system.

Figure 3.7 illustrates the portion of the Simulink model that simulates the e-drive. This model includes blocks to represent the hardware characteristics of the microcontroller's I/O peripherals. The power converter is modeled as an ideal voltage source inverter with two operational modes:

- **Ideal Switching Mode**: Simulates the detailed operation of the PWM unit.
- **Ideal Average Mode**: Models the average behavior of the inverter over a PWM period.

This dual-mode capability ensures that the same e-drive model can be reused in both offline and real-time simulations, which is particularly advantageous for maintaining consistency and simplifying transitions between the two phases.

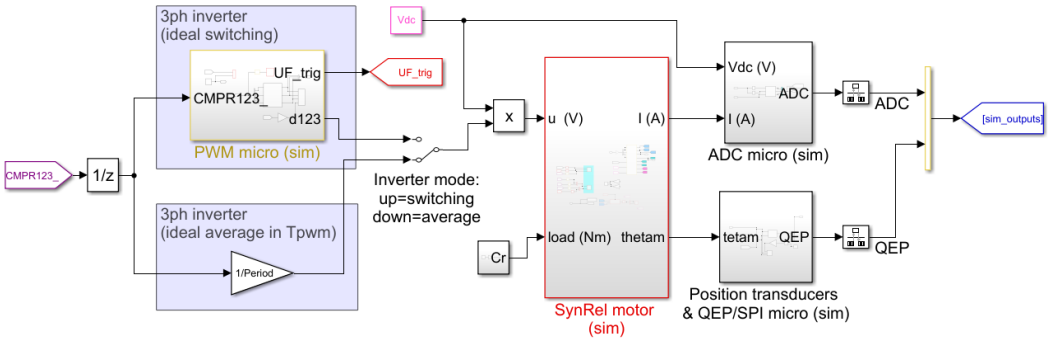

Figure 3.7: Model of the e-drive arranged for offline simulation

- **Real-Time Prototyping**

In real-time prototyping, the e-drive model is embedded within the real-time control code and executed directly on the microcontroller hardware. The same e-drive model used in offline simulation (as shown in Figure 3.7) can be adapted for real-time use by placing it inside the control ISR block. This adaptation introduces several requirements:

1. **Solver Implementation**: The motor model's nonlinear differential equations must be solved directly on the microcontroller. A 4th-order fixed-step Runge-Kutta algorithm is chosen for its balance between computational efficiency and solution accuracy [5].
2. **Time-Step Selection**: The solver's time step is set to match the PWM period (T_{PWM}), ensuring synchronization with the control step. While this approach simplifies integration, custom solver implementations could allow for more accurate solutions if finer time steps are desired.

In this real-time configuration, the simulation of the microcontroller's PWM unit is unnecessary. Instead, the inverter is modeled using its "average in the period"

behavior, which represents its effective output over a PWM cycle. This simplification reduces computational demands while maintaining sufficient accuracy for control purposes.

- **Dual Use of Models in Offline and Real-Time Simulations**

Simulink's capability to integrate custom solver algorithms directly into model subsystems enables the same e-drive model, including the embedded model, to be used for both offline and real-time simulations. This dual usage offers two significant advantages:

1. **Direct Comparisons**: The identical e-drive model ensures that offline and real-time responses can be directly compared, facilitating an evaluation of the accuracy of the integration time step.
2. **Simplified Workflow**: By reusing the same model across both phases, development time is reduced, and consistency between simulation environments is maintained.

The control ISR subsystem configured for real-time simulation is shown in Figure 3.8, while the overall system structure corresponds to Figure 3.3. Notably, the real-time simulation retains communication facilities for the host-user interface, allowing for monitoring and debugging during real-time execution.
The integration of offline and real-time simulation methodologies enables a streamlined and consistent approach to e-drive prototyping. Offline simulation provides a comprehensive environment for initial validation, while real-time simulation ensures accurate execution under real-world constraints. The ability to reuse models and compare responses across both phases ensures efficiency, accuracy, and consistency in the development process. The described methodology

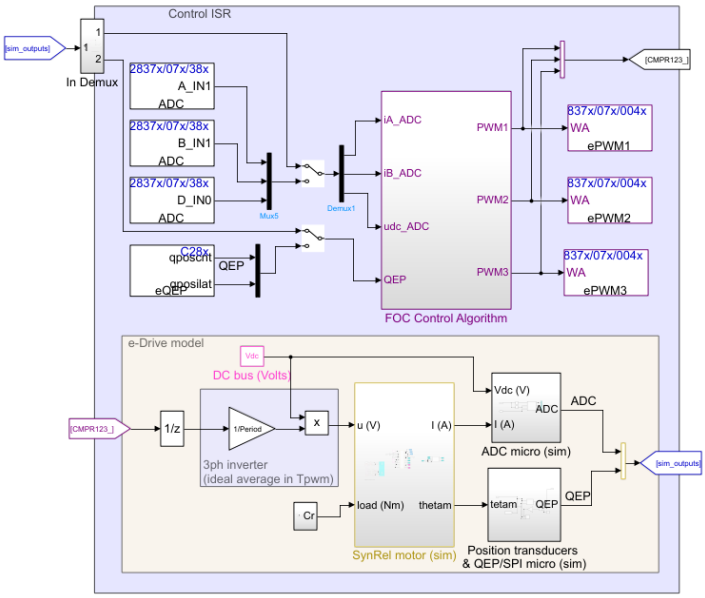

Figure 3.8: Control ISR Configuration for Real-Time Simulation in MATLAB/Simulink

leverages the strengths of Simulink and custom solver configurations to meet the demands of modern control prototyping.

3.2.6 SynRM Modeling and Control Scheme

The development of a real-time simulation approach requires a simulation model of the controlled e-drive that is both computationally efficient and reliable, while still maintaining a sufficient level of accuracy. Among the components of the drive system, as outlined in Fig. 3.8, the electric motor demands the most attention. This is because the motor model typically consists of differential equations with inherent nonlinear characteristics. For motors such as the SynRM, where electromagnetic nonlinearity is significant, traditional lumped parameter models are insufficient. Instead, advanced modeling techniques must be employed.

- **SynRM Model**

The mathematical model of the motor, expressed in formulas (1) to (10), will refer to the following nomenclature.

dq	rotor-fixed two-phase reference
$\alpha\beta$	stator fixed two-phase reference
v_{dq}, i_{dq}	dq voltage and current components
$v_{\alpha\beta}, i_{\alpha\beta}$	$\alpha\beta$ voltage and current components
$\psi_{dq}, \psi_{\alpha\beta}$	dq and $\alpha\beta$ flux linkages components
C_e, C_r	electromagnetic/load torque
m_e	per unit electromagnetic torque
θ_r, ω_r	rotor electrical position/speed
R	stator phase resistance
p	pole pairs
J	rotor plus load inertia
B	viscous load coefficient
$\boldsymbol{u}, \boldsymbol{i}$	3ph inverter voltage/current vector
$\boldsymbol{C}, \boldsymbol{P}$	Clarke/Park axis transformations
$\cdot$	d/dt
$*$	reference signal in control scheme

The SynRM is represented by an equivalent two-phase model, arranged in the rotor-fixed ***d-q*** reference frame. The input voltages are transformed using the Park transformation, which is nested within a Runge-Kutta (RK) solver algorithm to improve the accuracy of the simulation. To account for the nonlinearities and cross-couplings characteristic of the SynRM, inverse flux vs. current maps are utilized. These maps are precomputed using Finite Element Analysis (FEA) of the motor, as shown in Fig. 8. Consequently, the fluxes are treated as state variables within the differential model.

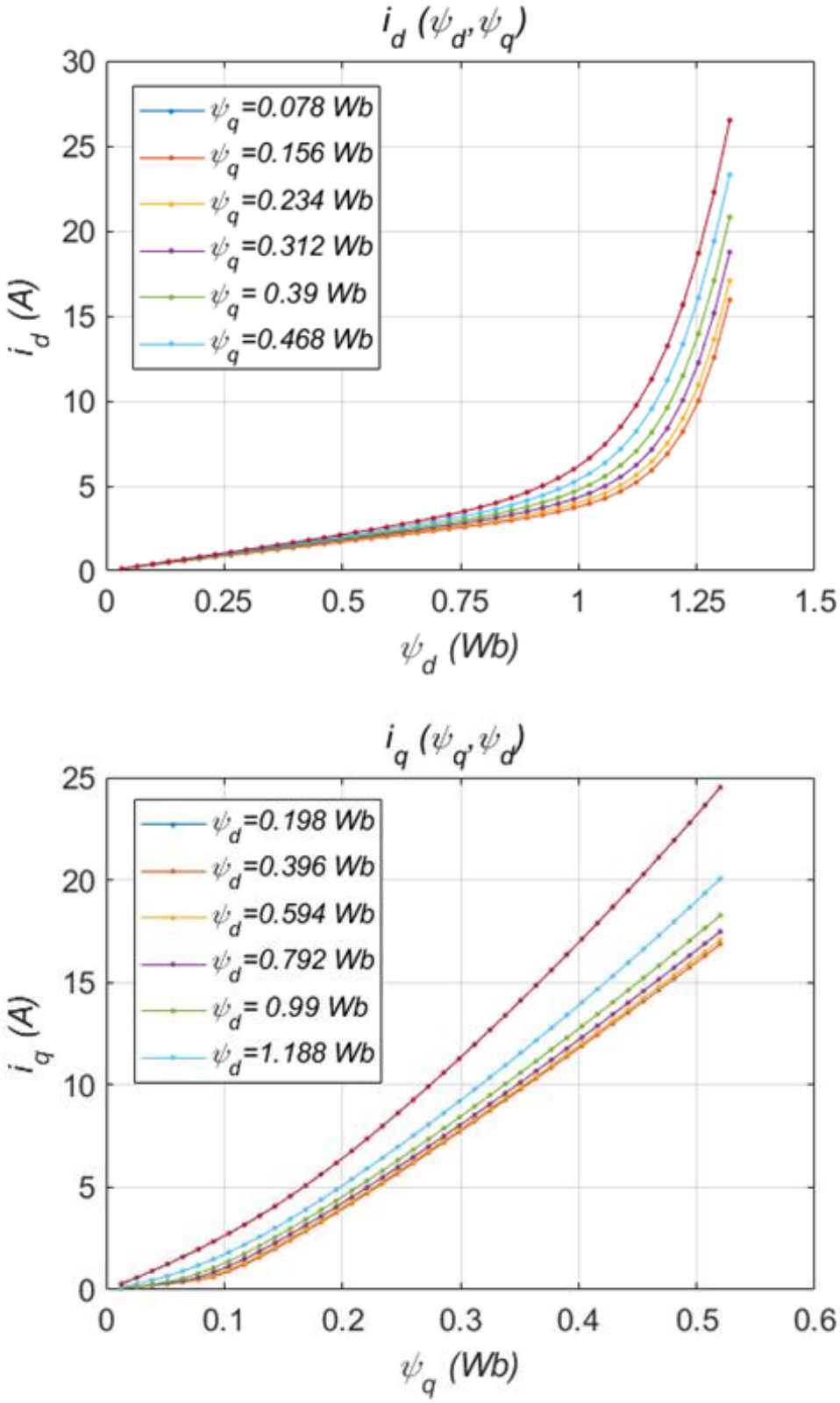

Figure 3.9: Inverse flux vs. current maps of the considered SynRM

The discretized electromagnetic model of the SynRM motor is described by the following equations where "$\boldsymbol{k}$" denotes the time step of the solver and "$\boldsymbol{z}$" the generic iteration sub-step in which "$\boldsymbol{k}$" is divided in the RK algorithm.

1. Transformation of input voltages into the d-q reference frame:

$$v_{d,z} = v_{\alpha,k} cos\theta_{r,z-1} + v_{\beta,k} sin\theta_{r,z-1}$$

$$v_{q,z} = -v_{\alpha,k} sin\theta_{r,z-1} + v_{\beta,k} cos\theta_{r,z-1}$$

2. Current values derived from flux maps:

$$i_{d,z-1} = i_d(\psi_{d,z-1}, \psi_{q,z-1})$$

$$i_{q,z-1} = i_q(\psi_{d,z-1}, \psi_{q,z-1})$$

3. Electromagnetic torque:

$$C_{e,z} = 1.5\, p(\psi_{d,z-1} i_{q,z} - \psi_{q,z-1} i_{d,z})$$

4. Flux derivatives:

$$\dot{\psi}_{d,z} = v_{d,z-1|z} - R i_{d,z-1} + \omega_{r,z-1} \psi_{q,z-1}$$
$$\dot{\psi}_{q,z} = v_{q,z-1|z} - R i_{q,z-1} - \omega_{r,z-1} \psi_{d,z-1}$$

5. Rotor speed dynamics:

$$\dot{\omega}_{r,z} = \frac{p}{J}(C_{e,z} - sign(\omega_{r,z-1}) \cdot C_{r,k} - B\omega_{r,z-1})$$

6. Rotor position dynamics:

$$\dot{\theta}_{r,z} = \omega_{r,z-1}$$

7. Input voltages in (1):

$$\boldsymbol{v}_{\alpha\beta,k} = \boldsymbol{C} \cdot \boldsymbol{u}_{123,k}$$

8. Output phase currents

$$\boldsymbol{i}_{abc,k} = \boldsymbol{P}^{-1}(\theta_{r,k}) \cdot \boldsymbol{i}_{dq,k}$$

This model is applicable for both real-time and offline simulations.
In the case of real-time simulation, the inverter is represented as an "ideal average over the PWM period."

9. Inverter branch voltages in real-time simulation in (7):

$$\boldsymbol{u}_{123,k} = V_{dc} \frac{CMPR_{123,k}}{Period}$$

Here, $CMPR_{123}$ represents the values of the compare registers that control the three-phase inverter branch commands d_{123}, and $Period$ refers to the PWM period T_{PWM} both expressed in counts of the microcontroller's PWM unit (refer to Figure 3.5). In contrast, during offline simulation, the time-domain waveforms of the PWM voltages are explicitly represented; this involves modeling the inverter as an "ideal switching" unit, with equation (9) replaced by:

10. Inverter branch voltages in offline simulations

$$\boldsymbol{u}_{123,k} = V_{dc}\, d_{123,k}$$

where $\boldsymbol{d_{123,k}}$ represents the duty cycles. The solver step in offline simulations must be sufficiently small to comply with the resolution of the PWM counter of the target microcontroller and resolve the PWM switching dynamics accurately.

- **SynRM Control Scheme**

The control scheme for the SynRM, implemented within the Control ISR, is shown in Figure 3.10, it includes:

1. **Outer Speed Loop**: Generates torque commands and ensures speed regulation.
2. **Maximum Torque Per Ampere (MTPA) Optimization**: Uses precomputed lookup tables to minimize current usage for a given torque.
3. **Inner d-q Current Loops**: Employ multivariable PI regulators to manage motor currents.

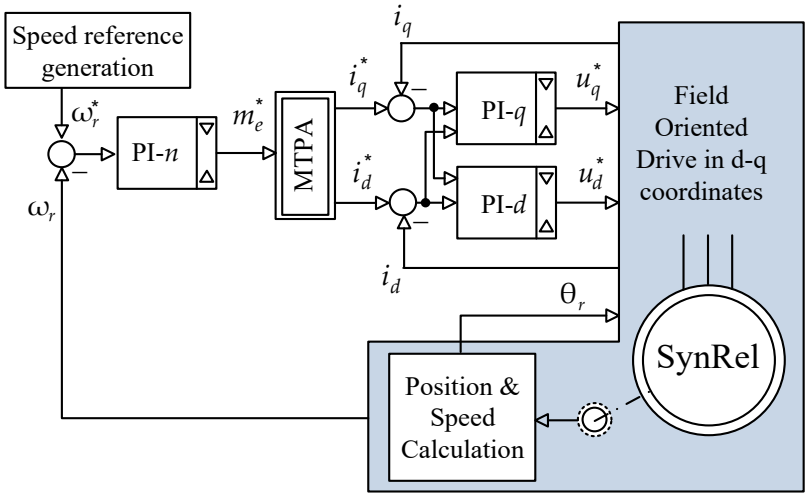

Figure 3.10: Field Oriented Control scheme of the SynRM

Additional prototyping features are integrated into the scheme, such as:

- Rotor alignment and estimation procedures for encoder initialization.
- Support for speed, torque, and current control modes.
- Step current response tests on the d- and q-axes.
- Implementation of flux observers and other diagnostic tools.

The control scheme is implemented using floating-point arithmetic, leveraging the 32-bit capabilities of the TI Delfino F28379S microcontroller. Each functional block is modular, with configurable parameters and enable flags, allowing for flexible setup and rapid adjustments. The developer needs only to link the modules appropriately, ensuring that input/output variables match the overall structure of the control scheme.
The SynRM model and control scheme, as developed, provide a robust framework for both offline and real-time simulations. The use of advanced modeling techniques, combined with the flexibility and computational efficiency of the control ISR, ensures high accuracy and reliability in prototyping applications. The modular architecture of the control scheme further simplifies implementation, making it ideal for rapid prototyping and testing.

3.3 Experimental Results and Data Analysis

The experimental setup used to verify the proposed Rapid Control Prototyping (RCP) techniques is illustrated in Figure 3.11. The system comprises the following components: the power converter/inverter, a prototype SynRM equipped with an incremental encoder, a control and development board, and a host PC.

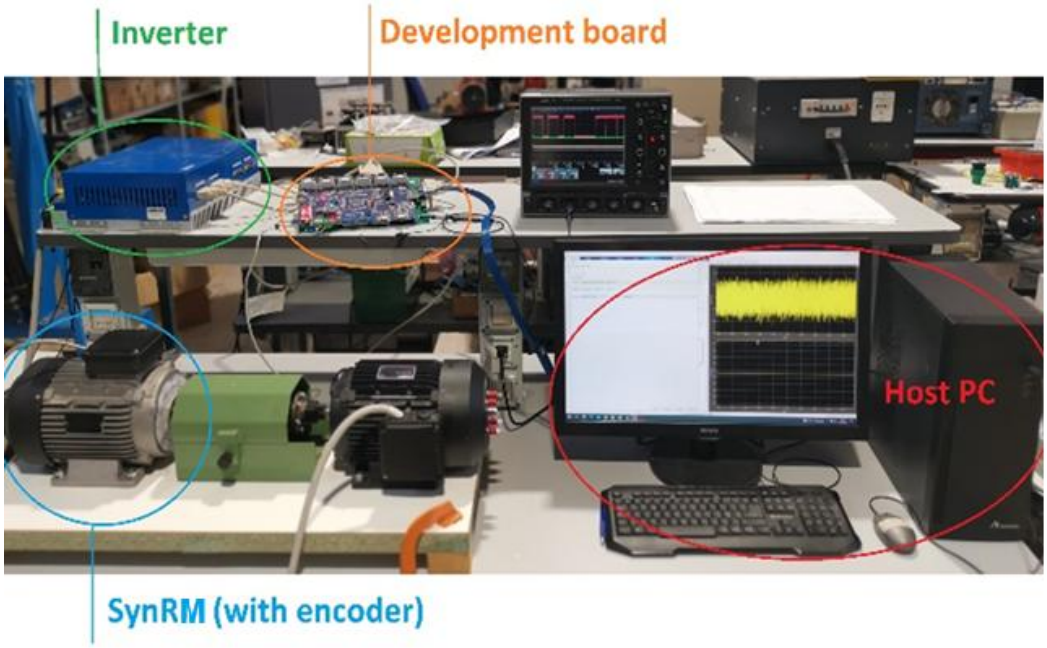

Figure 3.11: Prototyping platform for experimental tests

- **SynRM under test**

The SynRM is designed for industrial applications, featuring two pole pairs and four flux barriers on the rotor (Figure 3.12a). Its primary parameters are summarized in Table 3.1. This motor was selected for its nonlinear electromagnetic characteristics, which present a challenging test case for the proposed prototyping methods.

Figure 3.12a: SynRM utilized for the tests

TABLE 3.1
SYNRM MOTOR DATA

pole-pairs	2	phase voltage	220 V_{rms}
speed	1500 *rpm*	phase current	10.6 A_{pk}
power	3.14 *Kw*	d-current	3.9 A_{pk}
torque	20 *Nm*	q-current	9.9 A_{pk}
inertia	35.7 *Kg cm^2*		

- **Power Converter/Inverter**

The power converter is a commercial inverter (*RECTIFICADORES GUASCH S.A. MTL-CBI0060F12IXHF*) composed of two IGBT-based CBI (Converter + Brake + Inverter**)** modules, complete with a heatsink, optocoupled drivers, and sensors for output phase currents and DC-link voltage. Additionally, the inverter is equipped with an internal NTC module to monitor its temperature.

- **Development Board**

The control system is implemented on a development board that integrates a TI Delfino F28379S microcontroller (Figure 3.1). The microcontroller is mounted on a custom interface board that hosts signal conditioning circuits for control input/output and debugging signals. (The authors gratefully acknowledge R13 Technology Srl, https://r13technology.it/ , for providing the development board used in this work.).

- **Host PC**

The host PC communicates with the development board via an RS-232 serial port. Real-time functionality is achieved through a custom console implemented as a standalone Simulink model. This console provides a user interface, illustrated in Figure 3.12b, that enables:

- Selection of test modes.
- Transmission of set points and parameters.
- Selection and real-time visualization of control variables using Simulink scopes.

- **Experimental parameters**

All experiments were conducted under the following conditions:

- PWM frequency: 10 kHz.
- Inverter dead time: 0.5 µs.
- DC bus voltage: Vdc=300 V.

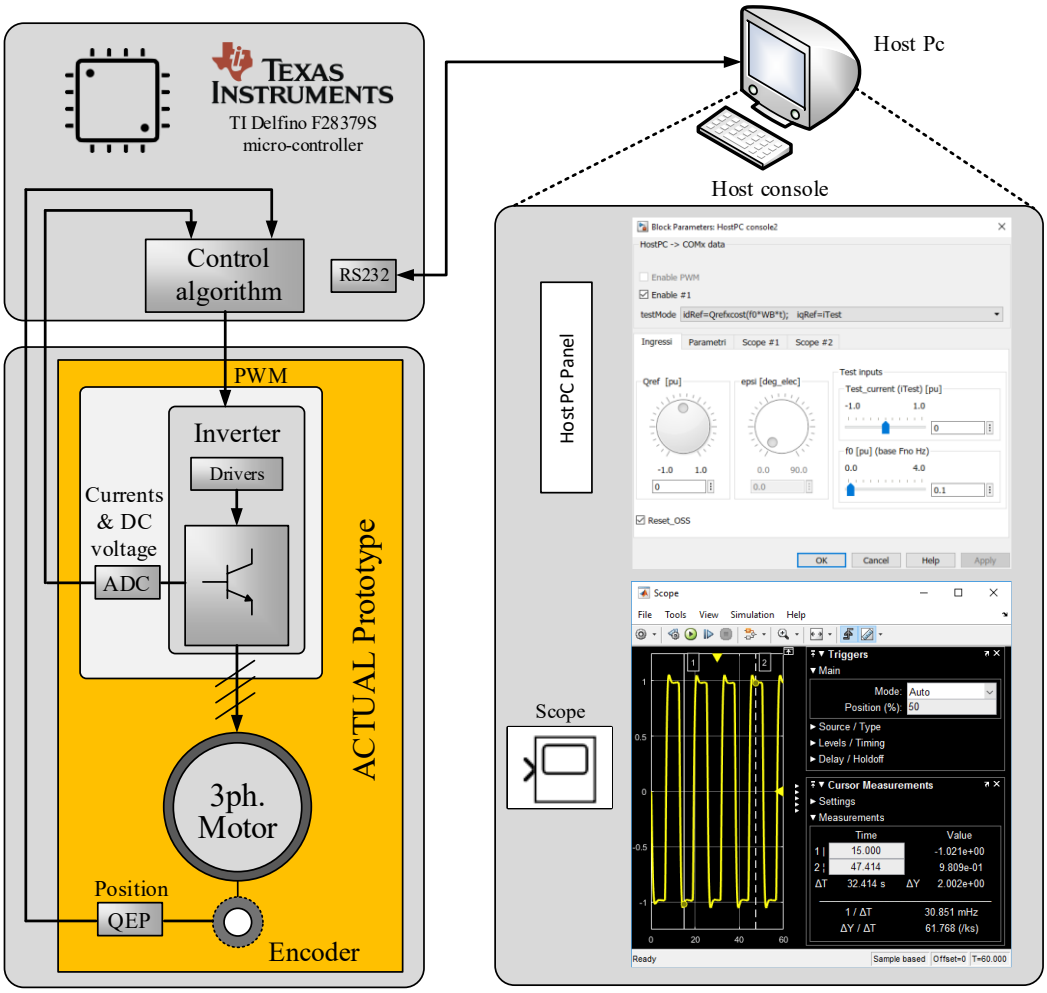

Figure 3.12b: Diagram of the prototyping drive system highlighting the Simulink user interface panel and monitoring framework.

3.3.1 Experimental Validation

- **Initialization Procedure**

The initialization procedure involves compensating for ADC offset errors and aligning the rotor. Rotor alignment is achieved by applying a stationary field magnetomotive force (FMM) aligned with the reference phase "**a**" and setting this position as the encoder's zero point. Figure 3.13 presents the real-time simulation of the initialization transient, while Figure 3.14 shows its experimental validation. The rotor's initial position is set at 60 electrical degrees, with an aligning current of 0.3 pu, maintained long enough to ensure alignment before reducing to 0.05 pu, which is the minimum current required for Maximum Torque Per Ampere (MTPA) control. Although mechanical parameters were estimated approximately, the real-time simulation proved effective in setting up the procedure, particularly regarding timing and alignment current levels.

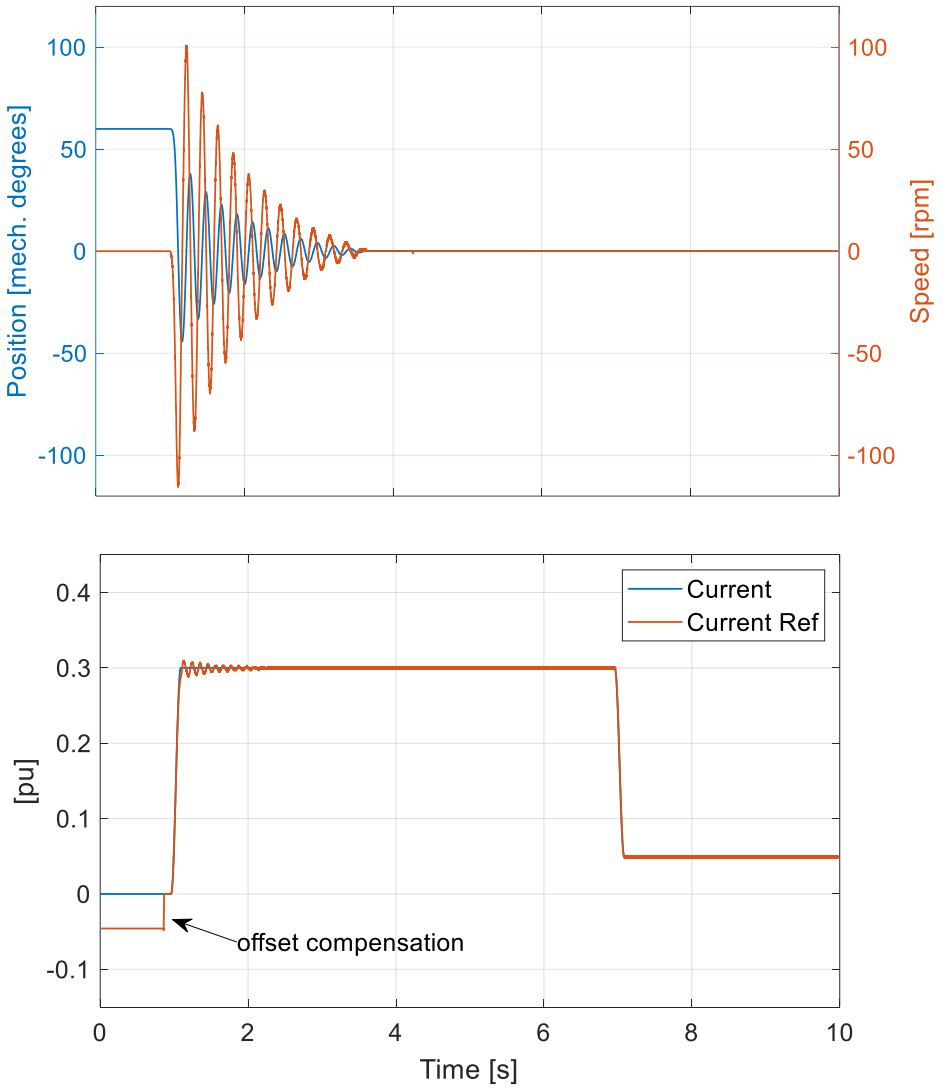

Figure 3.13: Initialization procedure: real-time simulation

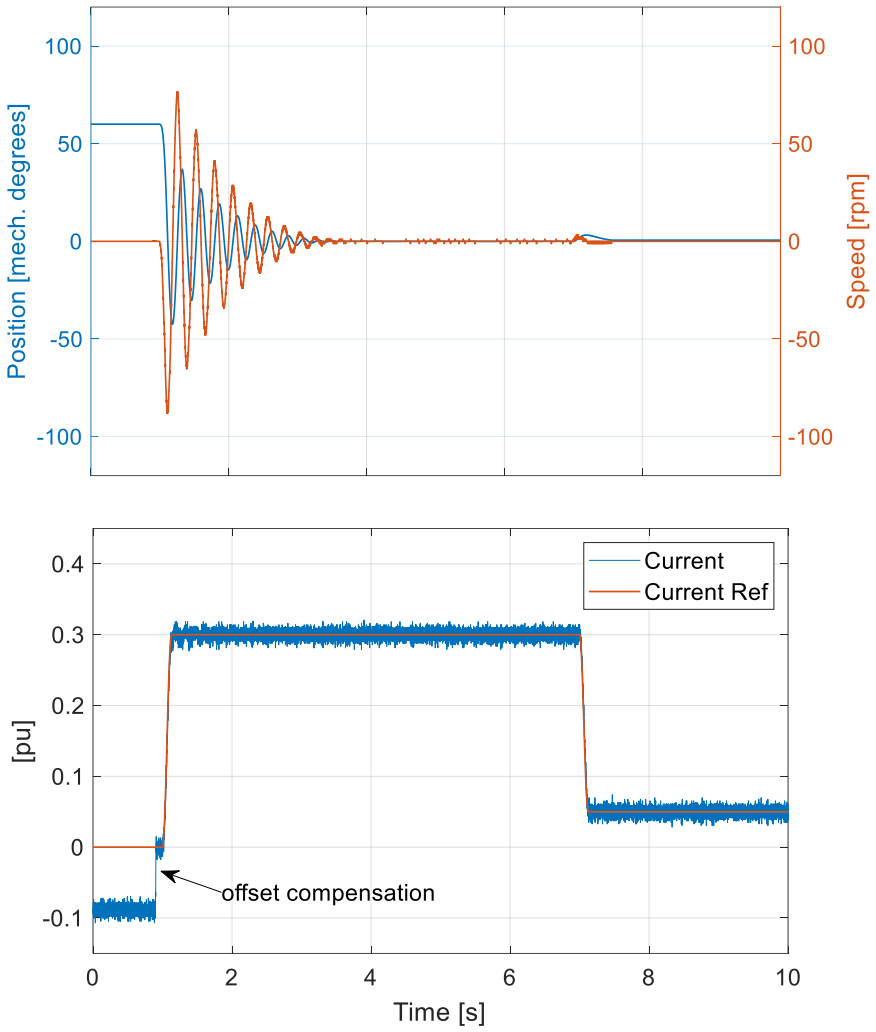

Figure 3.14: Initialization procedure: experimental validation

- **Current Control Response**

The response to d-current steps was analyzed to study the impact of saturation characteristics on the SynRM. Figure 3.15 compares the results obtained from offline simulation, real-time simulation, and experimental tests, all performed with the rotor locked and q-current controlled at zero. The transients of the d-voltage reference are also shown. The same PI regulator gains were used across all tests to ensure consistency.
In all the test cases the parameters of the d-current regulator are selected as follows: proportional gain KpD = 11.4564; integral gain KiD = 0.01 (per unit arrangement). They are tuned considering the apparent d-axis inductance at rated operating point. The voltage limit (visible in Figure 3.15) is equal to the base voltage Vdc/sqrt(3).
The results reveal an increase in the slope of the current response at higher current levels, a direct consequence of saturation effects. This behavior transitions the step response from a purely damped to a damped-oscillatory nature, as documented in the literature.

The case at 0.8 pu current setpoint shows strong oscillations, even at steady-state highlighting a critical control condition at the transition from a purely damped to a damped oscillatory response.
The offline simulations, performed with the RK ode4 solver in Simulink using a 1 µs fixed step, closely align with the experimental results, despite the ideal inverter modeling.

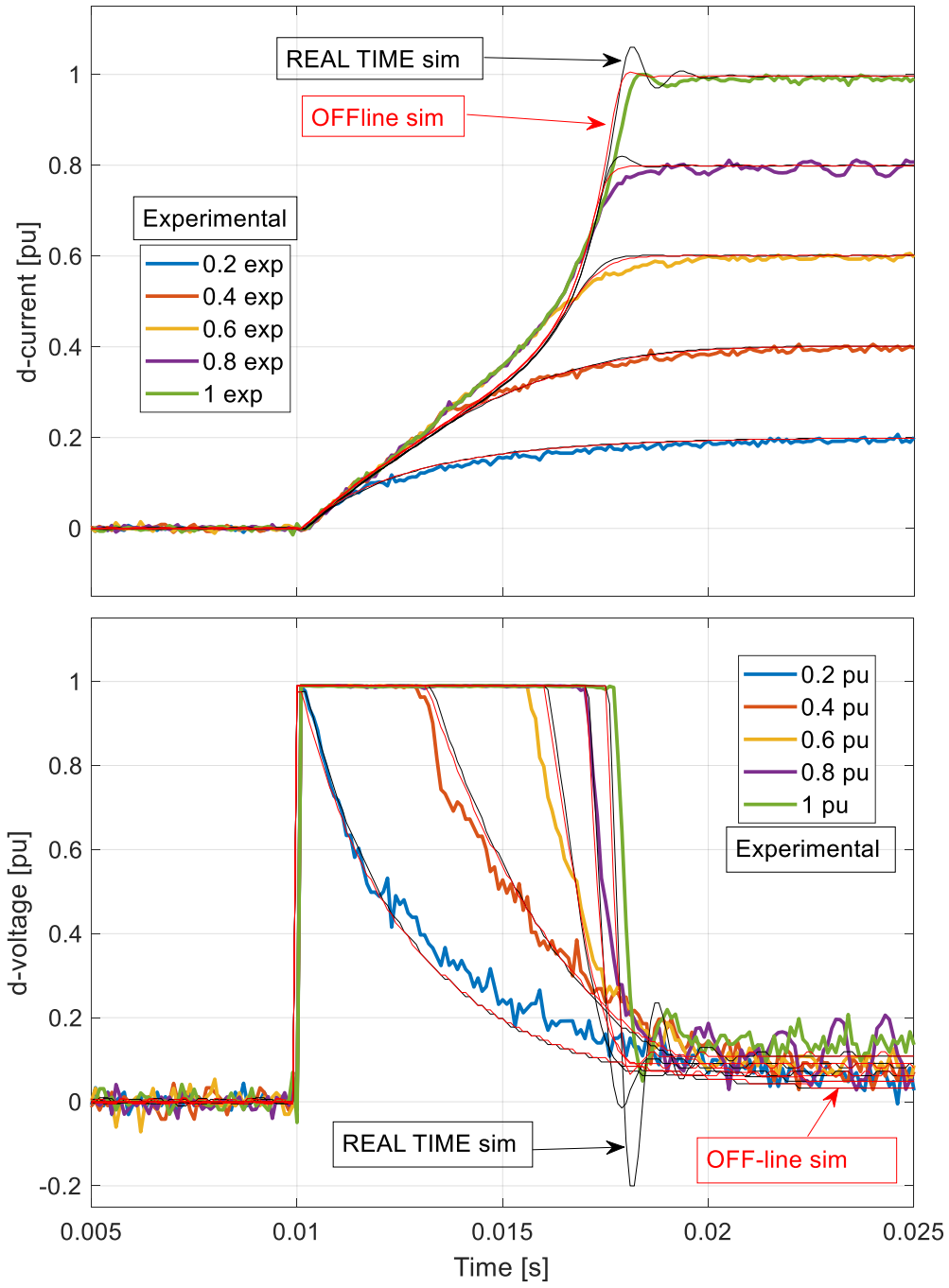

Figure 3.15: Current response: comparison among offline simulation, real-time simulation, and experiments.

No significant differences have been found between “ideal average” and “ideal switching” modeling. The **inverse simulation rate** was 335 on an Intel Core i7 7th-generation processor.
This **simulation rate** in offline simulation refers to the ratio between the actual simulated time of the system and the computational time required to execute the simulation. It is a measure of the speed-up of the simulation and is calculated as: Simulation Rate = Simulated Time / Computational Time. The **inverse simulation rate** is defined as the ratio between the elapsed real (wall-clock) time required to execute the simulation and the corresponding advancement of simulated time. It represents a measure of the computational cost of the simulation with respect to real time.

The factors Influencing the Simulation Rate are:

1. **System Model Complexity**: Highly detailed models, such as those including nonlinearities or finite element analysis (FEA), increase computational demands.
2. **Solver Type**: High-precision solvers (e.g., 4th-order Runge-Kutta) can slow down the simulation compared to simplified solvers.
3. **Time Step**: A smaller time step enhances accuracy but requires more computational time per simulated second.
4. **Hardware Performance**: Processor speed and overall computational capabilities significantly impact the simulation rate.
5. **Iterative Computations**: Models requiring iterative solutions for each step further increase simulation time.

In real-time simulation, the RK algorithm was implemented as a custom S-function in Simulink. On the TI Delfino F28379S microcontroller (operating at 200 MHz), the RK algorithm required approximately 20 μs to compute the SynRM model described in section 3.2.6. The complete Control ISR, including the RK computation, executed in 84 μs. However, the 100 μs fixed step (equal to the PWM period) used for integration proved insufficient to accurately capture the motor's transients at high current levels. This limitation, exacerbated by reduced differential inductance due to saturation, led to increased oscillations and potential instability at maximum current levels.

3.3.2 Improving Real-Time Simulation Accuracy

The current step-responses obtained in real-time simulation exhibit a more oscillatory behavior compared to those from offline simulation, with the oscillatory trend becoming more pronounced as the current level increases. Using an integration step equal to the PWM period (100 μs) appears to be too large to accurately simulate the motor's transients. This is particularly evident under conditions where saturation causes a significant reduction in the differential inductance, leading to a sharp increase in current dynamics beyond a certain threshold. At maximum current levels, the extent of these oscillations could even trigger instability in the simulation algorithm.
This observation is corroborated by the comparative results shown in Figure 3.16. In this case, the Runge-Kutta (RK) integration was executed twice within each

PWM period, effectively reducing the fixed integration step to 50 µs. This adjustment significantly mitigated the oscillatory trend observed in the real-time simulations.

However, to accommodate the additional computational load introduced by the reduced integration step, it was necessary to increase the PWM period to 120 µs (corresponding to a frequency of 8.33 kHz). This change ensured sufficient time for the complete execution of the control ISR. Additionally, the integral gains of the PI regulators were modified accordingly to maintain system stability and performance under the adjusted timing constraints.

This work presents an identical target offline and real-time simulation framework for rapid control prototyping (RCP) of e-drives using MATLAB/Simulink. Both approaches utilize the same control algorithm implemented on the target microcontroller, ensuring consistency in testing while operating on different platforms (a PC for offline simulation and the microcontroller for real-time simulation). Validation tests, conducted on a drive equipped with a Synchronous Reluctance Motor, demonstrate the effectiveness of this methodology. To date, such applications for SynRM drives have not been extensively explored in prior works.

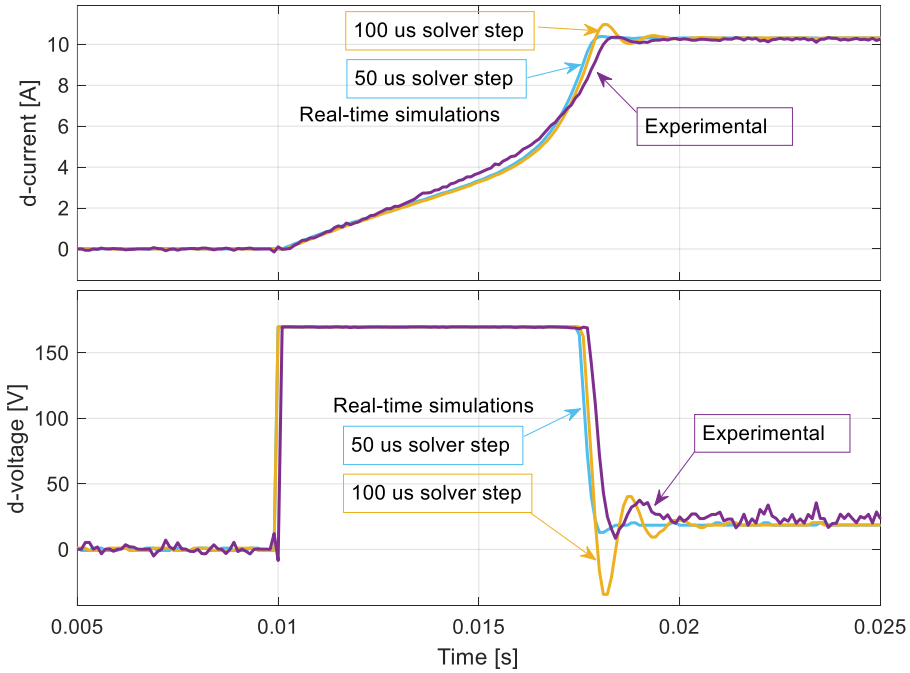

Figure 3.16: Influence of the solver step sizes in real-time simulations

The validation results confirm the accuracy of the offline simulation, with responses closely matching experimental results, even during fast transients, provided that the plant model is sufficiently accurate. Real-time simulation, while capable of achieving similar accuracy, offers the significant advantage of real-time operation. The discrepancy between experimental and simulation results lays mainly (first) in the slope during constant-voltage transient and (second) in the damping (overshoot) at the end of the transient. The first discrepancy is probably due to model mismatch (flux maps), while the second one can be related to the accuracy of the solver, as visible from the difference between the 50 and 100 us solver step cases.

In fact the integration step size for the motor model plays a critical role in determining the accuracy of the simulation. A fixed step equal to the PWM period may introduce parasitic oscillations during fast current transients due to insufficient resolution of rapid dynamics. Reducing the integration step effectively mitigates these oscillations but increases computational demand, which may challenge the processing capabilities of even the latest generation microcontrollers. The proposed RCP techniques effectively address the nonlinear dynamics of SynRM motors, leveraging the flexibility of the prototyping platform and the robust capabilities of MATLAB/Simulink paired with the TI Delfino microcontroller. This combination enables detailed analysis, rapid adjustments, and reliable control performance across a variety of operating conditions. Furthermore, integrating offline and real-time simulations provides a comprehensive framework to handle the complexities of modern motor control systems efficiently.

As discussed in the subsequent chapter, the accuracy of the real-time simulation can be further improved by reducing the computational time required for the SynRM model through the use of parallel programming techniques. This approach enhances the processing efficiency of the microcontroller, enabling the use of smaller integration steps without exceeding hardware limitations and thereby increasing the fidelity of real-time simulations. Despite these challenges, real-time simulation remains an appealing option for small-scale market production, offering a practical balance between accuracy, real-time operation, and system performance.

Chapter 4

Enhancing Accuracy in Real-Time Simulation for SynRM drives.

Part of the work presented in this chapter has been previously published in [21]

4.1 Challenges in Real-Time Simulation

Building on the discussion in Section 3.3.2, which highlighted the need to improve the accuracy of real-time simulations, this section delves into the specific challenges encountered when implementing real-time simulation for Synchronous Reluctance motor drives. The inherent complexities of SynRM, such as high magnetic circuit nonlinearity and rapid dynamic transients, place significant demands on computational accuracy and efficiency.
RTS involves executing the plant model on the same target microcontroller at the same control rate as the final application. While this approach offers significant advantages, including low-cost prototyping and the ability to perform virtual upgrades throughout a product's lifecycle, it also requires both precise modeling of the plant and efficient computation within tight timing constraints. In the context of SynRM, the primary challenge lies in integrating the nonlinear differential equations governing the motor model with sufficient accuracy, particularly during fast transients caused by rapid current changes.
In prior implementations, MATLAB/Simulink was used to deploy RTS on the Texas Instruments Delfino F28379S microcontroller, employing a fourth-order Runge-Kutta (RK4) solver for the motor model. To achieve acceptable accuracy, the integration step was limited to a maximum of 50 µs. However, with the PWM period (T_{PWM}) and control sampling period set at 100 µs, this required two integration steps per control cycle. A detailed analysis of execution times for sequential processing revealed the following breakdown:

- Motor model integration: 34 µs per RK4 step (68 µs for two steps).
- Standard control tasks (e.g., field-oriented control and MTPA): 12 µs.
- Communication tasks (e.g., data exchange with the host): 20 µs.
- Auxiliary tasks (e.g., parameter estimation, gain adaptation): 30 µs

The cumulative execution time for these tasks totaled 128 µs, exceeding the available 100 µs control period. This computational bottleneck underscored the need for a more efficient approach.
To address this limitation, the parallel processing capabilities of the TI Delfino F28379S microcontroller, particularly its Control Law Accelerator (CLA) coprocessor, were explored. Operating at the same 200 MHz clock speed as the CPU, the CLA enabled the distribution of computational tasks [17][18]:

- **CPU**: Executed the computationally intensive motor model integration and communication tasks.
- **CLA**: Managed FOC control.

By leveraging parallel processing, the total computation time was reduced to under 80 µs, allowing the system to operate within the 100 µs control period. This efficiency gain also enabled the use of more accurate solvers and finer integration steps, further enhancing the fidelity of the simulation.

The modular implementation of the SynRM model in MATLAB/Simulink was pivotal in this process. By incorporating a flux-based representation that accounted for saturation and cross-coupling effects, the model maintained high accuracy while optimizing computational performance. Additionally, alternative solver algorithms, such as the Predictor-Corrector method [19], were evaluated and demonstrated faster computational performance compared to the Runge-Kutta method, while maintaining comparable precision.

The simulation of the FOC control system for the SynRM, analyzed in the previous chapter, is revisited in this chapter with the tasks divided between the CPU and the CLA and executed simultaneously in parallel, as illustrated in the scheme of Figure 4.1.

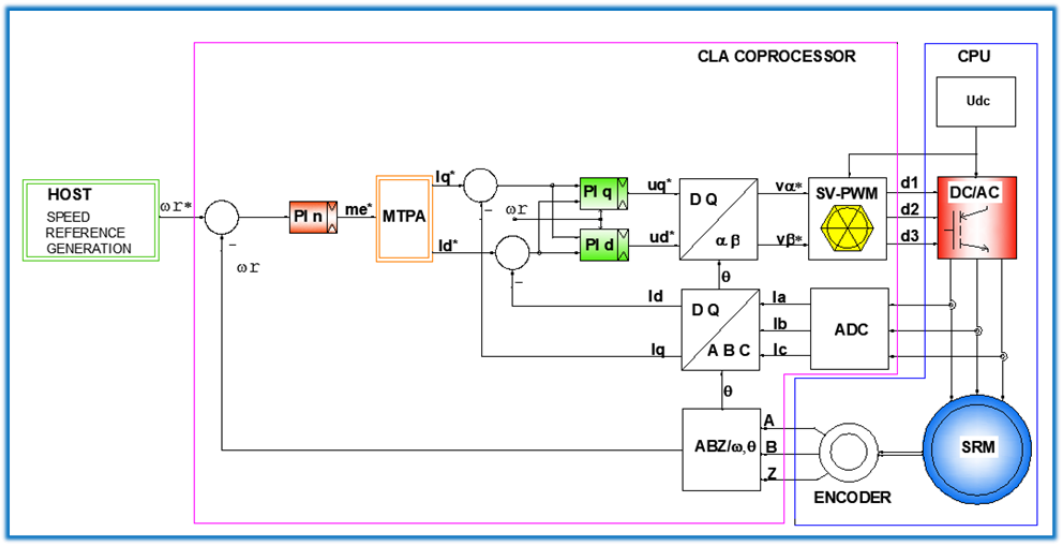

Figure 4.1: Field Oriented Control scheme of SynRM, implemented in CLA and in CPU.

Overall, the challenges of RTS for SynRM are closely tied to the need for efficient computation of complex, nonlinear motor models within strict timing constraints. Through parallel processing and advanced modeling techniques, these challenges can be effectively addressed, providing a foundation for high-fidelity, real-time control prototyping.

4.2 Leveraging the Control Law Accelerator (CLA): Parallel Processing for High-Precision Simulations

In this work, all the blocks shown in Figure 4.1 are implemented on a Texas Instruments Delfino F28379S microcontroller using C-code software generated by MATLAB/Simulink through the Embedded Coder Support Packages. These packages, specifically designed for TI C2000 processors, provide several key features:

- Automated build and execution.
- Block libraries for on-chip and on-board peripherals, including ADC, digital I/O, ePWM, SPI, I2C, and others.
- Real-time parameter tuning and data logging using the external mode.
- Processor-optimized code with libraries such as DMC and IQMath.
- Capability to perform processor-in-the-loop (PIL) testing with execution profiling.
- Support for code generation on the Control Law Accelerator (CLA), a co-processor available on select TI processors.

This setup allows for the real-time simulation of the entire e-drive system within the MATLAB/Simulink environment. By leveraging the microcontroller's peripherals and directly downloading the generated code into the target board's memory, the system is ready for execution.
Figure 4.2 illustrates the process of software implementation in the MATLAB/Simulink environment.

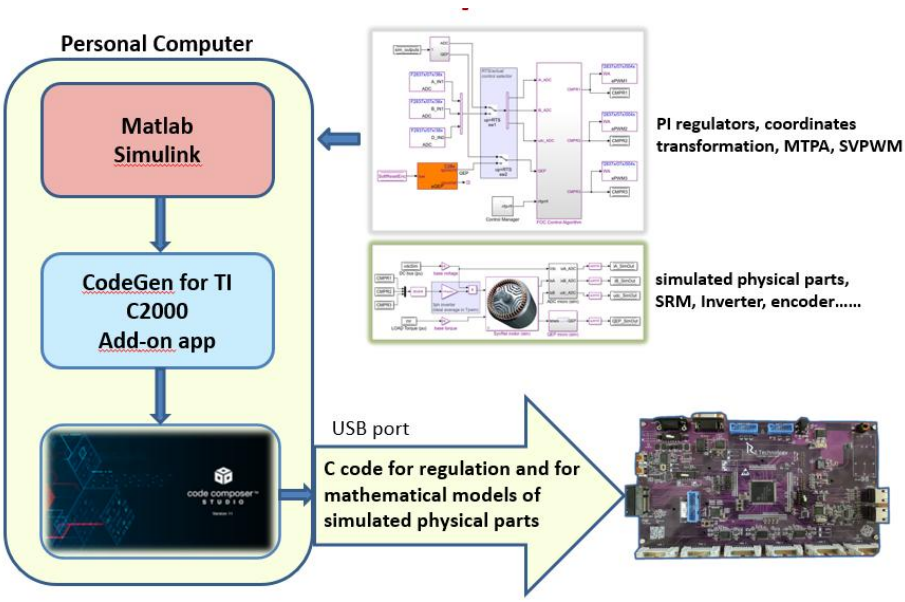

Figure 4.2: Process of software implementation in the MATLAB/Simulink.

- **Sequential Execution and its Limitations**

The real-time architecture, shown in Figure 4.3 implements the scheme in Figure 4.1 using an interrupt-based timing structure for efficient execution of the core control code within an interrupt service routine (ISR). Figure 4.3 shows the real-time architecture in the case of sequential execution of all the code developed. The control ISR incorporates the entire left section of Figure 4.1. It is triggered

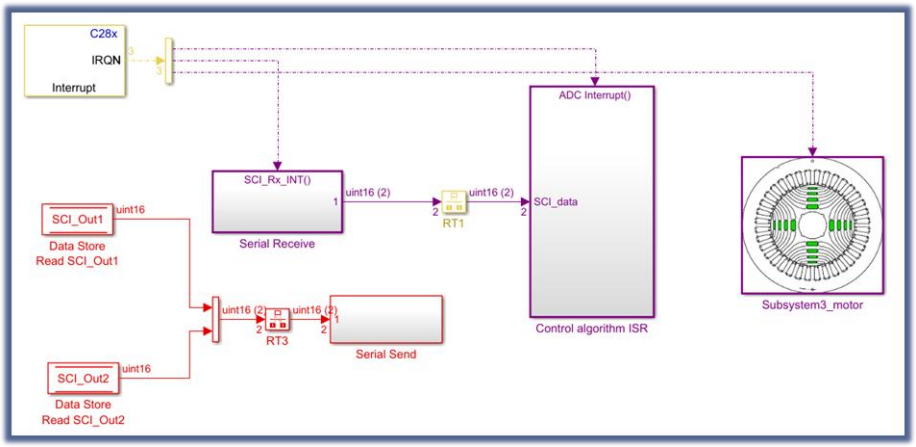

Figure 4.3: Field Oriented Control scheme of SynRM, implemented in sequential mode in the CPU

synchronously with the PWM carrier and the ADC conversions of high-dynamic control inputs (e.g., currents and DC bus voltage).

The sequence begins with the rotor position measurement via the quadrature encoder peripheral (QEP), followed by the computation of the rotor speed. This is followed, in sequential order, by the regulation tasks and, finally, by the execution of the mathematical model of the SynRM. The transition from one task to the next is managed by end-of-task interrupts, which trigger the execution of the subsequent

task. Any remaining time within the PWM period is used for low-priority tasks, such as communication between the microcontroller and the user, typically over a serial link.
However, sequential execution of all blocks in Figure 4.1 nearly exhausts the available PWM period of 100 µs, leaving little room for further control enhancements, such as implementing observers or advanced diagnostic features. This computational bottleneck underscores the need for a more efficient approach.

4.2.1 Parallel Programming with the CLA

To overcome these limitations, parallel processing is employed, utilizing both the CPU and the CLA available in the Delfino F28379S microcontroller. This approach effectively doubles computational capacity and reduces execution times by up to 50% (Figure 4.4).

The CLA is an independent math co-processor operating at the same 200 MHz clock frequency as the CPU. It features:

- Independent program and data buses.
- A dedicated set of registers and RAM for program and data storage.
- Direct access to peripherals such as ADC result registers, comparators, and PWMs (Figure 4.5).

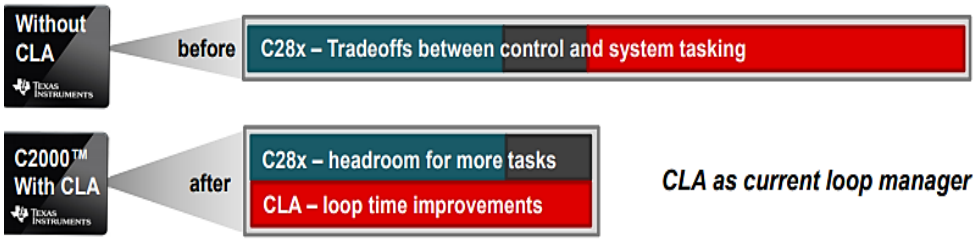

Figure 4.4: Benefits of using CLA and CPU in F28379S microcontroller

Tasks are divided between the CPU and CLA (Figures 4.6, 4.7, 4.8):

- **CPU**: Manages tasks related to e-drive simulation, including the inverter, SynRM, and encoder
- **CLA**: Executes regulation blocks, including field-oriented control and MTPA optimization.

Synchronization between the CPU and CLA is achieved through peripheral interrupts or specific register operations. Additionally, the CLA can independently trigger up to eight tasks, mapped to hardware events such as ADC data availability or timer expirations. These tasks run to completion without further CPU involvement, significantly reducing CPU load and allowing for more complex control loops or system-level tasks.

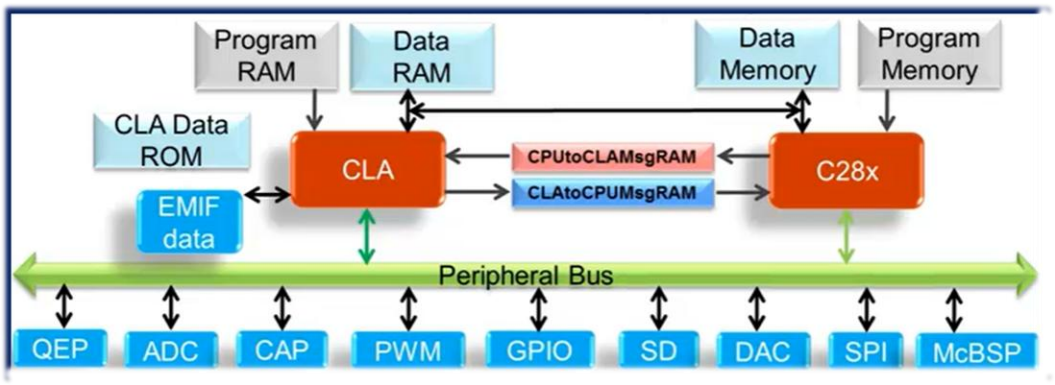

Figure 4.5: CPU and CLA architecture in F28379S microcontroller

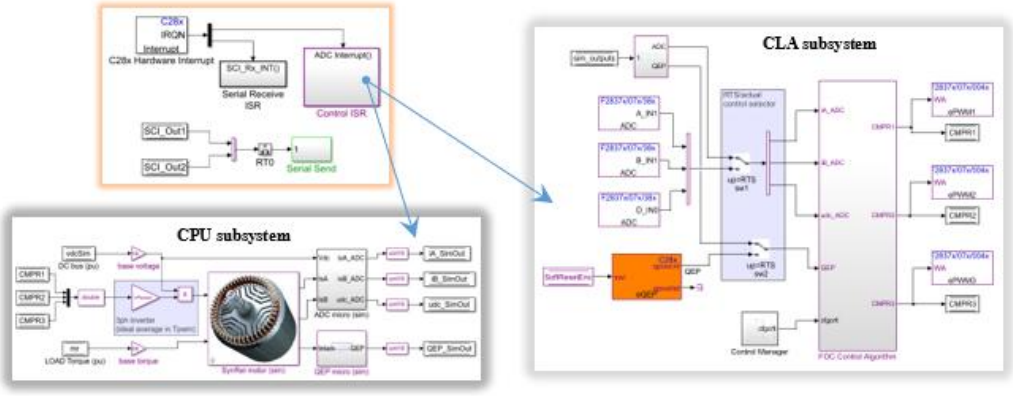

Figure 4.6: Interrupt-based control architecture in MATLAB/Simulink and Control ISR arranged for RTS

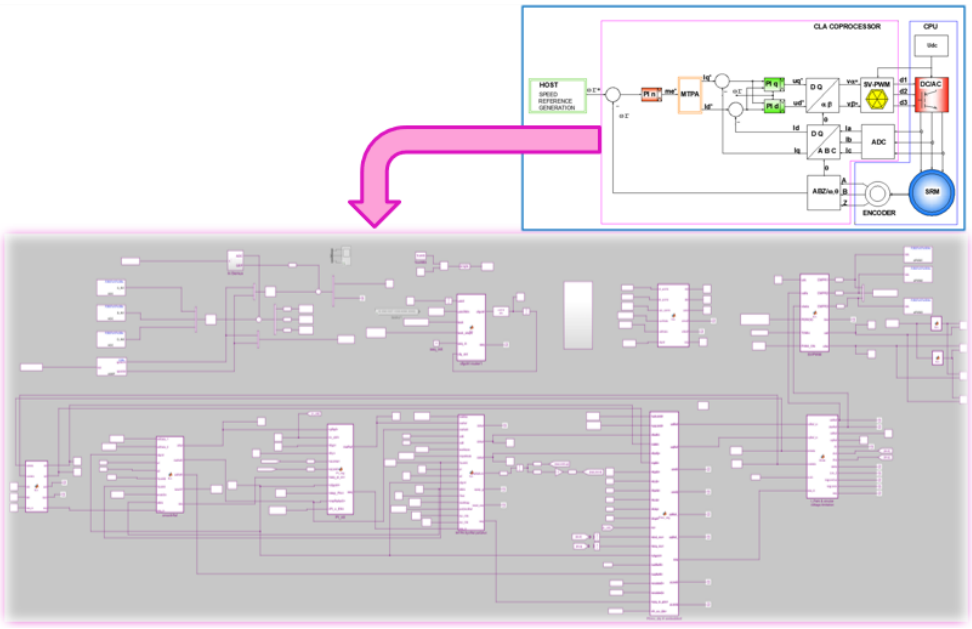

Figure 4.7: FOC of the e-drive implemented by Simulink into the CLA subsystem

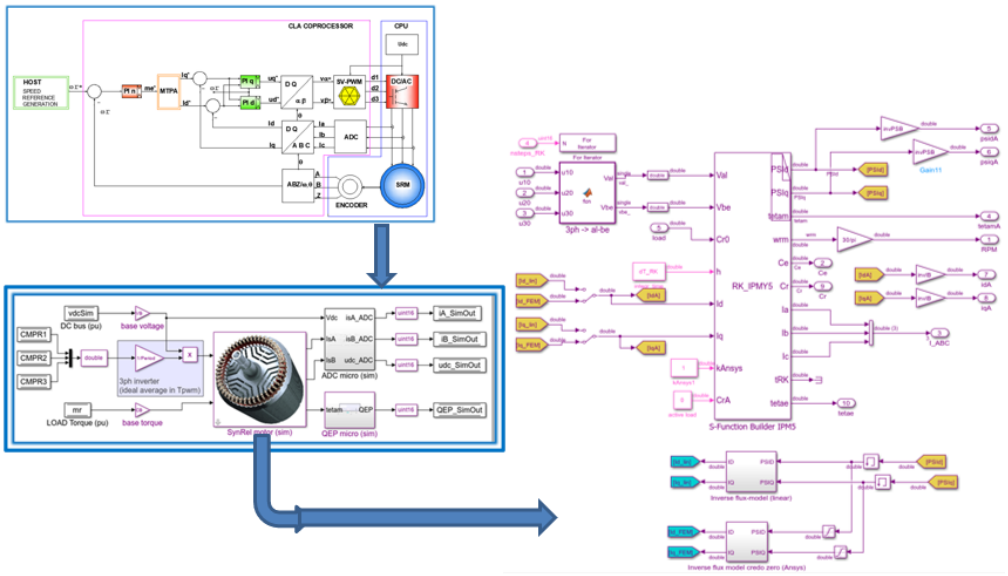

Figure 4.8: Physical models of the SynRM drive implemented by Simulink into the CPU subsystem

- **Advantages and Constraints of the CLA**

Both the CPU and the Control Law Accelerator (CLA) support 32-bit floating-point calculations. However, the CLA's instruction set is a subset of the Floating-Point Unit (FPU) instruction set available on the CPU. While the CPU offers a broader range of FPU instructions, the CLA has specialized instructions tailored for specific tasks, which helps optimize its performance in certain applications.
The CLA operates differently from the CPU in terms of task synchronization. Unlike the CPU, which relies on interrupts for hardware synchronization, the CLA supports up to eight independent tasks that are mapped to hardware events, such as a timer or the availability of data on an ADC. Each task, once initiated, executes to completion without requiring further CPU involvement. This autonomous operation significantly reduces the CPU's workload, enabling it to focus on other high-priority or system-level tasks.
The CLA's capability to handle up to eight separate tasks makes it well-suited for supporting multiple control loops or managing multiple phases simultaneously. However, there are specific considerations and limitations when working with the CLA:

- **Task Triggering**: CLA application code can only be triggered by C28x events. Tasks can be initiated by the C28x CPU through software or by various peripheral interrupts.
- **Data Communication**: Communication between the CLA and CPU must occur through dedicated memory sections. The `CpuToCla1MsgRAM` memory section is used to send data from the CPU to the CLA, while the `Cla1ToCpuMsgRAM` section is used for data transfer in the opposite direction (Figure 4.9).
- **Global Variables**: CLA does not have access to global variables, which requires careful design of data handling strategies.

- **Recursive Functions**: Recursive function calls are not supported on the CLA.
- **Arithmetic Limitations**: Integer division, modulus operations, and unsigned integer comparisons are not supported by the CLA C compiler.

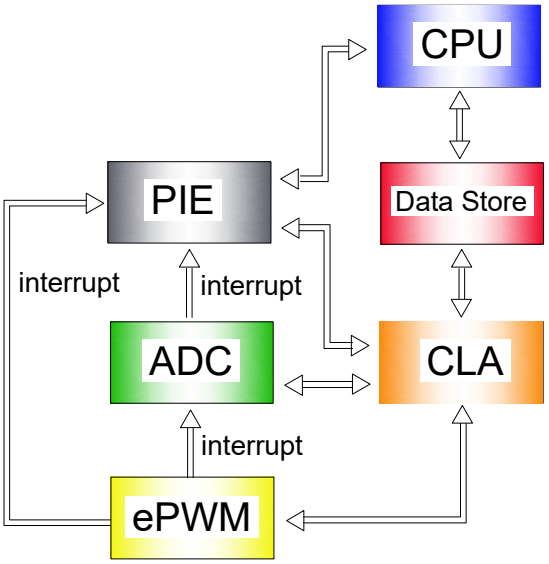

Figure 4.9: Data exchange between the CLA and CPU.

However, CLA lacks the hardware required to fully support a standard C compiler. For instance, it does not include a stack and is limited to one-level nesting of function calls to minimize overhead. Additionally, its instruction set is reduced and does not accommodate all the functionalities of a standard C compiler. To address these limitations, a specialized "CLA-C Compiler" is provided, which supports most—but not all—standard C compiler functions. Consequently, transferring a function written for the CPU to the CLA is a complex process that requires careful adaptation. An example of the circular voltage limitation implemented in the CLA, utilizing specific CLA mathematical instructions, is shown in Figure 4.10.
Given these constraints, software initially developed for the CPU must be carefully adapted to be executed on the CLA. Similarly, tasks designed for the CLA need to align with its specific architecture and capabilities. This process involves reworking the code to ensure compatibility and optimal performance across both processing units. By efficiently distributing tasks between the CPU and CLA, systems can achieve higher computational efficiency and handle complex real-time control requirements more effectively.

```
% check modulo dentro il limite
if vs>vLim
 if isequal(coder.target,'rtw')
   x = coder.ceval('CLAdiv',vs,vLim);
   dv = vs-vLim;  % riduzione modulo
   vdRef = coder.ceval('CLAdiv',vdRef_in,x);
   vqRef = coder.ceval('CLAdiv',vqRef_in,x);
   Lim_2=single(1);
 else
  x = vs/vLim;   % limitazione
  dv = vs-vLim;  % riduzione modulo
  vdRef = vdRef_in/x;     % riduzione tensione d
  vqRef = vqRef_in/x;     % riduzione tensione q
  Lim_2=single(1);
 end
end
```

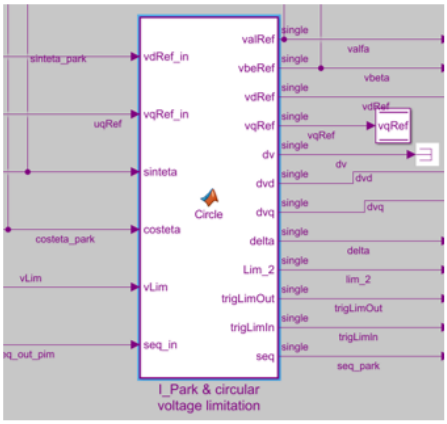

Figure 4.10: Control Law Acceleration (CLA): example of implementation using specific CLA mathematical instructions.

Figure 4.11 illustrates the timing structure of the Real-Time Simulation (RTS) for both sequential and parallel implementations, with the example of the Runge-Kutta (RK) solver algorithm. In a sequential implementation, a microcontroller equipped with a single CPU executes tasks sequentially (such as the "FOC control" and "motor drive" tasks). However, in real-world scenarios, the microcontroller's processing and the actual motor drive operate concurrently. To replicate the near-exact timing of real-time control in a sequential setup, the drive model inputs (i.e., the outputs of the control) must refer to the previous control period. As a result, the motor drive task must precede the FOC control task in execution order. Simulink enables the assignment of calculation priorities for subsystems within the same model level, ensuring the required sequencing. However, in a sequential approach, the total computation time within the Control ISR period equals the sum of the computation times of both tasks (Fig. 4.11, left).

In contrast, utilizing the Control Law Accelerator (CLA) available in the Delfino microcontroller enables a parallel task allocation strategy, as depicted in Figures 4.11(right),4.12.

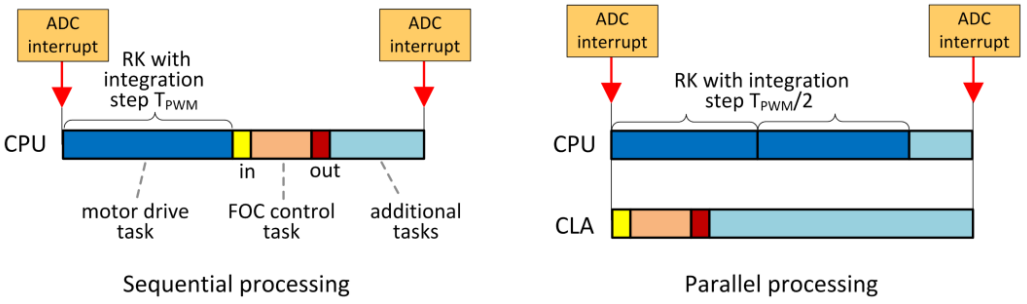

Figure 4.11: The timing structure of the RTS for both sequential and parallel implementations.

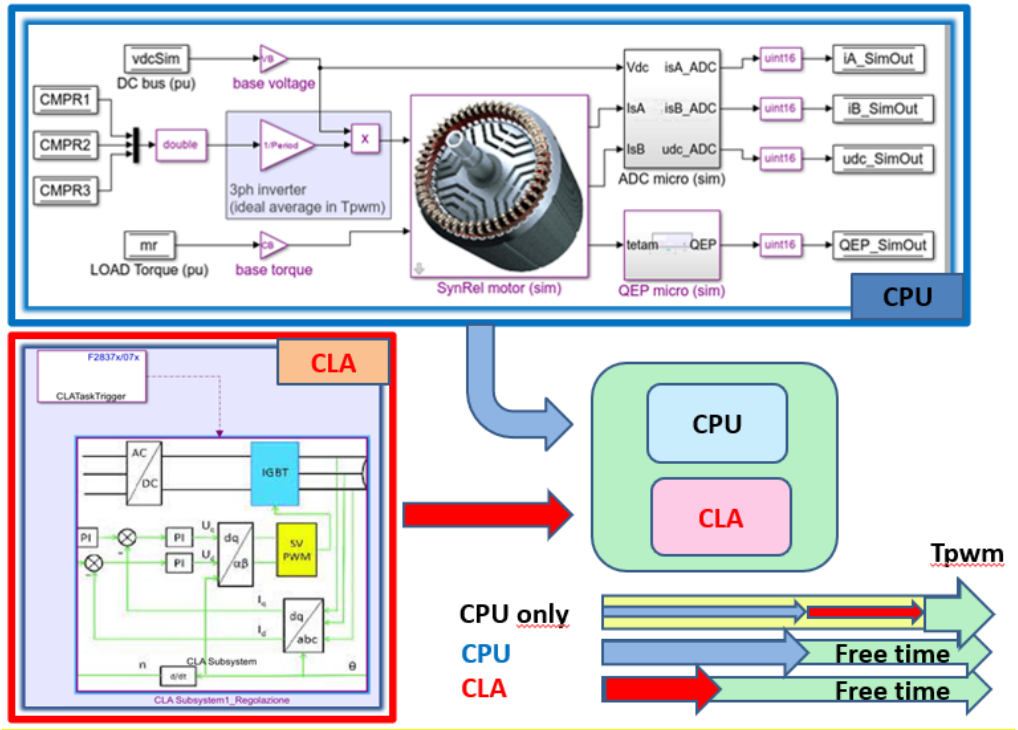

Figure 4.12: SynRM drive implemented into the CPU and the FOC into the CLA: parallel programming advantages.

4.2.2 Evaluation of Solver Algorithms for Accurate Motor Model Simulation: Runge-Kutta and Predictor-Corrector Methods

The essential requirements for a plant model in Real-Time Simulation (RTS) are low computational burden, high reliability, and sufficient accuracy. In the case of the Synchronous Reluctance (SynRM), the model inherently consists of differential equations that are analytically non-linear. Due to the significant electromagnetic nonlinearity present in SynRM, the commonly used lumped parameter models are unsuitable for accurate representation.

- **Model Implementation**

To address these challenges, the SynRM is simulated using an equivalent two-phase model represented in the rotor-fixed d-q reference frame. This involves employing the well-known Park transformation to convert phase values into the d-q components. Furthermore, the inverse flux versus current maps, derived from a Finite Element Analysis (FEA) model of the motor, are used to capture the effects of magnetic nonlinearity and cross-coupling. These flux maps serve as the basis for defining the fluxes as state variables in the differential model.
The mathematical representation of the SynRM model is as follows:

$$\frac{d\psi_d}{dt} = v_d - Ri_d + p\omega_{rm}\psi_q \quad (4.1)$$

$$\frac{d\psi_q}{dt} = v_q - Ri_q - p\omega_{rm}\psi_d \quad (4.2)$$

$$\frac{d\omega_{rm}}{dt} = \frac{1}{J}(T_e - T_l) \quad (4.3)$$

$$\frac{d\theta_{rm}}{dt} = \omega_{rm} \quad (4.4)$$

Where:

- ψ_d, ψ_q: d-q axis flux components
- v_d, v_q: d-q axis voltage components
- i_d, i_q : d-q axis current components
- R: Phase resistance
- p: Number of pole pairs
- ω_{rm} and θ_{rm}: Rotor mechanical speed and position
- J: Sum of rotor and load inertia
- T_e and T_l: Electromagnetic torque and load torque, respectively

The electromagnetic torque T_e and load torque T_l: are computed using the following equations:

$$T_e = \frac{3}{2}p(\psi_d i_q - \psi_q i_d) \quad (4.5)$$

$$T_l = T_{lAct} + b_1 sign(\omega_{rm}) + B\omega_{rm} \quad (4.6)$$

Where:

- T_{lAct}: Speed-independent active load component
- b_1: Static friction coefficient
- B: Damping coefficient

The d-q currents in equations (1), (2), and (5) are provided by the inverse flux maps:

$$i_d = i_d(\psi_d, \psi_q) \quad i_q = i_q(\psi_d, \psi_q) \quad (4.7)$$

- **Computational Considerations**

The use of flux-current maps introduces significant challenges in terms of memory usage and computational complexity for the microcontroller. These include:

1. **Map Size Selection**: Determining an optimal resolution for the maps to balance accuracy and memory consumption.
2. **Search and Interpolation Algorithms**: Efficient algorithms are required for real-time retrieval and interpolation of values from the maps.

Although the selection of the inverse flux vs. current maps size, made up by two 81 by 81 arrays, and the associated interpolation techniques by the linear-point slope algorithm are critical for RTS, they fall beyond the scope of this discussion. Nevertheless, these challenges highlight the need for advanced optimization techniques to ensure that the model meets the stringent requirements of real-time applications while maintaining high accuracy and computational efficiency.

- **Characteristics of the RK4 and PC Solvers**

Two distinct solver algorithms, the fourth-order **Runge-Kutta** (RK4) and the **Predictor-Corrector** (PC), have been evaluated for implementing the motor model [20]. These solvers were analyzed and compared based on their execution time and accuracy.
The RK4 algorithm, a single-step method, involves iterative computation with five evaluations of the motor model equations (4.1) to (4.6) for each integration time step. This process requires approximately 34 µs per time step. While the single-step nature of RK4 makes it computationally intensive, it offers significant flexibility in choosing intermediate points and weights. This adaptability allows for fine-tuning the algorithm's stability and accuracy characteristics.
In contrast, the PC algorithm is a multi-step method that performs four sequential calculations of equations (4.1) to (4.6) for each integration time step, requiring about 12.5 µs per step. Although it demands less computation time, it inherently sacrifices some flexibility in designing stability and accuracy properties compared to the RK4 algorithm.

4.2.3 Runge-Kutta and Predictor-Corrector Comparison

- **Performance Analysis and Task Allocation**

Table 4.1 provides an overview of the Real-Time Simulation (RTS) task allocation and the associated computation times, while Table 4.2 focuses on the CPU workload for different solvers, assuming a PWM period of 100 µs. The analysis carried out on the calculation times allows us to hypothesize the accuracy of the solvers by relating it to the possible integration step. For a more in-depth analysis, some accuracy indices (e.g., the absolute error integral) could be used to characterize the performance of each implementation, based on a reasonable use case (stimulus). The comparison reveals several important insights:

- The RK4 solver places a significantly higher computational demand on the CPU compared to the PC solver.
- The CLA remains underutilized in both cases, providing an opportunity to allocate additional control or diagnostic tasks to this co-processor.

- **Impact on Real-Time Simulation Accuracy**

When aiming to ensure a CPU workload below 90% a common safety threshold for real-time applications the PC solver offers greater flexibility in reducing the integration time step. Specifically, with the PC solver, the integration time step can be reduced to 20 µs, allowing up to five iterations within the PWM period (100 µs).

This reduction theoretically enhances accuracy by improving the resolution of the motor model simulation.
In contrast, the RK4 solver is limited to a minimum integration time step of 50 µs due to its computational intensity, constraining the achievable accuracy. The RK4's higher computational demand makes it less suitable for scenarios where finer time resolution is required.

TABLE 4.1: COMPUTATION TIMES AND ALLOCATION OF TASKS (TMS F28379S)

	FOC control	***Motor-drive***		***Host comm.***
		RK4 solver	***PC solver***	
CPU	**–**	**34µs[1]**	**12.5 µs[1]**	**20 µs**
CLA	**12 µs**	**–**	**–**	**–**

[1] ONE INTEGRATION STEP

TABLE 4.2: CPU COMMITMENT VS. DIFFERENT SOLVER ARRANGEMENTS (TMS F28279S)

Solver	***Steps***	***Computation time (µs)***	***Integration time-step (µs)***	***CPU occupation (solver + Host comm.) in % of T_{PWM} = 100µs***
RK4	**1**	**34**	**100**	**54**
	2	**68**	**50**	**88.5**
PC	**1**	**12.5**	**100**	**32.5**
	2	**25**	**50**	**45**
	5	**62.5**	**20**	**82.5**

The choice between the RK4 and PC solvers depends on the desired balance between accuracy and computational efficiency. The PC solver's reduced computational burden enables finer integration steps, making it a favorable choice for enhancing real-time simulation accuracy. Meanwhile, the RK4 solver, while offering superior flexibility in algorithm design, imposes stricter limitations on the achievable time resolution due to its higher execution time per step. These findings highlight the importance of selecting the appropriate solver based on the specific requirements and constraints of the motor control application.

4.4 Experimental results

Figure 3.10 illustrates the laboratory setup used in this study, comprising the SynRM, a three-phase inverter module by Rectificadores Guasch S.A.U, the Delfino F28379S microcontroller board (Figure 3.1), and the host desktop. The main motor data are summarized in Table 3.1. The Delfino microcontroller board was utilized for both real-time simulations (RTS) and experimental drive tests, employing identical software parameterization for consistency. To ensure safe operation of the IGBT inverter, the PWM period was fixed at 100 µs for all tests.

The development environment included Code Composer Studio (release 11.0.0) and MATLAB/Simulink (release 2022b) with the Embedded Coder Support Package for Texas Instruments C2000 Processors (version 22.2.1). The presented results compare the RTS and experimental outcomes.

Figure 4.13 shows a test case of current control with a square-shaped d-current reference increasing at a frequency of 0.2 Hz. Both the d-current and d-voltage reference traces are shown. The SynRM rotor (Figure 3.11) was locked, and the maximum current amplitude was chosen to exceed the saturation knee of the d-flux. Under these conditions, the motor behaves as an RL load, with the inductance treated as a differential inductance varying with the current level. Using the same current regulator gains, varying saturation levels of the machine produce different responses at different set-point values.

Comparisons are made between RTS results obtained with RK4 and PC solver algorithms and the experimental results. Both solvers were executed with two integration steps per PWM period, corresponding to a fixed integration time step of 50 μs (refer to Table II).

The results demonstrate that the PC and RK4 traces are nearly indistinguishable, and the RTS responses align closely with experimental results for current steps below the saturation knee (between 4 and 5 A). For current steps above the saturation knee, discrepancies appear in the settling transients, increasing with the magnitude of the current step.

Figures 4.14, 4.15 zooms in on the largest step response at approximately 10 A (deep saturation). Minor deviations are observed during the increasing and decreasing transients at intermediate current values, likely due to iron related hysteresis effects in the actual motor, which are not modeled, while sampling, control and inverter delays (which might result in similar artifacts) are carefully modelled.

Despite these nuances, the increasing rate-of-change in current response at high current values due to saturation is accurately captured by the RTS. The overall accuracy of the RTS is further validated by its ability to closely approximate experimental results, even when considering unmodeled phenomena such as inverter nonlinearities.

The PC solver emerges as the preferred option, as it utilizes the CLA effectively, leaving approximately 55 μs of CPU free time for further control and communication developments. In comparison, the RK4 solver leaves only 11 μs of CPU free time. In both cases, an additional 88 μs of computation time is available in the CLA, enabling further system optimizations. Figure 4.16 presents results for speed control mode, specifically during a speed ramp-up from 0 to 750 rpm (half-rated speed) followed by a steady-state condition. The speed reference was smoothed using an "S" profile, and the d-q currents were controlled based on the MTPA strategy with a current angle of approximately 60 degrees. The test was performed at no load due to limitations of the test bench (the loading machine was disconnected for this setup). Despite this limitation, the results are meaningful, as they provide insights into the transient behavior of d-q current and voltage components. Through a trial-and-error adjustment of uncertain mechanical parameters (inertia and damping coefficient), the RTS and experimental responses show near-identical behavior. In this test, the PC solver with a 50 μs integration time step was used. To enhance the accuracy of real-time simulations, this work leveraged the floating-point CLA coprocessor available in the Texas Instruments Delfino F28379S microcontroller. This approach enabled parallel processing, with

the CPU handling the integration of the motor drive model while the CLA executed the field-oriented control task and potential auxiliary control tasks.

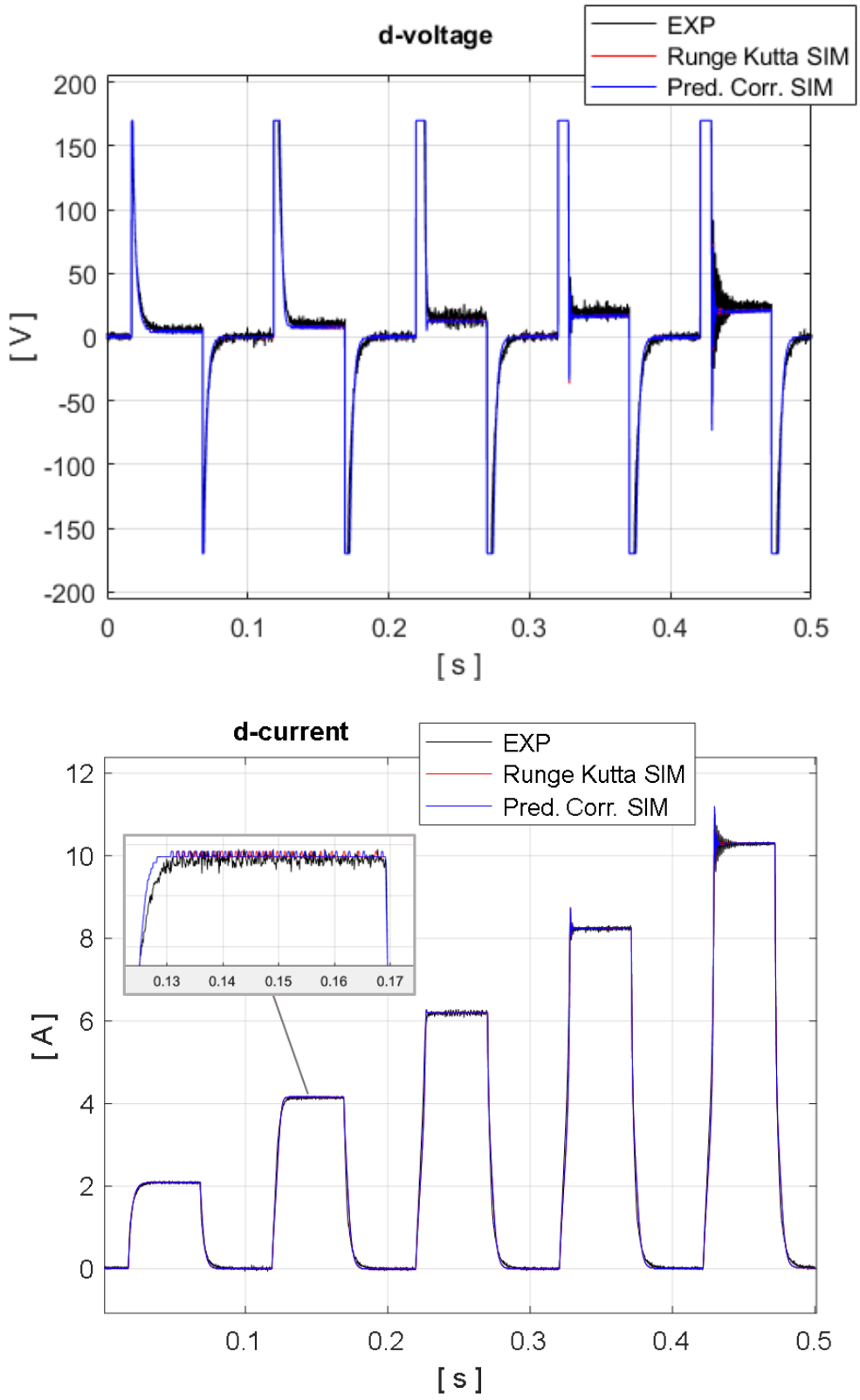

Figure 4.13: d-axis voltage e current step responses

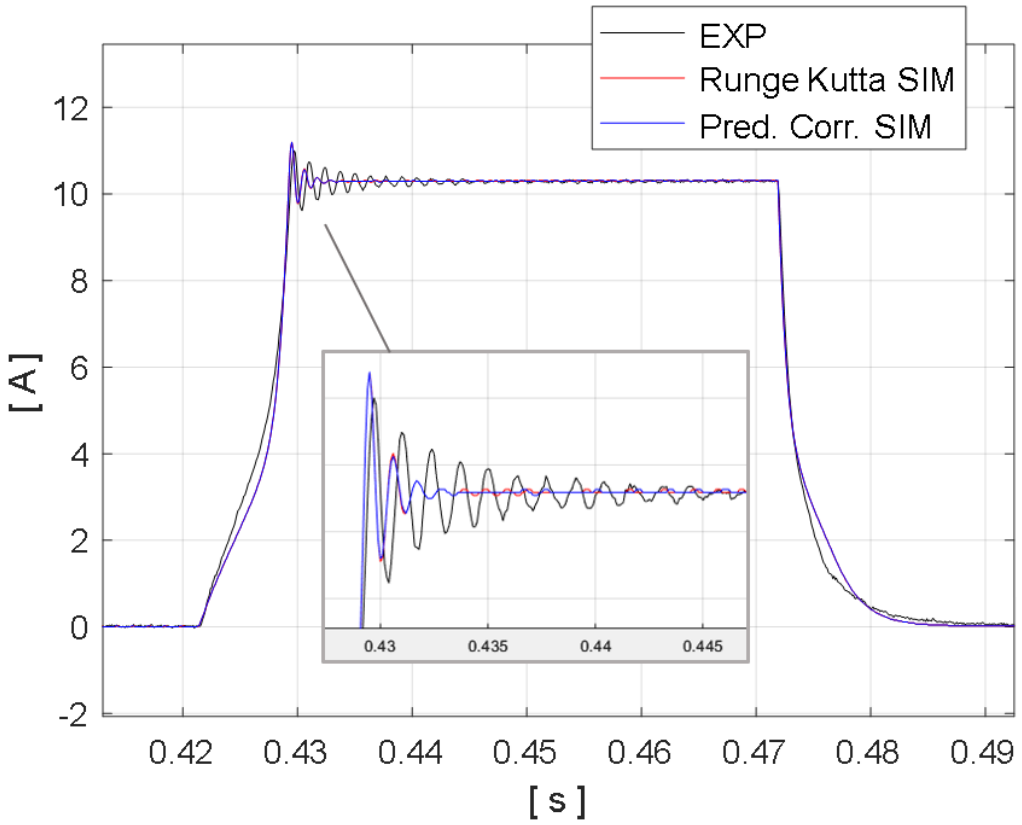

Figure 4.14: Large step response of the d-axis current (detail).

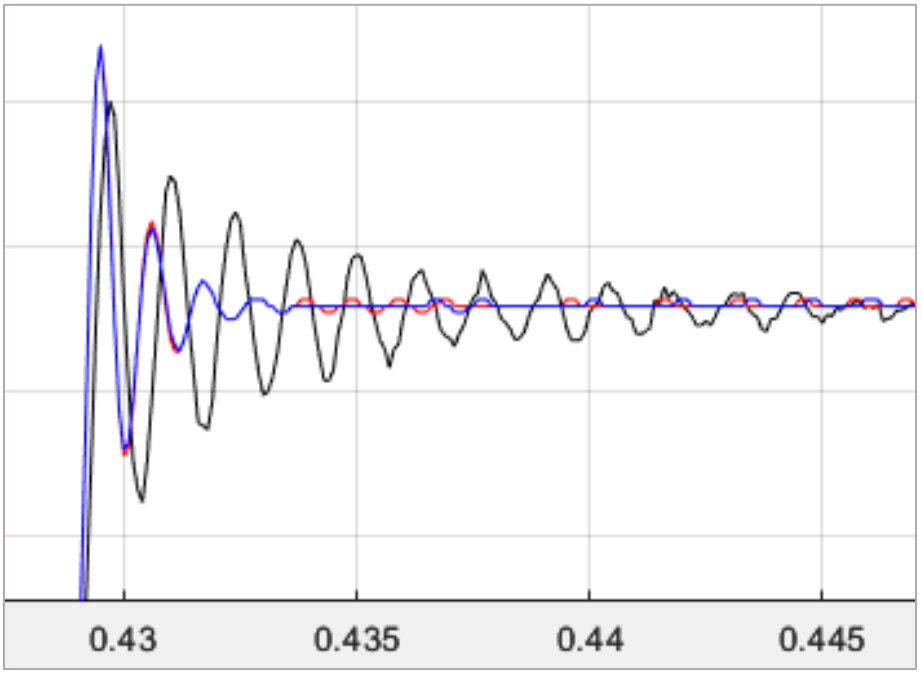

Figure 4.15: Overshoot detail of Figure 4.14.

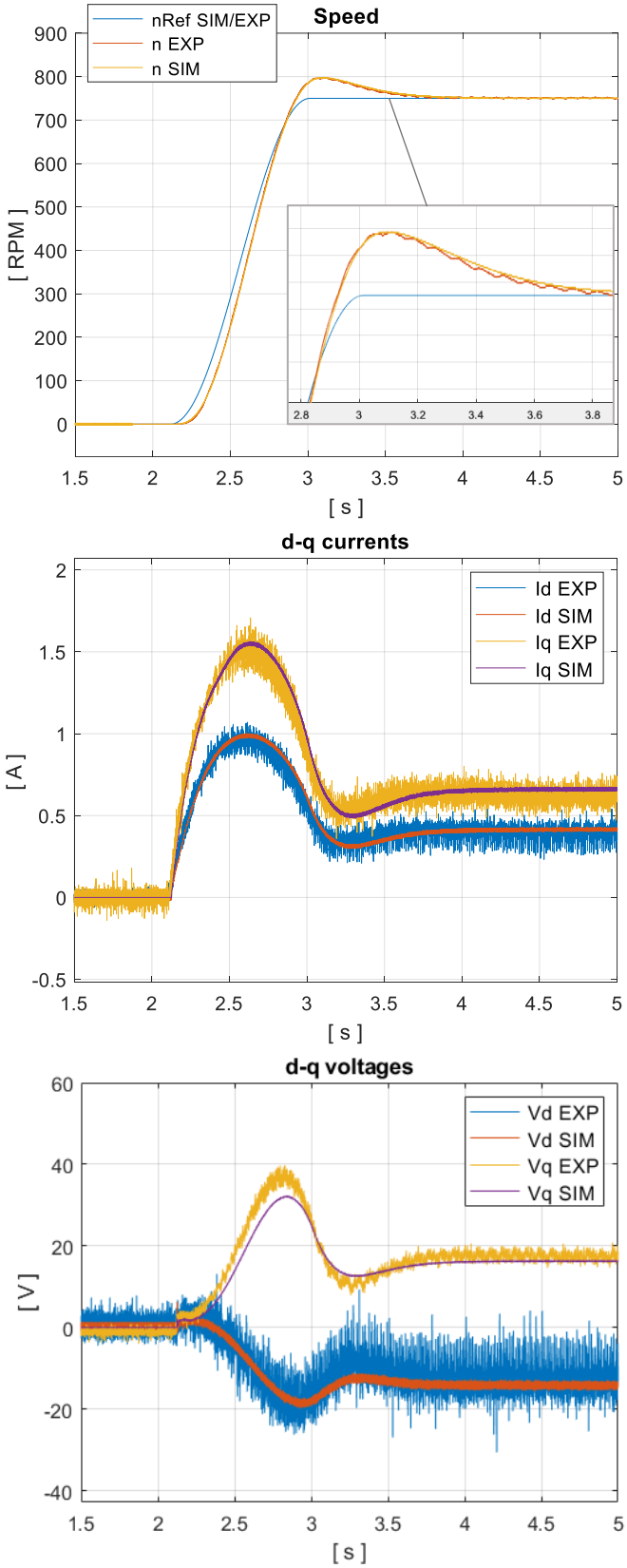

Figure 4.16: Comparison Between Speed Step Response in Simulated and Experimental Tests

Using a 4th-order Runge-Kutta solver, two integrations of the SynRM model were achieved within each 100 µs control/PWM period, corresponding to a 50 µs integration time step. Furthermore, the PC solver proved to be a faster alternative, allowing up to five integrations per period with a 20 µs integration time step. This flexibility enables developers to balance accuracy and computational efficiency effectively.

The experimental validation presented in this study demonstrates the effectiveness of the RTS technique for SynRM drives, including the advantages of parallel processing using the CLA. To the best of our knowledge, no previous work in the literature has validated RTS with parallel processing for SynRM using the CLA. Future work will focus on optimizing computation times further, with the goal of achieving real-time simulation for motor drives operating at PWM frequencies of up to 20 kHz.

Chapter 5

Improving AC/DC Converter Operation Using Neural Networks

Part of the work presented in this chapter has been previously published in [48].

5.1 Core Concepts of AC/DC Converter.

An AC/DC converter is an essential component in modern electrical engineering, designed to facilitate the bidirectional transformation of electrical energy. These devices operate as rectifiers when converting three-phase sinusoidal AC voltages into DC voltage, and as inverters when performing the reverse operation, converting DC voltage back to AC. AC/DC converters are pivotal in various applications, including power networks, renewable energy systems, power quality enhancement, Power factor correctors, and industrial processes involving machinery and motor drives. Their controllable features enable precise and efficient energy management, adapting to diverse operating conditions and system requirements.
In the realm of sustainable mobility, AC/DC rectifiers play a key role in electric vehicle (EV) charging stations. These systems convert AC energy from the grid into DC energy required to charge vehicle batteries, ensuring efficient energy transfer. Additionally, they support Vehicle-to-Grid (V2G) technology, enabling the reverse flow of energy from vehicle batteries back to the grid to balance energy demand and supply (Figure 5.1).

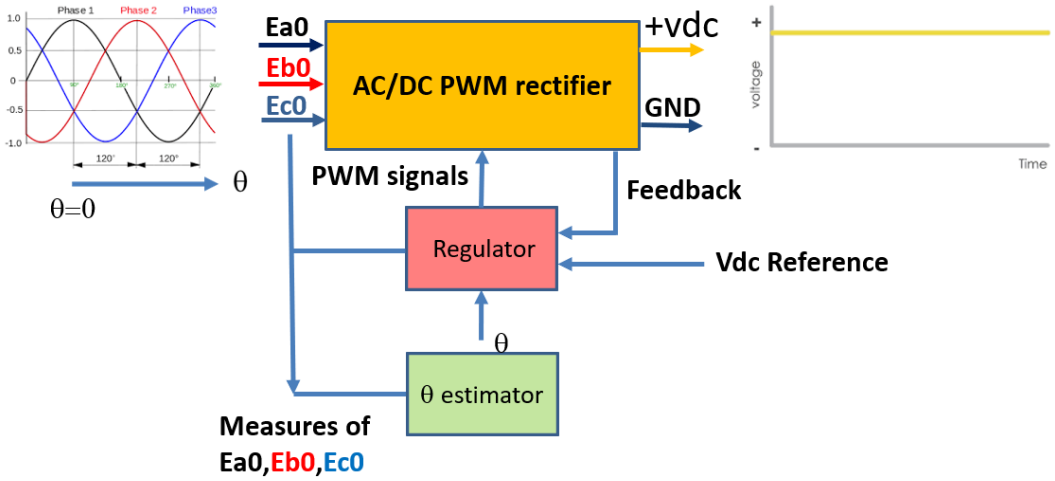

Figure 5.1: AC/DC Converter scheme

The physical implementation of the AC/DC converter typically consists of a PWM inverter bridge, which employs Insulated Gate Bipolar Transistor (IGBT) technology. Operating at a high switching frequency of 10 kHz, the bridge ensures efficient and precise voltage regulation. Complementing this hardware are advanced control systems, including a phase estimator for real-time measurement and synchronization of electrical signals, and a regulator for maintaining optimal operational conditions. In our work, these control functions are executed on an electronics board featuring the Texas Instruments Delfino F28379S microcontroller, which provides the computational power and flexibility required for high-performance AC/DC conversion in complex applications.

The study and development of control systems for AC-DC PWM rectifiers have been a significant focus in the field of power electronics. These systems have been extensively analyzed and simulated in numerous research works [22]-[27], as they play a critical role in various applications. The ability of these rectifiers to regulate and maintain a stable DC output under varying load and grid conditions has driven the exploration of advanced control strategies.

Numerous researchers have made valuable contributions to the study of power converters, focusing on their topology, control strategies, and applications in electric vehicles [31]-[43].

PWM rectifiers can be implemented using different control system architectures, each tailored to achieve specific performance goals such as high efficiency, low harmonic distortion, or robust operation under dynamic conditions. Among the widely studied control strategies, the synchronous reference frame control commonly referred to as "*d-q control"*, has emerged as one of the most effective methods for high-performance applications, as highlighted in [28].

The *d-q control* method is based on the transformation of the three-phase stationary reference frame (*abc)* into a two-axis rotating reference frame (*d-q*). This transformation enables the decoupling of active and reactive power components, simplifying the control of the AC-DC rectifier. The key to this approach lies in the accurate computation of the synchronous angle θ which represents the angular position of phase "*a* "of the three-phase grid voltages (E_{ao},E_{bo},E_{co}) relative to the fixed *d-axis* reference frame. Furthermore, the synchronous *d-axis* is aligned with the grid voltage vector and rotates at the grid's synchronous frequency, ensuring that the transformed *d-q*-variables are steady-state values under balanced conditions (Figure 5.2). The transformation process is mathematically realized using Park's transformation, which converts the time-varying sinusoidal signals of the *abc*-reference frame into DC-like signals in the *d-q*-reference frame. This simplifies the design of controllers, as the *d-q*-signals can be independently regulated using conventional PI (Proportional-Integral) controllers. By regulating the *d axis* current, the DC voltage can be precisely controlled, while the *q-axis* current is typically regulated to zero to achieve unity power factor operation, minimizing reactive power flow.

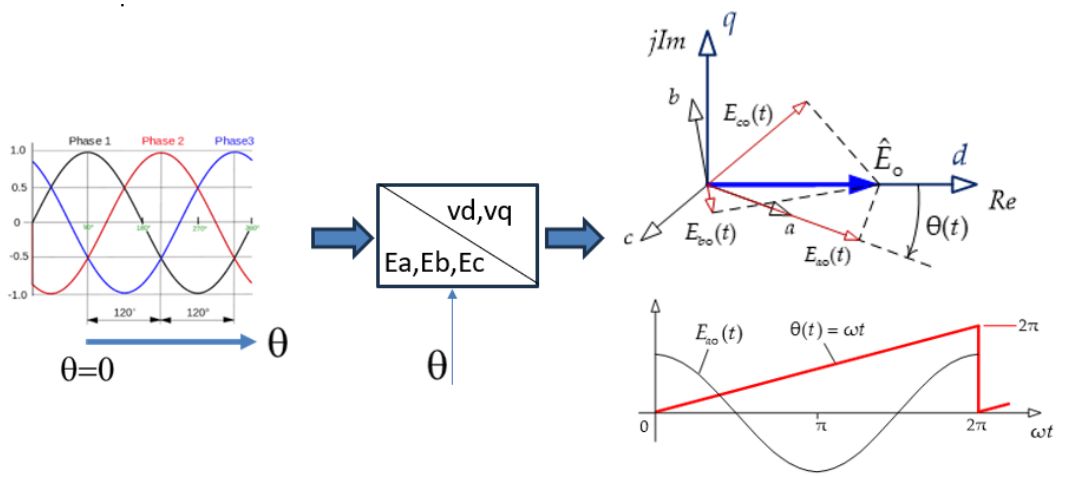

Figure 5.2: Phasor diagram of the grid voltages and synchronous angle θ.

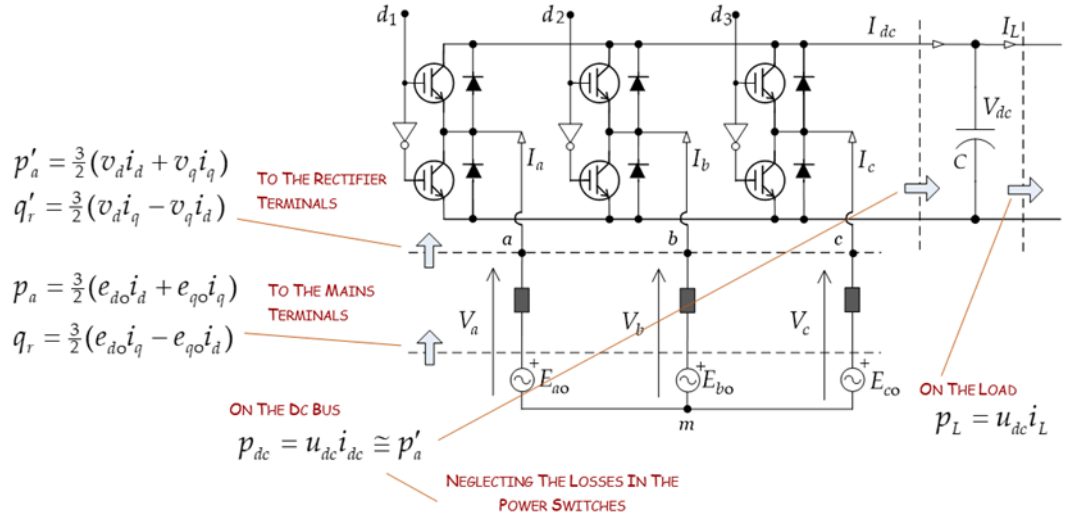

Figure 5.3: Structure of the grid converter (formulas in p.u.)

The system architecture presented in this study builds upon these principles and is designed to optimize the performance of the AC-DC rectifier. The control system employs a phase-locked loop (PLL) to accurately estimate the synchronous angle θ by tracking the phase of the grid voltage. This ensures that the coordinate transformation remains synchronized with the grid, even under conditions of grid voltage distortion or imbalance. Figures 5.2 and 5.3 provides a visual representation of the synchronous angle θ, the grid voltages (E_{ao},E_{bo},E_{co}), the rotating *dq*-reference frame and the structure of the grid converter.

The synchronous reference frame control offers a robust and efficient framework for the control of AC-DC PWM rectifiers, enabling precise regulation of the DC output voltage and improving the overall performance of the system under dynamic operating conditions.

The accurate estimation of the synchronous angle, derived from the measurements of three-phase grid voltages, is vital for ensuring the efficient operation of the

rectifier. Anyway, disturbances in power transmission and distribution lines can introduce voltage distortions, compromising the precision of angle estimation. Such distortions are primarily caused by the generation of even harmonics, which challenge the performance of standard phase-locked loops (PLLs). To address this issue, some researchers have proposed enhanced PLL algorithms that incorporate repetitive controllers functioning as bandpass filters to attenuate even harmonics [28][29]. Other approaches involve the use of pre-filters or extended loop filters to improve estimation accuracy [30]. While these techniques effectively mitigate harmonic interference, they require careful gain tuning to balance rapid harmonic compensation with system stability. By doing so, these methods can eliminate the impact of faults on synchronous angle estimation within approximately 80 ms [29].
In this study, we adopt an alternative approach that identifies the type of fault in the grid to enhance synchronous angle estimation accuracy. Previous research has demonstrated the effectiveness of Wavelet Transforms (WT) in detecting and classifying faults in both AC and DC grids, although these methods often require extensive voltage measurements [44][45]. More recently, Artificial Intelligence (AI)-based methods, including Fuzzy Logic (FL), Adaptive Neuro-Fuzzy Inference Systems (ANFIS), Artificial Neural Networks (ANN), and Genetic Algorithms (GA), have gained prominence for fault detection [46]. Advanced AI techniques, such as Convolutional Neural Networks (CNN) and Recurrent Neural Networks (RNN), have also been employed for precise fault localization in power transmission and distribution networks, with the added capability of executing corrective actions to maintain grid functionality [47]-[49].
Since the focus of this work is on fault classification rather than localization, a Back Propagation Artificial Neural Network (BP-ANN) is utilized for its computational efficiency. Using line voltage measurements, the BP-ANN effectively classifies different types of faults in the three-phase AC grid. It distinguishes between symmetric faults (e.g., three-phase short circuits and three-phase-to-ground shorts), where no phase shift occurs, and asymmetric faults (e.g., single-phase-to-ground and two-phase-to-ground short circuits), which involve a phase shift. Once the fault type is identified, a secondary BP-ANN system estimates the synchronous phase angle, compensating for any distortion or shift caused by the fault. Within a transient period of approximately 10 ms, the estimated phase aligns with the actual grid phase, as if the fault had not occurred. This ensures optimal operation of the AC-DC PWM rectifier, maintaining the stability of the output DC voltage despite fault-induced distortions in the synchronous angle θ.
The proposed solution is distinguished by its simplicity, high effectiveness in managing various fault scenarios, minimal transient response time, and precise phase estimation. The control system for the AC-DC PWM rectifier, based on neural networks, has been developed and simulated on the MATLAB/Simulink platform. It is compatible with Texas Instruments microcontrollers through the Embedded Coder Support Packages for the TI C2000 family [46][50][51]. Experimental validation is illustrated in paragraph 5.5, employing the Texas Instruments Delfino F28379S microcontroller to implement and evaluate the proposed control strategy.

5.1.1 PWM Power Rectifier: Structure and Mathematical Model

An inductive-resistive (L-R) series filter is utilized as an interface between the grid and the converter to ensure proper operation and mitigate high-frequency harmonics (Figure 5.3). The mathematical modeling of the converter begins by introducing the switching functions, which represent the states of the power switches in the converter. Let d_1, d_2, and d_3 denote the control signals for the upper switches of each converter branch. Based on these control signals, the switching functions can be defined as follows:

$$s_a = \frac{2d_1 - (d_2 + d_3)}{3} \tag{5.2}$$

$$s_b = \frac{2d_2 - (d_1 + d_3)}{3} \tag{5.3}$$

$$s_c = \frac{2d_3 - (d_1 + d_2)}{3} \tag{5.4}$$

These switching functions allow the representation of the converter's input voltages as functions of the DC-side voltage V_{dc}, as follows:

$$V_a = s_a V_{dc} \tag{5.5}$$

$$V_b = s_b V_{dc} \tag{5.6}$$

$$V_c = s_c V_{dc} \tag{5.7}$$

Using these equations, the voltages can be incorporated into the grid-side model of the converter, which is expressed in the natural reference frame. Considering the generator convention, the mathematical model includes the grid-side currents I_a, I_b and I_c , the three grid-side currents, E_{ao}, E_{bo} and E_{co} , the grid voltages and I_L the load current. The governing equations for the converter are:

$$\begin{bmatrix} E_{ao} \\ E_{bo} \\ E_{co} \end{bmatrix} = R \begin{bmatrix} I_a \\ I_b \\ I_c \end{bmatrix} + L \frac{d}{dt} \begin{bmatrix} I_a \\ I_b \\ I_c \end{bmatrix} + \begin{bmatrix} V_a \\ V_b \\ V_c \end{bmatrix} \tag{5.8}$$

$$C \frac{dV_{dc}}{dt} = d_1 I_a + d_2 I_b + d_3 I_c - I_L \tag{5.9}$$

Here, equation (5.8) represents the current balance at the upper node of the bulk capacitor C, which is part of the DC-link.

To simplify the analysis and control, the system can be transformed from the natural frame to a synchronous *dq*-reference frame using Clarke and Park transformations. These transformations project the three-phase system into two orthogonal axes (*d*-axis and *q*-axis), rotating synchronously with the grid angular frequency ω. In this transformed frame, the equations become:

$$\begin{cases} E_{do} = RI_d + L\dfrac{dI_d}{dt} - \omega L I_q + V_d \\ E_{qo} = RI_q + L\dfrac{dI_q}{dt} + \omega L I_d + V_q \\ \dfrac{dV_{dc}}{dt} = \dfrac{3}{2}\left(s_d I_d + s_q I_q\right) - I_L \end{cases} \quad (5.10)$$

In these equations:

- E_{do} and E_{qo} are the *d*- and *q*-axis components of the grid voltage.
- I_d and I_q are the *d*- and *q*-axis components of the grid-side currents.
- V_d and V_q are the *d*- and *q*-axis components of the converter's input voltages.
- s_d and s_q are the switching functions in the *dq*-reference frame.

The use of the *dq*-reference frame simplifies the control design by decoupling the active and reactive power components, enabling independent control of the DC-side voltage V_{dc} and the grid-side power factor. This transformation is fundamental to modern control strategies for grid-connected converters, improving their performance under dynamic conditions and facilitating harmonic mitigation.

5.1.2 Control Strategy

Even if the control problem could be easily generalized to non-unitary power factor, since the reactive power is controlled anyway, the main objectives of this grid-connected converter control are

1. Achieving a **unity power factor**.
2. Maintaining a **constant DC voltage**.

- **Control of Active and Reactive Power**

To achieve unity power factor, the active p_a and reactive q_r powers are expressed in the *d-q* synchronous reference frame as:

$$p_a = \frac{3}{2}\left(E_{do} I_d + E_{qo} I_q\right) \quad (5.11)$$

$$q_r = \frac{3}{2}\left(E_{do} I_q - E_{qo} I_d\right) \quad (5.12)$$

- **Alignment of the d-Axis**

The first step to ensure zero reactive power, and hence unity power factor, involves aligning the rotating *d*-axis of the reference frame with the grid voltage. In order to synchronize the reference frame, the space vector's angle (Clarke's transformation)

is considered. In ideal conditions (balanced voltage, no homopolar component), this angle equals the argument of sine in the voltage signal of phase a. In this configuration, the q-axis grid voltage E_0 voltage, E_{q0}, becomes zero. Under this alignment condition, the equations for active and reactive powers simplify to:

$$p_a = \frac{3}{2}(E_{do} I_d) \tag{5.12}$$

$$q_r = \frac{3}{2}(E_{do} I_q) \tag{5.13}$$

The active power is proportional to the 'I_d' current, the reactive power to the 'I_q' current and their controls are independent. To achieve the first objective, imposing a zero current on the q-axis is necessary. The active power instead will be controlled via the 'I_d' current control loop. In this manner, the active and reactive powers absorbed by the AC grid are:

$$p_a = \frac{3}{2}(E_{do} I_d) \tag{5.14}$$

$$q_r = 0 \tag{5.15}$$

For the second objective, a reference value *udc** is imposed to control the DC output voltage, V_{dc}, through the external feedback loop.

- **Current and Voltage Regulation**

Figure 5.4 illustrates the control scheme of the PWM rectifier. The control structure involves two main loops:

1. **Outer Voltage Control Loop**: This loop compares the reference DC voltage V_{dc} with the actual voltage measured across the DC-link capacitor. The resulting error is processed by a PI voltage controller, which generates the reference Id
2. **Inner Current Control Loop**: This loop uses the *d-q* reference currents (I_d, I_q) and compares them with the measured *d-q* currents, obtained through Clarke and Park transformations. The errors are fed into PI current regulators to produce the reference voltages in the *d-q* frame.

- **Control Decoupling**

A key consideration in the control design is the coupling between the *d* and *q*-axis components, as evident from equations (10) and (11). The *d*-axis current depends not only on the *d*-axis voltage but also on the *q*-axis current, and vice versa. To address this, a decoupling algorithm is implemented, often using a multivariable PI controller, extensively analyzed in [132], to ensure independent control of the *d* and *q*-axis currents. The outputs of the current regulators are the reference voltages in the *d-q* frame. These reference voltages are transformed back to the stationary *α-β* frame using an inverse Park transformation. The resulting signals are then used to generate switching commands through Space Vector Pulse Width Modulation (SVPWM), enabling precise control of the converter's operation.

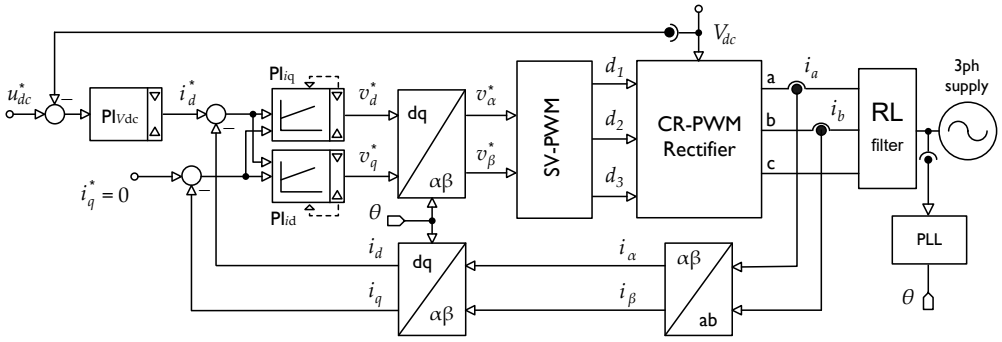

Figure 5.4: Zero Reactive Power Control scheme for PWM Rectifiers

5.1.3 Grid Synchronization with Three-Phase PWM Converters

As mentioned in the previous paragraph, the accurate detection of the grid angle θ is a critical requirement for performing Park transformations ($\alpha\beta/dq$), which are fundamental to the implementation of the Voltage Oriented Control (VOC) strategy. These transformations, as previously detailed, enable the conversion of variables between the stationary reference frame ($\alpha\beta$) and the rotating synchronous reference frame (dq), ensuring effective decoupled control of active and reactive power in grid-connected converters. This precise angle detection is essential for maintaining system stability and achieving optimal performance under various operating conditions. This study focuses on the robustness of grid angle detection methods, particularly under fault conditions that can distort grid voltages and compromise the stability of the control system. Two approaches are analyzed and compared: the traditional Quadrature Phase-Locked Loop (Q-PLL) algorithm and a novel Artificial Neural Network (ANN)-based method. The Q-PLL algorithm, a widely used technique, relies on phase-tracking mechanisms to estimate θ by locking onto the grid voltage phase. While effective under nominal grid conditions, Q-PLL performance can degrade in the presence of voltage sags, harmonic distortions, or other grid anomalies. In contrast, the proposed ANN-based method leverages the pattern recognition and learning capabilities of neural networks to estimate θ more accurately and reliably. By training the ANN to recognize and adapt to various grid conditions, including faults, this approach demonstrates enhanced robustness and adaptability compared to Q-PLL. The comparative evaluation of these two methods in terms of fault tolerance, dynamic response, and steady-state accuracy provides valuable insights into the suitability of each for advanced control systems in grid-connected applications. The Q-PLL algorithm is illustrated in Figure 5.5. Adopting the measurements of the three-phase grid voltages, Clarke transformation is performed to obtain the $\alpha\beta$ components E_α, E_β

$$\begin{aligned} E_\alpha &= -|E_o|\, sin\,\theta \\ E_\beta &= |E_o|\, cos\,\theta \end{aligned} \tag{5.16}$$

of the resultant voltage space vector $\vec{E}_o$, that is normalizing with respect to amplitude makes the calculation independent of angular velocity, obtaining:

$$\begin{aligned} e_a &= \frac{E_a}{|E_o|} = -sin\,\theta \\ e_\beta &= \frac{E_\beta}{|E_o|} = cos\,\theta \end{aligned} \tag{5.17}$$

At this point, the estimation error between the actual (θ) and the computed angle $\hat{\theta}$ is given by:

$$\varepsilon = -e_\alpha \cos\hat{\theta} - e_\beta \sin\hat{\theta} = \sin\theta\cos\hat{\theta} - \cos\theta\sin\hat{\theta} = \sin(\theta - \hat{\theta}) \cong (\theta - \hat{\theta}) \quad (5.18)$$

This error is used to estimate the grid frequency $\hat{\omega}$, through a PI regulator. By integrating the angular frequency, the estimated grid angle $\hat{\theta}$ is obtained and used as feedback (through $sin\,\hat{\theta}$ and $cos\,\hat{\theta}$) to close the angular loop. Finally, the estimated angle must be limited to -2π to 2π for numeric issues.

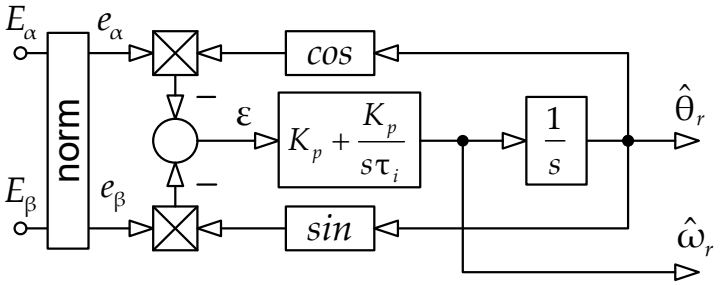

Figure 5.5: Quadrature Phase Locked Loop

The Quadrature Phase-Locked Loop (Q-PLL) algorithm, widely used for grid synchronization, requires only initial tuning, by imposing natural frequency and damping factor, and performs well under normal grid conditions without significant disturbances or faults. However, its dependency on direct grid voltage measurements makes it highly susceptible to reliability issues when voltage distortions occur due to grid faults. In particular, the presence of even harmonics in the grid voltage significantly impacts the accuracy of angle estimation, reducing the effectiveness of standard Q-PLL implementations.

5.2 Matlab/Simulink Offline Simulation

To evaluate the performance of the PWM AC/DC rectifier and its control system, a detailed simulation model was developed in MATLAB/Simulink®. The simulation includes a three-phase power grid modeled according to European standards, with a phase-to-phase voltage of 400 V and a frequency of 50 Hz. The rectifier itself was implemented using the Plexim/PLECS® toolbox, which allows for circuit-level modeling and integration within the Simulink environment using controlled voltage sources. The schematic representation of the PLL is shown in Figure 5.6, where the block diagram of Figure 5.5 is implemented with the angle estimation spanning a range from 0 to 2*pi, the rectifier is provided in Figure 5.7. The simulation setup incorporated a "Three-Phase Fault" block to introduce grid disturbances and evaluate the system's fault-tolerant control capabilities. Various fault conditions were tested, including single-phase-to-ground faults, two-phase-to-ground faults, and three-phase faults, both with and without ground involvement. The faults were programmed to occur at specific time intervals during the simulation, allowing for a detailed analysis of the system's transient and steady-state responses.

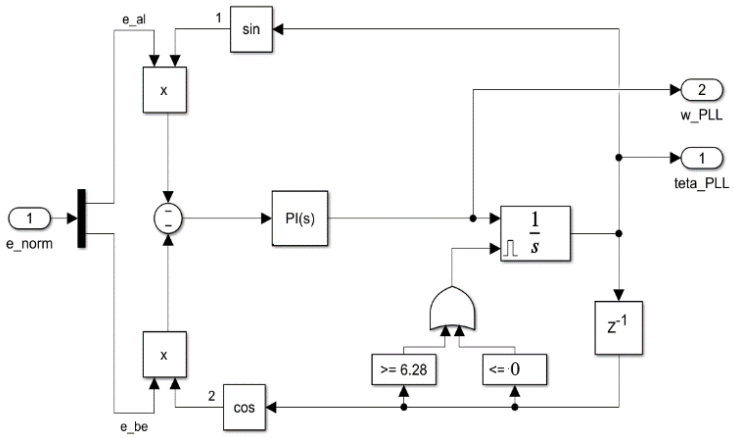

Figure 5.6 Quadrature Phase Locked Loop Simulink algorithm

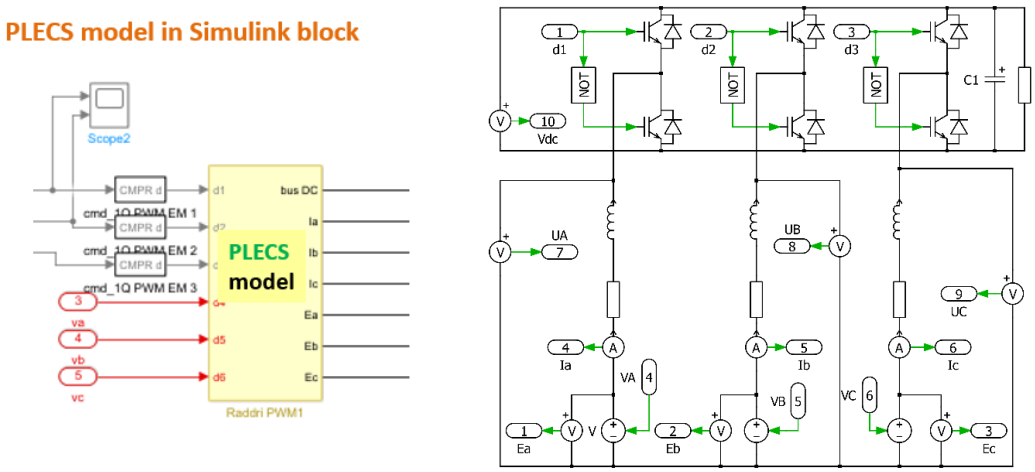

Figure 5.7 PLECS schematic of the PWM rectifier

The fault types, durations, and resistances used in the simulation are summarized as follows in figure 5.8a:

- Phase a to ground (e_{ao}/G): 0.2 s to 0.4 s
- Phase b to ground (e_{bo}/G): 0.4 s to 0.6 s
- Phase c to ground (e_{co}/G): 0.6 s to 0.8 s
- Phase a and phase b to ground (e_{ab}/G): 0.8 s to 1.0 s
- Phase b and phase c to ground (e_{bc}/G): 1.0 s to 1.2 s
- Phase a and phase c to ground (e_{ac}/G): 1.2 s to 1.4 s
- Phase a to phase b short-circuit (e_{ab}/S): 1.4 s to 1.6 s
- Phase b to phase c short-circuit (e_{bc}/S): 1.6 s to 1.8 s
- Phase c to phase a short-circuit (e_{ca}/S): 1.8 s to 2.0 s
- Three-phase to ground (e_{abc}/G): 2.0 s to 2.2 s

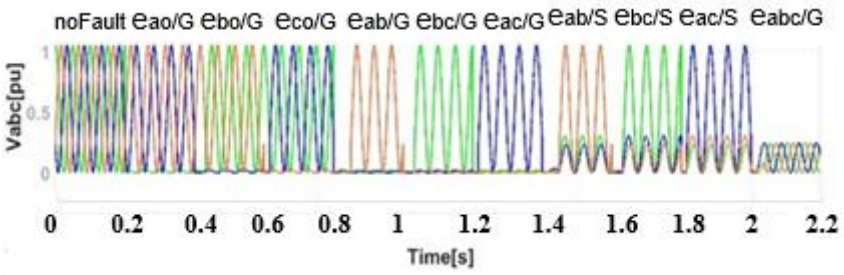

Figure 5.8a Fault types on the AC line.

During the first 0.2 seconds of the simulation, the grid operated under nominal conditions without any faults, serving as a baseline for comparison. Figure 5.8b illustrates the schematic diagram of the simulated electrical distribution system, highlighting the application of these fault scenarios, Figure 5.9 shows the fault block.

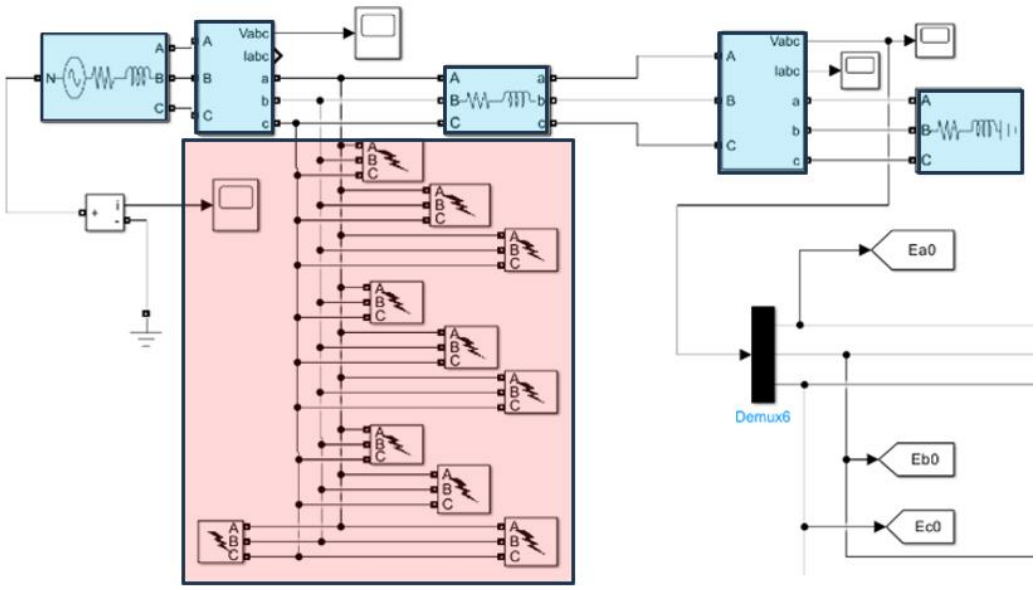

Figure 5.8b Simulation of faults on the AC line.

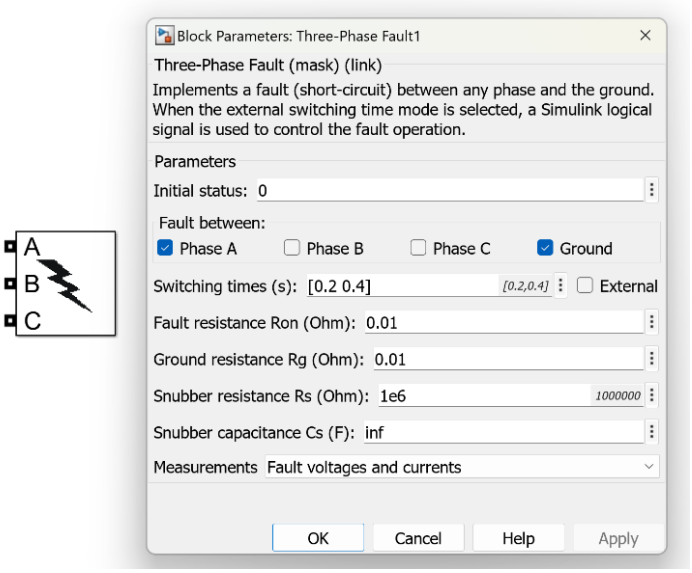

Figure 5.9 Fault setting block and dialog mask.

By using controlled voltage sources in the PLECS model, the faults were accurately introduced into the simulation. The fault parameters, such as fault resistance and line-to-ground resistance, were adjustable to mimic real-world conditions. The previously described control system has been implemented in MATLAB/Simulink, how shown in Figure 5.10 and Figure 5.11, to simulate its behavior under all the AC grid fault conditions discussed earlier. This simulation framework allows for the evaluation of the control strategy's performance using both the standard Phase-Locked Loop (PLL) algorithm and Artificial Neural Networks (ANNs). By applying identical fault scenarios to both configurations, it is possible to carry out a comparative analysis of their robustness, particularly in terms of synchronization angle estimation and stability of the DC output voltage during disturbances.

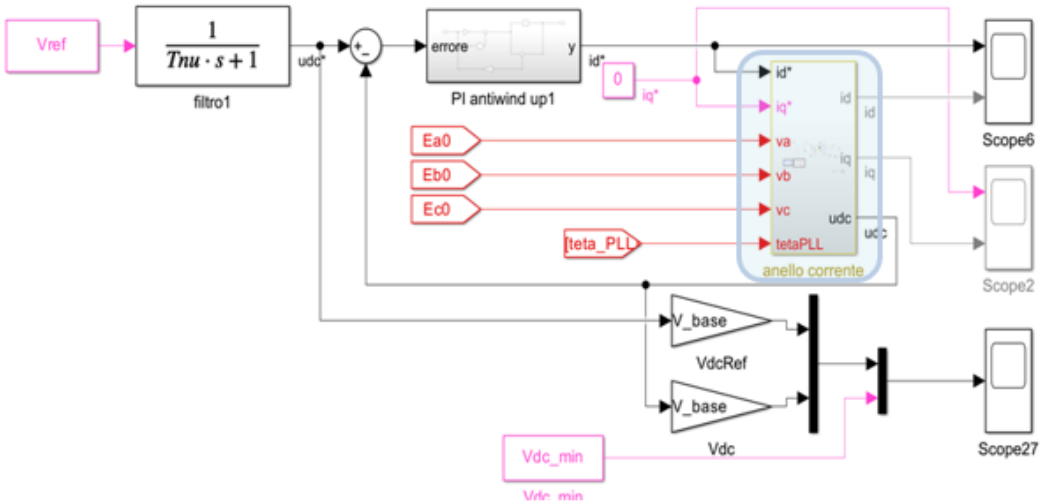

Figure 5.10 Control system of AC/DC Rectifier implemented in Simulink

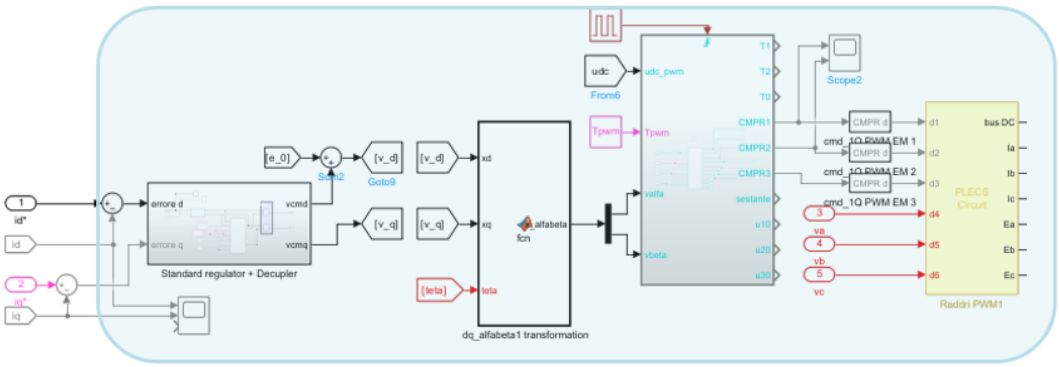

Figure 5.11 Inner control loop of AC/DC Rectifier implemented in Simulink

5.2.1 Fault Analysis and System Behavior with Standard PLL

When a three-phase voltage is applied to the AC PWM rectifier under the fault conditions outlined in the simulation setup, the standard Phase-Locked Loop (PLL) struggles to accurately estimate the synchronization angle θ due to the presence of voltage distortions introduced by these faults. The distortions, caused by phenomena such as unbalanced voltages or harmonic generation, interfere with the PLL's ability to lock onto the correct phase angle, leading to significant deviations in θ from its expected values. This behavior is clearly depicted in Figure 5.12, which illustrates the variation of the θ angle during the occurrence of different types of faults. The incorrect estimation of θ directly impacts the performance of the rectifier, as the control strategy relies on precise angle detection for effective operation.

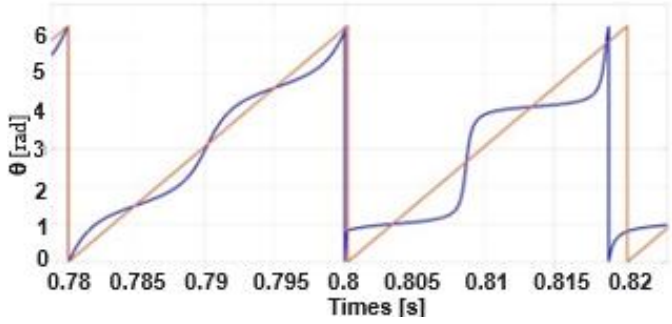

***Figure 5.12**: Comparison of the ideal synchronization angle (red) and the angle estimated by the standard PLL (blue) during the transition from a single-phase fault to a two-phase fault at t=0.8s.*

Figure 5.13 further demonstrates the impact of voltage distortions on the rectifier's output. During fault conditions, the rectifier's output voltage exhibits a noticeable reduction, highlighting the system's inability to maintain a stable DC voltage under such circumstances.

This drop in voltage is particularly critical as it compromises the rectifier's ability to deliver consistent power to the load. These results underscore the limitations of the standard PLL in handling grid faults, emphasizing the need for more robust synchronization techniques to ensure accurate angle estimation and maintain rectifier performance during adverse grid conditions.

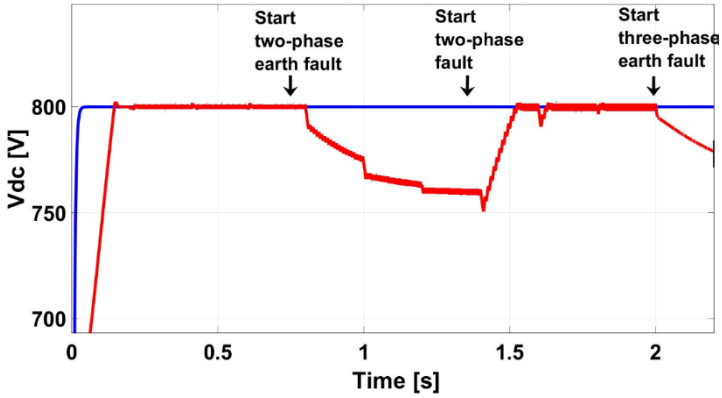

Figure 5.13: Vdc output of the rectifier during fault conditions, highlighting the impact on DC voltage stability.

5.3 A Brief Introduction to Biological Neural Networks

The human brain, composed of approximately 100 billion neurons (Figure 5.14), is an extraordinary interconnected network in which each neuron communicates through up to 10,000 synaptic channels [141]-[145]. These neurons form the foundation of all cognitive processes, including information processing, memory, and learning.

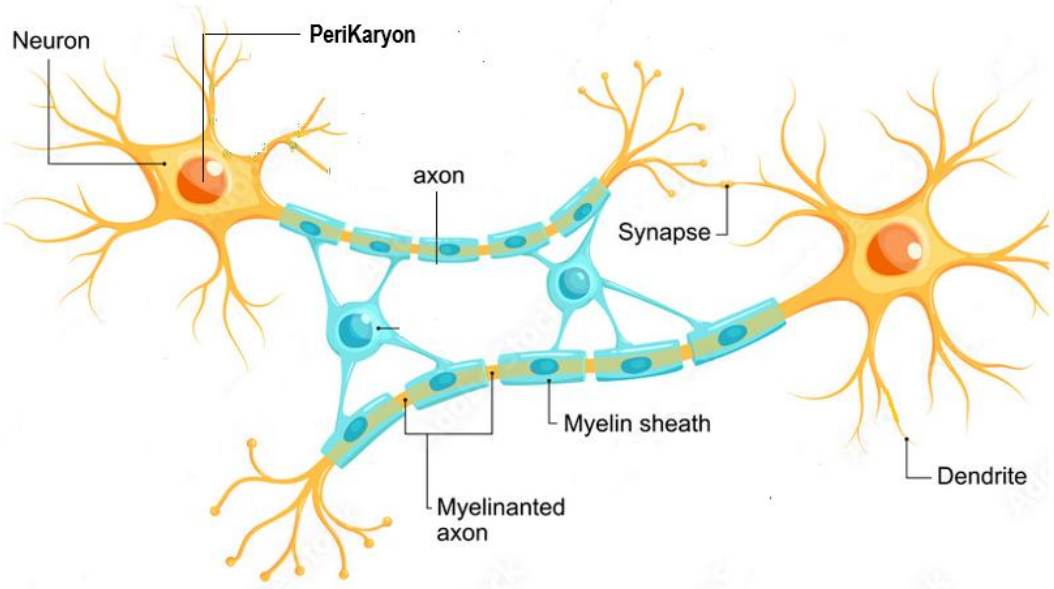

Figure 5.14: Structure and interaction of two neurons in a neural network

5.3.4 Neuron Structure and Signal Transmission

A neuron (Figure 5.14) is composed of four main parts:

1. **Dendrites**: These are the input terminals, resembling a branching network, that receive electrical signals from other neurons via synapses.
2. **Perikaryon** (or cell body): This is the central nucleus of the neuron where information is processed. It integrates incoming signals from the dendrites and evaluates whether the cumulative electrical potential surpasses a critical threshold.
3. **Axon**: A long projection through which processed signals are transmitted to synapses, ready to communicate with other neurons.
4. **Synapses:** The connection points between the axon terminals of the first neuron and the dendrites of the second neuron, where neurotransmitters facilitate the transmission of signals.

Signal transmission begins when electrical potentials arrive at the neuron through the dendrites. These signals, originating from synaptic activity, are integrated in the perikaryon. If the cumulative electrical potential exceeds an activation threshold, the neuron generates an electrical impulse, or action potential. This impulse travels along the axon to the synapses, where it stimulates other neurons, creating a continuous chain of communication. This process underpins the brain's ability to process information and respond to external stimuli.

5.3.2 What is Learning and How Does it Occur.

Learning is the process through which the brain modifies its neural connections to acquire new information, skills, or behaviors. It is a manifestation of neuroplasticity, the brain's remarkable ability to adapt and reorganize in response to experiences and external stimuli.

- **How Learning Occurs:**

1. **Synaptic Plasticity**:

   Synapses can strengthen or weaken over time, a process known as **synaptic plasticity**:

   - **Long-Term Potentiation (LTP)**: Frequently stimulated synapses increase their efficiency in transmitting signals, reinforcing neural connections.
   - **Long-Term Depression (LTD)**: Less-used synapses weaken, facilitating the reorganization of neural networks. These mechanisms are critical for memory formation and associative learning.

2. **Formation of New Connections**:

Learning also involves **synaptogenesis**, the creation of new synaptic connections between neurons.

3. **Modification of Existing Networks**:

   Neural networks are optimized through frequent use, consolidating efficient pathways while pruning unnecessary ones.

4. **Role of Neurotransmitters**:

   Chemicals like dopamine play a key role in reinforcing neural connections associated with meaningful or rewarding experiences.

- Example: How a Child Learns to Distinguish and Recognize Objects

A compelling example of the learning process is how a child learns to distinguish and recognize objects.

1. **Initial Exposure**:
   In the early months of life, a child is exposed to various visual stimuli, such as toys, faces, or everyday objects (e.g., a ball). The brain processes these visual inputs through the **visual cortex**, which analyzes features such as shape, size, and color.

2. **Feature Recognition**:
   The child begins identifying key characteristics of objects. For instance, a ball might be recognized for its round shape and bright color. These features are encoded in the brain and associated with specific neural patterns.

3. **Association with Meaning**:
   The child starts linking objects with names or functions. For example, when a caregiver repeatedly says the word "ball" while showing or playing with a ball, the child's brain strengthens the association between the auditory input (the word "ball") and the visual representation of the object. This is achieved through **LTP**, which consolidates the involved neural pathways.

4. **Reinforcement Through Repetition**:
   Every interaction with the ball reinforces the association between its name and appearance. With repeated exposure, the brain optimizes its recognition process, making it more automatic and efficient.

5. **Generalization**:
   Once the association is established, the child can generalize the concept to recognize other balls, even if they differ in size, color, or material. This ability arises from the brain's capacity to abstract general rules from specific experiences, enabling flexible and adaptive learning.

A child's ability to distinguish and recognize objects is a prime example of **neuroplasticity**. Through repeated exposure, association, and generalization, the brain develops increasingly refined neural networks that enable it to categorize and understand the surrounding world. This process forms the foundation of cognitive development and paves the way for acquiring more complex skills over time. It highlights the dynamic interplay between sensory input, synaptic plasticity, and neural optimization in shaping human learning.

5.3.3 Mathematical Model and Learning Process of Neural Networks

In a mathematical model, the behavior of a biological neuron is approximated using simplified parameters (Figure 5.15). The response intensity of the neuron depends on connection weights (W), which represent the strength of connections between neurons, and a bias term (b), which influences the activation threshold of the neuron. Specifically, for a connection between two neurons i and j, there is a weight *Wij* and for each neuron n, a bias term bn. To replicate the non-linear behavior of biological neurons, the mathematical model incorporates an activation function ϕ (e.g., ReLU, Sigmoid, or Tanh), which determines the output of the neuron by applying a non-linear transformation.

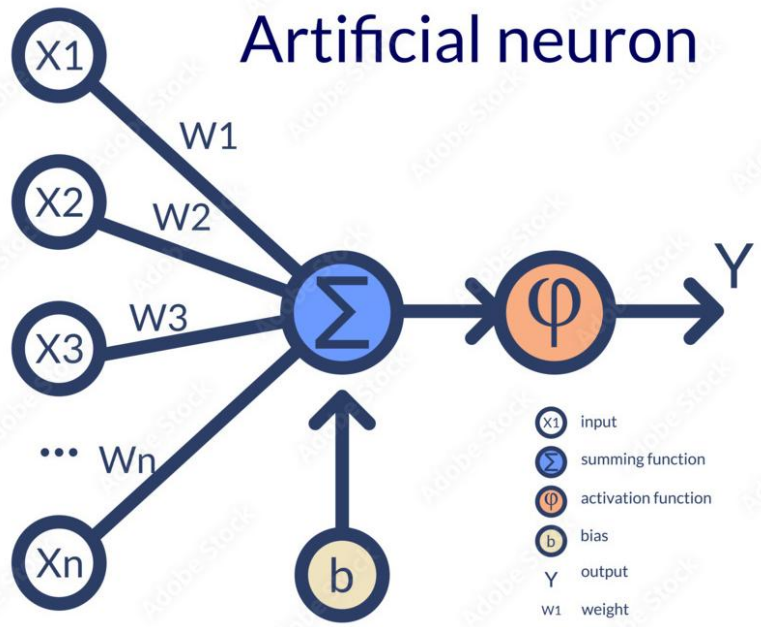

5.15: Mathematical model of the neuron

The output of a single neuron can be expressed as:

$$Y = \varphi\ (X_1W_1 + X_2W_2 + .. X_nW_n\ + b)$$

where $X_1, X_2 \ldots . X_n$ are the inputs, $W_1, W_2 \ldots . W_n$ are the weights, and b is the bias term. This model forms the building block of artificial neural networks.

- **Neural Network Structure and Learning**

A neural network consists of multiple interconnected neurons organized into three types of layers: input layers (which receive raw data), hidden layers (where intermediate computations occur), and output layers (which produce the final results), as depicted in Figure 5.16. These layers collectively enable the network to map complex relationships between input and output data.

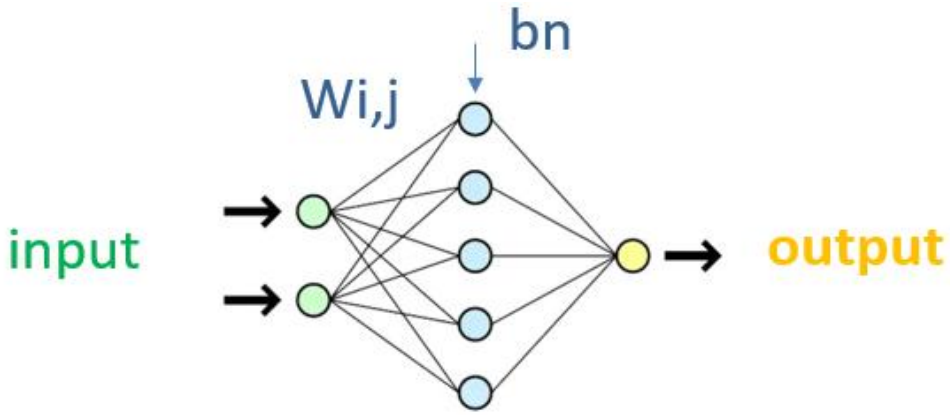

5.16: Typical Neural Network with input layer (green), hidden layer (cyan) and output layer (yellow)

The universal approximation theorem, proven by George Cybenko in 1989, states that a neural network with a single hidden layer containing a sufficient and finite number of neurons can approximate any continuous function to arbitrary accuracy. This property underscores the theoretical ability of neural networks to serve as powerful function approximators. Once the neural network structure is defined, the learning process begins. During this phase, the parameters of the network weights (W_{ij}) and biases (b_k) are adjusted to minimize the difference between the network's output and the desired target output. Initially, these parameters are set to random values, which typically result in outputs that deviate significantly from the target. To quantify this deviation, a cost function is introduced, commonly defined as the square of the difference between the target and network's predicted output. The fundamental process of network learning allows the gradual adjustment of these parameters (W_{ij}) and biases (b_k) over multiple steps, called epochs, to minimize the cost function. At the end of the procedure, the output of the network becomes very close to the target. This optimization is achieved through a method called backpropagation, which updates the parameters based on the gradients of the cost function. By iteratively refining the weights and biases during each epoch, the neural network's performance improves steadily. The process continues until the cost function falls below a predefined threshold. At this point, the Back Propagation-Artificial Neural Network (BP-ANN) is considered trained and ready to be deployed for tasks such as classification, prediction, or decision-making.

5.4 Neural Network Implementation for Fault Management.

5.4.1 Developing Neural Networks Using MATLAB Neural Fitting App

For the design and implementation of the neural networks, the MATLAB Neural Fitting app, shown in Figure 5.17, was utilized. This tool offers a user-friendly interface that simplifies the configuration, creation, training, and export of neural networks as Simulink blocks for further analysis and simulation. The Neural Fitting app allows customization of network parameters, enabling the adjustment of key properties to meet specific design requirements, thereby streamlining the entire workflow from network design to integration.

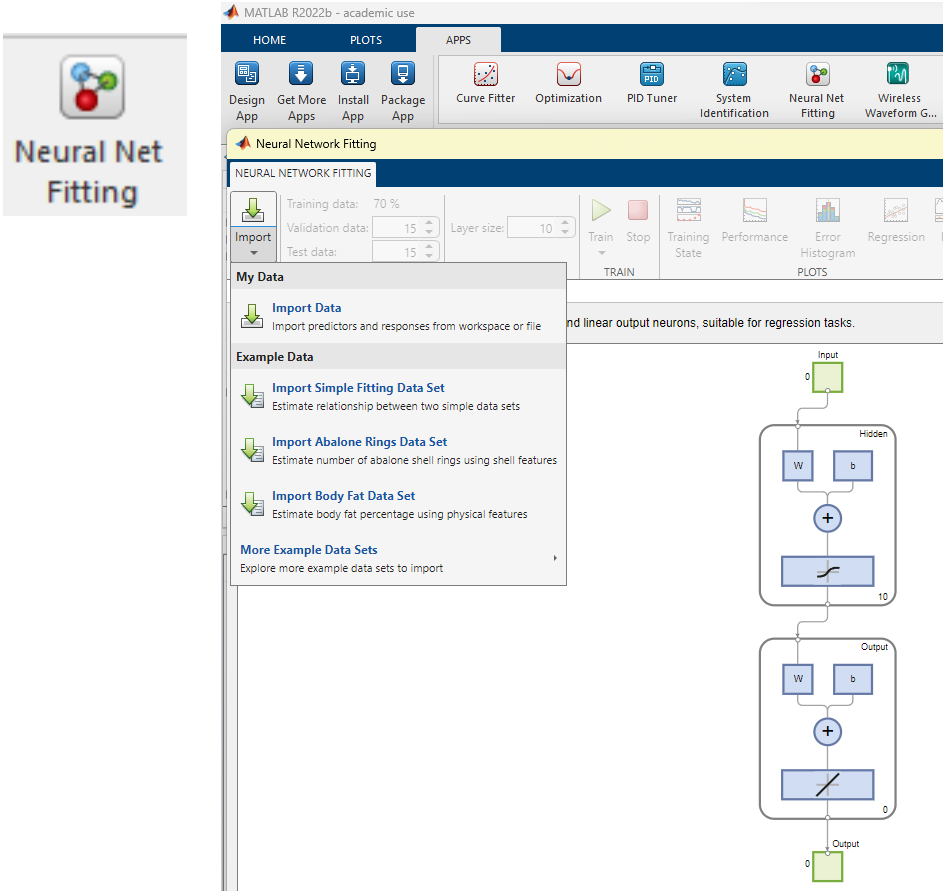

5.17: Neural Net Fitting App in MATLAB/Simulink Tools.

- **General Neural Network Workflow**

The general steps for preparing and training a neural network with the Neural Fitting app include:

1. **Network Creation:** Define the structure, including input, hidden, and output layers.
2. **Dataset Preparation:** Configure the input signals, target outputs, activation functions, and training algorithm.
3. **Initialization:** Randomly initialize the weights parameters (W_{ij}) and biases (b_k)
4. **Training:** Iteratively update weights and biases during each epoch to minimize the error between the predicted and target outputs by computing the gradient of the loss function. This optimization process continues until all parameters (W_{ij}) and biases (b_k) are refined, achieving a trained network ready for operation.

This structured approach, supported by the Neural Fitting app, ensures efficient and accurate design, training, and deployment of neural networks for advanced engineering applications.

5.4.2 Artificial Neural Networks to detect the type of failure

- **Initial Attempts and Challenges**

The initial objective was to design a Backpropagation Artificial Neural Network (BP-ANN) to estimate the correct synchronous angle (θ) based on measurements of the three-phase voltages. Despite multiple attempts, this approach failed to achieve satisfactory precision. The network struggled to generalize its operation effectively, resulting in an inability to accurately reconstruct θ under varying fault conditions. This limitation prompted a shift in strategy: instead of directly estimating θ, a BP-ANN was developed to first detect the type of fault. The results from this fault detection network would then differentiate and guide the angle estimation process, improving overall performance.

- **Fault Detection Neural Network Architecture**

The fault detection neural network was ultimately designed with the following architecture after extensive experimentation. Numerous attempts were made by varying the number of layers, the number of neurons per layer, and the type and number of input signals to identify the optimal configuration. These iterative adjustments, without any kind of memory effect, aimed to achieve a balance between performance and accuracy, leading to the final architecture as follows (:

1. **Input Layer:** Comprising three neurons, corresponding to the three normalized and squared line voltages as input signals.
2. **Hidden Layers:** Three layers, each with 10 neurons, using arctangent activation functions for efficient nonlinear transformations.
3. **Output Layer:** Containing 11 neurons, each representing a specific fault type.

The output consisted of 11 signals, each detecting a specific type of fault. For example, $out1$ would commutate from zero to one if an E_a/G fault was present, $out2$ would follow the same pattern for an E_b/G fault, and so on until $out11$ for a E_{abc}/G fault. This architecture reliably distinguished fault types and achieved a high accuracy rate, as shown in the test results, the neural network takes less than half a period to detect the fault. Figure 5.18 illustrates the neural network architecture, while Figure 5.19 shows the corresponding input voltages and desired outputs for each fault type. The training dataset, along with fault-specific outputs, was stored in the workspace and visualized using the blocks depicted in Figure 5.20.-

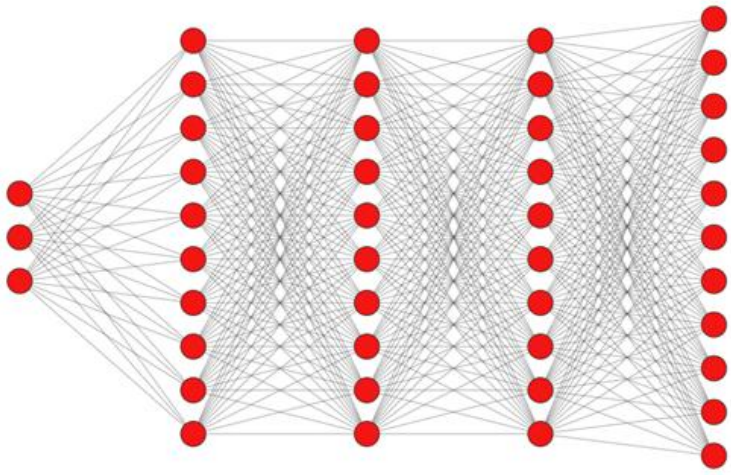

5.18: Neural Network architecture for fault detector.

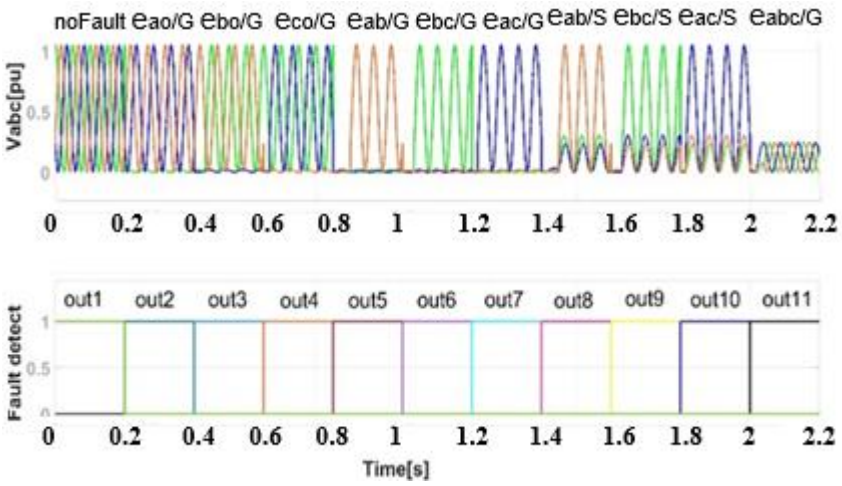

5.19: Input voltage to the fault detection neural network and desired output.

- **Training Process and Algorithm Selection**

The neural network was trained using the Backpropagation method with the Bayesian Regularization algorithm (Trainbr). This algorithm, while computationally slower, produced the most accurate results by reducing overfitting and enhancing generalization. Comparatively:

- **Trainlm (Levenberg-Marquardt backpropagation)** is the fastest option but may consume more memory, making it suitable for smaller datasets or systems with high computational capacity.
- **Trainscg (Scaled Conjugate Gradient)** is a memory-efficient alternative, ideal for low-memory systems.

The dataset was divided into three subsets:

- **70%** for training,
- **15%** for validation, and
- **15%** for testing.

The output layer employed a linear activation function to ensure precise mapping of results, complementing the non-linear transformations in the hidden layers.

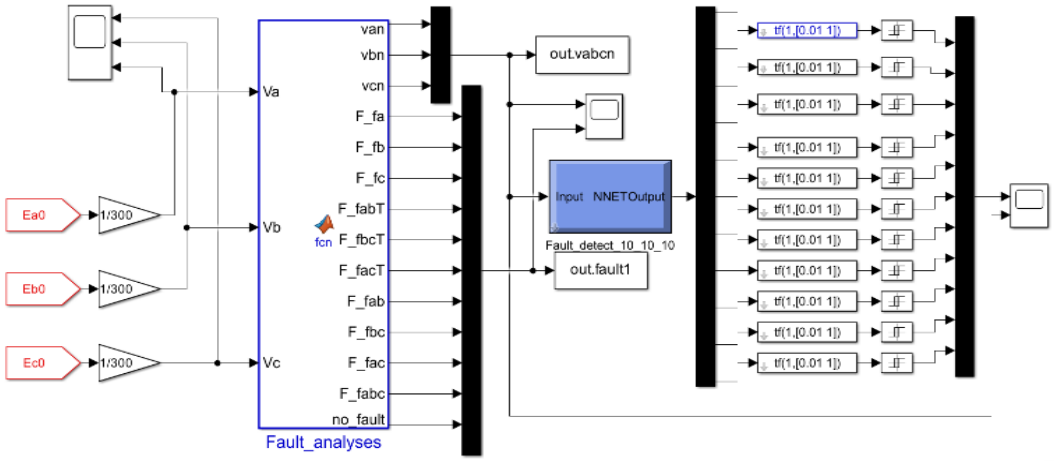

5.20: Data-set preparation and fault detection in MATLAB/Simulink.

- **Post-Processing and Results**

After training, the network's output signals were filtered and squared to ensure consistency and reliability in fault detection, as shown in Figure 5.20. This fault detection system demonstrated excellent performance in identifying specific fault types with a regression R equal to 0.8, thereby enhancing the accuracy of subsequent angle estimation tasks. The success of this neural network design underscores the effectiveness of combining tailored architectures, robust training algorithms, and post-processing steps for solving complex tasks in electrical fault detection and classification.

5.5 Synchronous Angle Estimators Using Neural Networks

For every fault type, encompassing single-phase ground faults, two-phase faults (both with and without ground), and three-phase faults (with and without ground), was carefully designed a Backpropagation Artificial Neural Network for the estimation of the synchronous angle. The dataset used for training this network consisted of 2000 input samples, representing the two E_{alpha} and E_{beta}, (output of a,b,c/α,β transformation block). The corresponding desired outputs represented the ideal phase in the absence of faults.

The design process adhered to a structured and iterative approach, culminating in a final network architecture comprising:

- **Two input neurons** to process the voltages E_{alpha} and E_{beta}
- **Two hidden layers** with 10 neurons each to capture the non-linear relationships inherent in fault scenarios,
- **One output neuron** to estimate the synchronous phase angle under different fault conditions.

This architecture, depicted in Figure 5.21, was the result of extensive experimentation. Numerous iterations were performed to optimize the network by varying the number of layers, the number of neurons per layer, the type of backpropagation algorithm, and the composition of the dataset used for training, validation, and testing. These adjustments were essential to prevent overfitting and to ensure the network's ability to generalize across diverse fault conditions. The results obtained through this process were highly satisfactory, with a regression R equal to 0.999, demonstrating the robustness and precision of the final BP-ANN design.

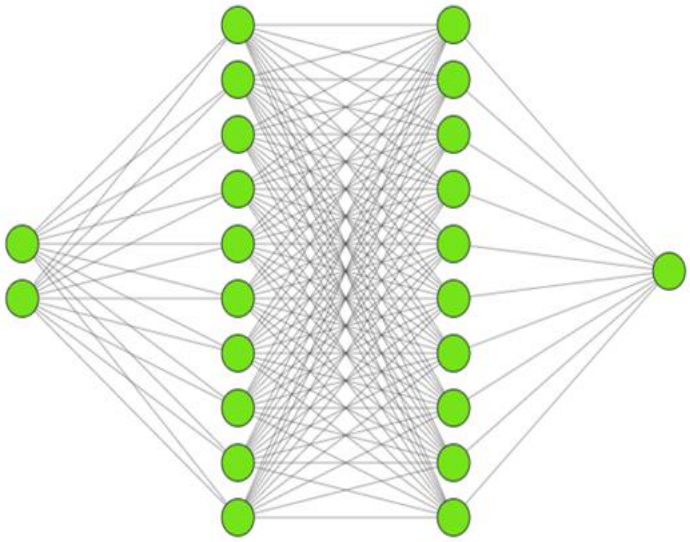

Figure 5.21: ANN for synchronous angle estimation.

5.5.1 Comparative Analysis of BP-ANN and Standard PLL

To evaluate the performance of the BP-ANN, the estimated phase was compared to the results obtained using a standard Phase-Locked Loop (PLL). Figures 5.22 and 5.23 present this comparison, where the green curve represents the phase estimated by the BP-ANN, the blue curve corresponds to the PLL estimation, and the red line indicates the ideal phase. Notably, in Figure 5.23, following a two-phase fault at t=0.8 s, the BP-ANN estimation (green) realigns with the ideal phase (red) after a transient period of approximately half a cycle. In contrast, the PLL estimation (blue) remains significantly distorted throughout the fault period.

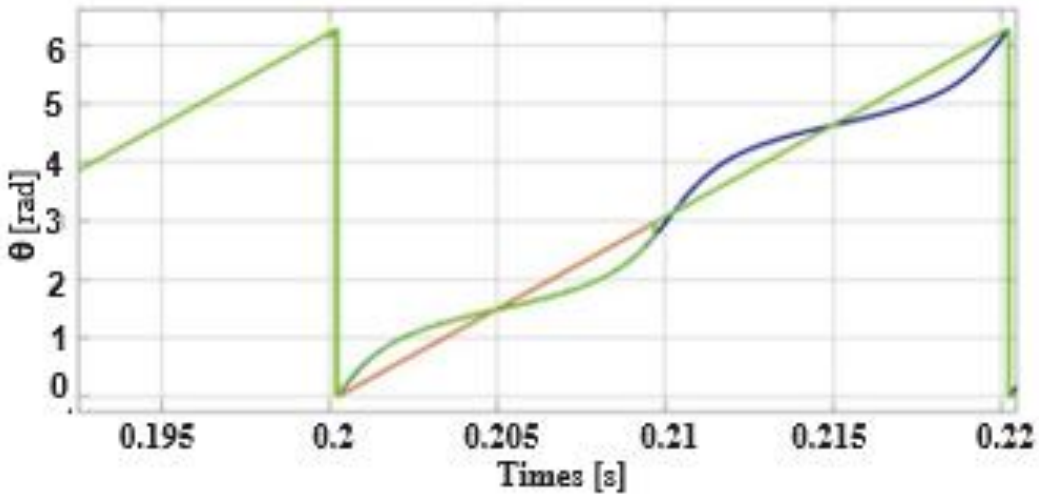

Figure 5.22: Angle estimation in E_a/T fault conditions: with PLL (blue), with BP-ANN (green) ideal angle (red)

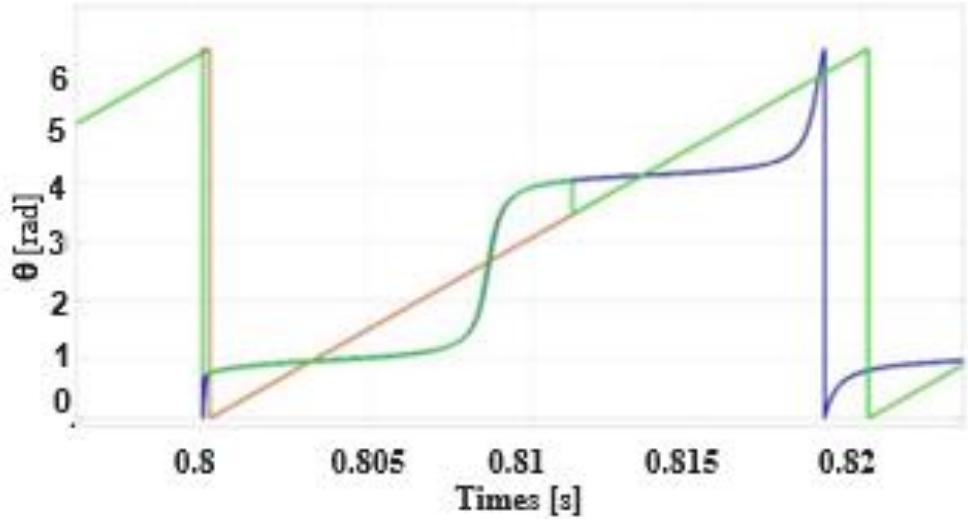

Figure 5.23: Angle estimation in E_{ab}/S fault conditions: with PLL (blue), with BP-ANN (green), ideal angle (red).

This demonstrates the superior fault-handling capabilities of the BP-ANN compared to traditional methods, particularly in quickly adapting to transient conditions and maintaining accuracy. Figure 5.24 further highlights this advantage by showing the output voltage of an AC PWM rectifier controlled using the phase

estimated by the BP-ANN. Compared to the rectifier behavior depicted in Figure 5.13, the influence of faults on the rectifier output voltage with ANN is markedly reduced, underscoring the reliability of the BP-ANN in maintaining system stability. With the current solution utilizing neural networks, the variation in output voltage is only 1.3%, compared to 6.25% observed when the synchronous angle estimation is performed using a PLL.

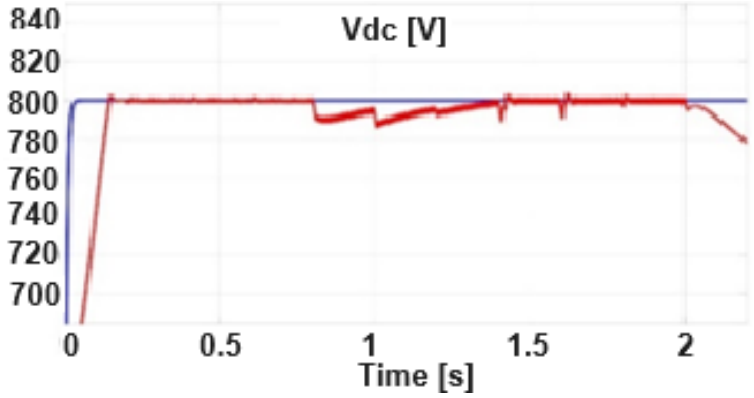

Figure 5.24 DC voltage (red) and its reference (blue) during faults, using the angle estimated by the BP-ANN.

The proposed methodology leverages neural networks to estimate the synchronous angle required for the control of grid-connected PWM rectifiers. By integrating fault detection capabilities directly into the network, this approach achieves enhanced reliability in maintaining stable DC voltage, even under fault conditions. The BP-ANN exhibits robust performance, effectively mitigating the negative effects of disturbances originating from the AC network.

This study highlights the potential of neural network-based estimation techniques for practical applications. By outperforming traditional methods like PLL in fault-prone scenarios, the BP-ANN demonstrates its viability for real-world implementation in grid-connected systems, contributing to greater system stability and resilience. The findings emphasize the transformative impact of neural networks in advancing fault-tolerant control strategies, paving the way for broader adoption in industrial and renewable energy systems.

5.6 Experimental implementation of the Neural Networks

Building upon the previous chapter, which focused on simulation studies, this chapter delves into the experimental application of artificial neural networks for enhancing the control of grid-connected AC/DC converters. Unlike the simulations conducted earlier, this section analyzes the real-world implementation and effectiveness of the proposed approach. The study addresses the complex challenges posed by AC grid faults and considers a three-phase PWM rectifier featuring IGBT technology, operating at a switching frequency of 10 kHz. To simulate realistic grid conditions, a specialized power supply facility capable of emulating common grid failures is employed. The crucial task of estimating the grid

angle, essential for efficient control in the synchronous d-q reference frame, is carried out by a set of neural networks specifically trained to adapt their operation based on the type of fault. These faults are also identified by neural networks, providing a comprehensive solution for fault detection and control adaptation. The training and simulation of the neural networks are conducted in the MATLAB/Simulink environment, which also facilitates the generation of control code for deployment on the Texas Instruments Delfino F28379S microcontroller (Figure 3.1). For comparison, the conventional quadrature phase-locked loop (Q-PLL) method, commonly used for grid synchronization, is used as a benchmark.

5.6.1 Experimental Fault detection using BP-ANN

In this work, since the electronic control board available for experiments only has the measurements of two-phase voltages, e_{ao} and e_{bo}, tests were carried out for three types of fault: short circuit (ground) e_{ao}/G and e_{bo}/G with fault resistance of 200 mΩ, and the short circuit (ground) of two phases e_{ab}/G with 150 mΩ fault resistance. As shown in Fig.2.25, the detection neural network was implemented using an input layer of two neurons, two hidden layers with 4 neurons each, and an output layer with 4 neurons (the three fault cases and the healthy one). The two measured phase voltages, e_{ao} and e_{bo}, normalized and squared, were connected as inputs to the network.

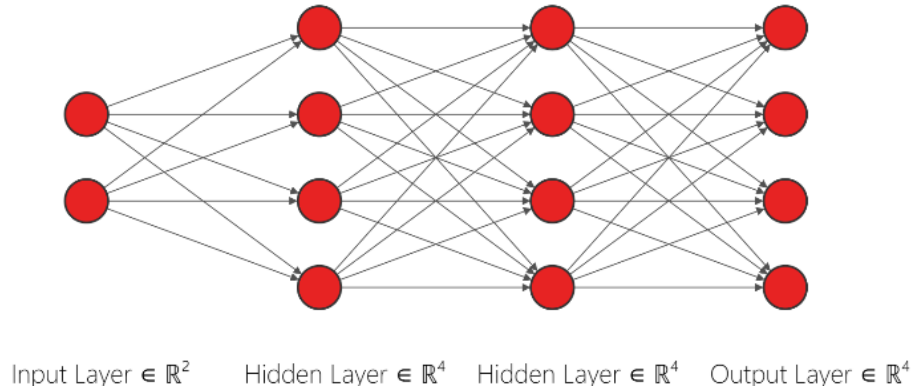

Fig.2.25: BP-ANN for experimental grid fault detection.

The output of the system consisted of four distinct signals, each designed to detect a specific type of fault. Specifically, the first output transitions from zero to one upon detection of an e_{ao}/G fault, the second output indicates the presence of an e_{bo}/G fault, and the third output identifies an e_{ab}/G fault (the e_{ab} fault is very similar to the e_{ab}/G fault). The fourth output is used in cases where no faults are detected.

Figure 5.26 illustrates the time-based behavior of the fault detection process simulated in Simulink. This figure presents the input voltages applied to the neural network alongside the corresponding outputs for each fault type. During simulation, variables were stored in real-time in the MATLAB workspace using “To Workspace” blocks. The fault detection process requires approximately 10 milliseconds for each scenario, with a regression R value of 0.8.

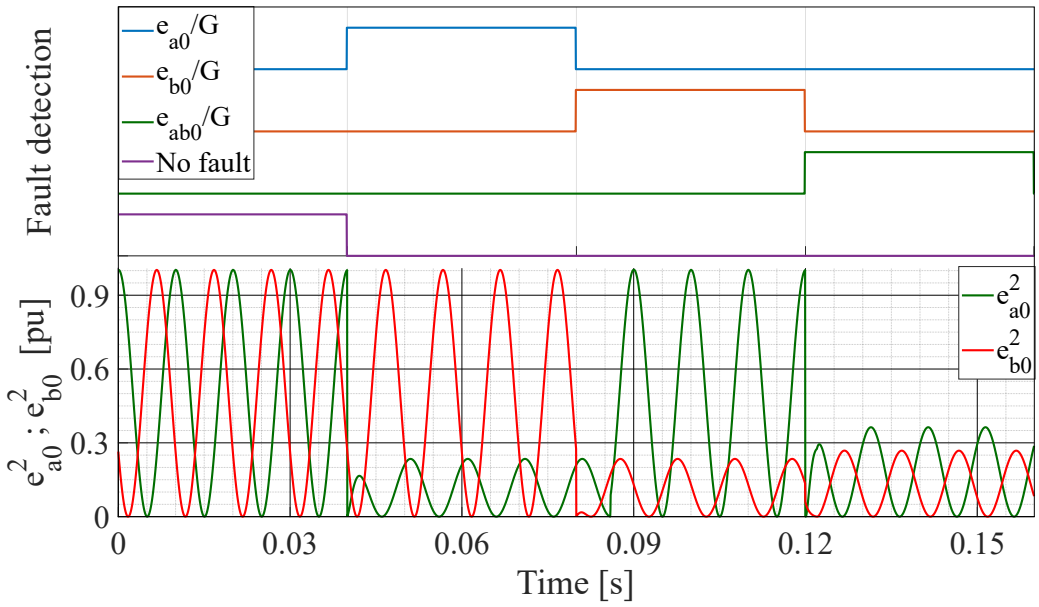

Figure 5.26: Input voltages to the fault-detection neural network (down) and network outputs (up).

While increasing the complexity of the neural network architecture can enhance both the reliability and speed of fault detection, this approach poses challenges for traditional hardware platforms. Specifically, more complex networks can exceed the processing capabilities of standard hardware, particularly when real-time responses within short cycle times are required. To address these limitations, system-on-chip (SoC) architectures with field-programmable gate arrays (FPGA) present a viable solution. These platforms enable parallel processing and hardware acceleration, allowing the implementation of sophisticated algorithms, such as neural networks, with significantly reduced processing times. This approach not only accelerates fault detection tasks but also ensures compliance with stringent real-time operational constraints, as highlighted in studies [125][129][130][131].

5.6.2 BP-ANN for Synchronous Angle Estimation

For each fault type, a Backpropagation Artificial Neural Network is designed and rigorously tested using a dataset of 2000 input samples, with a sampling time of 10 µs. Each sample consists of the two voltage components e_α and e_β (obtained by the $ab/\alpha\beta$ transformation of the measured three-phase voltages. The corresponding desired output represents the ideal behavior of the grid angle in the absence of faults, serving as a reference for network training.

The design procedure follows a structured and iterative methodology, ensuring optimal performance. The final network architecture consists of:

- **Two input neurons**, corresponding to e_α and e_β ,
- **Two hidden layers**, each containing five neurons to capture fault-induced variations effectively,
- **One output neuron**, responsible for estimating the synchronous grid angle under different fault conditions.

This architecture, illustrated in Figure 5.27, was achieved after multiple optimization cycles. Several iterations were performed, systematically varying the number of layers, the number of neurons per layer, the type of BP algorithm, and the size and structure of the dataset to enhance generalization and prevent overfitting. The training process resulted in high-accuracy performance, achieving a regression value between 0.99 and 1.0, with a mean squared error (MSE) of 0.01. These results validate the effectiveness of the proposed BP-ANN configuration in accurately estimating the grid angle while ensuring robustness against different fault conditions.

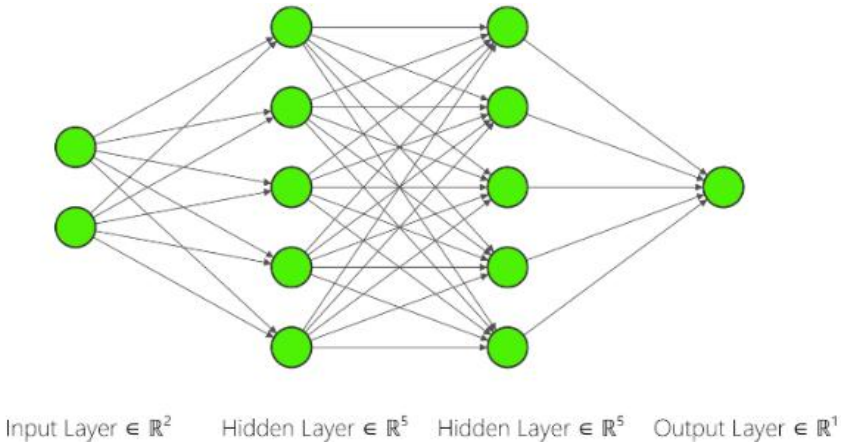

Fig.5.27: ANN for experimental grid angle estimation

5.6.3 Experimental System Implementation

- Experimental Setup for Neural Network-Based AC-DC Converter Control

The experimental setup utilized in this study is depicted in Figure 5.28 and consists of a PWM AC-DC converter, which forms one side of a back-to-back converter system manufactured by Rectificadores GUASCH S.A.U.. This converter is based on IGBT technology, designed to operate at 750 V DC voltage, with a peak AC current capacity of 30 A, and incorporates a 1000 μF bulk electrolytic capacitor for energy storage. To accurately simulate grid conditions and various fault scenarios, a full four-quadrant three-phase AC power source with grid emulation capability, the TC.ACS system from REGATRON, is employed. This setup enables precise testing of the neural network's response under realistic operating conditions. Between the grid simulator and the converter AC terminals, input RL filters are installed to ensure signal integrity and stability, with component values set at:

- Resistance R=0.047 Ω
- Inductance L=1.18 mH

On the DC bus, a resistive load is connected, composed of eight 50 Ω power resistors (1 kW each), configured in parallel/series combinations to facilitate controlled power dissipation and system evaluation.

Figure 5.28: Experimental setup: 1) Control board, 2) Converter, 3) Input filter, 4) Grid voltages transducers, 5) Grid simulator.

- Control System Implementation

The entire system is managed by an advanced digital control board based on the Texas Instruments Delfino F28379S microcontroller, which features both a primary CPU and an auxiliary CLA (Control Law Accelerator). This hardware architecture enables parallelized execution of critical tasks, optimizing performance and minimizing computational delays. The control software is developed within the MATLAB/Simulink environment, utilizing the Embedded Coder Support Package for Texas Instruments C2000 Processors. Once compiled, the control algorithm is deployed to the microcontroller using Code Composer Studio, which also facilitates real-time debugging and system tuning, [16]. To further optimize computation time and mitigate the processing overhead introduced by neural network calculations, the software architecture is designed with a parallel task execution strategy, [21]. This approach leverages the auxiliary CLA processor to handle regulators and other conventional control functions (represented by red blocks in Figure 5.29), while the primary CPU executes the neural network

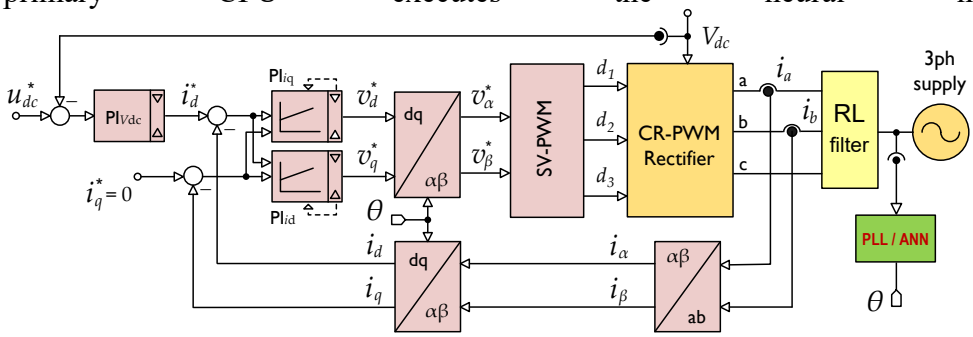

Figure 5.29: PWM rectifier zero reactive power control scheme

computations and host communication tasks (depicted by the green block in Figure 5.28). By efficiently distributing computational workloads across the Delfino F28379S architecture, the system ensures real-time operation, robust control performance, and minimal latency in fault detection and grid synchronization tasks.

This configuration enables seamless integration of neural networks into power electronics applications, demonstrating their feasibility for real-world deployment in AC-DC conversion systems. Table 5.1 and Figure 5.30 provide a detailed breakdown of the computation times and the allocation of tasks within the microcontroller. The control code is executed within a tight timeframe, corresponding to the PWM period of 100 µs, aligned with the 10 kHz switching frequency of the system. This strict timing constraint highlights the efficiency of the control system in meeting real-time processing requirements. However, certain limitations in data acquisition affected the experimental setup. Specifically, the control board used in this study allowed for the measurement of only two-phase voltages from the grid voltage transducers. This limitation introduced a challenge for the artificial neural network (ANN)-based control, which had been trained on a dataset containing measurements from three-phase voltage sensors. The absence of complete sensor data degraded the performance of the ANN, particularly under single-phase-to-ground short-circuit conditions. As a result, the control strategy exhibited reduced effectiveness in such scenarios, leading to the decision to exclude the single-phase-to-ground fault case from the scope of this study. Future research will aim to address this limitation by employing an enhanced control board capable of acquiring all three-phase voltage measurements. This upgrade will enable the ANN to operate under optimal conditions, thereby improving its performance in handling all fault scenarios, including single-phase-to-ground short circuits. The insights gained from such advancements are expected to further solidify the ANN's reliability and effectiveness in practical grid-connected applications.

Table 5.1: Computation times and allocation of tasks (TMS F28379S)

T_{PWM} (100µs)	**Timing (µs)**			
	Regulators and control functions	***ANN fault detection***	***ANN angle estimation***	***Q-PLL***
CPU	-	25	27	-
CLA	12	-	-	8

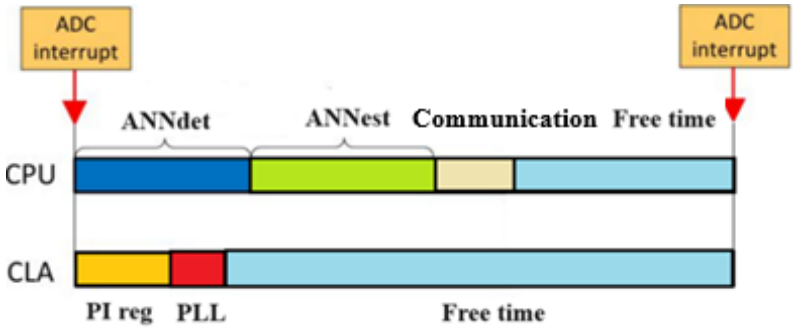

Figure 5.30: Parallel processing times in the MCU within the 100ms PWM period

5.6.4 Experimental Results

The experimental results demonstrate the effectiveness of the Backpropagation Artificial Neural Network (BP-ANN) in accurately estimating the grid angle and detecting faults. Figure 5.31 illustrates the system dynamics during the occurrence of an e_{ab}/G fault, including its detection and the grid angle estimation performed by the BP-ANN. The waveforms from two tests are superimposed for comparison, derived through post-processing of real-time acquisitions. The first waveform represents the grid angle computed by the ANN during the fault (along with the corresponding fault detection flag), while the second shows the grid angle under ideal conditions without any fault.

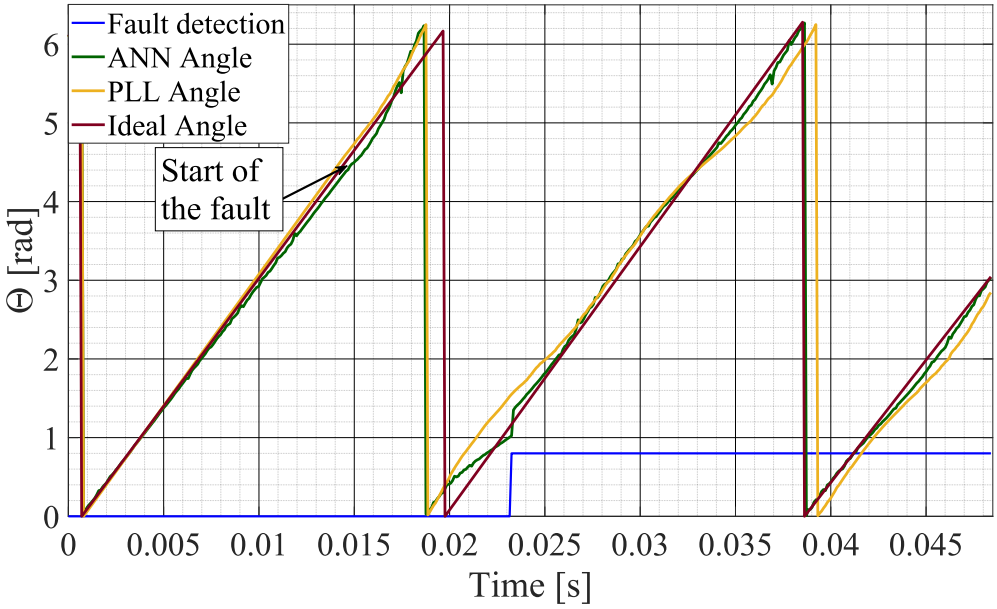

Figure 5.31: Operating dynamics of e_{ab}/G fault detection and grid angle estimation by neural networks.

From the moment the fault begins (t=15 ms) to its detection (t=23 ms), the BP-ANN accurately identifies the fault in less than half a cycle (10 ms) and quickly realigns the estimated grid angle with the ideal no-fault angle (red line). This highlights the network's rapid response and robustness under fault conditions. Figure 5.32 presents the steady-state response following the e_{ab}/G fault, comparing the grid angle estimation from the BP-ANN (green) and the standard quadrature phase-locked loop (Q-PLL, blue), with the ideal grid angle represented by the red line. The Q-PLL shows significant waveform distortion, resulting in incorrect grid angle estimation during the fault, whereas the BP-ANN provides a much more accurate estimate, closely tracking the ideal grid angle.

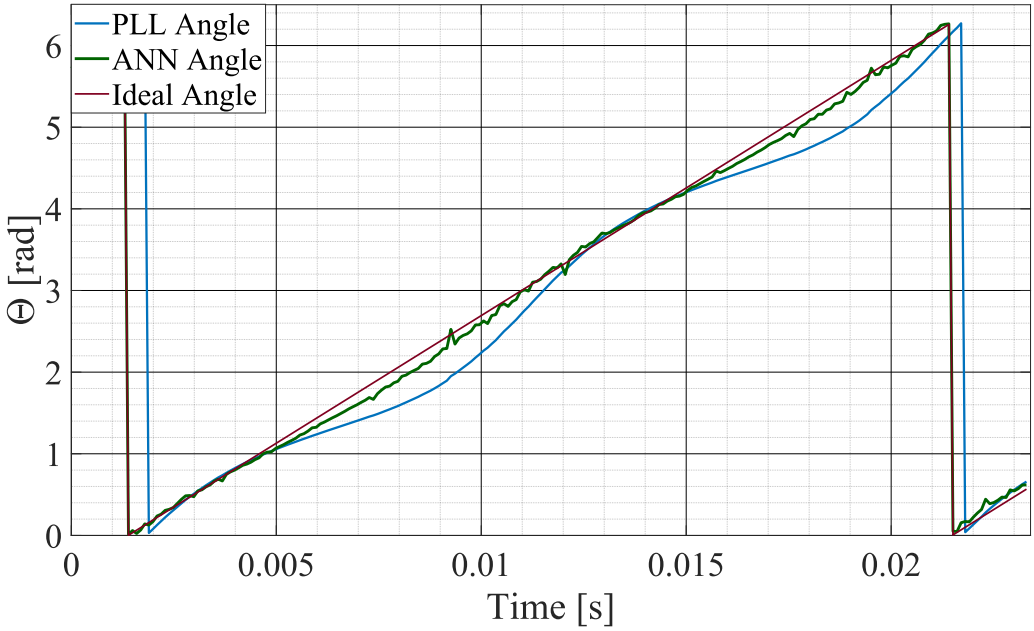

Figure 5.32: Grid angle estimation in e_{ab}/G fault conditions PLL (blue), BP-ANN (green), ideal angle (red).

The AC voltages applied through the grid simulator are shown in Figures 5.33 and 5.34. Figure 5.33 displays the waveform of a single-phase voltage acquired by the microcontroller, triggered at the occurrence of the e_{ab}/G fault, along with the corresponding fault detection flag. Figure 5.34 illustrates the three-phase grid voltages measured by the transducers at the grid simulator output under steady-state conditions for the same fault scenario. The rectifier's DC output voltage, controlled to maintain a constant reference of 340 V, is shown in Figure 5.35 for the e_{ab}/G fault. Two cases are superimposed for comparison: one where the grid angle is estimated by the BP-ANN, and another where the grid angle is computed by the Q-PLL. With the BP-ANN, the target voltage is maintained apart from a minor oscillating component of approximately 20 V (6% of the reference). In contrast, when using the Q-PLL, a static error arises, leading to a noticeable deviation from the desired output voltage.

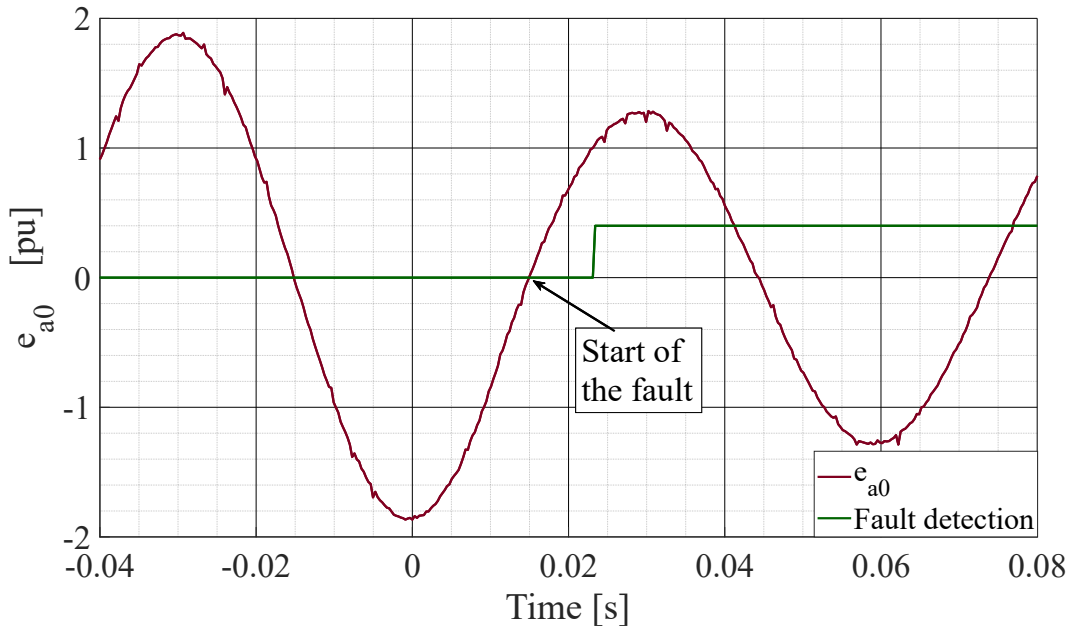

Figure 5.33: e_{ao} voltage at occurrence of the e_{ab}/G fault at t=15ms and respective fault-detection flag (real-time acquisition from the micro at t=23ms)

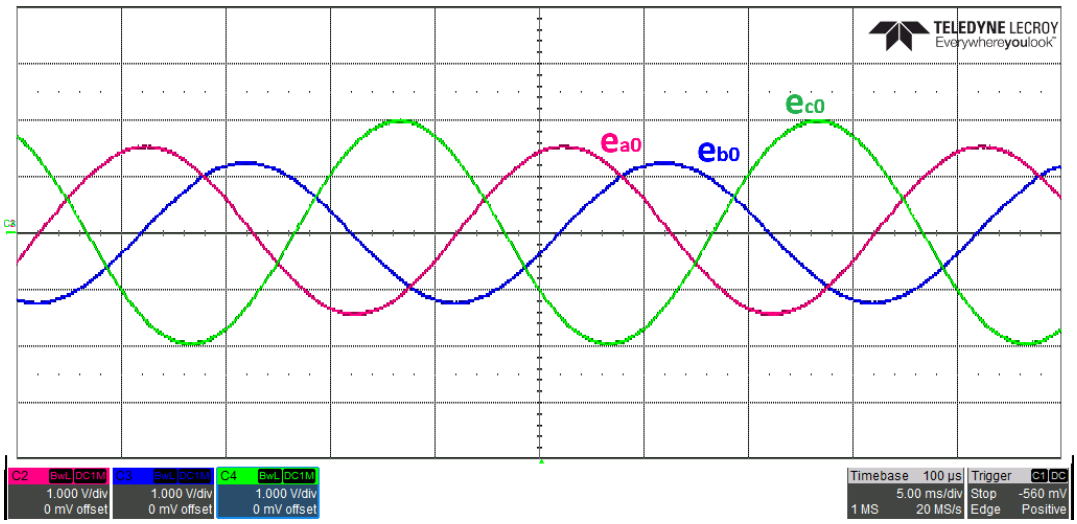

Figure 5.34: AC input voltages in e_{ab}/G fault condition (screenshoot from the transducers with an output voltage of 1V with an input of 85V).

In conclusion, this study presents the experimental application of artificial neural networks for improving the control of grid-connected AC/DC converters. Utilizing a custom control board based on the TI Delfino F28379S MCU, neural networks were implemented to detect faults in the AC grid and estimate the grid angle required for voltage-oriented control of the PWM rectifier. The proposed solution has proven to be highly promising in mitigating the negative effects of network faults. Its feasibility was validated by analyzing the neural network's impact on the computational load of the microcontroller in a real-time setting, demonstrating its ability to function effectively in practical applications. Overall, the experimental results showcase the significant potential of neural network-based estimation techniques for highly dynamic systems. However, they also emphasize the

limitations of current implementations, highlighting areas for future development and optimization in this field.

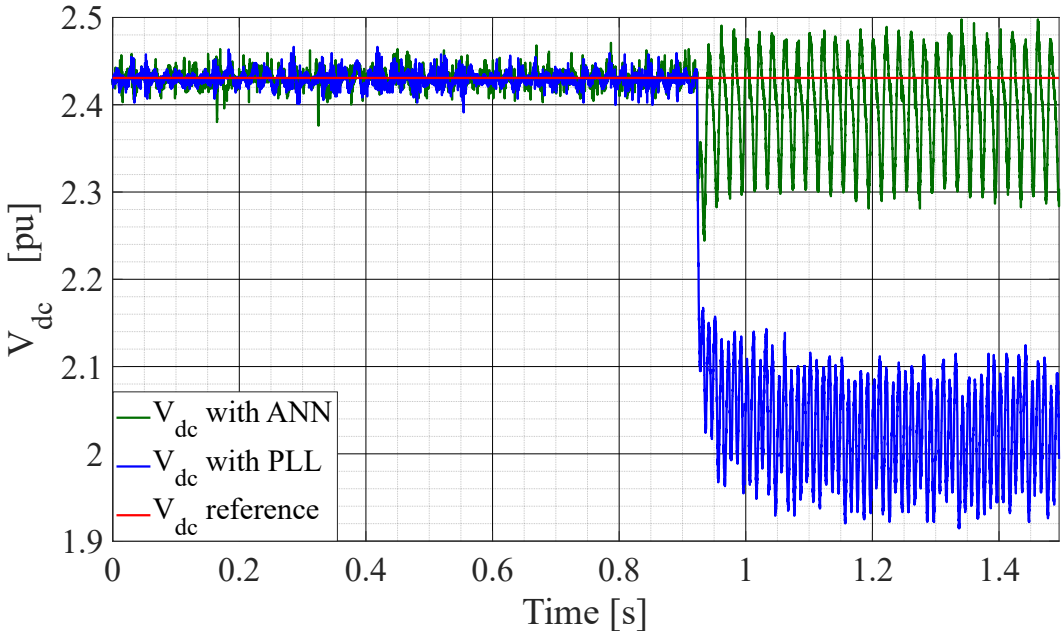

Figure 5.35: DC voltage and its reference (red) during the e_{ab}/G fault using the BP-ANN (green) and Q-PLL(blue) for control.

Chapter 6

Efficient Testing for Performance Evaluation of Synchronous Reluctance Motors (SynRMs)

Part of the work presented in this chapter has been previously published in [71].

6.1 Back-to-Back Testing Methodology for energy-efficient performance evaluation

The optimal control of SynRM drive requires accurate control maps, which are dependent on motor-specific parameters. The experimental acquisition of these maps through traditional dissipative braking test benches is highly energy-intensive and requires long testing periods. A more energy-efficient alternative is the Back-to-Back (BTB) test configuration, which allows for real-time performance evaluation with minimal energy consumption. This work introduces a BTB test facility for SynRM performance assessment, enabling efficient mapping of optimal torque per ampere (MTPA) and efficiency characteristics.

6.1.1 Understanding the Back-to-Back Configuration

The Back-to-Back (BTB) configuration is a testing methodology widely used for high-power electric machines, allowing for energy-efficient performance evaluation. In a BTB test setup, two identical electric machines are:

- Mechanically coupled via a torque transducer, ensuring synchronized operation,
- Electrically interconnected, forming a closed energy loop,
- Fed by the same power supply, with only the system's total power losses being drawn from the external DC source.

One machine operates in motor mode, supplying mechanical power, while the second machine functions as a generator (brake machine), converting mechanical

energy back into electrical energy and feeding it back into the system. As a result, only the power losses of the system (friction, copper, iron, and converter losses) are supplied externally, making the approach highly energy-efficient [65][66].

- Key Benefits of the Back-to-Back Configuration:

1. **Energy Recovery**: Unlike conventional test benches that dissipate braking energy as heat, BTB systems reuse the energy within the system, significantly reducing power consumption.
2. **Cost-Effective Testing**: Since only the losses need to be covered by the power supply, operational costs are considerably reduced.
3. **Real-Time Control Mapping**: Enables accurate and dynamic testing under real operational conditions.
4. **Precise Torque and Speed Control**: The braking machine can be controlled to impose specific speed-torque profiles, enabling high-accuracy control strategy evaluation.

A schematic representation of the BTB test configuration is provided in Figure 6.1, showing the energy flow and system components.

6.1.2 Test Bench Configuration

The BTB test system (Figure 6.1) consists of two identical 3 kW synchronous reluctance machines (Table 3.1), mechanically coupled via a torque transducer with a constant of 250 mV/Nm and a measuring range of ±20 Nm. The system is powered by a Back-to-Back IGBT-based power supply, operating at:

- **Maximum DC voltage:** 750V
- **Maximum phase current:** 30A
- **Bulk electrolytic capacitor:** 1000 µF for energy buffering

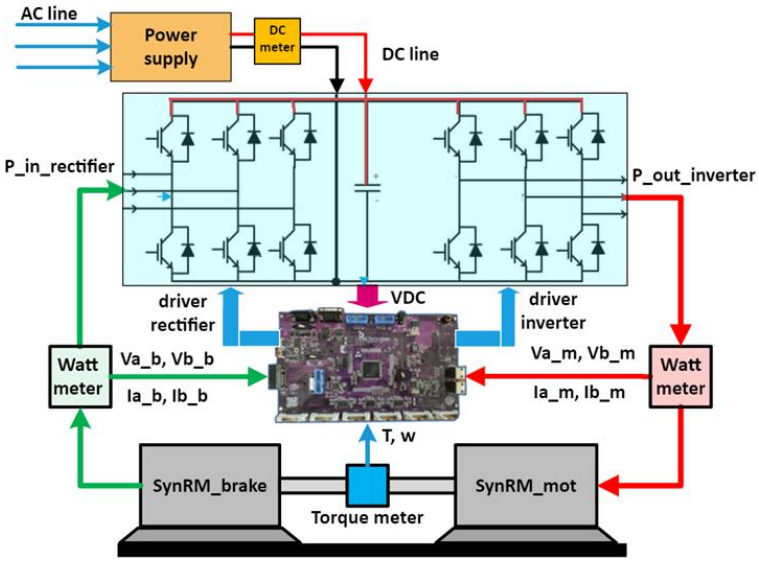

Figure 6.1: Test bench connection diagram

The test system is controlled by a custom electronic board based on the Texas Instruments Delfino F28379S microcontroller from the C2000 family (Figure 3.1). The control algorithms are implemented in MATLAB/Simulink, and real-time execution is managed through Code Composer Studio.

In this system:

- The motor under test operates under predefined speed-torque profiles,
- The braking machine recovers mechanical energy and converts it back into electrical energy,
- The DC power supply only compensates for system losses, making the approach highly efficient.

As shown in Figure 6.2, the power drawn from the DC source corresponds solely to the total power loss of the two machines, demonstrating the energy-saving advantage of this method.

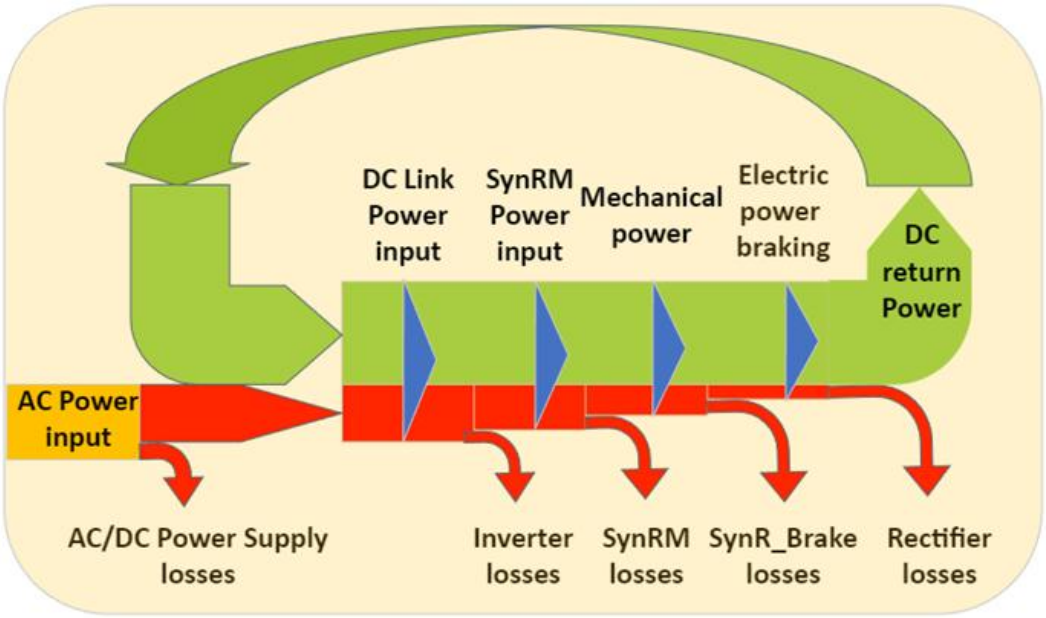

Figure 6.2: Power distribution flow of the test bench.

6.1.3 Control System Structure

The software architecture consists of two control sections:

- Motor under test control.
- Motor brake control

To optimize computational performance, parallel programming techniques are utilized. The Control Law Accelerator (CLA) of the Delfino F28379S microcontroller is leveraged to execute:

- Braking control in the CLA,
- Motor control and host Communication in the CPU (Figure 6.3).

The PWM switching frequency is set at 10 kHz, with ADC sampling occurring every 100 µs. The software is structured in MATLAB/Simulink, with real-time debugging and deployment via Code Composer Studio [16],[17].

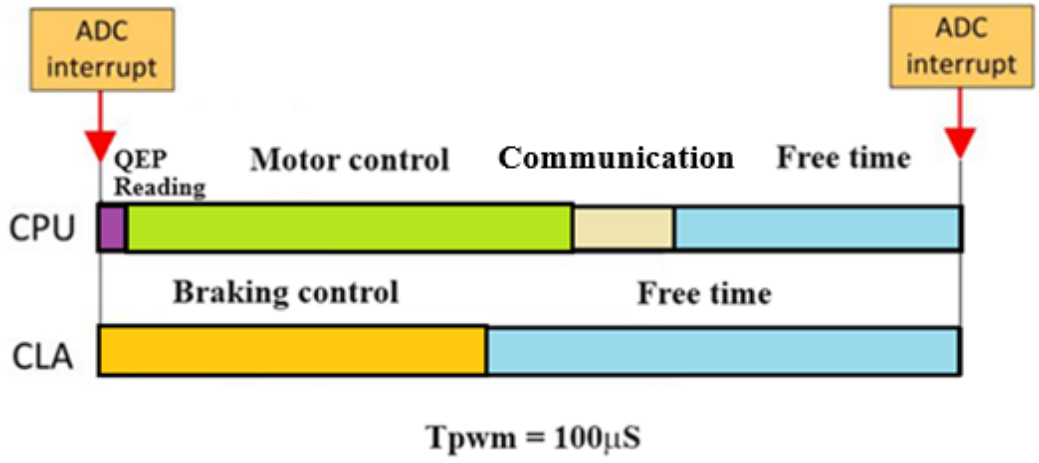

Figure 6.3: Parallel programming architecture for test bench control.

- **Performance Mapping and Experimental Validation**

Using this BTB test facility, we obtained key performance maps, including:

1. Maximum Torque Per Ampere (MTPA): Identifies the most energy-efficient operating points.
2. Maximum Efficiency Mapping: Determines the optimal efficiency regions under different load conditions.

These maps were generated while considering voltage and current constraints, providing a detailed characterization of the motor's performance. The back-to-back testing methodology enabled highly accurate data collection with minimal energy consumption compared to traditional dissipative braking test benches.

6.2 Optimum Control Strategies of the SynRM

According to well established literature, the optimization criteria of the SynRM refer to maximum torque/current, maximum torque/flux, and maximum power factor [133]. In this work, the curves relating to the maximum torque-current ratio and the further ***maximum efficiency strategy*** are determined experimentally. Each of these strategies corresponds to a given curve on the d-q currents plane.

6.2.1 Motor model in the d-q Currents Plane.

This section provides a fundamental analysis of Synchronous Reluctance Motors (SynRMs), focusing on how their performance can be optimized through proper current vector control strategies. The two-phase Park model (d-q reference frame) is adopted to describe the machine's behavior under steady-state conditions. To simplify the analysis, the model assumes linearity in the flux model, meaning that saturation effects, cross-coupling between d and q axes, and iron losses are neglected. This assumption allows for a clearer understanding of the fundamental constraints governing voltage, torque, and current limitations in the motor. Based on the equivalent electrical circuit of the machine, as depicted in Figure 6.4, the steady-state stator voltage equations, flux linkages, and electromagnetic torque are expressed as follows:

$$V_d = RI_d - \omega\Psi_q \ , \quad V_q = RI_q + \omega\Psi_d \tag{6.1}$$

$$\Psi_d = L_d I_d \ , \qquad \Psi_q = L_q I_q \tag{6.2}$$

$$T_e = \frac{3}{2}\, p(\Psi_d I_q - \Psi_q I_d) \tag{6.3}$$

where V_d, V_q are the stator voltages, I_d , I_q are the current components in the d-q frame, L_d, L_q are the d-q inductances, Ψ_d, Ψ_q are the flux linkages, ω is the electrical angular velocity, and T_e is the electromagnetic torque. By elaborating these equations, three fundamental constraints governing the operation of the SynRM in the d-q plane can be derived:

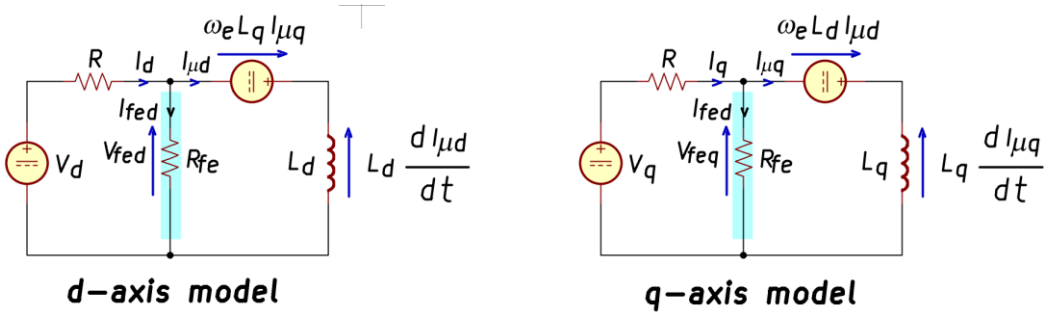

Figure 6.4: Equivalent electrical circuit of the SynRM expressed on the d-q plane, in the formulas the resistance that considers the iron losses, indicated in the blue box, is neglected

1. **Constant Voltage Constraint (Voltage Ellipse):** The total voltage available at the stator terminals is constrained by:

$$V_S^2 = \left(V_d^2 + V_q^2\right) = \left(R^2 + \omega^2 L_d^2\right) I_d^2 + \left(R^2 + \omega^2 L_q^2\right) I_q^2 + 2R\omega\left(L_d - L_q\right) I_d I_q \qquad (6.4)$$

This equation defines an ellipse in the d-q plane, which represents the maximum allowable stator voltage at a given speed. As the speed increases, this ellipse shrinks toward the origin, imposing a natural limitation on the motor's operating region.

2. **Constant Torque Constraint (Torque Hyperbola):** The torque equation can be rewritten as:

$$T_e = \frac{3}{2}\, p(L_d - L_q) I_d I_q \qquad (6.5)$$

This relation forms a hyperbolic locus in the d-q plane, indicating that torque production requires both d- and q-axis current components. The optimal utilization of this constraint leads to strategies such as Maximum Torque per Ampere (MTPA), which aims to maximize torque output while minimizing current consumption.

3. **Constant Current Constraint (Current Circle):** The stator current must satisfy:

$$I_S^2 = I_d^2 + I_q^2 \qquad (6.6)$$

which defines a circular boundary in the d-q plane, representing the rated current limit of the motor. Any operating point must remain within this boundary to avoid overheating and excessive losses.

6.2.2 Graphical Representation of Voltage, Torque, and Current Constraints

Figure 6.5 illustrates these constraints by showing:

- The black ellipses corresponding to constant voltage contours at different speeds.
- The pink hyperbolas representing constant torque loci.
- The red circle denoting the maximum current limit.

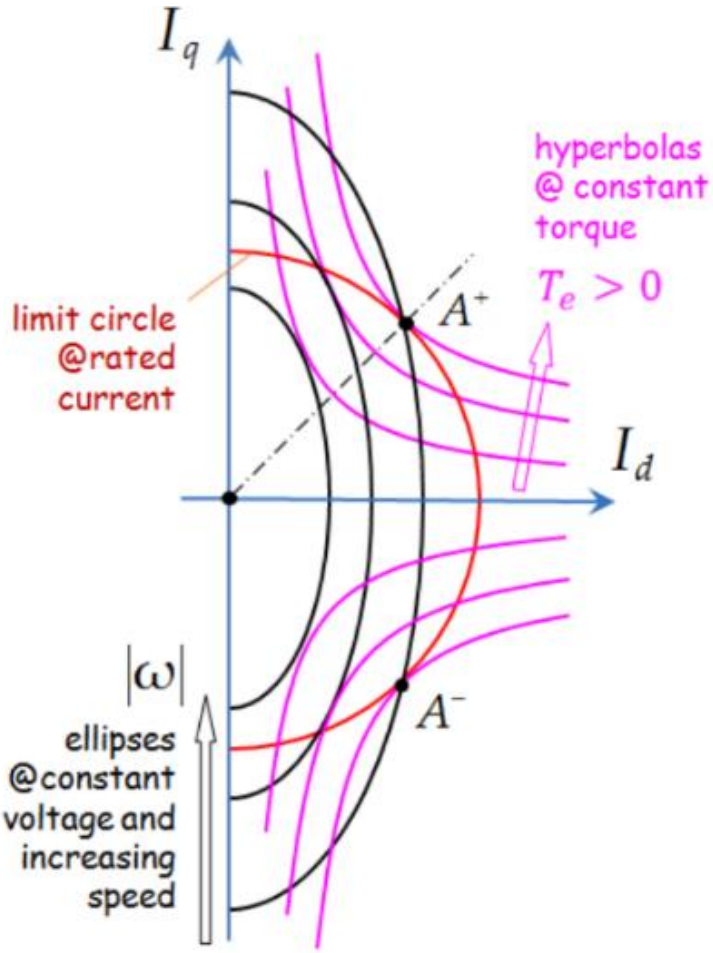

Figure 6.5: Constant torque, voltage, and current loci in the d-q currents plane.

The base operating point of the motor (point A* in the figure) is where these constraints intersect at nominal conditions (rated speed and rated current). According to Equation (4), as speed increases while maintaining constant nominal voltage, the voltage ellipses shrink and converge toward the origin, ultimately limiting the maximum torque that can be achieved.

At the theoretical limit, an infinite speed could be reached if zero torque were required. However, practical constraints such as iron losses, saturation effects, and

thermal limitations impose strict boundaries on real-world applications. Understanding these constraints is crucial for optimizing control strategies, such as:

- Field-Weakening Control to extend the operating range beyond base speed.
- Maximum Torque per Ampere (MTPA) to enhance efficiency.
- Flux-Weakening Strategies to achieve high-speed operation with minimal current draw.

This analytical framework lays the foundation for developing advanced control strategies for SynRM drives, ensuring optimal performance across a wide range of operating conditions.

6.2.3 Performance optimization of SynRMs.

The performance optimization of Synchronous Reluctance Motors (SynRMs) is widely discussed in literature [64][133], with primary focus on three key optimization criteria:

1. Maximum Torque per Current (MTPA) – Maximizing torque output while minimizing current consumption.
2. Maximum Torque per Flux (MTPF) – Optimizing torque production relative to the flux linkage.
3. Maximum Power Factor (MPF) – Enhancing power factor to improve overall efficiency.

Each of these strategies corresponds to a distinct trajectory in the d-q current plane, defining an optimal path for current vector control under various operating conditions. In this study, the maximum torque-to-current ratio curve and an additional strategy focusing on maximum efficiency are experimentally analyzed and validated. These control strategies play a crucial role in improving the energy efficiency and performance of SynRM drives, ensuring that the motor operates optimally across different torque and speed ranges.

- Mathematical Formulation of Optimization Strategies

1. Maximum Torque per Current (MTPA) Strategy

The Maximum Torque per Current (MTPA) criterion aims to minimize copper losses by selecting the operating point closest to the origin of the d-q plane on a given constant torque hyperbola. Mathematically, this relationship for ideal SynRMs is given by:

$$I_{qc} = I_{dc} \tag{6.7}$$

In real-world conditions, as we will see in the following analyses, the MTPA is not $I_{qc} = I_{dc}$, but depends on the actual characteristics of the machine.

Optimization is typically used to identify the optimal MTPA trajectory based on the machine's flux maps or torque map, either through actual tests or through FEM simulation. This strategy ensures optimal utilization of stator current, leading to higher torque production with reduced power losses. The MTPA trajectory is particularly beneficial for low-speed operation, where minimizing current magnitude is critical to improving motor efficiency.

2. Maximum Power Factor (MPF) Strategy

The Maximum Power Factor (MPF) criterion aims to minimize reactive current, thereby improving the power factor of the motor. By neglecting stator resistance, this condition is expressed as:

$$I_{q\Psi} = \sqrt{\frac{L_d}{L_q}}\, I_{d\Psi} \tag{6.8}$$

This strategy is particularly useful when the motor begins to approach saturation conditions, as excessive d-axis current reduces reluctance anisotropy, thereby diminishing the torque-generating capability. By controlling the power factor, the motor can sustain higher torque output without excessive current draw.

3. Maximum Torque per Flux (MTPF) Strategy

The Maximum Torque per Flux (MTPF) criterion ensures that the torque production is maximized at a given flux level. This is particularly relevant at higher speeds, where voltage constraints become significant. Under the assumption of negligible stator resistance, this criterion can be expressed as:

$$I_{q\Psi} = \frac{L_d}{L_q}\, I_{d\Psi} \tag{6.9}$$

By implementing this strategy, the motor can maintain efficient torque production across an extended speed range, making it particularly beneficial for applications where high-speed operation and flux weakening are required.

- **Selection of Control Strategies Based on Operating Conditions**

Figure 6.6 illustrates the three optimization strategies in the d-q plane when saturation neglected. The choice of the most suitable control strategy depends on torque demand, speed, and magnetic saturation levels:

- For low torque values, the MTPA strategy is preferred as it minimizes copper losses while keeping current consumption low.
- As torque demand increases, saturation effects begin to decrease the reluctance anisotropy ratio, leading to a reduction in the motor's torque-generating capability. At this point, the MPF strategy is adopted to prevent

excessive Id currents and to maintain a balance between efficiency and torque capacity.
- At higher speeds, the MTPF strategy becomes necessary to compensate for voltage limitations, ensuring that torque production remains maximized without exceeding voltage constraints.

Figure 6.7 shows the effect of saturation, (the *d*-axis magnetic path is more susceptible to saturation) and the transitions between the various strategies driven by the increasing speed ω at voltage supply limit, demonstrating how the motor dynamically adjusts its current vector as operating conditions change.

- Practical Considerations and Implementation Challenges

To prevent excessive magnetic saturation, a design constraint is often introduced, limiting the d-axis current component to approximately half of the rated current. This ensures that the motor operates within its optimal flux range, thereby maintaining stable performance and high efficiency.

However, implementing real-time transitions between control strategies requires precise tuning of current regulators and adaptive control algorithms. Advanced model predictive control (MPC) and artificial intelligence-based optimization techniques can further enhance the dynamic selection of control strategies, ensuring seamless adaptation to changing load and speed conditions.

The three primary optimization strategies for SynRM control—MTPA, MPF, and MTPF—serve distinct purposes depending on operating conditions. By selecting the appropriate current vector trajectory, it is possible to achieve:

- Higher torque output per ampere,
- Improved power factor,
- Optimized performance across varying speed ranges.

The experimental validation of these strategies, as presented in this study, provides critical insights into real-world SynRM behavior, further reinforcing their suitability for high-efficiency industrial and electric mobility applications.

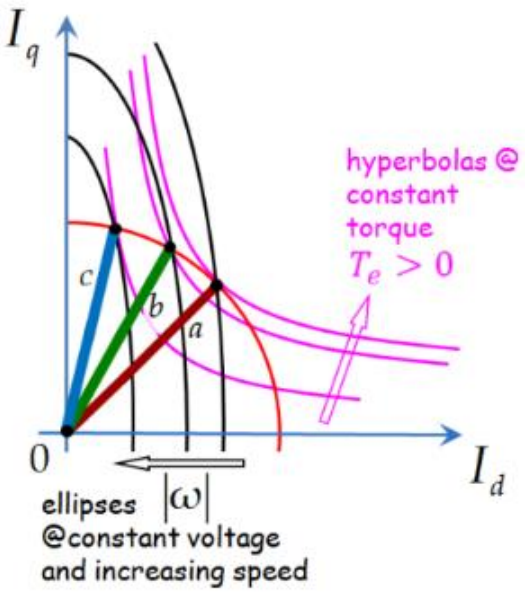

Figure 6.6: Control criteria of the SynRM

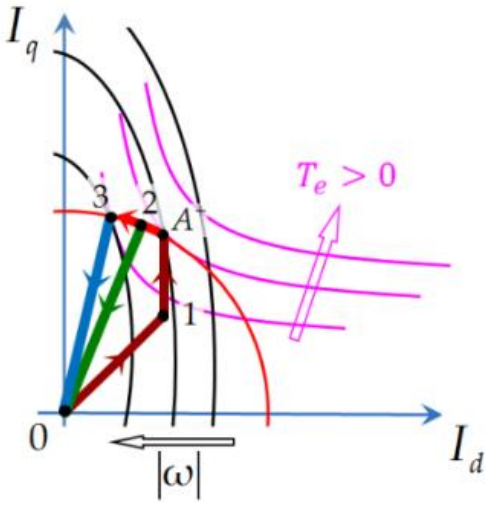

b)

a) maximum torque/current
b) maximum power factor
c) maximum torque/flux

Figure 6.7: Control criteria of the SynRM, effect of saturation.

6.2.4 Maximum Efficiency Strategy

The optimization strategies for Synchronous Reluctance Motors (SynRMs), though derived from simplified motor modeling, offer significant insights into the complexity of current control in real-world applications. Unlike conventional AC motors, where a single current component primarily governs torque production, both the d- and q-axis currents in an SynRM must be actively controlled based on the specific torque-speed operating point. The relationship between these current components is not only dependent on motor parameters but is also influenced by typically unmodeled effects, such as magnetic saturation, cross-coupling between d-q axes, and iron losses [134]-[136].

To achieve optimal performance, an accurate characterization of the motor is required, which can be conducted through precise design methodologies and/or extensive experimental testing. This need becomes even more pronounced when optimizing maximum efficiency, as iron losses cannot be ignored, making the standard Park model insufficient for accurate analysis.

In [64], an off-line optimization approach was developed, utilizing finite element (FE) analysis to map iron losses across the motor's entire operational range. The FE-based modeling was used to optimize the stator current angle (ε) to minimize power losses. However, in this study, a real-time experimental approach is adopted, where comprehensive power measurements, encompassing both electrical power input and mechanical power output, are directly utilized.

By leveraging real-time power measurements, an iterative procedure was implemented where the stator current angle (ε) was systematically adjusted from its minimum to maximum possible values at each speed level, while applying a constant resistive torque on the mechanical axis. The objective function in this optimization was defined as the input electrical power, which was minimized by continuously tuning ε for each specific torque-speed condition. This methodology ensures that the motor operates at optimal efficiency, accounting for real-world losses rather than relying solely on simplified analytical models.

- **Vector Control Strategy for Optimal SynRM Performance**

The theoretical considerations discussed above are implemented through vector control, where the d-q components of the stator current are regulated using a closed-loop control scheme. In SynRM drives, vector control enables precise adjustment of the current space vector to achieve desired torque and efficiency characteristics.

Considering the current space vector representation shown in Figure 6.8, the transformation from Cartesian (d-q) to polar coordinates is expressed as:

$$I_d = I_S cos\varepsilon, \quad I_q = I_S sin\varepsilon \tag{6.10}$$

where:

- $\boldsymbol{I_S}$ is the total stator current magnitude,
- $\boldsymbol{I_d}$ and $\boldsymbol{I_q}$ are the d- and q-axis current components,
- $\boldsymbol{\varepsilon}$ is the **phase angle** of the current vector.

By substituting these expressions into the electromagnetic torque equation (6.5), the torque expression becomes:

$$T_e = \frac{3}{2}\, p(L_d - L_q) I_S^2 sin2\varepsilon \tag{6.11}$$

This formulation highlights that torque generation is maximized when the phase angle ε is carefully tuned based on operating conditions.

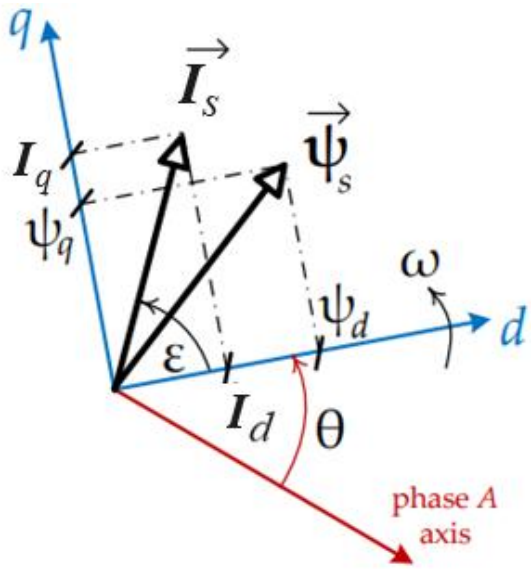

Figure 6.8: Current and flux space vectors

- Implementation of the Control Scheme

The real-time control structure for speed and torque regulation is outlined in Figure 6.9. It consists of:

1. **Motor Side Control (Red Block):**
   - Computes the d-q current references as functions of the desired torque T_e^* and the optimized current phase angle ε.
   - Ensures that torque production follows the predefined optimization strategy (e.g., Maximum Torque per Ampere, Maximum Power Factor, or Maximum Torque per Flux).

2. **Braking Side Control (Yellow Block):**
   - Regulates the braking torque by adjusting the current magnitude (I_S^*) and phase angle ε.
   - Ensures that energy is efficiently managed, particularly in regenerative braking scenarios where the recovered power is fed back into the system.

The optimization criteria are implemented by dynamically selecting the appropriate phase angles ε_a, ε_b, or ε_c, corresponding to the optimization strategies MTPA, MPF, and MTPF, respectively:

$$\varepsilon_a = \frac{\pi}{4}; \quad \varepsilon_b = \text{atan}\left(\sqrt{\frac{L_d}{L_q}}\right); \quad \varepsilon_c = atan\left(\frac{L_d}{L_q}\right) \tag{6.12}$$

These angles define the optimal current vector trajectories, ensuring that the motor operates at maximum efficiency while maintaining stable torque production.

The implementation of advanced vector control strategies for SynRMs enables precise torque-speed optimization, accounting for nonlinear motor behaviors such as saturation, cross-coupling, and iron losses. By experimentally tuning the stator current angle (ε) in real-time, the input power consumption is minimized, leading to an overall increase in system efficiency.

This study bridges the gap between finite-element-based theoretical optimization and practical experimental validation, providing real-world insights into SynRM control strategy refinement. The combination of high-precision torque control, power optimization, and adaptive real-time tuning makes this methodology highly effective for industrial applications requiring energy-efficient motor drives.

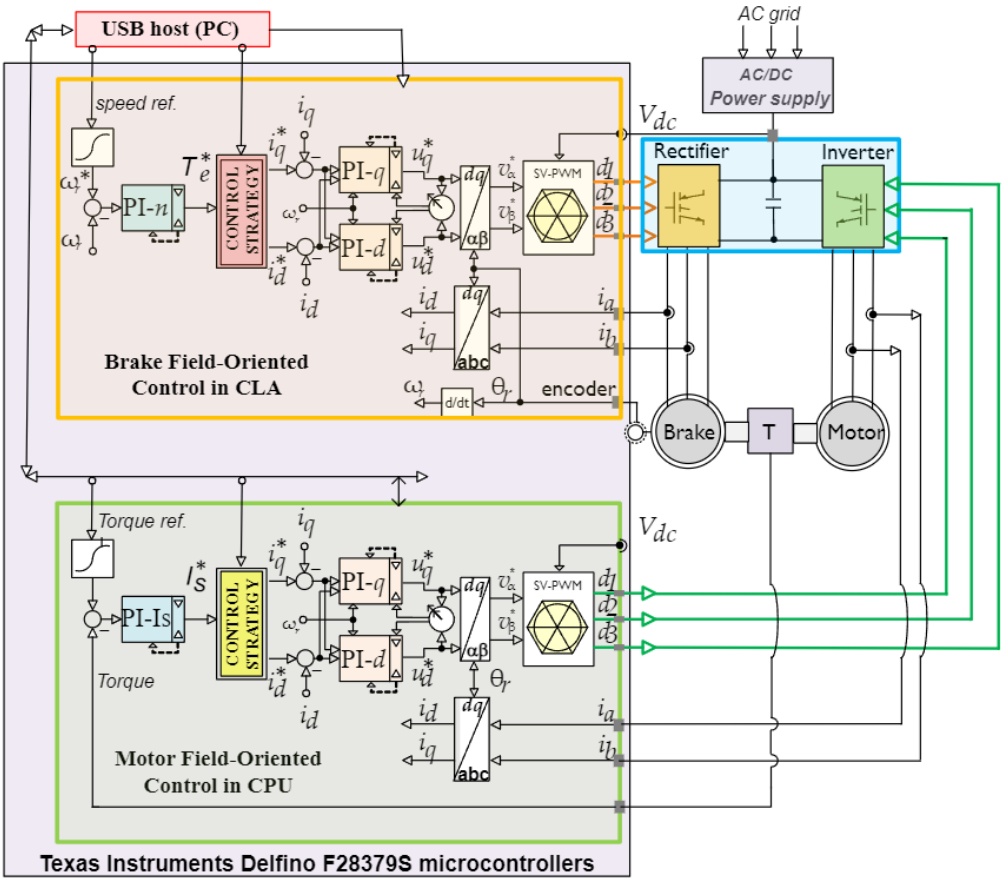

Figure 6.9 Field Oriented Control (FOC) scheme of motor and braking side.

6.2.5 Implementation of Field-Oriented Control (FOC) in the Vector Control System

The control system architecture depicted in Figure 6.9 comprises two independent vector control loops—one for the motor and one for the brake—both implemented using Field-Oriented Control (FOC). This advanced control strategy allows precise regulation of torque and speed, ensuring optimal performance under varying operating conditions. It should be noted that for safety reasons in carrying out experimental tests, the conventions for the control of the motor side and the brake side were reversed.

- **Motor Side: Torque-Oriented Field-Oriented Control (FOC)**

On the motor side, the control strategy is designed to regulate the electromagnetic torque, ensuring that the machine delivers the desired driving torque. The system features an outer torque control loop, where a torque transducer provides real-time feedback, generating the reference current magnitude I_S*. The control strategy block (represented as the red block in Figure 6.9) determines the d-q components of the reference currents based on the optimized current angle ϵ provided by the host controller. These reference currents are then processed by an inner current

control loop, which consists of two nested proportional-integral (PI) controllers regulating the d-axis and q-axis currents.

To generate control signals for the three-phase inverter, the system utilizes Space Vector Pulse Width Modulation (SV-PWM), a technique that ensures:

- **Efficient inverter switching**,
- **Minimized harmonic distortion**,
- **Optimized voltage utilization** for improved motor performance.

The integration of FOC in the motor controller allows precise torque tracking, reducing torque ripples and maximizing efficiency across various speed ranges.

- Brake Side: Speed-Oriented Field-Oriented Control (FOC)

On the brake side, the control system is designed to regulate the rotational speed of the braking machine. Unlike the motor-side control, which is torque-based, the brake-side control follows a speed-oriented approach to maintain a desired rotational velocity, ensuring proper energy dissipation and stabilization of the mechanical system.

A dedicated outer speed control loop receives real-time feedback from an encoder, which measures the actual rotor speed. This feedback signal is used to generate the torque reference T_e*, ensuring that the braking machine operates at the required speed.

The control strategy block (represented as the yellow block in Figure 6.9) calculates the d-q current references required to achieve the target speed. As with the motor-side controller, these references are processed through an inner PI-based current loop and subsequently used to generate SV-PWM control signals for the braking machine's three-phase inverter.

By employing FOC-based speed control, the brake-side system ensures precise speed regulation, effectively balancing mechanical power while optimizing the energy recovery process in the Back-to-Back (BTB) configuration.

- Real-Time Architecture and Implementation on Microcontrollers

The real-time execution of the control system is depicted in Figure 6.4, where a timing structure based on interrupts is used to optimize the execution of the main control algorithms. The implementation follows a high-performance ISR (Interrupt Service Routine) structure, which is synchronized with the PWM carrier frequency and the Analog-to-Digital Conversion (ADC) system.

During each PWM cycle, the ISR:

1. Acquires rotor position data from an encoder,
2. Computes the real-time rotational speed,
3. Executes current control loops,
4. Updates torque and speed references,
5. Generates SV-PWM signals for inverter switching.

The remaining ISR execution time allows for the implementation of auxiliary tasks, such as:

- Data exchange with the host via serial communication,
- Real-time monitoring of system performance,
- Logging and debugging for further analysis.

To maximize computational efficiency, the control system is implemented using parallel programming techniques, distributing tasks across both the CPU and the Control Law Accelerator (CLA). Specifically:

- The CPU handles high-level control tasks, including torque and speed reference calculations and communication with the host system.
- The CLA manages time-critical operations, such as current loop regulation, PWM generation, and ADC sampling, significantly improving real-time execution speed.

This parallel execution strategy ensures:

- Optimized resource utilization,
- Reduced computational latency,
- Improved system responsiveness,
- High-performance real-time control even at high switching frequencies.

The Field-Oriented Control (FOC) architecture implemented in this work allows for precise and efficient torque and speed regulation in both the motor and brake sides of the system. The use of nested PI controllers, Space Vector PWM, and real-time ISR execution ensures robust control dynamics while maintaining high energy efficiency.

By leveraging parallel processing capabilities of the Texas Instruments Delfino F28379S microcontroller, the system achieves optimal performance with minimal computational overhead, making it well-suited for applications requiring high-precision torque and speed control in power electronics and motor drive systems.

6.3 Test Procedure and experimental Results

6.3.1 Flowchart of the test procedure

With reference to the SynRM whose technical characteristics are indicated in table 6.1, through systematic experimental measurements, the control strategies for maximum torque per current (MTPA), maximum power factor (MPF), maximum torque per flux (MTPF), and maximum efficiency were analyzed by mapping their trajectories in the d-q current plane under varying operating conditions. The experimental procedure, summarized in Figure 6.10, was designed to obtain a precise characterization of the constant torque loci at different constant speed levels, as illustrated in Figure 6.6.

Table 6.1 SynRM rated values

Rated values	
phase (base) voltage	$\hat{V}_n = 220 \times \sqrt{2}\ V_{pk}$
phase (base) current	$\hat{I}_n = 10.67\ A_{pk}$
direct current	$\hat{I}_{dn} = 3.93\ A_{pk}$
quadrature current	$\hat{I}_{qn} = 9.92\ A_{pk}$
speed (base)	$n_n = 1500\ rpm$
power	$P_n = 3.142\ kW$
torque	$T_{en} = 20\ Nm$
Parameters	
number of pole pairs	$p = 2$
direct inductance	$L_d = 186\ mH$
quadrature inductance	$L_q = 34.1\ mH$
phase resistance	$R = 1.83\Omega\ @20°C$
saliency ratio	5.45

Nomenclature of the main symbols

Ψ_d, Ψ_q	d-q flux linkages;
I_d, I_q	d-q current components and amplitude;
V_d, V_q	d-q voltage components and amplitude;
L_d, L_q	d-q synchronous inductances;
R	Phase winding resistance;
ω	Angular (electrical) rotor speed;
θ	Angular (electrical) position;
T_e	Electromagnetic torque;
p	Motor pole pairs.

The testing methodology involved operating the tested machine as a brake, controlling the coupled machine at the predefined reference speed ω∗. The torque reference T* was applied to the motor, and the stator current angle ε was systematically varied from 87.5 degrees down to a minimum value. This variation was carefully controlled to ensure that the voltage constraint V_{Smax} , defined by the voltage ellipse in Figure 6.6, was never exceeded. For each value of the current angle ε, the following physical quantities were measured in real-time:

- Stator current magnitude (I_S) – Essential for determining the current distribution in the d-q reference frame.
- Electrical power absorbed by the motor (P_{in}) – Quantifying the total power drawn from the DC source.
- Mechanical power delivered to the shaft (P_{out}) – Providing insight into the electromechanical conversion efficiency.
- Electrical power recovered by the brake (P_{rec}) – Assessing the effectiveness of regenerative braking in the Back-to-Back (BTB) configuration.
- Electric power supplied by the generator in DC (P_{dc}) – Reflecting the net electrical input to the system.

- Motor efficiency (η) – Defined as the ratio of mechanical output power to electrical input power, used to evaluate the effectiveness of different control strategies.
- Motor power factor (cosφ) – A crucial parameter indicating the efficiency of power conversion in the stator windings.
- Input voltage (V_S) – Monitored to ensure compliance with system constraints.

By systematically mapping these performance indicators across different control strategies, a comprehensive understanding of the motor's behavior in the d-q plane was achieved. This experimental validation allowed for the precise identification of the most efficient operating conditions, ensuring that the control algorithms were finely tuned to maximize energy efficiency, torque production, and power factor optimization.

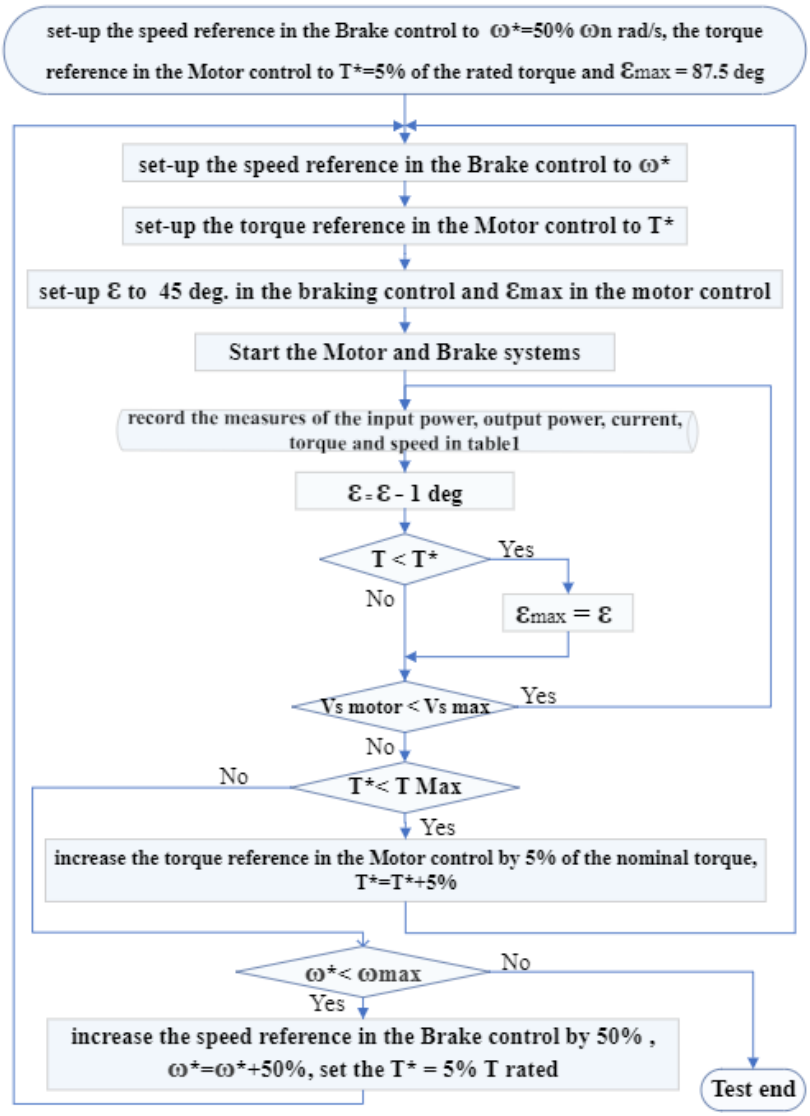

Figure 6.10 Flowchart of the test procedure.

6.3.2 Experimental Results

The experimental setup, illustrated in Figure 6.11, was designed to evaluate the optimal control strategies for a Synchronous Reluctance Motor (SynRM) under real operating conditions. The system comprises the following key components:

- Synchronous Reluctance Motor (SynRM) – The tested motor, operated in both driving and braking modes to assess its performance under various control strategies.
- Power Converter – A general-purpose voltage source inverter, powered by a 600V, 15kW DC power supply (Elektro Automatik). The inverter is equipped with IGBT power modules, operating at a PWM switching frequency of 10 kHz, ensuring high-speed control and efficient energy conversion.
- Control Module – A custom electronic board featuring a Texas Instruments Delfino F28379S microcontroller. The control module is connected to a host PC via both RS232 serial communication and JTAG interface. The host PC serves as both a software development environment and a real-time data acquisition system, allowing for the setting of parameters and the retrieval of computed data and control measurements.
- Real-Time Monitoring and Measurement System – The control module includes a digital-to-analog converter (DAC), which enables the real-time visualization of computed control variables on an oscilloscope. A Yokogawa WT3000 three-phase digital power wattmeter is used for precise measurements of motor terminal voltages, phase currents, power factor, and input electrical power.
- Torque and Speed Measurement – A torque transducer provides analog feedback of the mechanical speed and torque, ensuring accurate experimental validation of the motor's performance.

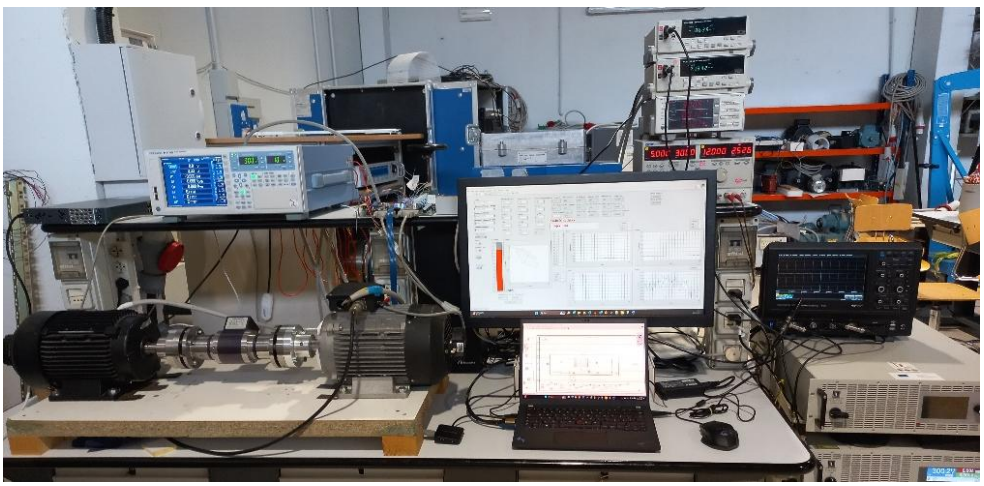

Figure 6.11: Experimental set-up and test-bench

The experimental tests focused on obtaining constant torque loci and optimum control trajectories, as depicted in Figures 6.12, 6.13, 6.14. The results demonstrate the relationship between the current d-q plane limits, the voltage constraints, and the torque-speed characteristics of the SynRM.

- The base current limit defines the current level required to achieve rated torque in the constant torque operating range. At this point, the operating condition aligns precisely with the Maximum Torque per Current (MTPA) curve.
- At higher speeds, the voltage limit restricts the d-axis current, reducing the effective operating area for torque production. This is due to the shrinking voltage ellipses, which impose constraints on current vector control.
- The nominal torque value, determined experimentally, corresponds to a slightly higher current (+3%) compared to theoretical predictions. This deviation accounts for nonlinear effects such as magnetic saturation, d cross-coupling between the d-q axes and even internal mechanical losses contribute to this mismatch.
- The maximum efficiency trajectory lies between the maximum power factor (MPF) curve and the maximum torque/current (MTPA) curve. However, at higher speeds, the efficiency trajectory shifts closer to the power factor curve, as iron losses begin to dominate over Joule losses due to increasing operating frequency.

Figures 6.15, 6.16, 6.17 present the experimental efficiency results, demonstrating how the SynRM achieves peak efficiency under optimal control conditions:

- At 375 rpm (Figure 6.15), the maximum efficiency reaches 65%, with a torque of 5.5 Nm and a power factor of 0.478. The motor input power is 298 W, but the DC source consumption is reduced to 243.8 W, resulting in a 19% decrease in grid power demand.
- At 750 rpm (Figure 6.16), the maximum efficiency reaches 78%, with a torque of 5.5 Nm and a power factor of 0.573. The motor input power is 568 W, but the DC source consumption is reduced to 315.6 W, resulting in a 55% decrease in grid power demand.
- At 1125 rpm (Figure 6.17), the maximum efficiency of 82% is achieved with a torque of 3.2 Nm and a power factor of 0.567. The motor absorbs 465 W of input power, but due to the back-to-back regenerative system, the actual power drawn from the DC source is only 238.15 W, leading to a 51% reduction in power consumption from the AC supply.

These findings confirm that the energy-efficient back-to-back testing approach significantly reduces power losses and AC grid dependency, demonstrating its effectiveness for industrial SynRM drive optimization. The impact of inverter losses on the optimal operating point should be evaluated for a more accurate analysis.

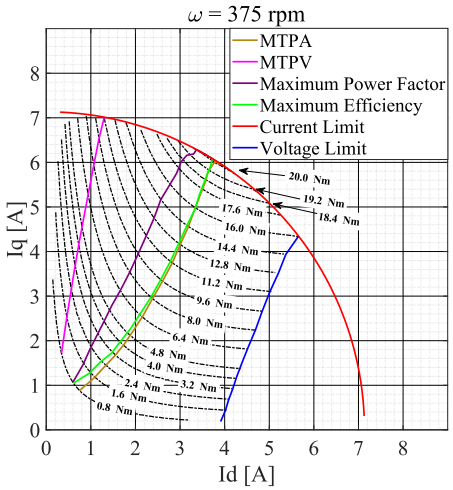

Figure 6.12: Constant torque loci end optimum control trajectories at 375rpm

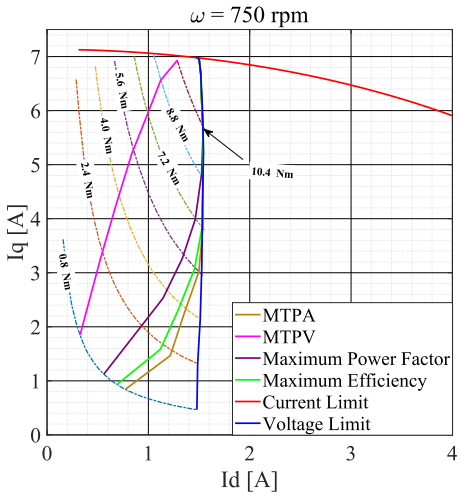

Figure6.13: Constant torque loci end optimum control trajectories at 750rpm

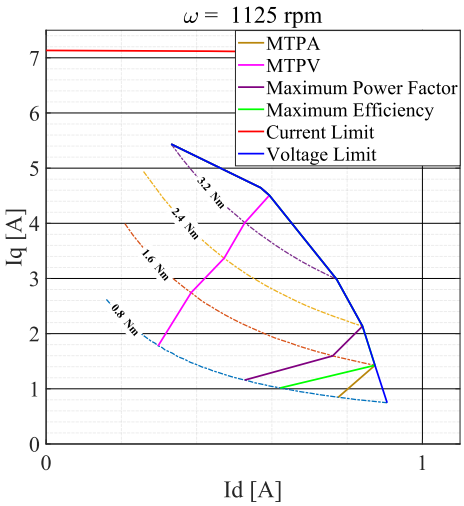

Figure 6.14: Constant torque loci end optimum control trajectories at 1125rpm

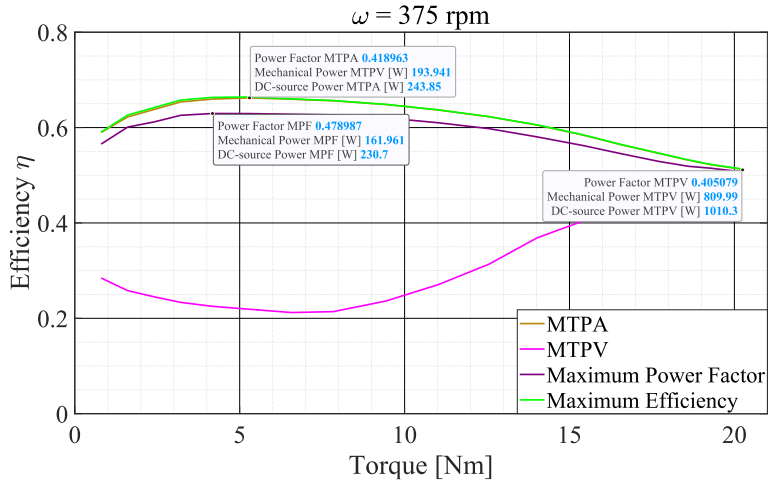

Figure 6.15: Efficiency with different control strategies (experimental) at 375 rpm

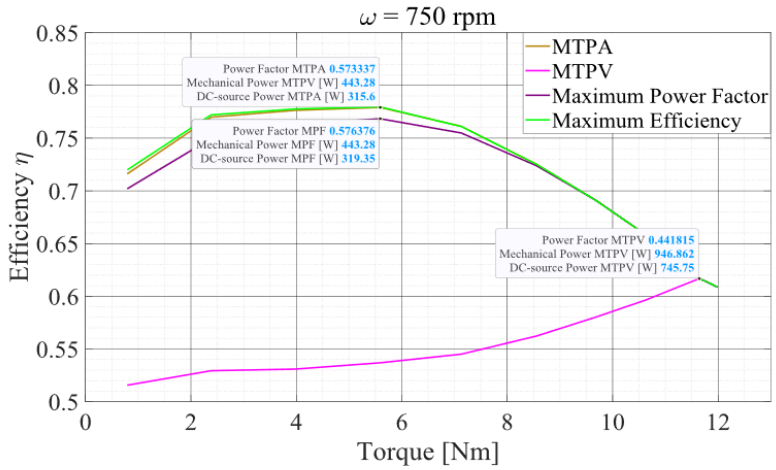

Figure 6.16: Efficiency with different control strategies (experimental) at 750 rpm

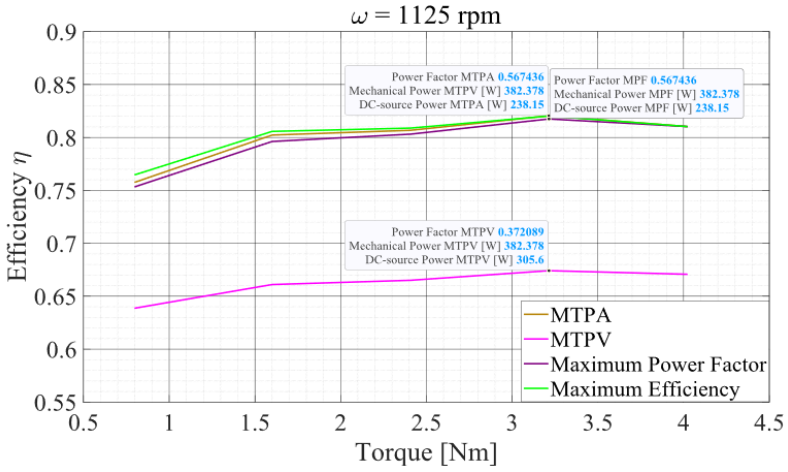

Figure 6.17: Efficiency with different control strategies (experimental) at 1125 rpm

- Conclusion

This chapter presents a comprehensive experimental evaluation of optimal control strategies for Synchronous Reluctance Motors (SynRM), focusing on maximizing torque-to-current ratio (MTPA), power factor (MPF), and efficiency. A back-to-back power system was implemented to ensure energy-efficient testing, allowing for real-time measurement of electrical, mechanical, and efficiency parameters. The energy recovered during braking was not dissipated but instead redirected to the DC link through a PWM-controlled inverter. As a result, the DC supply only compensates for the net power difference between motor input requirements and regenerated braking energy. This methodology enables experimental testing with significantly reduced electrical power consumption, highlighting the potential for sustainable and energy-efficient motor drive control. The experimental results validate the effectiveness of advanced vector control and field-oriented control (FOC) in optimizing SynRM performance, making this approach suitable for high-efficiency industrial applications and next-generation electric mobility solutions. Since the comparative analysis of different control strategies reveals only marginal variations in overall efficiency, the reliability and significance of the experimental results become strongly dependent on the accuracy and consistency of the measurement framework. In this context, high-precision electrical and mechanical measurements are mandatory, together with strict control of the thermal operating conditions of the machine. In particular, the repeatability of the motor temperature must be carefully ensured, as even small temperature variations significantly affect copper losses, magnetic properties, and therefore the efficiency of the drive system. Furthermore, the contribution of mechanical losses, such as bearing friction, windage, and ventilation losses, cannot be neglected, especially in high-speed operating conditions, where they represent a non-negligible portion of the total power balance. Accurate estimation or direct measurement of these losses is therefore essential to correctly interpret the measured performance. The inclusion of converter losses together with motor losses in the proposed experimental setup has important implications for the generality and the interpretation of the results. On one hand, measuring the overall drive efficiency, rather than the motor alone, provides a realistic and application-oriented figure of merit, since in practical electric drive systems the inverter is an integral part of the drivetrain. This approach is particularly meaningful for traction and industrial applications, where the end user is interested in the efficiency of the complete electromechanical conversion chain from DC link to mechanical shaft. On the other hand, this methodology introduces a certain dependency of the results on the specific hardware used for the power converter. Different inverter topologies, semiconductor technologies (e.g., silicon versus SiC), switching frequencies, dead-time strategies, and modulation methods may lead to significantly different loss distributions, potentially affecting the comparability and generality of the measured data. For this reason, while it is not strictly mandatory to use the same inverter hardware as in the final application, it is highly desirable when the objective is to predict the real-world performance of the target system. Using a representative inverter ensures that the measured efficiencies and thermal behaviors are directly transferable to the final product. However, when the focus of the analysis is on the intrinsic performance of the motor and the control strategy, it becomes advantageous to separate motor losses from

converter losses. This can be achieved by combining direct electrical measurements at the motor terminals with independent inverter loss models or calorimetric methods, thus allowing the motor performance to be evaluated in a more hardware-independent manner. The separation of motor and converter losses is particularly relevant when comparing different control strategies. In such cases, variations in inverter losses due to changes in switching patterns, current ripple, or modulation index may mask or distort the actual impact of the control law on the electromagnetic performance of the motor. Therefore, a hybrid approach that provides both the overall drive efficiency and the decoupled motor and inverter loss contributions offers the most complete and scientifically meaningful characterization. Another critical aspect concerns the accurate definition of the operating point, especially in terms of the current vector orientation in the d-q reference frame. In high-speed operation, the precise imposition of the current angle is inherently challenging due to the presence of sampling delays, computational delays, and inverter-induced phase shifts. These effects cause a misalignment between the commanded and the actual stator current vector, which directly impacts torque production, losses, and flux regulation. Consequently, even small angular errors can lead to significant deviations in the measured efficiency and torque. To address this issue, the operating point must be defined based on the measured currents rather than on their references. In practice, the d-q currents used for loss and efficiency calculations should be reconstructed from high-resolution phase current measurements and transformed using an accurately estimated electrical angle. Advanced phase-locked loop (PLL) or observer-based angle estimation techniques can be employed to minimize phase errors. Furthermore, delay compensation strategies can be implemented in the control, such as predictive current control or phase-advance techniques, which anticipate the inverter and sampling delays and correct the d-q frame orientation accordingly. In addition, the use of real-time platforms and rapid control prototyping, as adopted in this work, allows tight synchronization between measurement, control, and signal processing. This makes it possible to quantify and compensate for delay-induced errors, ensuring that the actual operating point of the motor corresponds closely to the intended one. As a result, the efficiency maps and performance comparisons obtained under these conditions become more reliable, repeatable, and physically meaningful, even in the demanding high-speed operating regions typical of modern electric drive applications.

Chapter 7

New Opportunities and Challenges in Synchronous Reluctance Motors.

Part of the work presented in this chapter has been previously published in [80].

This chapter investigates the potential of Synchronous Reluctance Motors (SynRMs) as a promising alternative to conventional electric motors, with a particular emphasis on the integration of additive manufacturing and advanced materials. The study examines recent advancements in additive manufacturing techniques and the utilization of novel materials for motor construction, aiming to enhance efficiency, performance, and sustainability. Furthermore, the research explores the development of intelligent control strategies based on machine learning and artificial neural networks (ANNs), replacing traditional PID controllers to improve rotor position and speed estimation accuracy. Additionally, hardware solutions such as multiprocessor systems and System-on-Chip Field-Programmable Gate Arrays (SoC FPGAs) are analyzed to optimize real-time control capabilities. The study also scrutinizes MATLAB/Simulink toolboxes designed for neural network fitting and reinforcement learning, alongside C++ and VHDL coders that facilitate software implementation on microcontrollers and FPGAs. These computational tools and programming frameworks enable the seamless integration of advanced control algorithms, thereby improving the overall system responsiveness and adaptability. These advancements collectively highlight the transformative impact of SynRMs, including variants such as the Line-Start Synchronous Reluctance Motor (LSSynRM) and the Permanent Magnet-Assisted Synchronous Reluctance Motor (PMaSynRM). Positioned as a cutting-edge solution, these motor types are poised to become the next-generation standard, offering superior performance, energy efficiency, and environmental sustainability across a wide range of applications.

7.1 Impact of Additive Manufacturing and New Materials on Motor Performance

Despite recent advancements, Synchronous Reluctance Motors are approaching their theoretical performance limits, necessitating significant research investments to achieve incremental improvements. Additionally, compliance with increasingly stringent energy efficiency regulations poses challenges for motor designers. To overcome these barriers, a paradigm shift in motor design is required, involving novel topologies, advanced materials, and innovative manufacturing methodologies. Traditional production techniques limit the feasibility of emerging conductive and magnetic materials, impeding the development of next-generation SynRM designs. As a solution, Additive Manufacturing (AM) is emerging as a disruptive technology capable of revolutionizing motor fabrication [85],[86]. AM, a core pillar of Industry 4.0's smart manufacturing paradigm, offers unparalleled design flexibility compared to conventional subtractive and formative processes. This technology enables the production of optimized SynRM components, including iron cores, windings, insulation, and cooling systems, while allowing for intricate geometries that are otherwise unattainable. By leveraging 3D printing, engineers can integrate novel topologies, advanced materials, and high-performance structural configurations, paving the way for the next generation of high-efficiency electric motors [87]-[94]. The strategic integration of AM in SynRM production allows for the development of highly customized and functionally optimized components. One of the key advantages of AM is its capability to fabricate complex magnetic cores with enhanced flux-guiding properties, improving the overall motor efficiency. Additionally, AM facilitates the use of advanced materials such as soft magnetic composites (SMCs) and high-performance ferromagnetic alloys, which can significantly reduce core losses and improve thermal management. Another critical aspect of AM in motor production is the potential for integrating cooling solutions directly within the motor structure. Traditional cooling systems require external components and additional manufacturing steps, whereas AM enables the fabrication of intricate internal cooling channels within stator and rotor assemblies. This capability enhances thermal performance, reduces overheating risks, and prolongs motor lifespan. Beyond magnetic cores, AM also contributes to advancements in winding technologies. Conventional copper windings often suffer from limitations related to space constraints and inefficient heat dissipation. With AM, it is possible to design and manufacture optimized conductor geometries that maximize electrical performance while minimizing resistive losses. Researchers are also exploring the use of conductive materials beyond copper, such as aluminum-based alloys or advanced composites, to enhance electrical efficiency and reduce weight. The adoption of AM in SynRM manufacturing is not only driven by performance improvements but also by sustainability considerations. Traditional motor manufacturing methods generate significant material waste due to machining and subtractive processes. AM, by contrast, enables near-net-shape production, minimizing material waste and reducing the environmental footprint of motor fabrication. Furthermore, the potential for localizing AM-based production could

reduce supply chain dependencies and transportation costs, making SynRMs a more viable alternative in global markets. While AM presents numerous advantages, challenges remain in terms of material properties, process repeatability, and scalability for mass production. Ongoing research aims to optimize AM techniques for high-volume manufacturing, ensuring that SynRM components produced via 3D printing meet industrial standards for mechanical strength, durability, and efficiency. The combination of AM, novel materials, and advanced design methodologies is set to revolutionize SynRM production, positioning it as a key technology in the future of high-performance electric motors.

7.1.1 Additive Manufacturing Technologies and Applications for Electric Motors

Additive Manufacturing (AM), commonly known as 3D printing, is a transformative technology that enables the layer-by-layer fabrication of complex components with high precision. Unlike traditional subtractive or formative manufacturing processes, AM allows for the production of intricate geometries with minimal material waste, making it a highly efficient and sustainable approach. The growing interest in AM for electric motor production, particularly for Synchronous Reluctance Motors (SynRMs) and Permanent Magnet Synchronous Motors (PMSMs), is driven by its ability to create optimized magnetic cores, conductive windings, and advanced cooling structures. Several AM technologies are used for fabricating electric motor components, each offering distinct advantages depending on material requirements, design complexity, and mechanical properties. The most relevant AM techniques for motor manufacturing include:

1. Powder Bed Fusion (PBF) Technologies

PBF is one of the most widely used 3D printing methods for producing high-performance metallic components (Figure 7.1). This category includes several sub-techniques:

- Selective Laser Melting (SLM) / Laser Beam Melting (LBM): SLM is one of the most commonly used metal AM technologies, ideal for manufacturing complex magnetic parts such as iron cores for reluctance synchronous motors. It involves the successive melting of thin layers of metal powder using a high-powered laser beam. This process achieves near-full density components, making it particularly useful for fabricating stators, rotors, and structural motor components with high magnetic permeability and minimal losses. Additionally, SLM allows for the integration of multiple materials, enabling the creation of hybrid structures with enhanced electromagnetic properties.
- Selective Laser Sintering (SLS): Unlike SLM, SLS does not fully melt the material but instead sinters it at a high temperature, allowing the metal

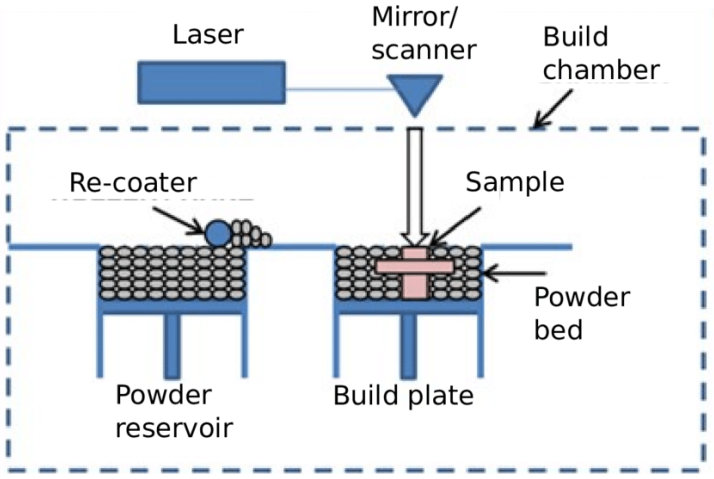

Figure 7.1 L-PBF process (Fritsch, Tobias. (2019). A multiscale analysis of additively manufactur)

particles to fuse without reaching their liquid state. This technique is suitable for producing components with high mechanical strength and wear resistance.

- Direct Metal Laser Sintering (DMLS): DMLS, developed for processing metal alloys with different melting points, is particularly useful for manufacturing composite iron cores, which require optimized magnetic and thermal properties. It enables the fusion of materials at the molecular level, ensuring homogeneous distribution of elements within the motor components.

PBF technologies are particularly beneficial for producing electric motor components due to their ability to manufacture geometrically complex structures, such as intricate magnetic flux paths and internal cooling channels, which are challenging to achieve using conventional methods.

2. Fused Deposition Modeling (FDM)

FDM is a cost-effective and widely used AM technique that deposits thermoplastic materials layer by layer to form a component (Figure 7.2). While primarily used for prototyping, FDM has significant applications in electric motor manufacturing, particularly for fabricating permanent magnets.

- Permanent Magnet Fabrication: By using specialized thermoplastic filaments embedded with magnetic particles (e.g., ferrite or rare-earth-based composites), FDM can be employed to print custom-shaped permanent magnets. This approach enables the production of magnets with optimized flux distribution and complex geometries, which are difficult to achieve using traditional pressing and sintering techniques.

- Housing and Insulation Components: FDM can also be used to manufacture non-magnetic motor components, such as insulation layers, motor casings, and winding supports, reducing weight and improving heat dissipation.

Although FDM is limited in terms of mechanical strength and conductivity compared to metal AM methods, its ability to create intricate polymer-based components makes it a valuable tool in electric motor prototyping and secondary component fabrication.

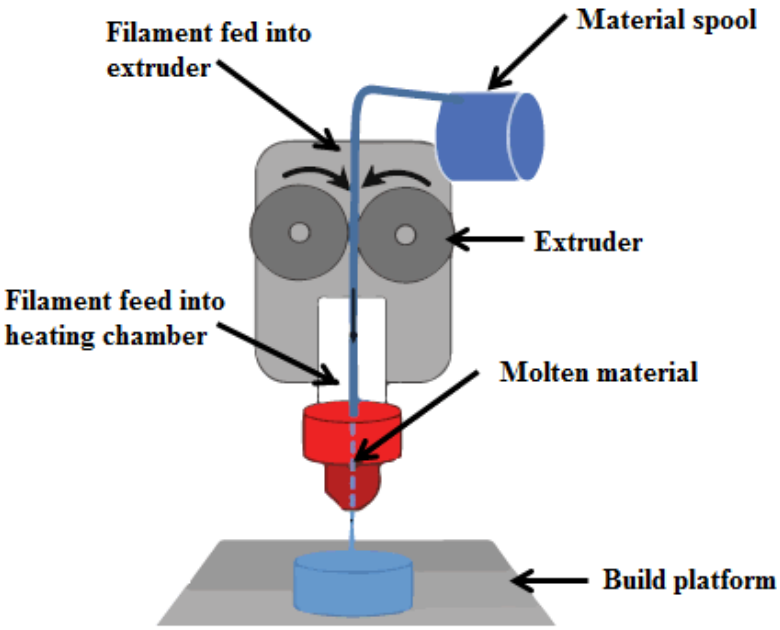

Figure 7.2 Schematic of the FDM process [137]

3. Directed Energy Deposition (DED) Technologies

DED processes involve the direct deposition of metal material using a high-energy heat source, such as a laser, electron beam, or electric arc (Figures 7.3, 7.4). This category includes several key techniques:

- Laser Engineering Net Shaping (LENS): LENS technology uses a laser to selectively melt metal powders and deposit successive layers to build a component. This method is particularly well-suited for producing large electric motor cores with high efficiency. The ability to deposit metal powders directly onto complex curved surfaces makes LENS highly adaptable for motor applications, including:

    - Manufacturing iron cores: By using soft magnetic alloys such as Fe-Si, Fe-Co, and Fe-Ni, LENS enables the production of high-performance laminated cores with reduced eddy current losses.

- Repairing and upgrading motor components: LENS allows for in-situ material deposition, making it possible to repair worn-out iron cores or enhance existing components with additional magnetic layers.

- Wire Arc Additive Manufacturing (WAAM): WAAM, which utilizes an electric arc to melt and deposit wire feedstock, is particularly useful for large-scale motor components. It provides a cost-effective solution for manufacturing heavy-duty stators and rotors with high structural integrity.

DED technologies excel in fabricating large and highly customized motor parts, offering the advantage of rapid material deposition and high-strength bonding. However, they typically require post-processing steps, such as machining and heat treatment, to achieve the desired surface finish and magnetic properties.

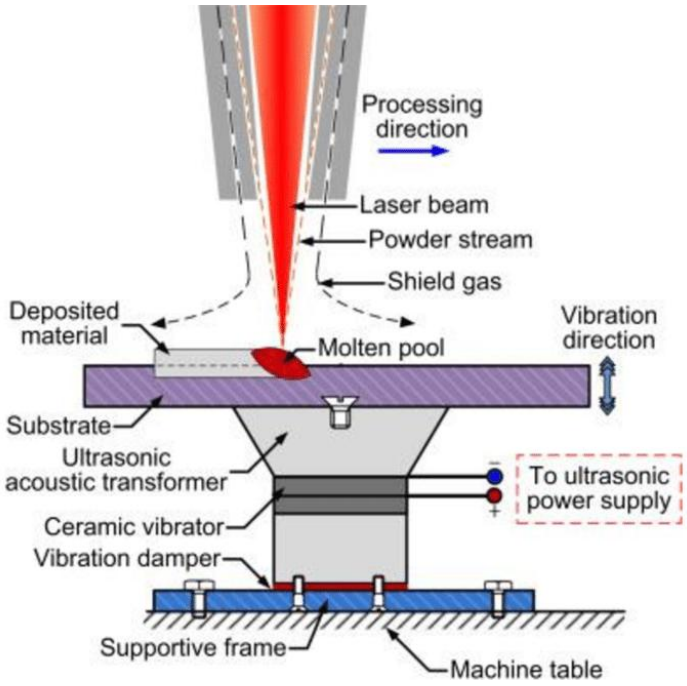

Figure 7.3 Laser Engineered Net Shaping (LENS) process [138]

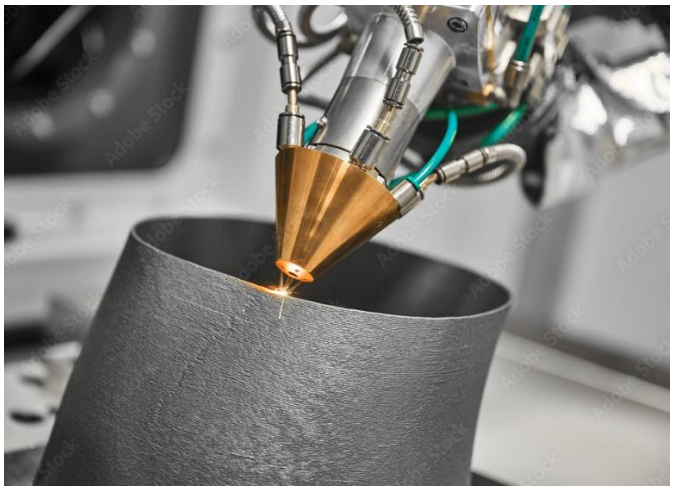

Figure 7.4 Example of Laser DED process

4. Hybrid Additive Manufacturing for Electric Motors

Hybrid AM combines 3D printing with traditional manufacturing techniques to optimize the performance of electric motor components. Some innovative approaches include:

- Combining PBF with Conventional Machining: This method is used to produce highly precise iron cores with smooth surfaces and tight tolerances. The components are printed using SLM or DMLS and then finished with CNC machining for enhanced dimensional accuracy.
- Integrating AM with Soft Magnetic Composites (SMCs): AM enables the fabrication of 3D-printed iron cores with embedded SMCs, which help reduce core losses and improve energy efficiency. These composite materials, composed of insulated iron particles, offer superior electromagnetic performance with lower hysteresis losses.

  • 3D Printing of Copper Windings: Some advanced AM techniques, such as laser-based metal deposition, are being explored for printing copper windings directly onto motor stators. This innovation has the potential to improve electrical conductivity, reduce resistive losses, and enhance thermal management. The schematic in Figure 7.5 represents a hybrid manufacturing machine that combines additive and subtractive manufacturing, used for the production of complex components in electric motors.

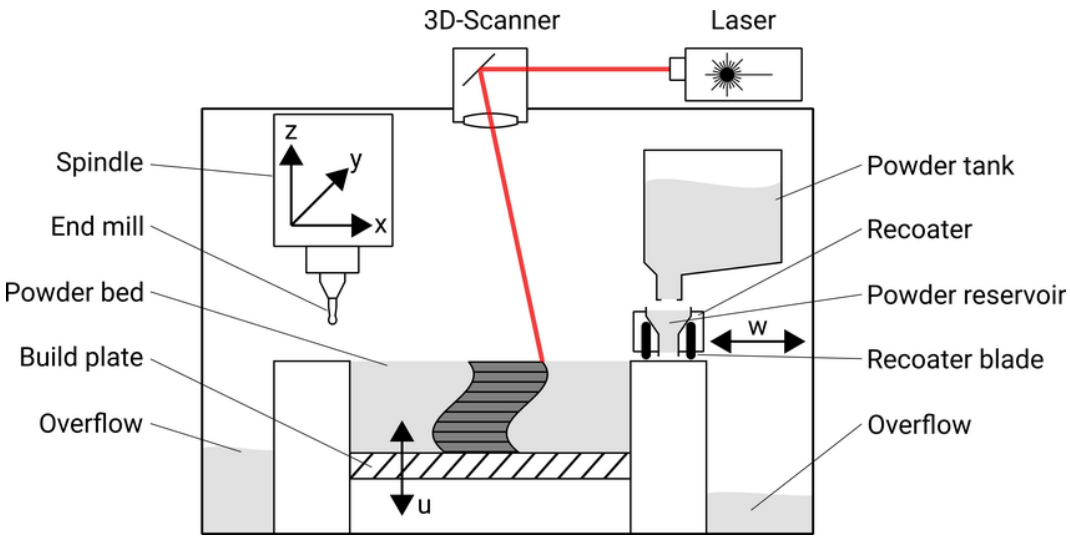

Figure 7.5 Diagram of the additive hybrid manufacturing process[139]

7.1.2 Advantages of Additive Manufacturing in Electric Motor Production

The integration of AM in electric motor manufacturing offers several key benefits:

1. Design Freedom: AM allows for the production of complex geometries that optimize electromagnetic efficiency, such as flux barriers, custom-shaped stator slots, and intricate cooling channels.
2. Material Efficiency: Unlike traditional machining, which generates significant waste, AM enables near-net-shape manufacturing, reducing material consumption and production costs.
3. Performance Optimization: By utilizing advanced materials and custom layer structures, AM enhances the magnetic, thermal, and mechanical properties of motor components.
4. Rapid Prototyping and Customization: AM significantly shortens the development cycle for new motor designs, enabling quick iteration and optimization of prototypes.
5. Sustainability: Reduced material waste and energy-efficient production processes contribute to a lower environmental impact.

- **Challenges and Future Directions**

Despite its numerous advantages, AM still faces challenges in electric motor manufacturing, including:

- Material Limitations: The availability of AM-compatible magnetic materials, such as high-performance ferromagnetic alloys and conductive composites, is still limited.
- Process Repeatability: Ensuring consistent material properties across printed components remains a challenge due to variations in powder composition, laser parameters, and build orientation.

- Surface Finish and Post-Processing: Many AM methods require additional machining and heat treatment to achieve optimal surface quality and mechanical properties.

To fully realize the potential of AM in electric motor manufacturing, ongoing research focuses on improving material formulations, refining printing techniques, and integrating AI-driven process optimization. The future of AM in motor production lies in the convergence of advanced materials, real-time process monitoring, and hybrid manufacturing approaches, paving the way for next-generation high-performance electric motors.

7.2 New Materials for 3D Printing of SynRM: Advancements in Magnetic, Conductive, and Insulating Materials

7.2.1 Magnetic Materials in Additive Manufacturing

Additive Manufacturing (AM) has revolutionized the field of electric motor design by enabling the use of a diverse range of magnetic materials. This advancement allows for precise customization, enhancing the efficiency and performance of electric machines. Various magnetic materials, as outlined in [86], are particularly suited for AM processes:

- Iron-Silicon Alloys (Fe-Si, Fe-6.5Si): These alloys are extensively used for manufacturing iron cores due to their excellent magnetic properties, including low core losses and high permeability. Technologies such as Direct Metal Laser Sintering (DMLS) and Powder Bed Fusion (PBF) are well-suited for printing these materials, enabling the fabrication of optimized core structures with minimal energy loss.
- Iron-Nickel Alloys (Fe-Ni, Permalloy): Known for their high magnetic permeability, these materials are ideal for applications requiring efficient magnetic flux conduction. AM technologies like Directed Energy Deposition (DED), Selective Laser Melting (SLM), and Fused Deposition Modeling (FDM) have been employed to manufacture these cores with complex geometries tailored for specific electromagnetic performance requirements.
- Iron-Cobalt Alloys (Fe-Co, Permendur): These materials offer high magnetic flux density, making them suitable for applications requiring high saturation magnetization. The combination of SLM and Laser Engineering Net Shaping (LENS) technologies enables the precise fabrication of iron-cobalt components, ensuring optimal performance in high-power density electric motors.

- Soft Magnetic Composite (SMC) Materials: These are designed for 3D printing of magnetic cores with complex shapes. Unlike conventional laminated steel, SMCs consist of insulated ferromagnetic particles, which help reduce eddy current losses, making them particularly effective in high-frequency applications.
- Amorphous Iron (MetalGlass): Characterized by its lack of crystalline structure, amorphous iron significantly improves electric motor efficiency and is a key material for achieving IE5 efficiency standards. AM processes like SLM and LENS are currently being developed to enable the effective printing of amorphous metal cores, further reducing energy dissipation and improving motor performance.
- Nanocrystalline Iron Alloy (FINEMET): This material consists of ultra-small grains (<50 nm) of iron, boron, phosphorus, silicon, and noble metals, offering outstanding electromagnetic properties. However, its brittleness poses challenges in handling and integration into electric motors. Researchers are actively investigating the feasibility of printing FINEMET using LENS technology to harness its superior magnetic characteristics while mitigating fragility concerns.

Figure 7.6 and table 7.1 provides a comparative analysis of the strengths and weaknesses of these new magnetic materials in AM, rating their performance attributes from 0 (not possible) to 5 (excellent).

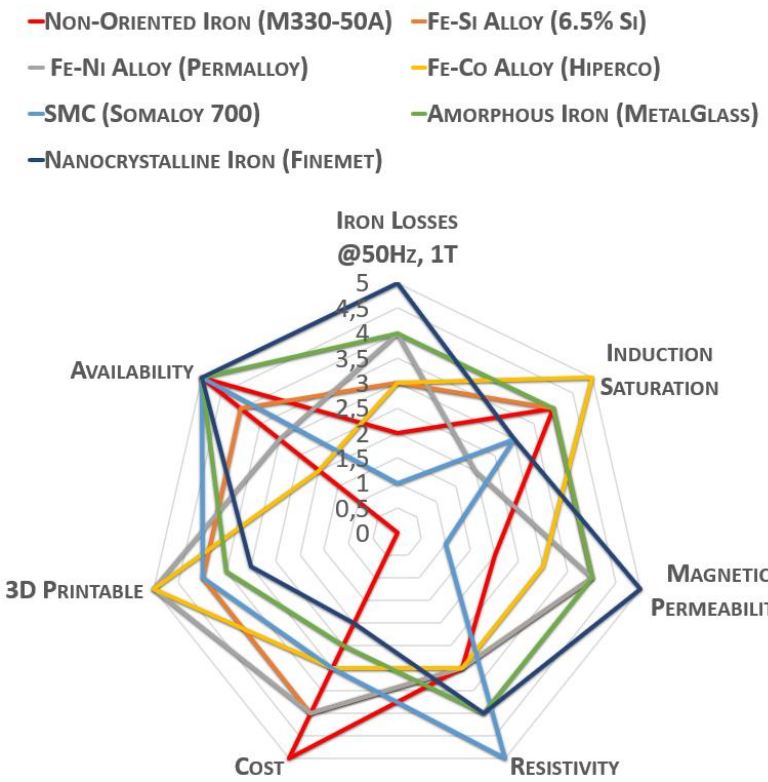

Figure 7.6: Characteristics of new magnetic materials, 5= excellent, 1= very bad, 0= not possible.

Materials & Alloy	3D Printing for Magnetic Cores of Electric Machines		
	Technologies	*Best Features*	*Drawbacks*
Fe-Si, Fe-6.5Si	DMLS	Optimal Magnetic Properties	High iron loss
Fe-Ni (Permalloy)	DED, SLM, FDM	High Magnetic Permeability	Low saturation
Fe-Co (Permendur)	SLM, LENS	High magnetic flux density for high saturation applications	Low availability, high cost
Soft Magnetic Composite (SMC)	SLM, PBF	Complex shape	High iron loss
Amorphous Iron (MetalGlass)	SLM, LENS	It is crucial for increasing the efficiency of electric motors for the IE5 efficiency standard.	High cost, difficult to print
Nano Crystalline Iron Alloy (Finemet) (<50nm of iron boron, phosphorus, silicon, and noble metals	LENS	Excellent performance	High fragility, high cost, difficult to print

Table 7.1: Magnetic Materials and AM technologies.

7.2.2 Conductive Materials: Beyond Copper and Aluminum

Traditionally, copper has been the predominant material for electric motor (EM) windings. However, the direct 3D printing of pure copper presents significant challenges due to its **exceptional thermal conductivity**, which leads to premature cooling during the AM process. Additionally, the high oxidation rate of freshly printed copper complicates its use in additive manufacturing. To address these limitations, alternative conductive materials have emerged:

- CuCrZr Alloy (C18150): This copper-chromium-zirconium alloy retains 80-90% of pure copper's electrical conductivity while being more compatible with AM processes like DMLS and PBF. It offers improved thermal stability and oxidation resistance, making it a promising candidate for printed EM windings.
- Aluminum-Based Conductors (AlSi10Mg): Given its lightweight properties, aluminum has been explored as an alternative in EM applications. The AlSi10Mg alloy is particularly compatible with DMLS and SLM processes, enabling the fabrication of high-performance conductive components. Although aluminum is not as conductive as copper, its lower density makes it a viable option for weight-sensitive applications, such as electric vehicle motors.
- Graphene-Based Conductors: Graphene (Figure 7.7a) and its one-dimensional allotrope, carbon nanotubes (CNTs) (Figure 7.7b), have been recognized as revolutionary materials for improving electrical and thermal

conductivity in EM windings. The incorporation of CNTs into copper matrices has led to the development of CNT-Cu composites, which exhibit:

- 2.6 times higher electrical conductivity compared to pure copper.
- Lower resistivity temperature coefficient, making them more stable across varying operating conditions.
- Reduced density, making them suitable for lightweight applications in mobile and aerospace electric motors.

Research has shown that these CNT-Cu composites can be fabricated using Fused Deposition Modeling (FDM), making them an ideal candidate for next-generation 3D-printed EM windings. Furthermore, the use of graphene-PLA composites in FDM allows for the development of flexible winding structures, further broadening the scope of 3D-printed conductive materials in electric motor design.. Table 7.2 offers a comparative assessment of the strengths and challenges of these advanced conductive materials in additive manufacturing.

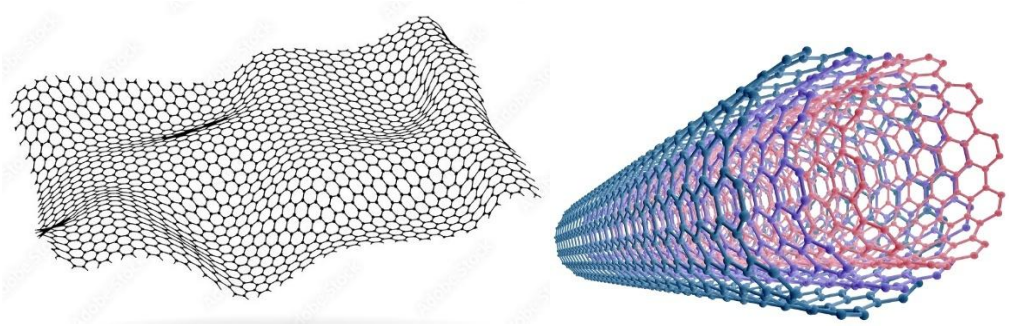

a) **b)**

Figure 7.7: Graphene a) layer with hexagonal lattices b) nested nanotubes

Materials & Alloy	**3D Printing for conductive parts of Electric Machines**		
	Technologies	***Best Features***	***Drawbacks***
C18150 CuCrZr	DMLS, PBF	Non-oxidation	80% Cu conductivity
AlSi10Mg	DMLS, SLM	Non-oxidation Light weight	Lower conductivity
Carbon nanotubes (CNT)-Cu composites	FDM	Conductivity 2.6 times greater than that of pure copper, resistivity temperature coefficient one order of magnitude lower than conventional copper	high cost

Table 7.2: Conductive Materials and AM technologies

7.2.3 Advanced Insulation Materials for Electric Machines

The evolution of insulation materials in electric machines represents a major breakthrough in improving motor safety, efficiency, and longevity. Traditional insulation, typically composed of varnished enamels, has significant thermal and dielectric limitations. The introduction of advanced insulation materials via AM is revolutionizing the industry.

1. Ceramic-Based Insulation for High-Temperature Applications

Ceramic insulators have emerged as a game-changer in electric motor design. Compared to conventional Class H insulation (180°C max operating temperature), ceramics can withstand temperatures above 300°C, providing exceptional thermal resilience.

However, due to their high melting points, ceramics are difficult to process with traditional manufacturing techniques. The use of Laminated Object Manufacturing (LOM) and FDM enables the fabrication of ceramic insulators in custom geometries, opening new possibilities for motor design and thermal management.

2. PEEK Polymers: Enhanced Electrical Insulation and Leakage Current Protection

Polyether Ether Ketone (PEEK) has become an essential material for insulation in electric motors, particularly for:

- Slot insulation: Preventing short circuits between motor windings.
- Bearing insulation: Mitigating harmful leakage currents, which can lead to premature motor failure.

PEEK-based insulators can be fabricated using FDM, Stereolithography (SLA), and Selective Laser Sintering (SLS), offering high mechanical strength, excellent thermal resistance, and superior electrical insulation properties. Table 7.3 presents a comparative evaluation of the advantages and limitations of these advanced insulation materials in additive manufacturing

Materials & Alloy	3D Printing for insulation parts of Electric Machines		
	Technologies	***Best Features***	***Drawbacks***
Ceramic	LOM, FDM	Withstands temperatures above 300°C for conductor safeguarding	high cost
Polyether Ether Ketone (PEEK) polymers	FDM, SLS	For slot and bearing insulation	high cost

Table 7.3: Insulation Materials and AM technologies.

The integration of advanced magnetic, conductive, and insulation materials through Additive Manufacturing is paving the way for next-generation electric motors. The ability to 3D print highly customized materials enables:

- Optimized Magnetic Cores: Lower core losses and higher efficiency using Fe-Si, Fe-Co, and nanocrystalline materials.
- Revolutionary Conductive Windings: CNT-enhanced copper composites and graphene-based conductors for superior electrical performance.
- Advanced Insulation Solutions: Ceramic and PEEK-based insulation materials to enhance durability and thermal resistance.

While challenges remain, such as material brittleness (FINEMET), oxidation issues (copper), and AM process limitations, ongoing research is actively addressing these hurdles. With the continued development of hybrid AM techniques and material innovations, the future of electric motor manufacturing is set to become more efficient, sustainable, and high-performance than ever before.

7.3 Additive manufacturing: unlocking new opportunities for the advancement of SynRM

7.3.1 Manufacturing of Magnetic Components

One of the most significant challenges in the design and manufacturing of Synchronous Reluctance Motors (SynRMs) at high operating speeds is the requirement for reinforced air barriers within the rotor structure. These air barriers are typically strengthened using structural ribs, as illustrated in Figure 7.8. While these ribs are crucial for guiding magnetic flux along the intended pathways, they inadvertently degrade the motor's overall magnetic performance. This deterioration occurs because the ribs introduce discontinuities in the magnetic circuit, increasing

reluctance and reducing efficiency. Traditionally, SynRM rotors are manufactured using laminated steel sheets, a process that involves precise mechanical cutting and stacking. While effective, this approach introduces several limitations:

- Residual Mechanical Stress: Stamping, cutting, and stacking of laminations introduce internal stresses that negatively impact magnetic permeability and efficiency.
- Reduced Magnetic Performance: The presence of structural bridges and ribs diminishes the effective magnetic flux, leading to a decrease in torque production and power factor.
- Complex Assembly Process: The stacking of multiple laminations of varying shapes and sizes complicates the manufacturing process and increases production costs.

To overcome these challenges, Additive Manufacturing (AM) has emerged as a transformative solution. Through AM, it is possible to selectively modify the material properties of specific rotor regions, such as ribs, to render them non-magnetic using localized nitriding or similar treatment methods. This allows for the retention of mechanical strength while eliminating magnetic losses, significantly enhancing the overall performance of the SynRM.

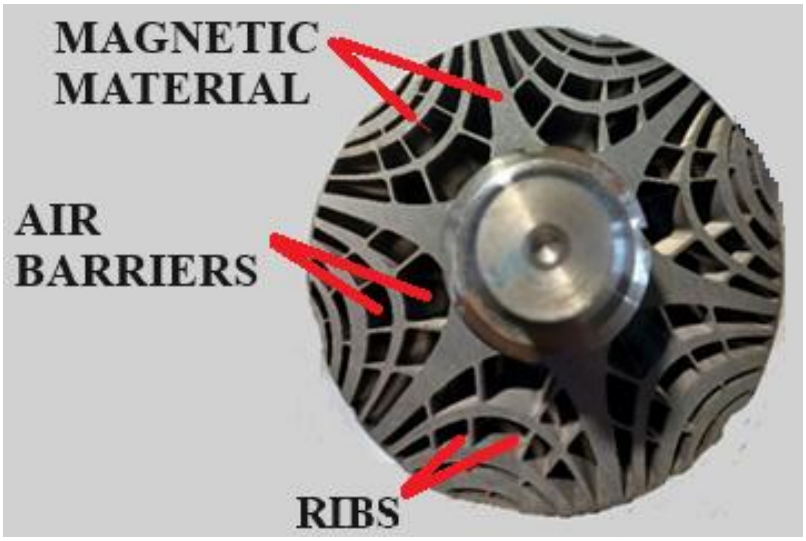

Figure 7.8: Cross section of a SynRM rotor for transversal lamination (TLA).

- Rotor Topologies and the Role of AM

From an AM design perspective, the rotor of a SynRM primarily adopts one of the following three configurations:

- Salient Pole (SP)
- Transversally Laminated Anisotropy (TLA) (Figure 7.9a)
- Axially Laminated Anisotropy (ALA) (Figure 7.9b)

Among these, the ALA topology demonstrates the highest saliency ratio and superior performance in torque, efficiency, and power factor, reaching a maximum value of 0.8 [78]. However, the traditional lamination-based fabrication of ALA rotors presents two fundamental challenges:

- Complexity and High Manufacturing Costs – The rotor structure is intricate, requiring multiple laminations of varying sizes to be precisely stacked and bonded, increasing production costs and assembly difficulty.
- Mechanical Weakness at High Speeds – The laminated rotor lacks structural robustness, limiting its operational speed range.

These manufacturing difficulties impose significant barriers to the widespread adoption of ALA rotors. This is where AM emerges as a transformative technology, enabling the efficient production of SynRM rotors while simultaneously allowing for enhanced design flexibility and performance optimization.

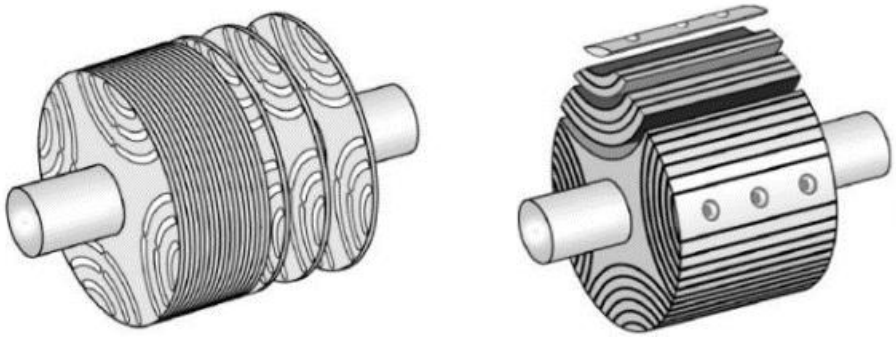

a) *b)*

Figure 7.9 ***a) Cross-lamination rotor (TLA). b) Axial lamination rotor (ALA)***

- Addressing Thermal Expansion and Structural Limitations with AM

Another major drawback of traditional SynRM manufacturing, especially in sandwiched rotor configurations, is the differential thermal expansion coefficients between laminated layers. This mismatch often necessitates additional mechanical bending and alignment procedures, increasing production complexity and failure rates. Through AM, these thermal mismatches can be addressed by:

- Directly printing the rotor in a single structure, eliminating the need for laminations.
- Tailoring material compositions to match expansion coefficients across the structure.
- Incorporating integrated cooling channels within the rotor design to regulate temperature fluctuations.

7.3.2 Performance Enhancements with Additively Manufactured PM-Assisted SynRM

Recent studies have demonstrated the feasibility of 3D printing iron cores and permanent magnets (PMs) using SLM and FDM technologies. This is particularly valuable for PM-assisted SynRMs (PMaSynRMs), where complex flux barriers must be precisely designed and fabricated. However, one of the persistent challenges in PMaSynRM manufacturing is the difficulty in obtaining permanent magnets with custom shapes, a challenge AM is uniquely suited to address. The study presented in [83] demonstrates an innovative PM-assisted SynRM design utilizing AM to integrate alternating layers of PM and Soft Magnetic Composite (SMC) materials in the rotor. Comparative simulations were conducted across four rotor configurations (Figure 7.10):

a) Standard rotor section
b) Segmented rotor section
c) PM-assisted rotor
d) Rotor with distributed magnets throughout the space

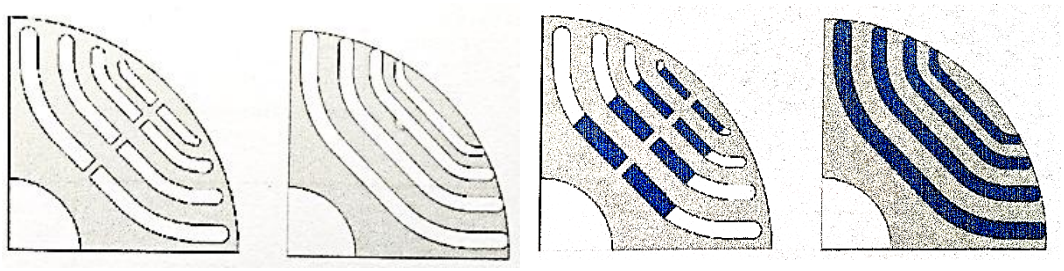

a) b) c) d)

Figure 7.10 : Rotor configurations under test [83]

Notable findings include (Table 7.4):

- The segmented rotor design, achieved by eliminating rotor bridges and center posts, increased maximum output torque by 37%.
- The incorporation of permanent magnets with a flux density of 0.49 T further elevated motor torque by 53%, attributed to additional magnetic torque contributions.
- Despite utilizing PMs with less than half the remanent flux density of conventional materials, the proposed AM-based rotor achieved a 23% higher output torque compared to traditional PM-assisted SynRM designs.

These findings underscore the potential of AM to enhance performance beyond conventional fabrication methods, even when using materials with lower magnetic properties.

Performance	Performance increase compared to conventional SynRMs		
	SynRM Segmented	***Conventional PMaSynRM (Br=1T)***	***PMaSynRM (with alternating layers of PM and SMC by AM, Br=0.49T)***
Output torque	+37%	+69,7%	+109%
Power factor	+32%	+63%	+85%

Table 7.4: Performance comparison increase compared to conventional SynRM

These results, summarized in Table 7.4, demonstrate that even though additively manufactured materials may have slightly lower magnetic properties compared to commercial alternatives, their geometric flexibility and optimized design compensate for this drawback, leading to higher overall performance.

- **Elimination of Structural Stress and Material Permeability Reduction**

Another key factor influencing SynRM performance is the mechanical stress induced by conventional magnetic component manufacturing techniques. These stresses can significantly impact performance, particularly in motors operating at different saturation levels. In cases where thin rotor ribs are required for mechanical reinforcement (e.g., cross-laminated SynRM rotors), the permeability of the material can decrease by up to 90% due to the extremely thin ribs used in traditional manufacturing processes [79]. With AM, such performance limitations are eliminated, as there is no mechanical stress from cutting or stamping processes. The ability to directly fabricate complex geometries without inducing residual stresses enhances both the structural integrity and magnetic performance of SynRMs, opening new avenues for high-speed and high-efficiency motor applications.

- **Conclusion**

The integration of AM in SynRM rotor manufacturing **represents a paradigm shift** in electric motor design and performance optimization. Key advantages include:

- Improved magnetic performance by eliminating traditional fabrication constraints (e.g., rotor ribs and bridges).
- Enhanced structural integrity through optimized AM-based designs that withstand higher operating speeds.
- Greater design flexibility, allowing for the direct fabrication of complex rotor geometries with minimal post-processing.
- Reduced material stress, leading to higher efficiency and reduced permeability losses.

With continued advancements in SLM, LENS, and FDM technologies, AM is poised to unlock the full potential of SynRM technology, paving the way for next-generation electric machines with superior efficiency, reliability, and performance.

7.3.3 Enhancing Cooling Mechanisms in SynRMs through Additive Manufacturing

The thermal management of Synchronous Reluctance Motors (SynRMs) is a crucial factor influencing their efficiency, reliability, and power density. Unlike Permanent Magnet Synchronous Motors (PMSMs), which benefit from the intrinsic heat dissipation properties of permanent magnets, SynRMs rely solely on their stator windings and core design for heat dissipation. Excessive heat accumulation can degrade electrical insulation, reduce efficiency, and shorten motor lifespan. Traditional cooling methods, such as forced air convection or liquid cooling systems, often impose design limitations and require additional external components. However, the emergence of Additive Manufacturing (AM) has revolutionized cooling strategies by enabling the direct integration of optimized cooling architectures into SynRM components.

- **AM-Enabled Cooling Architectures for SynRMs**

AM allows for the fabrication of intricate cooling geometries that were previously unfeasible using conventional manufacturing methods. Through Selective Laser Melting (SLM), Powder Bed Fusion (PBF), and Directed Energy Deposition (DED), it is now possible to integrate cooling channels, heat exchangers, and thermally conductive pathways directly within SynRM stators, windings, and housings. These advancements enhance the thermal performance of high-power SynRMs, ultimately improving their power density and reliability.

- **Internal Cooling Channels for Direct Heat Dissipation**

One of the most transformative applications of AM in SynRMs is the integration of internal cooling channels within conductor windings. This innovation offers several advantages:

- Direct Heat Extraction from Windings – Instead of relying on external airflow, cooling channels embedded within the copper or aluminum windings can facilitate localized heat dissipation.
- Improved Thermal Performance – These embedded cooling pathways prevent excessive temperature rise in high-power SynRMs, ensuring longer operational life and enhanced efficiency.
- Compact and Lightweight Design – The elimination of bulky external cooling components reduces motor size while maintaining optimal thermal performance.

- **AM-Fabricated Heat Exchangers and Frames**

Another significant breakthrough is the AM-based production of heat exchangers and motor housings with optimized cooling geometries. Using AM, designers can fabricate:

- Thin-walled heat exchangers with increased surface area for superior heat dissipation.
- Lightweight and structurally optimized motor frames that enhance convective and conductive cooling.
- Customized cooling ducts tailored to specific SynRM designs, improving overall thermal management.

These innovations increase the overall efficiency of the motor, particularly in high-speed and high-torque applications, where conventional cooling methods struggle to maintain thermal stability.

- **The Synergy Between Cooling and High-Performance Insulation Materials**

Beyond direct cooling enhancements, AM also facilitates the use of high-temperature-resistant insulation materials, further augmenting SynRM power density. The integration of ceramics and Polyether Ether Ketone (PEEK) polymers into AM-fabricated components allows these materials to withstand operating temperatures exceeding 300°C.

- Ceramic-Based Insulation – Provides superior dielectric properties and thermal stability, making it ideal for high-performance SynRMs.
- PEEK Polymers – Exhibit exceptional mechanical strength and low thermal conductivity, reducing thermal losses while maintaining insulation integrity.

By combining advanced cooling mechanisms with high-temperature insulation, AM technology bridges the power density gap between SynRMs and PMSMs, making reluctance motors a more viable alternative in high-performance applications.

- **The Future of AM-Driven Cooling Innovations for SynRMs**

The integration of AM-enabled cooling strategies in SynRM design represents a significant leap forward in thermal management, power density, and efficiency. Key takeaways include:

- Direct heat extraction through embedded cooling channels eliminates reliance on external airflow or convective cooling.
- Optimized heat exchangers and motor housings fabricated via AM maximize cooling efficiency while reducing weight.
- High-performance insulation materials (ceramics, PEEK) enhance thermal resistance, enabling SynRMs to operate at higher temperatures.

As AM technology continues to advance, it will further push the boundaries of SynRM performance, potentially positioning them as the preferred alternative to PMSMs in various industrial and transportation applications.

- **Quantitative comparative evaluation of conventional and additively produced SynRMs. [146]-[148]**

A quantitative comparison between synchronous reluctance motors (SynRMs) produced using conventional optimized manufacturing techniques and those realized through additive manufacturing (AM), particularly multi-material additive manufacturing (MMAM), reveals significant differences across key performance metrics. The rotor structure is of the TLA type; in the case of traditional production, it is made with FeSi laminations, while in the case of MMAM production, printable Fe-3.5Si silicon iron is used with ribs and bridges made of non-magnetic printable 316L material. The AM process used in this work is laser powder bed fusion (LPBF). MMAM rotors enable the fabrication of solid rotors with selective magnetic and non-magnetic materials to better guide flux.

Parameter	**Conventional SynRM**	**AM SynRM (MMAM)**	**Reference**
Torque (Nm)	~7.45	8.68	[146]
Torque Ripple (%)	27%	25%	[146]
Stator Iron Losses (W)	165.59	132	[146]
Rotor Iron Losses (W)	~20	~40 *(variable)*	[146]
Output Power (kW)	~1.17	~1.36	[146]
Efficiency (%)	~83.5%	~86%	[146]
Maximum Speed (krpm)	< ~40	> 55	[147][148]
Power Density (Normalized)	Baseline	Up to ~4×	[147][148]

Table 7.5: Quantitative comparative evaluation of conventional and MMAM produced SynRMs

This recent study explores SynRM rotors produced via MMAM, demonstrating, as described in the previous pages, that this technology can unlock performance levels previously unattainable with conventional techniques.
FEM results indicate potential increases in power density of up to 4× and much higher operating speeds at the same efficiency compared to conventional machines. The resulting AM rotors achieved rotational speeds over 55 krpm and tip speeds of ~300 m/s while maintaining comparable efficiency
This implies that AM can overcome structural limitations (mechanical weaknesses, suboptimal flow barrier paths) that normally limit traditional SynRMs.

7.4 Future Perspectives: Application of Machine Learning in Drive Control.

7.4.1 Machine Learning-Based Control Strategies for SynRM: Neural Networks and Reinforcement Learning

In synchronous reluctance motors (SynRMs), uncertainties and non-idealities are not secondary effects but constitute the dominant limitation to performance when conventional control strategies are employed. This is precisely the reason why SynRMs represent one of the electrical machine types that can benefit the most from neural networks and learning-based control techniques. The absence of permanent magnets makes the torque production mechanism entirely dependent on magnetic anisotropy, thereby amplifying the impact of magnetic, electrical, thermal, and mechanical uncertainties on the dynamic and steady-state behavior of the drive.

The electromagnetic torque of a SynRM is given by

$$T = \frac{3}{2} p (L_d - L_q) i_d i_q$$

where L_d and L_q are the d- and q-axis inductances. Unlike permanent-magnet synchronous machines (PMSMs) and induction motors (IMs), SynRMs do not possess a fixed magnetic flux reference. Consequently, all torque is generated solely through rotor saliency, making the torque production extremely sensitive to variations in the inductance difference (L_d - L_q). In practical machines, the inductances are not constants but highly nonlinear functions of the stator currents, temperature, and electrical speed, that is

$$L_d = L_d(i_d, i_q, T, \omega), \qquad L_q = L_q(i_d, i_q, T, \omega).$$

These inductances are strongly affected by iron saturation, cross-saturation between the magnetic axes, temperature-dependent permeability, and frequency-dependent effects. As a result, the optimal operating trajectories for maximum torque per ampere (MTPA) and maximum torque per voltage (MTPV) are not fixed but vary continuously across the operating domain. Even small errors in the current vector angle, on the order of a few electrical degrees, can produce significant reductions in torque and substantial increases in losses. Conventional deterministic controllers attempt to address this complexity through linearized models, lookup tables, or parametric identification; however, none of these approaches can accurately represent the full four-dimensional nonlinear mapping between (L_d , L_q , ω, T) and the resulting flux linkages and torque. In contrast, neural networks can learn this multidimensional nonlinear relationship directly from data, providing a much more faithful representation of the machine behavior. A further critical source of uncertainty is cross-saturation, which introduces strong coupling between the d and q axes. In real SynRMs, the d-axis current modifies the q-axis inductance, and vice

versa, violating the fundamental assumption of decoupled axes on which classical field-oriented control (FOC) is based. This results in misalignment of the current vector, torque nonlinearity, and degraded performance in flux-weakening operation. While PI regulators with decoupling networks can compensate for this effect only if the underlying model is accurate [100] [101], a neural network can directly learn the true coupling between axes and inherently compensate for it.

Thermal effects further compound these uncertainties. In a SynRM, the stator resistance can vary by more than 100% with temperature, the iron permeability changes, and the saturation characteristics of the magnetic circuit are altered. These variations distort the torque–current relationship and shift the MTPA and MTPV trajectories. Classical adaptive controllers typically estimate only the stator resistance, while the magnetization and saturation behavior remain unmodeled. Neural networks, by contrast, can implicitly capture the temperature dependence of the entire electromagnetic system.

Additional uncertainty arises from the mechanical and magnetic properties of the rotor. SynRM rotors rely on flux barriers and highly anisotropic magnetic paths, which are extremely sensitive to manufacturing tolerances, mechanical stress, and centrifugal deformation at high speed. These effects cause effective anisotropy to deviate from the design values and lead to significant motor-to-motor variability, as well as speed-dependent changes in magnetic behavior. Such phenomena cannot be accurately captured by analytical or parametric models, whereas a neural network trained on data from the real machine naturally incorporates them.

The inverter introduces yet another layer of uncertainty. Dead-time, semiconductor voltage drops, PWM delays, and filtering distort the applied voltages and introduce phase shifts between the commanded and actual stator currents. Because SynRM torque production is highly sensitive to d-q-axis orientation, these inverter-induced effects cause orientation errors, torque loss, and increased current demand. Classical PI controllers do not explicitly account for inverter non-idealities, whereas neural networks implicitly learn their influence through measured data.

The sensitivity of the SynRM to phase errors is considerably higher than in PMSMs. In PMSMs, torque depends primarily on the permanent magnet flux and is therefore relatively robust to d-q misalignment. In SynRMs, torque is proportional to the product $I_d * I_q$ so even a phase error of 2–3 electrical degrees can lead to a noticeable reduction in torque, increased losses, and instability in flux-weakening operation. Neural networks can estimate the true flux orientation and compensate for delays and distortions, thereby maintaining optimal current alignment.

Reinforcement learning (RL) further enhances this capability. SynRM characteristics vary with temperature, speed, aging, and inverter conditions. RL-based controllers can continuously self-adapt by minimizing performance errors and directly optimizing metrics such as torque, efficiency, and voltage utilization. This eliminates the need for explicit models, parameter identification, or look-up

tables, allowing the drive to be controlled in terms of performance rather than internal variables.

Consequently, based on the above and with the advent of modern microcontrollers equipped with high-speed processing capabilities has enabled the integration of artificial neural networks (ANN) into control schemes [102][103]. These systems, capable of parallel processing with microsecond-level response times, have facilitated the adoption of machine learning (ML)-based controllers as an alternative approach to traditional PI/PID regulators [104][105]. Unlike conventional controllers, ANN-based solutions can learn nonlinear relationships between input and output signals, allowing for more precise control and improved robustness against system disturbances. Previous studies [121][122] have demonstrated the advantages of replacing conventional PI controllers for d- and q-axis current regulation with backpropagation ANN-based controllers. The results highlighted significant improvements in current tracking accuracy, reduced oscillations, and lower harmonic distortions compared to traditional methodologies. Additionally, these ANN-based controllers exhibited enhanced robustness against detuning effects caused by variations in load and operating conditions, ensuring stable operation across a wider range of applications. Accurate estimation of rotor speed and position is crucial for the effective implementation of Field-Oriented Control (FOC) in SynRM [113]. ML-based parameter estimation techniques and temperature observers [108][109] provide a promising alternative to conventional sensor-based approaches. These methods leverage data-driven models to enhance the performance of control strategies, improving both efficiency and reliability. As illustrated in Figure 7.11, backpropagation neural networks enable real-time speed and current regulation, rotor speed estimation, and the generation of inverter driving signals, leading to superior system efficiency and stability [101]-[113].

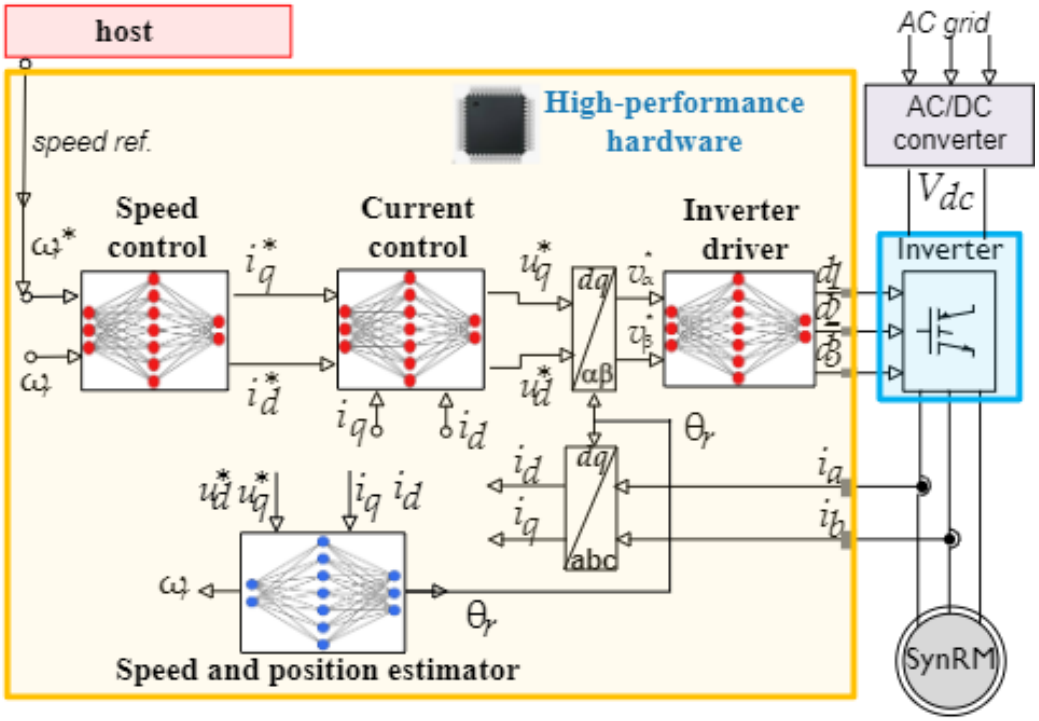

Figure 7.11: FOC control scheme of the SynRM based on Back propagation Neural Network and implemented on the high-performance hardware.

Additionally, deep learning techniques such as convolutional neural networks (CNNs) and recurrent neural networks (RNNs) are being explored for their potential to further refine estimation accuracy and dynamic response under varying load conditions [105][110][140]. Beyond ANN-based controllers, reinforcement learning (RL) has emerged as a promising subfield of unsupervised machine learning, offering significant advantages for adaptive motor control [114]-[120]. As depicted in Figure 7.12, RL operates in dynamic environments, where the controller (agent) learns optimal actions through trial-and-error interactions rather than relying on predefined datasets. Unlike traditional supervised and unsupervised learning approaches, RL eliminates the need for extensive labeled datasets, thus reducing preprocessing requirements. The RL agent interacts with the motor and drive system, selecting actions based on real-time observations and receiving feedback in the form of rewards. A policy, often represented by a deep neural network, determines the agent's actions, with parameters iteratively updated through learning algorithms to maximize cumulative rewards.

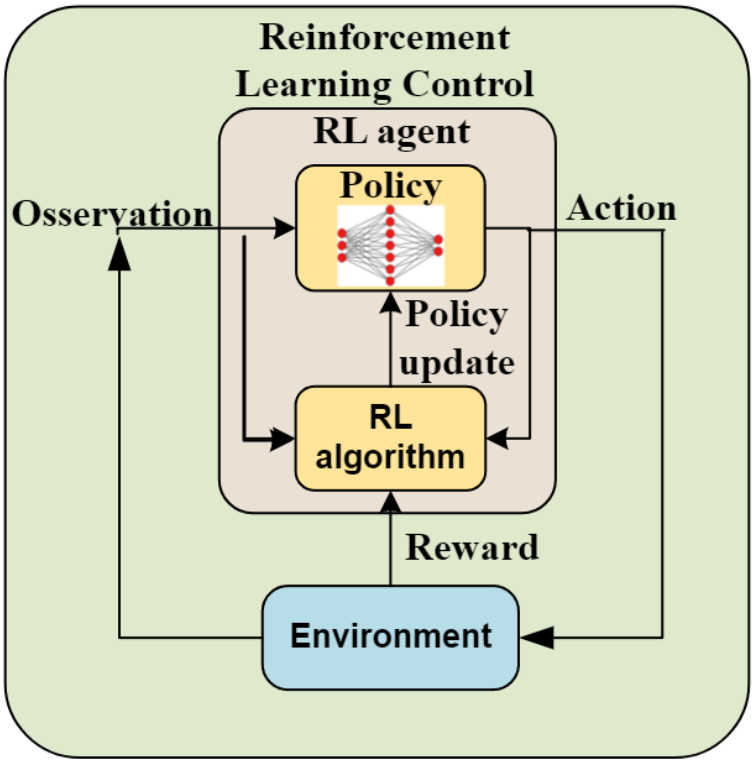

Figure 7.12. Reinforcement Learning control scheme

By employing RL, the SynRM drive system can autonomously acquire and refine optimal control actions that maximize operational efficiency and performance over time. Specifically, RL-based control strategies can optimize speed and torque according to application demands while dynamically adapting to variations in system parameters, such as temperature-dependent stator resistance and magnetic saturation. These capabilities ensure that the SynRM maintains high-performance torque and speed regulation across a broad range of operating conditions. Additionally, advanced RL techniques such as Deep Q-Networks (DQN) and Proximal Policy Optimization (PPO) are being explored to enhance real-time decision-making capabilities, allowing for seamless adaptation to external disturbances and load changes. The effectiveness of these approaches is demonstrated in Figure 7.13, where RL-based controllers enable enhanced adaptability and resilience against model uncertainties, ultimately contributing to the development of more efficient and reliable electric drive systems. Future research will further explore hybrid models that integrate RL with ANN-based estimators to create even more sophisticated, self-learning control strategies that push the boundaries of intelligent motor control.

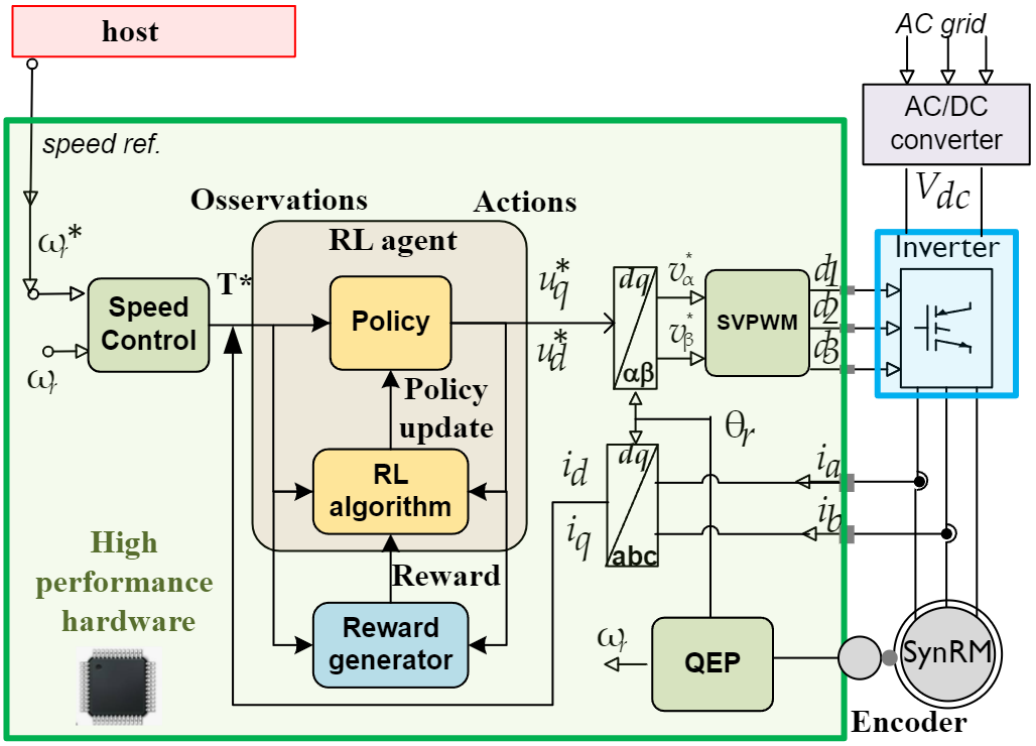

Figure 7.13: Reinforcement Learning-Based FOC Scheme for SynRM Implemented on High-Performance Hardware.

7.4.2 Real-Time Hardware Implementation for Supporting Machine Learning Algorithms

Microcontrollers featuring a single CPU are inherently unsuitable for implementing control systems based on neural networks due to their limited execution speeds and sequential processing capabilities, which are generally incompatible with the stringent cycle times required for high-performance electric motor control. Typical control cycle times range from 25 to 100 µs, and microcontrollers, even when supplemented with coprocessors and dedicated mathematical processing units, struggle to meet these real-time constraints. Their sequential execution model imposes fundamental limitations on inference speed, making them inadequate for advanced machine learning (ML)-based applications. For instance, in an experimental implementation detailed in [50], the execution time for a simple neural network inference, comprising two input neurons, two hidden layers with four neurons each, and an output layer with four neurons, was measured at 27 µs on a Texas Instruments Delfino F28379S microcontroller clocked at 200 MHz. This experiment illustrates the fundamental performance bottleneck of traditional microcontrollers when applied to real-time neural network inference for motor control applications.

- **FPGA-Based Acceleration for ML-Based SynRM Drives**

For high-performance machine learning (ML)-based SynRM drives, achieving ultra-low latency in the microsecond range is critical, particularly for applications

that require switching frequencies ranging from 10 to 40 kHz. In this context, Field-Programmable Gate Arrays (FPGAs) present a highly efficient alternative due to their capability to directly access peripheral hardware components, execute preprocessing tasks efficiently, and leverage parallel execution for significant improvements in computational throughput. Unlike microcontrollers, which process instructions sequentially, FPGAs implement ML inference through hardware acceleration, ensuring real-time operation with minimal latency. Additionally, their support for hardware-software co-design enables seamless integration of ML models with conventional control logic, optimizing both inference speed and computational efficiency. FPGAs, particularly those featuring System-on-Chip (SoC) architectures, provide a promising platform for deploying ML-based controllers in electric drives [126]-[128]. As illustrated in [105] and depicted in Figure 7.14, an ML-based SynRM control architecture implemented on a dual-core reconfigurable SoC follows a structured pipeline. The system workflow consists of:

1. Data Acquisition & Preprocessing: Sensor data is first collected via Analog-to-Digital Converters (ADCs) and subsequently processed through digital filters implemented within the FPGA fabric.
2. Neural Network Inference: The neural network model is executed within the FPGA fabric to estimate the system state x(k) in real time.
3. Outer Control Loop Execution: Running on ARM Core 0, this stage generates the reference command y(k), which may correspond to torque, speed, or position control.
4. Communication & Integration: The Advanced Extensible Interface (AXI) facilitates high-speed data exchange between the ARM processor and FPGA, ensuring minimal latency.
5. Auxiliary Functions: ARM Core 1 can be used for data logging, real-time communication, FPGA initialization, and management of essential software components, such as real-time operating systems, drivers, and application programming interfaces (APIs).

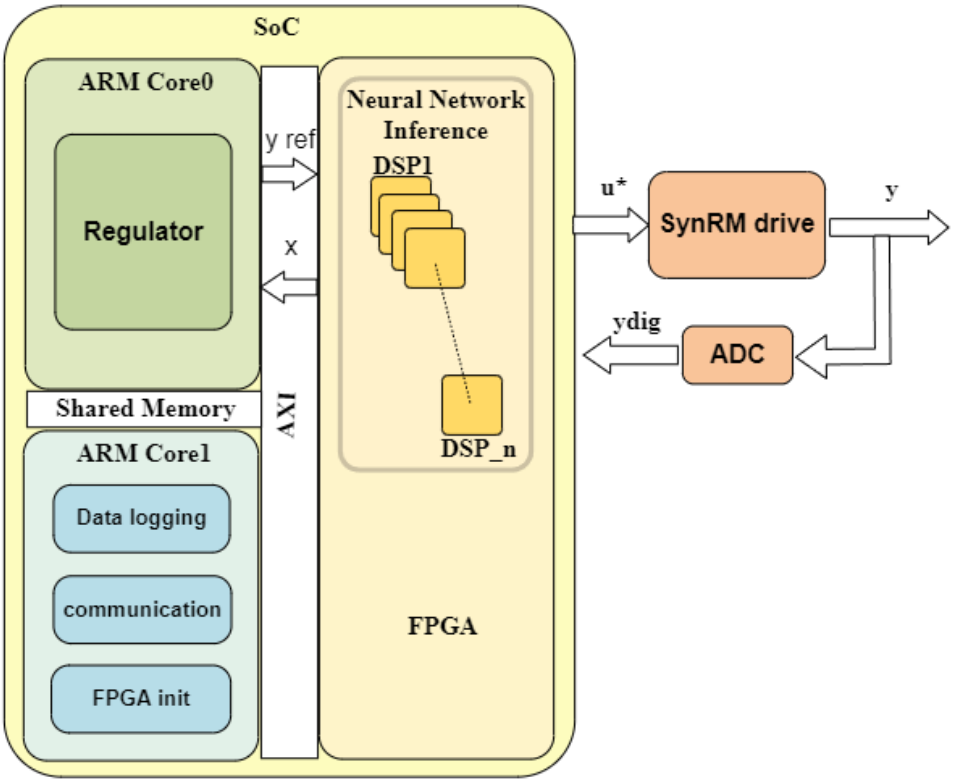

Figure 7.14. Possible FPGA-based SoC Structure for the inference of ML model for SynRM control applications

- **Advantages of Reconfigurable SoC Architectures**

Reconfigurable SoC architectures integrate memory, microprocessors, analog interfaces, and programmable logic blocks, providing an optimal balance of flexibility, computational performance, and energy efficiency. Notable examples include the Xilinx All-Programmable Zynq and Altera Reconfigurable SoC, both widely adopted in high-performance motor control applications. Recent advancements, such as the Xilinx Adaptive Computational Acceleration Platform (ACAP), further extend FPGA capabilities by enhancing computational parallelism, scalability, and adaptability for next-generation motor drive applications.

- **FPGA-Based Reinforcement Learning for SynRM Drives**

The feasibility of real-time ML-based motor control has been validated by experimental implementations on high-performance FPGA platforms. In [131], a case study involving the UltraZohm hardware platform, equipped with a Xilinx Zynq Ultrascale+ MPSoC processing unit, successfully demonstrated real-time inference of a reinforcement learning-based neural network model. The neural network architecture consisted of:

- Three hidden layers, each with 64 neurons
- An input layer with five neurons
- An output layer with seven neurons

The inference process was executed in just 7.36 µs using 32 parallel DSPs, marking a substantial performance improvement compared to single-DSP implementations, which required approximately 204 µs for the same operation. This result underscores the transformative potential of FPGA-based architectures in enabling real-time, ML-driven motor control, paving the way for highly efficient, adaptive, and scalable motor drive systems.

7.4.3 Toolchain and Custom Environments for Simplifying microcontroller Programming

- **Challenges in FPGA Programming**

Programming Field-Programmable Gate Arrays (FPGAs) presents significant challenges due to the requirement for extensive hardware design expertise and the prolonged learning curve necessary for their optimal utilization. Unlike general-purpose processors, FPGAs require the transformation of sequential high-level software descriptions into fully optimized parallel hardware architectures. This process is inherently complex, especially when deploying machine learning (ML) algorithms characterized by deep network structures and a large number of parameters. The primary challenges include:

- Computational Efficiency: Balancing processing power while minimizing resource consumption.
- Memory Access Latency: Ensuring efficient memory operations to support high-speed inference.
- Parallelism: Optimizing the implementation of ML models to leverage the full parallel processing capabilities of FPGAs.
- Resource Allocation: Managing logic blocks, memory, and processing elements to achieve optimal performance.

Despite these complexities, modern toolchains and customized environments have been developed to streamline FPGA programming, mitigating many of the difficulties associated with hardware design, as illustrated in Figure 7.15 [129][130].

- **FPGA Programming and Workflow Automation**

One of the most widely used tools for facilitating FPGA programming is HDL Coder, which provides a comprehensive workflow advisor for automating FPGA implementation across multiple platforms, including Xilinx, Microsemi, and Intel FPGAs. HDL Coder enables the generation of synthesizable Verilog and VHDL code from over 300 HDL-ready Simulink blocks, MATLAB functions, and Stateflow charts, significantly reducing the complexity of FPGA-based ML implementations. Key advantages include:

- High-Level FPGA Programming: Enabling seamless conversion of mathematical models into optimized hardware logic.
- Code Generation and Portability: Supporting Verilog/VHDL code that can be imported into Intel Quartus or Xilinx Vivado Design Suite.
- IP Core Integration: Allowing ML models to be directly integrated into FPGA-based motor controllers.

In addition to HDL Coder, Xilinx System Generator (XSG) enhances Simulink by integrating Xilinx-specific hardware blocks for system-level simulation and hardware deployment. XSG allows engineers to:

- Automatically generate HDL code for neural networks.
- Validate designs through system-level simulation.
- Efficiently deploy ML models onto FPGA platforms.

For instance, in [131], VHDL code for two multilayer perceptron (MLP) neural networks was successfully generated using HDL Coder, demonstrating its effectiveness in streamlining FPGA-based ML applications.

- **Model-Based FPGA Design Workflow**

A model-based design workflow leveraging HDL Coder and XSG offers several advantages:

- Simulation & Validation: System functionality is initially verified through MATLAB simulations, ensuring compliance with required performance metrics.
- Block Design & IP Core Integration: Once validated, the FPGA architecture is constructed using modular IP cores for efficient deployment.
- Ease of Use: Engineers unfamiliar with hardware description languages (HDLs), such as VHDL and Verilog, can utilize graphical modeling approaches for FPGA programming.
- Advanced Debugging & Verification: Simulink toolboxes provide automated testbenches and hardware-in-the-loop (HIL) simulation capabilities, simplifying HDL debugging.

As depicted in Figure 7.15, the toolchain workflow enables a streamlined process from high-level modeling to FPGA hardware deployment.

- **Neural Network Deployment on FPGA-Based Control Systems**

Regarding backpropagation neural networks, the MATLAB Neural Fitting app has proven highly effective for designing, training, and implementing neural network models. As demonstrated in [50], this tool facilitates:

- Neural Network Configuration: Allowing fine-tuning of model properties.
- Training with Diverse Datasets: Ensuring robustness and accuracy.
- Simulink Integration: Exporting trained networks as Simulink blocks for FPGA or microcontroller-based implementations.

These Simulink-based neural network models enable real-time ML inference for motor control applications, offering high-speed decision-making capabilities for intelligent drive systems.

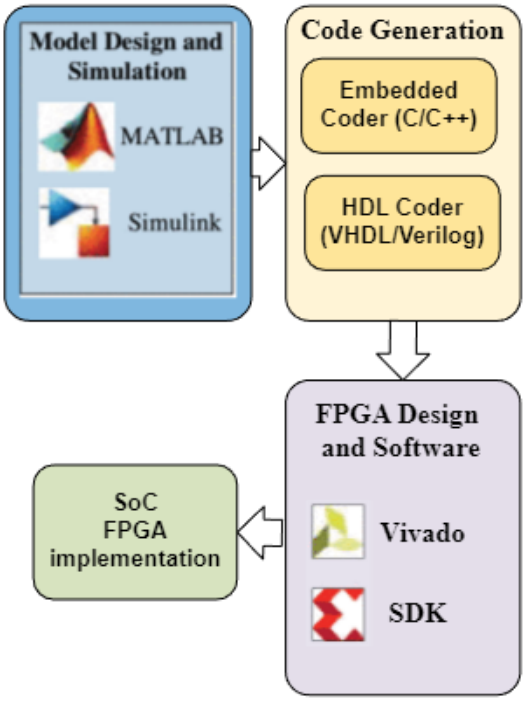

Figure 7.15 Workflow and toolchain

Modern FPGA development environments such as HDL Coder and XSG play a crucial role in bridging the gap between software-based ML models and hardware-optimized FPGA implementations. By adopting a model-based workflow, engineers can achieve:

- Efficient hardware acceleration of ML algorithms.
- Minimized development complexity.
- Optimized performance for high-speed, real-time motor control applications.

The integration of high-level design tools into FPGA programming workflows empowers engineers to focus on system-level optimizations rather than low-level hardware configurations, making FPGA-based ML deployments more accessible, scalable, and efficient for modern control applications.

Regarding backpropagation neural networks, the MATLAB tool Neural Fitting app has proven to be highly effective for designing, training, and implementing neural network models. As demonstrated in [50], this tool facilitates the configuration of various neural network properties, training of models using diverse datasets, and subsequent exportation of trained networks as Simulink blocks. These Simulink-based neural network models can then be integrated into FPGA architectures or microcontroller-based implementations, enabling real-time inference for ML-based motor control applications. In conclusion, modern FPGA development environments such as HDL Coder and XSG play a crucial role in bridging the gap between software-based ML models and hardware-optimized FPGA implementations. By adopting a model-based workflow, engineers can achieve efficient hardware acceleration of ML algorithms, minimize development complexity, and optimize performance for high-speed, real-time motor control applications.

Chapter 8

Conclusions and Future Developments

The increasing demand for sustainable and high-performance electric drives is driving the shift from internal combustion engine (ICE) vehicles to electric vehicles (EVs). This transition is influenced by stringent environmental regulations, advancements in power electronics, and the necessity for rare-earth-free motor technologies to ensure long-term sustainability and supply chain resilience. Among the emerging alternatives, synchronous reluctance motors (SynRMs) have demonstrated significant potential, providing a viable substitute for permanent magnet synchronous motors (PMSMs) by eliminating the reliance on rare-earth materials. However, despite their advantages in terms of cost-effectiveness and manufacturability, SynRMs face inherent challenges related to lower power density, torque capability, and control complexity compared to PMSMs. This doctoral research has systematically addressed these limitations by exploring advancements in motor design, power electronics, and control strategies to enhance the performance of SynRM-based electric drives.

The key findings include:

- Real-Time Simulation Platforms: The study utilized real-time simulation environments based on multiprocessor architectures to validate control algorithms before physical implementation, reducing development time, enhancing design accuracy, and improving reliability in real-world conditions.
- Innovative Motor Topologies: The study examined asymmetric rotor configurations and advanced magnetic materials such as amorphous and nanocrystalline alloys to reduce losses, enhance efficiency, and improve magnetic permeability, leading to higher torque density.
- Additive Manufacturing (AM): AM techniques have been explored to optimize rotor geometries, minimize torque ripple, and enable rapid prototyping, promoting a sustainable and resource-efficient manufacturing process. Furthermore, AM facilitates lightweight structures, allowing for improved mechanical properties and reduced energy consumption.
- Advanced Control Strategies: To address the increasing complexity of power electronics and motor control, machine learning-based methods such as artificial neural networks (ANNs) and reinforcement learning (RL) were

introduced. These techniques enable real-time adaptation to dynamic operating conditions, ensuring optimal torque control, robustness against parametric variations, and enhanced predictive maintenance capabilities.

- Multiprocessor and FPGA-Based Control: The implementation of multiprocessor control architectures, particularly FPGA-based solutions, has provided the necessary computational power for real-time motor control, overcoming the limitations of conventional microcontrollers. FPGA-based control has also enabled parallel processing for improved execution of complex control algorithms.
- Bidirectional Power Flow and Grid Integration: The research has explored the role of back-to-back converter systems for regenerative braking, energy recovery, and bidirectional grid integration, ensuring seamless interaction between electric drives and the power grid. This is particularly relevant for Vehicle-to-Grid (V2G) applications, where energy can be stored and supplied back to the grid to enhance energy efficiency.

By integrating these advancements, this research contributes to the broader goal of developing rare-earth-free, high-performance electric drives for mobility and industrial applications. Through a multidisciplinary approach encompassing motor design, advanced power electronics, artificial intelligence, and real-time control, the study lays the foundation for the widespread adoption of SynRMs in the next generation of sustainable transportation and industrial automation.

- **Future Developments**

While the research has achieved substantial progress in enhancing the viability of SynRMs, several areas warrant further investigation to push the boundaries of performance, efficiency, and practical implementation of these electrical motors:

- Optimization of Hybrid Motor Designs: The exploration of permanent magnet-assisted synchronous reluctance motors (PMaSynRMs) with ferrite magnets could further enhance torque density, power factor, and efficiency, offering a cost-effective and resource-efficient alternative to PMSMs.
- Advancements in Soft Magnetic Materials: Further studies on nanocrystalline, amorphous, and soft magnetic composite materials can improve magnetic performance and reduce hysteresis losses, contributing to higher efficiency standards, particularly for high-speed applications.
- Scalability and Industrial Implementation: Future research should focus on the scalability of SynRM designs for high-power applications, ensuring compatibility with industrial automation, railway traction, and heavy-duty electric mobility solutions. Additionally, modular motor topologies could be explored to enable cost-effective mass production.
- Innovative Cooling and Thermal Management Systems: The development of integrated cooling solutions using additive manufacturing and phase-change materials can enhance thermal management, allowing for higher operating speeds, increased power density, and extended motor lifespan.

Investigating immersive liquid cooling techniques may further push the boundaries of SynRM performance under extreme conditions.

- Additive manufacturing has the potential to enable a major technological leap for synchronous reluctance motors, provided that a paradigm shift in their design methodology is adopted. Instead of adapting SynRM geometries to the constraints of conventional lamination-based manufacturing, future designs can be conceived directly for additive processes, fully exploiting three-dimensional magnetic and mechanical optimization. This approach allows the creation of rotor and stator structures with unprecedented levels of magnetic anisotropy, optimized flux guidance, and reduced parasitic paths, which directly translate into higher torque density and improved efficiency. By enabling multi-material architectures and complex internal geometries, additive manufacturing can simultaneously enhance electromagnetic performance and mechanical robustness, particularly in high-speed applications. When combined with advanced soft magnetic materials and data-driven design optimization, this new design paradigm can overcome the traditional limitations of SynRMs, potentially elevating them to performance levels comparable to or exceeding those of permanent-magnet machines, while preserving their advantages in terms of cost, sustainability, and supply-chain security.
- Standardization and Regulatory Compliance: As SynRMs become more prevalent in various industries, future research must align with international standards and regulatory frameworks to ensure interoperability and widespread adoption. Developing automated optimization tools for compliance assessment could streamline the certification process for next-generation electric drives.

From the viewpoint of SynRM drive systems, including both control and power electronics, multiple research directions deserve deeper investigation to further extend the limits of performance, efficiency, and real-world deployability of these electric systems.

- AI-Driven Predictive Control: The application of deep reinforcement learning (DRL) and advanced neural networks for predictive maintenance and self-optimizing control could significantly improve drive performance, energy efficiency, and longevity. Adaptive AI algorithms could further reduce power losses and enhance operational stability in varying load conditions.
- Development of Ultra-Fast Real-Time Control Platforms: Continued improvements in FPGA-based and SoC control architectures will facilitate faster and more adaptive control algorithms, reducing response times and improving drive efficiency. Future developments should also investigate the use of neuromorphic computing for ultra-low-power, high-speed motor control.

- High-Efficiency Power Electronics Integration: The integration of GaN-based power devices alongside SiC MOSFETs may further enhance switching speeds and reduce conduction losses, paving the way for ultra-compact, high-efficiency power converters.
- As quantum computing technologies continue to evolve, they may offer a radically new approach to solving the highly complex optimization problems that arise in electric motor design and control. The electromagnetic, thermal, and mechanical design of machines such as synchronous reluctance motors involves a very large number of strongly coupled variables, including rotor geometry, flux barrier shapes, material properties, winding layouts, and operating constraints. These variables interact in a highly nonlinear way, creating a vast search space with many local optima that is extremely difficult to explore efficiently using conventional numerical optimization techniques.
- Integration with Vehicle-to-Grid (V2G) and Smart Grid Systems: The integration of SynRM-based electric drives into smart grids and bidirectional energy flow systems will enhance energy efficiency, grid stability, and vehicle energy management. When combined with advanced power converters and intelligent control algorithms, SynRM-based drivetrains can actively participate in smart grid services such as peak shaving, frequency regulation, and voltage support. Adaptive and learning-based control frameworks can optimize the power flow between the vehicle, the charging infrastructure, and the electrical grid, taking into account battery state of charge, grid conditions, and vehicle availability. This capability transforms electric vehicles from passive loads into active, distributed energy resources, thereby enhancing overall grid stability, increasing renewable energy utilization, and supporting the development of a more resilient and sustainable electrified ecosystem.

As the global transition toward sustainable transportation and renewable energy continues to accelerate, further innovation in SynRM technology will be essential. By addressing the identified challenges and leveraging emerging technological advancements, SynRMs hold significant potential as a cornerstone of high-efficiency, environmentally sustainable electric drive systems. This research lays a critical foundation for the development of next-generation solutions in electric mobility and industrial automation. In doing so, it contributes meaningfully to global initiatives focused on energy efficiency, sustainability, and technological innovation..

Chapter 9

Reference

1. Global Electric Motor Market Report 2021–2030: Development of High Power-to-Weight Ratio Electric Motors Gaining Momentum. Available online: https://www.globenewswire.com/news-release/2021/12/20/2355052/28124/en/Global-Electric-Motor-Market-Report-2021-2030-Development-of-High-Power-to-Weight-Ratio-Electric-Motors-Gaining-Momentum.html (27 January 2022).
2. M. Murataliyev, M. Degano, M. Di Nardo, N. Bianchi and C. Gerada, "Synchronous Reluctance Machines: A Comprehensive Review and Technology Comparison," in Proceedings of the IEEE, vol. 110, no. 3, pp. 382-399, March 2022, doi: 10.1109/JPROC.2022.3145662.
3. A. Credo, M. Villani, G. Fabri and M. Popescu, "Adoption of the Synchronous Reluctance Motor in Electric Vehicles: A Focus on the Flux Weakening Capability," in *IEEE Transactions on Transportation Electrification*, vol. 9, no. 1, pp. 805-818, March 2023, doi: 10.1109/TTE.2022. 3204435.
4. J. S. Lee and G. Choi, "Modeling and hardware-in-the-loop system realization of electric machine drives — A review," in CES Trans. on Electrical Machines and Systems, vol. 5, no. 3, pp. 194-201, Sept. 2021, doi: 10.30941/CESTEMS.2021.00023.
5. M. Tursini, L. Di Leonardo, C. Olivieri, and E. Della Loggia, "Rapid Control Prototyping of IPM Drives by Real-Time Simulation," 2013 8th EUROSIM Congress on Modelling and Simulation, 2013, pp. 364 371, doi: 10.1109/EUROSIM.2013.116.
6. R.B. Szilágyi and A. Dineva, "Case-study for HW Accelerated FEA Model for Electrical Machine Control Prototyping," 2021 17th Conf. on Electrical Machines, Drives and Power Systems (ELMA), 2021, pp. 1-5, doi: 10.1109/ELMA52514.2021.9503064.
7. L. Di Leonardo, M. Popescu, M. Tursini, and M. Villani, "Finite Elements Model Co-Simulation of an Induction Motor Drive for Traction Application," IECON 2019 - 45th Annual Conf. of the IEEE Ind. Electronics Society, 2019, pp. 1059-1065, doi: 10.1109/IECON.2019.8926853. Experimental 0.025
8. A. Rubaai, A. Ofoli, and M. Castro, "dSPACE DSP-Based Rapid Prototyping of Fuzzy PID Controls for High Performance Brushless Servo Drives," Conf. Record of the 2006 IEEE Ind. Appl. Conf. Forty First IAS Ann. Meeting, 2006, pp. 1360-1364, doi: 10.1109/IAS.2006.256707.

9. W. Werth, L. Faller, H. Liechtenecker, and C. Ungermanns, “Low Cost Rapid Control Prototyping – a useful method in Control Engineering Education,” 2020 43rd Int. Conv. on Information, Communication and Electronic Technology (MIPRO), 2020, pp. 711-715, doi: 10.23919/MIPRO48935.2020.9245122.
10. A. Kiffe, K. Witting, and F. Puschmann, “Systematic separation of electrical power systems for hardware-in-the-loop simulation,” 2017 19th European Conf. on Power Electronics and Applications (EPE’17 ECCE Europe), 2017, pp. P.1-P.10, doi: 10.23919/EPE17ECCEEurope.2017.8098995.
11. O. Vodyakho, F. Fleming, M. Steurer, and C. Edrington, “Implementation of a virtual induction machine test bed utilizing the power hardware-in-the-loop concept,” 2011 IEEE Electric Ship Technologies Symp., 2011, pp. 52-55, doi: 10.1109/ESTS.2011.5770840.
12. F. Montano, T. Ould-Bachir, and J. P. David, “An Evaluation of a High-Level Synthesis Approach to the FPGA-Based Submicrosecond Real-Time Simulation of Power Converters,” in IEEE Trans. on Ind. Electronics, vol. 65, no. 1, pp. 636-644, Jan. 2018, doi: 10.1109/TIE.2017.2716880.
13. S. Lentijo, S. D’Arco, and A. Monti, “Comparing the Dynamic Performances of Power Hardware-in-the-Loop Interfaces,” in IEEE Trans. on Ind. Electronics, vol. 57, no. 4, pp. 1195-1207, April 2010, doi: 10.1109/TIE.2009.2027246.
14. M. Caruso, A. O. Di Tommaso, M. Lombardo, R. Miceli, C. Nevoloso, and C. Spataro, “Maximum Torque Per Ampere control algorithm for low saliency ratio interior permanent magnet synchronous motors,” 2017 IEEE 6th Int. Conf. on Renewable Energy Research and Applications (ICRERA), 2017, pp. 1186-1191, doi: 10.1109/ICRERA.2017.8191241.
15. A. Di Gerlando, G. M. Foglia, and R. Perini, “Procedure to Define an Accurate Model for Saturation and Cross-Coupling in Interior Permanent Magnet Machines,” 2020 Int. Conf. on Electrical Machines (ICEM), 2020, pp. 291-297, doi: 10.1109/ICEM49940.2020.9270752.
16. M. Tursini, L. Di Leonardo, F. Verna, and D. Angrilli, “Rapid Control Prototyping of Synchronous Reluctance Motor Drives by Matlab/Simulink,” 2022 Int. Conf. on Electrical Machines, ICEM 2022, Valencia 5-8 Sept. 2022, pp. 1103–1109, doi: 10.1109/ICEM51905.2022.9910874.
17. Texas Instruments, “Sensorless Field Oriented Control of 3-Phase Induction Motors Using Control Law accelerator (CLA),” Application Report SPRABQ1-2013.
18. H. Chaudhary and A. Karuppiah, “Software Examples to Showcase Unique Capabilities of TI’s C2000 CLA,” Texas Instruments, Application note SPRACS0A-MAY 2020.
19. M. Tursini, G. Fabri, C. Olivieri, and L. Di Leonardo “A DSP-based Real-Time Simulation Equipment For Fast Motor Control Development,” Proc. of the 5th European DSP in Education and Research Conf. (EDERC),

Amsterdam, Sept. 13-14, 2012, doi: doi.org/10.1109/EDERC.2012.6532256.
20. W. H. Press, S. A. Teukolsky, W. T. Vetterling, B. P. Flannery, Numerical Recipes – The Art of Scientific Computing, 3rd ed., Cambridge University Press, 2007.
21. M. Tursini, D. Angrilli, A. Credo and G. Fabri, "High Accuracy Real-Time Simulation of Synchronous Reluctance Motor Drive Using Parallel Processing," 2023 IEEE International Electric Machines & Drives Conference (IEMDC), San Francisco, CA, USA, 2023, pp. 1-6, doi: 10.1109/IEMDC55163.2023.10238939.
22. J. W. Kolar, T. Friedli, J. Rodriguez, and P. W. Wheeler, "Review of Three-Phase PWM AC–AC Converter Topologies," *IEEE Transactions on Industrial Electronics*, vol. 58, no. 11, pp. 4988–5006, Nov. 2011, doi: 10.1109/TIE.2011.2159353.
23. J. W. Kolar and T. Friedli, "The Essence of Three-Phase PFC Rectifier Systems—Part I," *IEEE Transactions on Power Electronics*, vol. 28, no. 1, pp. 176–198, Jan. 2013, doi: 10.1109/TPEL.2012.2197867.
24. A. Marzouki, M. Hamouda, and F. Fnaiech, "A review of PWM voltage source converters based industrial applications," *2015 International Conference on Electrical Systems for Aircraft, Railway, Ship Propulsion and Road Vehicles (ESARS)*, Aachen, Germany, 2015, pp. 1–6, doi: 10.1109/ESARS.2015.7101520.
25. SP. Singh, B.L. Narasimharaju, N. Rajesh Kumar: 'Performance analysis of AC-DC power converter using PWM techniques', Energy Procedia, 2012, 14, pp. 880-886.
26. B. Wang, K. Huang, J. Cui, G. Wang: 'The Performance Analysis of Double-SVPWM in AC-DC-AC Bidirectional Converter for AC Excited Doubly Fed Generation System ', Proc. Int. Conf. on Power System Technology, Chongqing, China, 2006, pp. 1-7.
27. D. Ma, Y. Li, Y. Jin, D. Zhang, C. Wu, S. Liu: 'Design of Three-phase High Power Factor Correction Rectifier in Space AC-DC Energy System ', Proc. IEEE Int. Conf. on Information Technology, Big Data and Artificial Intelligence (ICIBA), Chongqing, China, November 2020, pp. 1116-1120.
28. F. Blaabjerg, R. Teodorescu, M. Liserre, A.V. Timbus: 'Overview of Control and Grid Synchronization for Distributed Power Generation Systems ', IEEE Trans. on Industrial Electronics, 2006, 53, (5), pp. 1398-1409.
29. N. Hoffmann, R. Lohde, M. Fischer, F.W. Fuchs, L. Asiminoaei, P.B. Thøgersen: 'A review on fundamental grid-voltage detection methods under highly distorted conditions in distributed power-generation networks', Proc. IEEE Energy Conversion Congress and Exposition, Phoenix, AZ, USA, 2011, pp. 3045-3052
30. V. Timbus, R. Teodorescu, F. Blaabjerg, M. Liserre, P. Rodriguez: 'PLL algorithm for power generation systems robust to grid voltage faults ', Proc. 37th IEEE Power

31. M. Safayatullah, M. T. Elrais, S. Ghosh, R. Rezaii and I. Batarseh, "A Comprehensive Review of Power Converter Topologies and Control Methods for Electric Vehicle Fast Charging Applications," in *IEEE Access*, vol. 10, pp. 40753-40793, 2022, doi: 10.1109/ACCESS.2022.3166935.
32. M. A. Perez, S. Bernet, J. Rodriguez, S. Kouro and R. Lizana, "Circuit Topologies, Modeling, Control Schemes, and Applications of Modular Multilevel Converters," in *IEEE Transactions on Power Electronics*, vol. 30, no. 1, pp. 4-17, Jan. 2015, doi: 10.1109/TPEL.2014.2310127.
33. A. Poorfakhraei, M. Narimani and A. Emadi, "A Review of Multilevel Inverter Topologies in Electric Vehicles: Current Status and Future Trends," in *IEEE Open Journal of Power Electronics*, vol. 2, pp. 155-170, 2021, doi: 10.1109/OJPEL.2021.3063550.
34. D. B. Rathnayake *et al*., "Grid Forming Inverter Modeling, Control, and Applications," in *IEEE Access*, vol. 9, pp. 114781-114807, 2021, doi: 10.1109/ACCESS.2021.3104617.
35. S. Thangavel, D. Mohanraj, T. Girijaprasanna, S. Raju, C. Dhanamjayulu and S. M. Muyeen, "A Comprehensive Review on Electric Vehicle: Battery Management System, Charging Station, Traction Motors," in *IEEE Access*, vol. 11, pp. 20994-21019, 2023, doi: 10.1109/ACCESS.2023.3250221.
36. A. K. Koshti and M. N. Rao, "A brief review on multilevel inverter topologies," *2017 International Conference on Data Management, Analytics and Innovation (ICDMAI)*, Pune, India, 2017, pp. 187-193, doi: 10.1109/ICDMAI.2017.8073508.
37. S. A. Q. Mohammed and J. -W. Jung, "A State-of-the-Art Review on Soft-Switching Techniques for DC–DC, DC–AC, AC–DC, and AC–AC Power Converters," in *IEEE Transactions on Industrial Informatics*, vol. 17, no. 10, pp. 6569-6582, Oct. 2021, doi: 10.1109/TII.2021.3058218.
38. S. S. G. Acharige, M. E. Haque, M. T. Arif, N. Hosseinzadeh, K. N. Hasan and A. M. T. Oo, "Review of Electric Vehicle Charging Technologies, Standards, Architectures, and Converter Configurations," in *IEEE Access*, vol. 11, pp. 41218-41255, 2023, doi: 10.1109/ACCESS.2023.3267164.
39. K. Matsuse and D. Matsuhashi, "New technical trends on adjustable speed AC motor drives," in *Chinese Journal of Electrical Engineering*, vol. 3, no. 1, pp. 1-9, 2017, doi: 10.23919/CJEE.2017.7961316.
40. M. Y. Metwly, C. L. Clark, J. He and B. Xie, "A Review of Robotic Arm Joint Motors and Online Health Monitoring Techniques," in *IEEE Access*, vol. 12, pp. 128791-128809, 2024, doi: 10.1109/ACCESS.2024.3447573.
41. M. P. Kazmierkowski and L. Malesani, "Current control techniques for three-phase voltage-source PWM converters: a survey," in *IEEE Transactions on Industrial Electronics*, vol. 45, no. 5, pp. 691-703, Oct. 1998, doi: 10.1109/41.720325.
42. Z. Liu, Y. Li and Z. Zheng, "A review of drive techniques for multiphase machines," in *CES Transactions on Electrical Machines and Systems*, vol. 2, no. 2, pp. 243-251, June 2018, doi: 10.30941/CESTEMS.2018.00030.
43. G. S. Buja and M. P. Kazmierkowski, "Direct torque control of PWM inverter-fed AC motors - a survey," in *IEEE Transactions on Industrial*

Electronics, vol. 51, no. 4, pp. 744-757, Aug. 2004, doi: 10.1109/TIE.2004.831717.
44. X. Tang, Z. Zhang, Q. Huang, and Y. Gong, “Fault Location and Fault Type Recognition of Power System Based on Wavelet Transform,” *Proc. IEEE Innovative Smart Grid Technologies - Asia (ISGT Asia)*, Chengdu, China, 2019.
45. D. K. J. S. Jayamaha, N. W. A. Lidula, and A. D. Rajapakse, “Wavelet-Based Artificial Neural Networks for Detection and Classification of DC Microgrid Faults,” *IEEE Power & Energy Society General Meeting (PESGM)*, Atlanta, GA, USA, 2019, pp. 1–5.
46. A. Khandelwal and J. Kumar, “Applications of AI for Power Electronics and Drives Systems: A Review,” *Innovations in Power and Advanced Computing Technologies (i-PACT)*, Vellore, India, 2019, pp. 1–6.
47. Y. Li, Z. Zhang, W. Liu, Z. Chen, Y. Li, and J. Yang, “A Fault Pattern and Convolutional Neural Network Based Single-phase Earth Fault Identification Method for Distribution Network,” *Proc. IEEE Innovative Smart Grid Technologies - Asia (ISGT Asia)*, Chengdu, China, 2019.
48. L. Qu, J. Zhang, and T. Gao, “Fault Diagnosis of Power Grid Based on Convolutional Neural Network,” *21st International Symposium on Distributed Computing and Applications for Business Engineering and Science (DCABES)*, Chizhou, China, 2022, pp. 82–86.
49. M. Baker, A. Y. Fard, H. Althuwaini, and M. B. Shadmand, “Real-Time AI-Based Anomaly Detection and Classification in Power Electronics Dominated Grids,” *IEEE Journal of Emerging and Selected Topics in Industrial Electronics*, vol. 4, no. 2, pp. 549–559, 2023.
50. D. Angrilli, F. Centi, and M. Tursini, “Fault-Tolerant Grid Synchronization of Three-Phase PWM Rectifiers Using Neural Network,” *12th International Conference on Power Electronics, Machines and Drives (PEMD 2023)*, Brussels, Belgium, 2023, pp. 402–409, doi: 10.1049/icp.2023.2029.
51. D. Angrilli, F. Centi, A. Credo and M. Tursini, "Neural Network Control of AC/DC Converters Robust to AC Grid Faults," *2024 IEEE 22nd Mediterranean Electrotechnical Conference (MELECON)*, Porto, Portugal, 2024, pp. 150-155, doi: 10.1109/MELECON56669.2024.10608575.
52. S. Zhao, F. Blaabjerg and H. Wang, "An Overview of Artificial Intelligence Applications for Power Electronics," in *IEEE Transactions on Power Electronics*, vol. 36, no. 4, pp. 4633-4658, April 2021, doi: 10.1109/TPEL.2020.3024914.
53. V. J. Patil, S. B. Khadake, D. A. Tamboli, H. M. Mallad, S. M. Takpere and V. A. Sawant, "Review of AI in Power Electronics and Drive Systems," *2024 3rd International conference on Power Electronics and IoT Applications in Renewable Energy and its Control (PARC)*, Mathura, India, 2024, pp. 94-99, doi: 10.1109/PARC59193.2024.10486488.
54. Y. Fassi, V. Heiries, J. Boutet and S. Boisseau, "Toward Physics-Informed Machine-Learning-Based Predictive Maintenance for Power Converters—A Review," in *IEEE Transactions on Power Electronics*, vol. 39, no. 2, pp. 2692-2720, Feb. 2024, doi: 10.1109/TPEL.2023.3328438.

55. B. Masri, H. Al Sheikh, N. Karami, H. Y. Kanaan and N. Moubayed, "A Review on Artificial Intelligence Based Strategies for Open-Circuit Switch Fault Detection in Multilevel Inverters," *IECON 2021 – 47th Annual Conference of the IEEE Industrial Electronics Society*, Toronto, ON, Canada, 2021, pp. 1-8, doi: 10.1109/IECON48115.2021.9589417.
56. Z. Zhang and X. Yuan, "Applications and Future of Automated and Additive Manufacturing for Power Electronics Components and Converters," in *IEEE Journal of Emerging and Selected Topics in Power Electronics*, vol. 10, no. 4, pp. 4509-4525, Aug. 2022, doi: 10.1109/JESTPE.2021.3135285.
57. L. Lopera, R. Rodriguez, M. Yakout, M. Elbestawi and A. Emadi, "Current and Potential Applications of Additive Manufacturing for Power Electronics," in *IEEE Open Journal of Power Electronics*, vol. 2, pp. 33-42, 2021, doi: 10.1109/OJPEL.2021.3052541.
58. X. She, A. Q. Huang, Ó. Lucía and B. Ozpineci, "Review of Silicon Carbide Power Devices and Their Applications," in *IEEE Transactions on Industrial Electronics*, vol. 64, no. 10, pp. 8193-8205, Oct. 2017, doi: 10.1109/TIE.2017.2652401.
59. M. Buffolo *et al*., "Review and Outlook on GaN and SiC Power Devices: Industrial State-of-the-Art, Applications, and Perspectives," in *IEEE Transactions on Electron Devices*, vol. 71, no. 3, pp. 1344-1355, March 2024, doi: 10.1109/TED.2023.3346369.
60. Z. Ma, S. Wang, Q. Huang and Y. Yang, "A Review of Radiated EMI Research in Power Electronics Systems," in *IEEE Journal of Emerging and Selected Topics in Power Electronics*, vol. 12, no. 1, pp. 675-694, Feb. 2024, doi: 10.1109/JESTPE.2023.3335972.
61. A. Hanif, Y. Yu, D. DeVoto and F. Khan, "A Comprehensive Review Toward the State-of-the-Art in Failure and Lifetime Predictions of Power Electronic Devices," in *IEEE Transactions on Power Electronics*, vol. 34, no. 5, pp. 4729-4746, May 2019, doi: 10.1109/TPEL.2018.2860587.
62. J. O. Gonzalez, R. Wu, S. Jahdi and O. Alatise, "Performance and Reliability Review of 650 V and 900 V Silicon and SiC Devices: MOSFETs, Cascode JFETs and IGBTs," in *IEEE Transactions on Industrial Electronics*, vol. 67, no. 9, pp. 7375-7385, Sept. 2020, doi: 10.1109/TIE.2019.2945299.
63. A. Credo, G. Fabri, M. Villani, and M. Popescu, "Adopting the Topology Optimization in the Design of High-Speed Synchronous Reluctance Motors for Electric Vehicles," in IEEE Trans. on Industry Applications, vol. 56, no. 5, pp. 5429-5438, Sept.-Oct. 2020.
64. M. Tursini, A. Credo, G. Fabri, F. Parasiliti, M. Villani: "Assessment of Control Strategies for Synchronous Reluctance Motors", Proc. Of EEMODS 2017, Rome, Italy, Sept. 6-8, 2017.
65. J. P. McSharry, P. S. Hamer, D. Morrison, J. Nessa and J. G. Rigsby, "Design, fabrication, back-to-back test of 14200-hp two-pole cylindrical-rotor synchronous motor for ASD application," in IEEE Trans. on Industry Applications, vol. 34, no. 3, pp. 526533, May-June 1998.

66. E. V. Beyerleyn and P. V. Tyuteva, “Energy efficiency of back-to-back method for induction Electron Devices (EDM)”, Novosibirsk, Russia, 2014, pp. 359-361.
67. G. V. Kumar, C. -H. Chuang, M. -Z. Lu and C. -M. Liaw, “Development of an Electric Vehicle Synchronous Reluctance Motor Drive,” in IEEE Transactions on Vehicular Technology, vol. 69, no. 5, pp. 5012-5024, May 2020, doi: 10.1109/TVT.2020.2983546.
68. K. Malekian , M.R. Sharif , J. Milimonfared “An Optimal Current Vector Control for Synchronous Reluctance Motors Incorporating Field Weakening.” 2008 10th IEEE Proc. of Int. Workshop on Advanced Motion Control, 2008, pp. 393-398, DOI: 10.1109/AMC.2008.4516099
69. A.E. Hoffer , R.H. Moncada, Pavez B. J., Tapia J. A., and Laurila L. A High “Efficiency Control Strategy for Synchronous Reluctance Generator Including Saturation.” Proc. of XXII Int. Conf. on Electrical Machines (ICEM), 2016, pp. 39-45, DOI: 10.1109/ ICELMACH.2016.7732503
70. M. E. Elsayed, O. M. Hebala, H. A. Ashour and M. S. Hamad, “A Comparative Study of Different Electric Vehicle MotorDrive Systems under Regenerative Breaking Operations,” 2021 31st International Conference on Computer Theory and Applications (ICCTA), Alexandria, Egypt, 2021, pp. 104-111, doi: 10.1109/ICCTA54562.2021.9916634.
71. D. Angrilli, F. Centi, A. Credo, G. Fabri, F. Parasiliti Collazzo, M. Tursini and M. Villani, “Energy-Efficient Back-To-Back Testing of Synchronous Reluctance Motors”, Proc. of 13th International Conference on Energy Efficiency in Motor Driven Systems (eemods) , Lucerne, Switzerland, September 2024.
72. H. Schillingmann, S. Gehler and M. Henke, "Life cycle assessment of electrical machine production considering resource requirements and sustainability," *2021 11th International Electric Drives Production Conference (EDPC)*, Erlangen, Germany, 2021, pp. 1-7, doi: 10.1109/EDPC53547.2021.9684195.
73. C. Koenen and H. -C. Reuss, "Sustainability optimization of the NdFeB magnet system of PMSMs by linking electromagnetic calculation and life cycle assessment," *Elektromechanische Antriebssysteme 2023; 9. Fachtagung (VDE OVE)*, Wien, Österreich, 2023, pp. 31-37.
74. R.-R. Moghaddam and F. Gyllensten, “Novel high-performance SynRM design method: An easy approach for a complicated rotor topology,” IEEE Trans. Ind. Electron., vol. 61, no. 9, pp. 5058–5065, Sep. 2014.
75. F. Cupertino, G. Pellegrino, and C. Gerada, “Design of synchronous reluctance motors with multiobjective optimization algorithms,” IEEE Trans. Ind. Appl., vol. 50, no. 6, pp. 3617–3627, Nov. 2014.
76. A. Credo, G. Fabri, M. Villani, and M. Popescu, “A robust design methodology for synchronous reluctance motors,” IEEE Trans. Energy Convers., vol. 35, no. 4, pp. 2095–2105, Dec. 2020.
77. V. Abramenko, I. Petrov, J. Nerg and J. Pyrhönen, "Synchronous Reluctance Motors With an Axially Laminated Anisotropic Rotor as an

Alternative in High-Speed Applications," in *IEEE Access*, vol. 8, pp. 29149-29158, 2020, doi: 10.1109/ACCESS.2020.2971685.

78. T. Matsuo and T. A. Lipo, "Rotor design optimization of synchronous reluctance machine," in IEEE Transactions on Energy Conversion, vol. 9, no. 2, pp. 359-365, June 1994, doi: 10.1109/60.300136.
79. A. Credo, I. Petrov, J. Pyrhönen and M. Villani, "Impact of Manufacturing Stresses On Multiple-Rib Synchronous Reluctance Motor Performance," in IEEE Transactions on Industry Applications, vol. 59, no. 2, pp. 1253-1262, March-April 2023, doi: 10.1109/TIA.2022.3207117.
80. D. Angrilli and E. Chiricozzi, "Synchronous Reluctance Motors: Opportunities in the Era of New Materials, Additive Manufacturing, and Machine Learning," *2024 International Conference on Electrical Machines (ICEM)*, Torino, Italy, 2024, pp. 1-7, doi: 10.1109/ICEM60801.2024.10700375.
81. A. Krings, M. Cossale, A. Tenconi, J. Soulard, A. Cavagnino and A. Boglietti, "Magnetic Materials Used in Electrical Machines: A Comparison and Selection Guide for Early Machine Design," in *IEEE Industry Applications Magazine*, vol. 23, no. 6, pp. 21-28, Nov.-Dec. 2017, doi: 10.1109/MIAS.2016.2600721.
82. A. Krings, A. Boglietti, A. Cavagnino and S. Sprague, "Soft Magnetic Material Status and Trends in Electric Machines," in *IEEE Transactions on Industrial Electronics*, vol. 64, no. 3, pp. 2405-2414, March 2017, doi: 10.1109/TIE.2016.2613844.
83. M. Ibrahim, F. Bernier, J.-M. Lamarre: “Design of a PM-Assisted Synchronous Reluctance Motor Utilizing Additive Manufacturing of Magnetic Materials” In Proceedings of the 2019 IEEE Energy Conversion Congress and Exposition (ECCE), Baltimore, MD, USA, 29 September–3 October 2019; pp. 1663–1668.
84. X. Wang, S. Zhou, L. Wu, M. Zhao and C. Hu, "Iron Loss and Thermal Analysis of High Speed PM motor Using Soft Magnetic Composite Material," *2019 22nd International Conference on Electrical Machines and Systems (ICEMS)*, Harbin, China, 2019, pp. 1-4, doi: 10.1109/ICEMS.2019.8922504.
85. T. Pham, P. Kwon, S. Foster: “Additive Manufacturing and Topology Optimization of Magnetic Materials for Electrical Machines, A Review.” *Energies* **2021**, *14*, 283. https://doi.org/10.3390/en14020283
86. L. Szabó, D. Fodor: “The Key Role of 3D Printing Technologies in the Further Development of Electrical Machines” in Machines 2022, 10, 330.
87. A. Selema, M. N. Ibrahim and P. Sergeant, "Additively Manufactured Ultralight Shaped-Profile Windings for HF Electrical Machines and Weight-Sensitive Applications," in IEEE Transactions on Transportation Electrification, vol. 8, no. 4, pp. 4313-4324, Dec. 2022, doi: 10.1109/TTE.2022.3173126
88. N. Simpson, D. J. North, S. M. Collins, and P. H. Mellor, “Additive manufacturing of shaped profile windings for minimal AC loss in electrical

machines," IEEE Trans. Ind. Appl., vol. 56, no. 3, pp. 2510–2519, May 2020, doi: 10.1109/TIA.2020.2975763.

89. F. Wu, A. El-Refaie, and A. Al-Qarni, "Additively manufactured hollow conductors integrated with heat pipes: Design tradeoffs and hardware demonstration," IEEE Trans. Ind. Appl., vol. 57, no. 4, pp. 3632–3642, Jul. 2021, doi: 10.1109/TIA.2021.3076423.
90. A. El-Refaie, "Role of advanced materials in electrical machines," in *CES Transactions on Electrical Machines and Systems*, vol. 3, no. 2, pp. 124-132, June 2019, doi: 10.30941/CESTEMS.2019.00018.
91. C. Subramaniam, T. Yamada, K. Kobashi, A. Sekiguchi, D.N. Futaba, M. Yumura, K. Hata: " One hundred fold increase in current carrying capacity in a carbon nanotube–copper composite." Nat. Commun. 2013, 4, 2202. https://doi.org/10.1038/ncomms3202.
92. Wu, F.; El-Refaie, A.M. Towards fully additively-manufactured permanent magnet synchronous machines: Opportunities and challenges. In Proceedings of the International Electric Machines & Drives Conference (IEMDC 2019), San Diego, CA, USA, 12 15 May 2019; pp. 2225–2232. https://doi.org/10.1109/IEMDC.2019.8785210.
93. Advanced APTIV™ Film Electrical Insulation for Cost-Effective, High Power Density E-Motors; Victrex Plc: Thornton-Cleveleys, UK, 2017.
94. M.U. Naseer, A. Kallaste, B. Asad, T. Vaimann, A. Rassõlkin: "A Review on Additive Manufacturing Possibilities for Electrical Machines." *Energies* **2021**, *14*,1940.
95. R. T. Ugale and B. N. Chaudhari, "Rotor Configurations for Improved Starting and Synchronous Performance of Line Start Permanent-Magnet Synchronous Motor," in *IEEE Transactions on Industrial Electronics*, vol. 64, no. 1, pp. 138-148, Jan. 2017, doi: 10.1109/TIE.2016.2606587.
96. M. Villani, G. Fabri, A. Credo, L. Di Leonardo and F. Parasiliti Collazzo, "Line-Start Synchronous Reluctance Motor: A Reduced Manufacturing Cost Avenue to Achieve IE4 Efficiency Class," in *IEEE Access*, vol. 10, pp. 100094-100103, 2022, doi: 10.1109/ACCESS.2022.3208154.
97. M. Barcaro, N. Bianchi and F. Magnussen, "Permanent-Magnet Optimization in Permanent-Magnet-Assisted Synchronous Reluctance Motor for a Wide Constant-Power Speed Range," in *IEEE Transactions on Industrial Electronics*, vol. 59, no. 6, pp. 2495-2502, June 2012, doi: 10.1109/TIE.2011.2167731.
98. H. Cai, B. Guan and L. Xu, "Low-Cost Ferrite PM-Assisted Synchronous Reluctance Machine for Electric Vehicles," in *IEEE Transactions on Industrial Electronics*, vol. 61, no. 10, pp. 5741-5748, Oct. 2014, doi: 10.1109/TIE.2014.2304702.
99. S.Richard Sutton and G. Andrew Barto, "Reinforcement Learning: An Introduction" in , The MIT Press, 2018. Cambridge, Massachusetts. London, England.
100. K.J. Åström, T. Hägglund,"The future of PID control, Control Engineering Practice" Volume 9, Issue 11,2001.

101. A. Najem, A. Moutabir, M. Rafik and A. Ouchatti, "Comparative Study of PMSM Control Using Reinforcement Learning and PID Control," 2023 3rd International Conference on Innovative Research in Applied Science, Engineering and Technology (IRASET), Mohammedia, Morocco, 2023, pp. 1-5, doi: 10.1109/IRASET57153.2023.10153024.
102. Z. Yanhong, Z. Dean and Z. Jiansheng, "Research on PID controller based on the BP neural network," Proceedings of 2011 International Conference on Electronic & Mechanical Engineering and Information Technology, Harbin, China, 2011, pp. 516-519, doi: 10.1109/EMEIT.2011.6022969.
103. M. Nicola and C. -I. Nicola, "Tuning of PI Speed Controller for PMSM Control System Using Computational Intelligence," 2021 21st International Symposium on Power Electronics (Ee), Novi Sad, Serbia, 2021, pp. 1-6, doi: 10.1109/Ee53374.2021.9628297.
104. M. Schenke, W. Kirchgässner and O. Wallscheid, "Controller design for electrical drives by deep reinforcement learning: A proof of concept", IEEE Trans. Ind. Informat., vol. 16, no. 7, pp. 4650-4658, Jul. 2020.
105. S. Zhang, O. Wallscheid and M. Porrmann, "Machine Learning for the Control and Monitoring of Electric Machine Drives: Advances and Trends," in IEEE Open Journal of Industry Applications, vol. 4, pp. 188-214, 2023, doi: 10.1109/OJIA.2023.3284717.
106. M. X. Bui, F. W, R. Duta and M. F. Rahman, "Reinforcement Learning based Method for Online Parameter Identification of the Permanent Magnet Synchronous Machines," *2024 IEEE 10th International Power Electronics and Motion Control Conference (IPEMC2024-ECCE Asia)*, Chengdu, China, 2024, pp. 2274-2279, doi: 10.1109/IPEMC-ECCEAsia60879.2024.10567595.
107. W. Nawae and K. Thongpull, "PMSM Torque Estimation Based on Machine Learning Techniques," *2020 International Conference on Power, Energy and Innovations (ICPEI)*, Chiangmai, Thailand, 2020, pp. 137-140, doi: 10.1109/ICPEI49860.2020.9431433.
108. W. Kirchgässner, O. Wallscheid and J. Böcker, "Estimating Electric Motor Temperatures With Deep Residual Machine Learning," in *IEEE Transactions on Power Electronics*, vol. 36, no. 7, pp. 7480-7488, July 2021, doi: 10.1109/TPEL.2020.3045596.
109. O. Wallscheid, "Thermal Monitoring of Electric Motors: State-of-the-Art Review and Future Challenges," in *IEEE Open Journal of Industry Applications*, vol. 2, pp. 204-223, 2021, doi: 10.1109/OJIA.2021.3091870.
110. O. Aydogmus and G. Boztas, "Deep Learning-Based Approach for Speed Estimation of a PMa-SynRM," *2019 11th International Conference on Electrical and Electronics Engineering (ELECO)*, Bursa, Turkey, 2019, pp. 172-176, doi: 10.23919/ELECO47770.2019.8990412.
111. Y. -J. Lee, M. -S. Lee and Y. -D. Yoon, "Estimation of SynRM Flux Saturation Model at Standstill using Artificial Neural Network," *2023 11th International Conference on Power Electronics and ECCE Asia (ICPE*

2023 - ECCE Asia), Jeju Island, Korea, Republic of, 2023, pp. 3051-3056, doi: 10.23919/ICPE2023-ECCEAsia54778.2023.10213956.

112. A. Hassan, M. El-Habrouk, T. H. Abdelhamid and S. Deghedie, "A Novel Neural Network-Based Method for the Implementation of Space Vector PWM for Three-Level Voltage-Source Inverters," 2020 8th ICCMA, Moscow, Russia, 2020, pp. 172-178, doi: 10.1109/ICCMA51325.2020.9301529.
113. M. E. Elbuluk, L. Tong and I. Husain, "Neural-network-based model reference adaptive systems for high-performance motor drives and motion controls", IEEE Trans. Ind. Appl., vol. 38, no. 3, pp. 879-886, May/Jun. 2002.
114. A. Deng, W. Yang, G. Hu, W. Huang and D. Xu, "Reinforcement Learning based Weight-Tuning Model Predictive Control of Permanent Magnet Synchronous Motor," 2024 IEEE 10th International Power Electronics and Motion Control Conference (IPEMC2024-ECCE Asia), Chengdu, China, 2024, pp. 317-322, doi: 10.1109/IPEMC-ECCEAsia60879.2024.10567931.
115. J. Zhao, C. Yang, W. Gao and L. Zhou, "Reinforcement Learning and Optimal Control of PMSM Speed Servo System," in *IEEE Transactions on Industrial Electronics*, vol. 70, no. 8, pp. 8305-8313, Aug. 2023, doi: 10.1109/TIE.2022.3220886.
116. D. García-Pérez, M. Saeed, I. Díaz, J. M. Enguita, J. M. Guerrero and F. Briz, "Machine Learning for Inverter-Fed Motors Monitoring and Fault Detection: An Overview," in *IEEE Access*, vol. 12, pp. 27167-27179, 2024, doi: 10.1109/ACCESS.2024.3366810.
117. A. Salah, O. A. Mohareb and H. -C. Reuss, "Fault Diagnosis for Automotive Electric Machines Based on a Combined Machine Learning and Parameter Estimation Method: An Approch for Predective Maintenance," 2023 International Conference on Control, Automation and Diagnosis (ICCAD), Rome, Italy, 2023, pp. 1-7, doi: 10.1109/ICCAD57653.2023.10152363.
118. S. Singh, R. Gill, R. Kumar, A. Shrivastava, A. P. Srivastava and G. Thakur, "A Comparative Analysis of Machine Learning Algorithms for Predictive Maintenance in Electrical Systems," 2024 4th International Conference on Innovative Practices in Technology and Management (ICIPTM), Noida, India, 2024, pp. 1-6, doi: 10.1109/ICIPTM59628.2024.10563826.
119. E. Kiliç, "Deep Reinforcement Learning-Based Controller for Field-Oriented Control of SynRM," in IEEE Access, vol. 13, pp. 2855-2861, 2025, doi: 10.1109/ACCESS.2024.3524156.
120. Z. Deng, X. Huo, Q. Du and Q. Liu, "Reinforcement Learning-based Data-driven Control Design for Motion Control Systems," 2024 36th Chinese Control and Decision Conference (CCDC), Xi'an, China, 2024, pp. 5745-5749, doi: 10.1109/CCDC62350.2024.10587783.

121. X. Fu and S. Li, "A Novel Neural Network Vector Control Technique for Induction Motor Drive," in IEEE Transactions on Energy Conversion, vol. 30, no. 4, pp. 1428-1437, Dec. 2015, doi: 10.1109/TEC.2015.2436914.
122. H. P. H. Anh, C. V. Kien, T. T. Huan and P. Q. Khanh, "Advanced Speed Control of PMSM Motor Using Neural FOC Method," 2018 4th International Conference on Green Technology and Sustainable Development (GTSD), Ho Chi Minh City, Vietnam, 2018, pp. 696-701, doi: 10.1109/GTSD.2018.8595688.
123. A. Traue, G. Book, W. Kirchgässner and O. Wallscheid, "Toward a Reinforcement Learning Environment Toolbox for Intelligent Electric Motor Control," in *IEEE Transactions on Neural Networks and Learning Systems*, vol. 33, no. 3, pp. 919-928, March 2022, doi: 10.1109/TNNLS.2020.3029573.
124. Reinforcement Learning Toolbox™ User's Guide, Matlab and Simulink, MathWorks, Natick, MA, USA, 2020
125. E. Monmasson, M. Hilairet, G. Spagnuolo and M. Cirstea, "System-on-chip FPGA devices for complex electrical energy systems control", IEEE Ind. Electron. Mag., vol. 16, no. 2, pp. 53-64, Jun. 2022.
126. A. M. Soares, L. C. Leite, J. O. Pinto, L. E. Da Silva, B. K. Bose and M. E. Romero, "Field programmable gate array (FPGA) based neural network implementation of stator flux oriented vector control of induction motor drive", Proc. IEEE Int. Conf. Ind. Technol., pp. 31-34, 2006.
127. A. Shawahna, S. M. Sait and A. El-Maleh, "FPGA-Based Accelerators of Deep Learning Networks for Learning and Classification: A Review", IEEE Access, vol. 7, pp. 7823-7859, 2019.
128. M. Rothmann and M. Porrmann, "A survey of domain-specific architectures for reinforcement learning", IEEE Access, vol. 10, pp. 13753-13767, 2022.
129. S. Wendel et al., "UltraZohm - a Powerful Real-Time Computation Platform for MPC and Multi-Level Inverters", Int. Symp. Pred. Control of Elect. Drives and Power Electron. (PRECEDE), pp. 1-6, 2019.
130. AMD XILINX, DS891 (v1.10) Novembre 7, 2022
https://docs.amd.com/v/u/en-US/ds891-zynq-ultrascale-plus-overview
131. T. Schindler and A. Dietz, "Real-time inference of neural networks on FPGAs for motor control applications", Proc. 10th Int. Electr. Drives Prod. Conf., pp. 1-6, 2020
132. MB. Bahrani, S. Kenzelmann and A. Rufer, "Multivariable-PI-Based dq Current Control of Voltage Source Converters With Superior Axis Decoupling Capability," in IEEE Trans. on Industrial Electronics, vol. 58, no. 7, pp. 3016-3026, July 2011, doi: 0.1109/TIE.2010.2070776.
133. I. Boldea: "Reluctance Synchronous Machines and Drives." Clarendon Press, Oxford (UK), 1996
134. K. Yahia, D. Matos, J.O. Estima, A.J.M. Cardoso: " Modeling Synchronous Reluctance Motors Including Saturation, Iron Losses and Mechanical

Losses." 2014 Proc. of Int. Symposium on Power Electronics, Electrical Drives, Automation and Motion, 2014, pp. 601-606, DOI: 10.1109/SPEEDAM.2014.6871965

135. P.H. Truong, D. Flieller, N.K. Nguyen, J. Mercklé, T. Mai: "Optimal Efficiency Control of Synchronous Reluctance Motors-based ANN Considering Cross Magnetic Saturation and Iron Losses. Proc. of 41st Annual Conf. of the IEEE Industrial Electronics Society, 2015, pp. 4690-4695, DOI: 10.1109/IECON.2015.7392832
136. M. N. Ibrahim, P. Sergeant, and E. M. Rashad: " Relevance of Including Saturation and Position Dependence in the Inductances for Accurate Dynamic Modeling and Control of SynRMs." IEEE Trans. on Industry Applications, 2017, Vol. 53, Issue 1.
137. M. Kumar, & Ramachandran, Ramakrishnan & Omarbekova, Alnura & Kumar, Santhosh. (2021). Experimental characterization of mechanical properties and microstructure study of polycarbonate (PC) reinforced acrylonitrile-butadiene-styrene (ABS) composite with varying PC loadings. AIMS Materials Science. 8. 18-28. 10.3934/matersci.2021002.
138. Raj, Karpaga & Ramesh, R & Kumar T, Selva & Kumar, N. (2020). The role of laser in manufacturing of shape memory alloy (sma). IOP Conference Series: Materials Science and Engineering. 912. 032008. 10.1088/1757-899X/912/3/032008.
139. Wüst, Philipp & Edelmann, Andre & Hellmann, Ralf. (2020). Areal Surface Roughness Optimization of Maraging Steel Parts Produced by Hybrid Additive Manufacturing. Materials. 13. 418. 10.3390/ma13020418.
140. H. Mesai Ahmed, I. Jlassi, A. J. Marques Cardoso and A. Bentaallah, "Model-Free Predictive Current Control of Synchronous Reluctance Motors Based on a Recurrent Neural Network," in *IEEE Transactions on Industrial Electronics*, vol. 69, no. 11, pp. 10984-10992, Nov. 2022, doi: 10.1109/TIE.2021.3120480.
141. Kandel, E. R., Schwartz, J. H., & Jessell, T. M. (2013). Principles of Neural Science, 5th ed.
(McGraw-Hill, New York)
142. Bear, M. F., Connors, B. W., & Paradiso, M. A. (2020). Neuroscience: Exploring the Brain, 5th ed. (Lippincott Williams & Wilkins)
143. Islam, Mohaiminul & Chen, Guorong & Jin, Shangzhu. (2019). An Overview of Neural Network. American Journal of Neural Networks and Applications. 5. 05. 10.11648/j.ajnna.20190501.12.
144. Mohaiminul Islam, Guorong Chen, Shangzhu Jin. An Overview of Neural Network. American Journal of Neural Networks and Applications. Vol. 5, No. 1, 2019, pp. 7-11. doi: 10.11648/j.ajnna.20190501.12
145. McCulloch, Warren & Pitts, Walter. (2021). A Logical Calculus of the Ideas Immanent in Nervous Activity (1943). 10.7551/mitpress/12274.003.0011.

146. S. Akbar, Y. T. Bekele, A. Ebrahimi and B. Ponick, "Enhanced Design and Electromagnetic Analysis of Synchronous Reluctance Machines Using Multi-Material Additive Manufacturing," *2025 IEEE International Electric Machines & Drives Conference (IEMDC)*, Houston, TX, USA, 2025, pp. 396-401, doi: 10.1109/IEMDC60492.2025.11061042.
147. D. Newman *et al*., "Solid High-Speed Synchronous Reluctance Rotor Enabled by Multi-Material Additive Manufacturing," *2023 IEEE Energy Conversion Congress and Exposition (ECCE)*, Nashville, TN, USA, 2023, pp. 3965-3972, doi: 10.1109/ECCE53617.2023.10362787.
148. D. Newman *et al*., "Development of Solid Synchronous Reluctance Rotors With Multi-Material Additive Manufacturing," in *IEEE Transactions on Industry Applications*, vol. 61, no. 2, pp. 2911-2923, March-April 2025, doi: 10.1109/TIA.2024.3522210.